

Enhancement of Controllability in Distribution Grid by Means of Power Electronics Components based Distributed and Centralized Solutions

Dissertation

zur Erlangung des akademischen Grades
eines Doktors der Ingenieurwissenschaften

(Dr. -Ing)

Technische Fakultät
der Christian-Albrechts-Universität zu Kiel

vorgelegt von

M.Sc. Xiang Gao

Jahr
2022

1. Gutachter:	Prof. Marco Liserre, Ph.D.
2. Gutachter:	Prof. Andreas Ulbig Dr. Sc.
3. Gutachter:	Prof. Krzysztof Rudion Dr.-Ing.
Datum der mündlichen Prüfung:	01.06.2022

Erklärung

Ich erkläre an Eides statt, dass ich die Dissertation zum Thema:

***Enhancement of Controllability in Distribution Grid by Means of Power Electronics
Components based Distributed and Centralized Solutions***

abgesehen von der Betreuung durch Herrn Prof. Marco Liserre selbstständig und ohne Hilfe angefertigt habe und bisher weder ganz noch zum Teil an einer anderen Stelle im Rahmen eines Prüfungsverfahrens vorgelegt, veröffentlicht oder zur Veröffentlichung eingereicht habe. Weiterhin versichere ich hiermit, dass ich die vorliegende Arbeit unter Einhaltung der Regeln guter wissenschaftlicher Praxis der Deutschen Forschungsgemeinschaft angefertigt habe und alle von anderen Autoren wörtlich übernommenen Stellen wie auch die sich an die Gedankengänge anderer Autoren eng anlehnenden Ausführungen meiner Arbeit besonders gekennzeichnet und die entsprechenden Quellen angegeben sind.

Kiel, den , Juni 2021

Xiang Gao

Danksagung

Die vorliegende Arbeit entstand während meiner Tätigkeit als wissenschaftlicher Mitarbeiter am Lehrstuhl für Leistungselektronik an der Technischen Fakultät der Christian-Albrechts-Universität zu Kiel. Die dieser Arbeit zugrundeliegenden Untersuchungen wurden im Rahmen des vom Bundesministerium für Wirtschaft und Klimaschutz (BMWK) Deutschland geförderten Projekts mit dem Titel "Kiel als Vorbild für die Errichtung von Ladeinfrastruktur in einem flexiblen Stromnetz zur Umsetzung einer Emissionsreduktion im Transportsektor" (KielFlex) erarbeitet.

Mein besonderer Dank gilt meinem Doktorvater, Prof. Marco Liserre, der mir die Möglichkeit zur Promotion eröffnet hat. Für die Betreuung und die Unterstützung möchte ich mich herzlich bedanken. Für die Übernahme der Koreferate bedanke ich mich herzlich bei Prof. Andreas Ulbig (RWTH Aachen University) und Prof. Krzysztof Rudion (Universität Stuttgart).

Bei Dr.-Ing. Giovanni De Carne, und Prof. Giampaolo Buticchi bedanke ich mich für die vielen fachlichen Diskussionen und Hinweise. Zusätzlich möchte ich mich bei Prof. Constantine Vournas (National Technical University of Athens), Prof. Mario Paolone (École Polytechnique Fédérale de Lausanne), Prof. Fabrizio Sossan (Mines ParisTech), und Dr. Konstantina Christakou für die Kooperation und die Diskussionen bedanken.

Meinen Kollegen, die mich in meiner Zeit am Lehrstuhl begleitet haben, insbesondere Prof. Rongwu Zhu, Prof. Zhi-xiang Zou, und Dr.-Ing. Marius Langwasser, möchte ich für die fachlichen Diskussionen und die gute Zusammenarbeit danken. Bei Dr. Sante Pugliese und Herrn Sebastian Brüske bedanke ich mich für die praktische Unterstützung bei der Validierung meiner Arbeit im Labor. Für die administrative Unterstützung bedanke ich mich bei Herrn Bernd Doneit und allen Sekretärinnen am Lehrstuhl.

Bedanken möchte ich mich zudem bei meiner Familie, die mich während meines Studiums und auch während meiner Promotion stets unterstützt haben.

Kiel im Juni 2022

Xiang Gao

Contents

Kurzfassung der Arbeit	V
Summary	VI
Used Symbols and Abbreviations	VII
1 Introduction	1
1.1 Motivation of Distribution Grid Controllability Enhancement	1
1.2 Motivation of Development of Grid Operation Solutions with Power Electronics Components	2
1.3 Research Proposal	3
1.4 Structure of the Thesis	4
1.5 Assignment of Publications to the Chapters of this Thesis	6
2 Operation in Distribution Grid with Power Electronics Components	9
2.1 Distribution Grid Operation: Development, Challenges, and Solutions	9
2.1.1 Development in distribution grid nowadays	9
2.1.2 Challenges caused by innovations in distribution grid nowadays	10
2.1.3 Existing solutions to counter the operation challenges	12
2.2 Power Electronics Components for Grid Controllability Enhancement	18
2.2.1 Smart transformer	18
2.2.2 Energy storage static synchronous compensator (ES-STATCOM)	22
2.2.3 Fast charging station	24
2.3 Development of Innovative Grid Controllability Enhancement Solutions based on Power Electronics Components	27
2.3.1 Grid connecting strategies	27
2.3.2 Distributed and centralized solutions	29
2.3.3 Common features of the developed grid enhancement solutions	29
2.4 Summary	31
3 Distributed Load-Leveling Solution with Fast Charging Stations	33
3.1 Power-Voltage Sensitivity based Load-Leveling	33
3.1.1 Power-voltage sensitivity	34
3.1.2 Online load identification	35
3.1.3 Power regulation with fast charging stations	36
3.1.4 Feasibility analysis with different grid conditions	39
3.1.5 On-load tap changer based conservation voltage reduction	39
3.1.6 Time-line for implementation of the proposed approach	40
3.2 Load-Leveling Scheme based on Power-Voltage Sensitivity	41
3.2.1 Stage 1: mitigation of power mismatch	41
3.2.2 Stage 2: minimization of losses	45
3.3 Case Study Setup for Analysis	45
3.3.1 Grid under study	46

3.3.2	Scenarios of Monte-Carlo analysis	48
3.3.3	Testing cases	49
3.4	Results and Analysis of Case Study	50
3.4.1	Load-leveling performance in time domain	50
3.4.2	Load-leveling performance based on the Monte-Carlo analysis . . .	52
3.4.3	Analysis of the losses with load-leveling	55
3.4.4	Analysis of the impacts on operation issues from the load-leveling .	58
3.5	Analysis with Power-Hardware-In-the-Loop Test	59
3.5.1	Concept of power-hardware-in-the-loop test	60
3.5.2	Setup in laboratory	62
3.5.3	Analysis of results	63
3.6	Summary	65
4	Voltage Regulation Solutions with ES-STATCOM and Smart Transformer . . .	67
4.1	Voltage Control Approaches with Power Electronics Components	67
4.1.1	Voltage regulation by means of reactive power injection	68
4.1.2	Voltage regulation by means of forming voltage	70
4.2	Voltage Regulation Schemes for ES-STATCOM and Smart Transformer . .	72
4.2.1	Voltage regulation scheme for ES-STATCOMs	74
4.2.2	Voltage regulation scheme for smart transformers	75
4.2.3	Reactive power-voltage correlation coefficients	76
4.2.4	Voltage-voltage correlation coefficients	78
4.3	Selection of Power Rating for Power Electronics Components	78
4.4	Setup for Performance Analysis	82
4.4.1	Testing grid	82
4.4.2	Selection of power rating for power electronics components	84
4.4.3	Scenarios, evaluation criterion, and streams for analysis	87
4.5	Analysis of Proposed Voltage Regulation Scheme	88
4.5.1	Stream A	88
4.5.2	Stream B	95
4.5.3	Stream C	98
4.6	Summary	100
5	Centralized Meshed Grid Solution based on Smart Transformer	102
5.1	Meshed Grid Operation with Smart Transformer	103
5.2	Operation Scheme of Smart Transformer based Meshed Grid	105
5.2.1	Operation constraints	107
5.2.2	Derivation of solutions for multi-objective operation scheme	108
5.3	Testing Grid and Scenarios for Case Study	110
5.3.1	Topology of testing grid	110
5.3.2	Testing scenarios	110
5.3.3	Indices of performance evaluation and values of constraints	112

5.4	Performance Analysis of Multi-Objective Operation Scheme	113
5.4.1	Case O: conventional operation of parallel feeders	113
5.4.2	Case 1: Meshed grid topology 1	114
5.4.3	Case 2: Meshed grid topology 2	121
5.4.4	Case 3: Meshed grid topology 3	127
5.4.5	Summary of performance analysis	130
5.5	Harmonics Compensation in Meshed Grid	132
5.5.1	Generation of harmonics compensation reference in smart transformer	132
5.5.2	Control scheme of smart transformer for harmonics compensation .	136
5.6	Performance Evaluation of Harmonics Compensation in Meshed Grid . . .	136
5.6.1	Setup of testing grid	136
5.6.2	Simulation results and analysis	137
5.7	Summary	138
6	Summary, Conclusion, and Future Research	140
6.1	Summary and Conclusion	140
6.2	Research Contribution	142
6.3	Future Research	143
7	Appendix	145
7.1	Line Impedance of MV and LV Grids	145
7.2	Composition of Load Components in MV Grid of Chapter 3	147
7.3	Composition of Power Components in MV Grid of Chapter 4	149
	References	151
	List of Figures	163
	List of Tables	169

Kurzfassung der Arbeit

Der steigende Anteil erneuerbarer Energien an der Stromerzeugung und neue Lasten wie die Elektromobilität stellen die Verteilernetze vor neue Herausforderungen. Die neuen Akteure beeinflussen den Netzbetrieb und können eine hohe intermittierende sowie stark variierende Stromerzeugung, einen umgekehrten Stromfluss, oder Spannungsbandverletzungen erzeugen. Daher sollten innovative Betriebsmaßnahmen und Komponenten eingesetzt werden, um den entstehenden Herausforderungen beim Netzbetrieb zu begegnen.

In diesem Zusammenhang kommt den Leistungselektronik-Komponenten (LEK) eine besondere Bedeutung zu, denn sie haben schnelle Reaktionszeiten und ermöglichen dadurch eine effektive Netzregelung. Durch LEK ergeben sich daher Möglichkeiten, um den wachsenden Herausforderungen zu begegnen. In dieser Dissertation werden Betriebsmodi für LEK entwickelt, welche auf eine Verstärkung der Netzsteuerbarkeit abzielen. Die eingesetzten LEK umfassen die Schnellladestation (FCS), den ES-STATCOM, sowie den Smart Transformer (ST).

Eine wesentliche Aufgabe des Netzbetriebs ist die Reduzierung der Leistungsabweichungen zwischen der Prognose und dem Echtzeit-Bedarf. Eine Load-Leveling Methode, die zur Einspeisung der Blindleistung die freie Kapazität der FCSs ausnutzt, wird vorgestellt. Die Methode kann die Netzspannung regulieren und schließlich den Leistungsbedarf der spannungsempfindlichen Lasten ausgleichen, wodurch die Abweichung zu der Prognose reduziert wird. Darüber hinaus koordiniert diese Methode zur Maximierung der Regelbarkeit die FCSs zusammen mit anderen Betriebsgeräten. Bei dieser Methode handelt es sich um eine verteilte Lösung, da sie die geografisch im Netz verteilten Akteure koordiniert und kein Master-Akteur existiert.

Eine zum Online-Betrieb geeignete Methode, die zur Spannungsunterstützung Spannungs-Korrelations Koeffizienten einsetzt, wird vorgestellt. Für LEK, wie ES-STATCOM und ST, müssen die angewendeten Koeffizienten entsprechend den Netzanschlussstrategien angepasst werden. Daher nutzt die Lösung für ES-STATCOMs Blindleistungs-Spannungs Koeffizienten. Die Lösung für STs umfasst hingegen sowohl Blindleistungs-Spannungs Koeffizienten als auch Spannungs-Spannungs Koeffizienten. Die Analyse zeigt die Effektivität der eingesetzten Maßnahmen und stellt die Unterschiede zwischen ES-STATCOMs und STs heraus.

Die vermaschte Netzkonfiguration bietet mehr Steuerungsflexibilität im Vergleich zur radialen Netzkonfiguration. In dieser Arbeit wird eine ST-basierte Methode für den vermaschten Netzbetrieb vorgeschlagen. Da der ST der einzige Akteur ist, stellt die Methode eine zentralisierte Lösung dar. Eine auf Pareto-Optimierung basierende Maßnahme wird entwickelt, um die auftretenden Probleme wie Ungleichgewicht in der Stromversorgung, Verluste, und Spannungsabweichungen anzugehen. Außerdem wird eine Maßnahme zur Reduzierung von Oberschwingungen im Strom entwickelt.

Summary

The contemporary distribution grid is undergoing evolutions due to the increased utilization of renewable energy generation and new loads such as electric vehicles. These new actors impact the operation of the distribution grid, introducing, such as high intermittent power generation, reversed power flow, voltage violation. Therefore, innovative operation schemes and components should be adopted to cope with the emerging grid operation issues.

Power electronics (PE) components can provide various functionalities to support grid regulation with a fast dynamic response. Exploiting PE components, grid operation approaches can address the issues under the increasing penetration of the new actors. In this thesis, PE components, including fast charging station (FCS), energy storage static synchronous compensator (ES-STATCOM), smart transformer (ST), have been analyzed in the development of different operation solutions to enhance grid controllability. The intelligent operation schemes of different operation solutions have been developed in this thesis, targeting maximization of the controllability that can be gained.

Alleviating power mismatch between the forecast and real-time power demand is an essential operation task. A load-leveling approach exploiting FCSs has been proposed. The reactive power injection, which utilizes the spare capacity of the FCSs, can regulate the grid voltage, eventually shaping the power demand of voltage-sensitive loads to track the demand forecast, reducing the mismatch, and keeping a satisfactory charging service. Moreover, this approach coordinates the FCSs together with other grid operation actuators, maximizing the controllability. This approach is a distributed solution since it coordinates the actuators spread geographically in the grid, and no actuator behaves as a master actuator.

A PE based approach employing voltage-correlation coefficients has been proposed to cope with voltage violation. This approach can be implemented with a low computation burden, making it suitable for online operation. For PE components with different grid connecting strategies, such as ES-STATCOM and ST, the applied correlation coefficients must be adapted accordingly. The solution of ES-STATCOMs exploits the reactive power-voltage coefficients, and the solution of STs exploits both reactive power-voltage coefficients and voltage-voltage coefficients. Corresponding voltage regulation schemes have been developed. The analysis has illustrated the effectiveness of the proposed schemes and distinguished some significant differences between ES-STATCOMs and STs.

The meshed/hybrid grid configuration can offer more flexibility respecting the radial grid configuration. This work has proposed an ST based meshed grid operation approach. As the only actuator, the ST based approach is a centralized solution. An operation scheme has been developed, employing a multi-objective operation algorithm to address the emerging issues such as power supply unbalance, losses, and voltage deviations. Besides, a power quality conditioning scheme has been developed to condition the harmonics in current.

Used Symbols and Abbreviations

General symbols

(t)	Time variable
u	Instantaneous value
\bar{u}	Constant value
\tilde{u}	Oscillation value
Δu	Small-signal perturbation
U	RMS value
\hat{U}	Peak value

Superscripts

*	Reference value
'	Value without control action
"	Value with control action

Subscripts

0	Nominal value
ac	Alternating current/voltage
dc	Direct current/voltage
abc	Phase a, b, c
dq	d- and q-components in reference frame
$\alpha\beta$	α - and β - components in reference frame
HV	High voltage
MV	Medium voltage
LV	Low voltage
max	Maximum value
min	Minimum value
hc	Harmonic compensation

Special symbols

δ	Bus angle
----------	-----------

ε	Deadband of OLTC
λ	Power factor
σ	Standard deviation
Δ	Threshold value of load-leveling algorithm
$a_{Z/I/P}$	ZIP active power coefficients
$b_{Z/I/P}$	ZIP reactive power coefficients
\bar{d}	Mean voltage deviation of grid
d^\uparrow	Maximal voltage deviation of grid
f	Frequency
f_1	Objective function of stage 1, load-leveling algorithm
f_2	Objective function of stage 2, load-leveling algorithm
$f_{\Delta V}$	Objective function of voltage deviation minimization for meshed grid
f_{losses}	Objective function of losses minimization for meshed grid
$f_{\text{ES-STA}}$	Objective function of voltage regulation algorithm for ES-STATCOM
f_{ST}	Objective function of selection of ST power rating in MV stage
$f_{\text{ST,LV}}$	Objective function of voltage regulation algorithm for ST in LV grid
$f_{\text{ST,MV}}$	Objective function of voltage regulation algorithm for ST in MV grid
f_{UB}	Objective function of power unbalance minimization for meshed grid
i_{hc}	ST injection instantaneous current for harmonics compensation
$i_{\text{ES-STA}}$	ES-STATCOM converter instantaneous current
i_{FCS}	FCS converter instantaneous current
i_{LFT}	Instantaneous current flowing from the MV grid via LFT
$i_{\text{LFT,load}}$	Instantaneous current via LFT to supply loads
i_{LV}	Instantaneous current in LV grid
i_{MV}	Instantaneous current in MV grid
$i_{\text{ST,load}}$	ST injection instantaneous current supplying loads
k_{pq}	Active/reactive power sensitivity coefficients
p_{ESS}	Instantaneous active power injection of ESS
p_{FCS}	Instantaneous active power injection of FCS
p_{LV}	Instantaneous active power of LV grid
$p_{\text{LV,ST}}$	Instantaneous active power injection of ST LV stage
$p_{\text{MV,ST}}$	Instantaneous active power injection of ST MV stage
$q_{\text{ES-STA}}$	Instantaneous reactive power injection of ES-STATCOM
q_{FCS}	Instantaneous reactive power injection of FCS
q_{LV}	Instantaneous reactive power of LV grid
$q_{\text{LV,ST}}$	Instantaneous reactive power injection of ST LV stage
$q_{\text{MV,ST}}$	Instantaneous reactive power injection of ST MV stage
s_k	Timestep k
tap_{OLTC}	Tap position of OLTC
$v_{\text{ESS,dc}}$	ES-STATCOM dc link instantaneous voltage

v_{ES-STA}	Instantaneous voltage of ES-STATCOM connected bus
v_{FCS}	Instantaneous voltage of FCS connected bus
$v_{FCS,dc}$	FCS dc link instantaneous voltage
v_{LV}	Instantaneous LV grid busbar voltage
$v_{LV,dc}$	ST LV dc link instantaneous voltage
v_{MV}	Instantaneous MV grid busbar voltage
$v_{MV,dc}$	ST MV dc link instantaneous voltage
$v_{MV,ST}$	Instantaneous voltage of ST connected MV bus
v_{PA}	Power amplifier input instantaneous voltage
B	Susceptance of a branch
G	Conductance of a branch
IDX_{λ}	Index of power factor
$IDX_{\Delta \bar{V}}$	Index of mean voltage deviation
IDX_{losses}	Index of losses
IDX_{UB}	Index of power supply unbalance
K_Q	Reactive power-voltage correlation coefficient
K_V	Voltage-voltage correlation coefficient
Load	Measurements set of a load
P_0	Load nominal active power
P_{grid}	Grid power consumption
P_{load}	Active power demand of load
P_{loss}	Power losses
P_{DG}	Power generation from DG
P_{ESS}	Active power of ESS
P_{EV}	Charging power of single EV
P_{FCS}	Active power of FCS
P_L	Active power of left side grid
P_{LFT}	Active power of LFT
$P_{LVdc,load}$	Active power demand of LV dc grid
$P_{LVdc,DG}$	Active power generation from DG of LV dc grid
$P_{LV,load}$	Active power demand of LV grid
$P_{MVdc,load}$	Active power demand of MV dc grid
$P_{MVdc,DG}$	Active power generation from DG of MV dc grid
P_R	Active power of right side grid
P_{RES}	Active power of RES
P_{ST}	Active power of ST
$P_{ST,dc}$	Power flow via ST dc stage
$P_{ST,LV}$	Active power flow via ST LV stage
$P_{ST,MV}$	Active power flow via ST MV stage
Q_0	Load nominal reactive power

Q_{load}	Reactive power demand of load
$Q_{\text{ES-STA}}$	Reactive power injection of ES-STATCOM
Q_{FCS}	Reactive power injection of FCS
Q_{L}	Reactive power of left side grid
Q_{LFT}	Reactive power flow via LFT
$Q_{\text{LV,load}}$	Reactive power demand of LV grid
Q_{PE}	Reactive power injection of PE component
Q_{R}	Reactive power of right side grid
Q_{ST}	Reactive power injection of ST
$Q_{\text{ST,LV}}$	Reactive power flow via ST LV stage
$Q_{\text{ST,MV}}$	Reactive power flow via ST MV stage
R	Resistance of a branch
$S_{\text{ES-STA}}$	Power rating of ES-STATCOM
S_{FCS}	Power rating of FCS
S_{ST}	Power rating of ST
$S_{\text{ST,dc}}$	Power rating of ST dc stage
$S_{\text{ST,LV}}$	Power rating of ST LV stage
$S_{\text{ST,LV,PF}}$	Apparent power flowing via ST LV stage
$S_{\text{ST,MV}}$	Power rating of ST MV stage
$S_{\text{ST,MV,PF}}$	Apparent power flowing via ST MV stage
T_{trigger}	Trigger time of OLTC for load-leveling algorithm
V_0	Nominal voltage
V_{load}	RMS voltage of load
V_{OLTC}	RMS voltage of OLTC
X	Reactance of a branch
$\bar{\mathbf{I}}$	Matrix of grid current
$\bar{\mathbf{V}}$	Matrix of grid voltage
$\bar{\mathbf{Y}}$	Matrix of grid admittance
\mathcal{D}	Set of grid voltage deviations
\mathcal{H}	Set of ST buses
\mathcal{N}	Set of buses in an ST-fed grid
\mathcal{S}	Set of slack buses in a grid
\mathcal{X}	Set of buses in a grid

Abbreviations

ac	Alternating current
dc	Direct current

pu	Per-unit
B2B	Back-to-back
BESS	Battery energy storage system
CC	Commercial charging
CD	Cumulative distribution
CHB	Cascaded half bridge
CL	Commercial load
CVR	Conservation voltage reduction
DAB	Dual active bridge
DER	Distributed energy resource
DG	Distributed generation
ESS	Energy storage system
ES-STA	Energy storage static synchronous compensator
ES-STATCOM	Energy storage static synchronous compensator
EV	Electric vehicle
FACTS	Flexible ac transmission system
FCS	Fast charging station
FFT	Fast Fourier transform
GAMS	General algebraic modeling system
HuT	Hardware under test
HC	Harmonics compensation
HV	High voltage
IM	Induction machine
LF	Lowpass filter
LFT	Low-frequency transformer
LHS	Latin hypercube sampling
LPC	Loop power controller
LV	Low voltage
MMC	Multilevel modular converter
MV	Medium voltage
NOP	Normally open point
NOVA	Network optimization before enhancement before upgrading
NPC	Neutral-point clamped
OLTC	On-load tap changer
P	Active power
PA	Power amplifier
PD	Probability density
PE	Power electronics
PHIL	Power-hardware-in-the-loop
PMU	Phasor measurement unit

PV	Photovoltaic
PWM	Pulse width modulation
Q	Reactive power
RC	Residential charging
RES	Renewable energy system
RL	Residential load
RTDS	Real time digital simulator
SCC	Short circuit capacity
SD	Standard deviation
SOC	State-of-charge
SRC	Series resonant converter
SST	Solid state transformer
ST	Smart transformer
STATCOM	Static synchronous compensator
THD	Total harmonics distortion
V2G	Vehicle-to-grid
ZIP	Constant impedance/current/power load

1 Introduction

This chapter motivates the development of various distributed and centralized power system operation solutions based on power electronics (PE) components, targeting to enhance the controllability in the distribution grid. A research proposal for this thesis has been formulated afterward. The thesis structure is then explained, and all related publications to the corresponding chapters are highlighted.

1.1 Motivation of Distribution Grid Controllability Enhancement

The conventional distribution grid has a relatively simple operation pattern. The electric power is generated from the large-scale power plants and delivered via the transmission grid to the distribution grid. Consumers, such as households or business offices, are the end-users fed by the distribution grid. The power flow in the distribution grid is primarily unidirectional, from the medium voltage (MV) to low voltage (LV) and finally to the consumers.

To promote the utilization of renewable energy, the distributed generation (DG) based energy production units have been continuously installed on the side of consumers. With a combination of generation and consumption, the conventional consumers in the distribution grid have evolved to the prosumers. The grid operation has gained some benefits from the prosumers. For instance, the power generation becomes more flexible and more localized thanks to the DG, reducing the losses of power transmission. However, challenges have arisen simultaneously. Due to the intermittent characteristics, the power dispatch of renewable energy generation is not always upon demand, increasing the uncertainty of power generation, which can eventually introduce considerable power mismatch, endangering the grid frequency stability. Moreover, if the energy from the DG covers the local power demand and leads to reversed power flow, operation challenges regarding the voltage regulation and protection can emerge [1, 2].

On the other hand, electric energy becomes the energy resource for applications that conventionally use other energy resources due to the electrification in different sectors. For instance, electric energy becomes an important resource for the transportation sector with the increased number of electric vehicles (EVs). More and more new types of loads are connected to the distribution grid, which results in the amount of electric power demand has grown significantly. Furthermore, with various types of users, the power demand shows more randomness. Operation challenges such as undesirable voltage drop, overload of essential components, and power deviation from demand forecast can emerge, degrading the quality of the power supply.

The system operators must address these challenges, hosting the increasing penetration of new actors while maintaining the reliability, stability, and good quality of power supply.

One option of grid reinforcement is to upgrade the existing network infrastructure, e.g., constructing new transformers and lines/cables. However, approaches targeting grid controllability enhancement by means of intelligent algorithms and innovative regulation components are also widely adopted by the system operators. Approaches, for example, intelligent power/load management with the aid of energy storage system (ESS); schemes for reversed power flow limitation; assessments to identify the instability issues, have been proposed in the previous researches.

This work aims to develop innovative solutions to enhance the controllability in the distribution grid by exploiting the PE components. These solutions, implemented by regulation of the power or the voltage in the controlled grid, aim to optimize the grid states in terms of power demand and voltage behavior, overcome the challenges introduced by the new actors, and reinforce grid robustness and stability. Depending on how the PE components are coordinated, the solutions can be categorized into distributed and centralized solutions. A distribution solution involves various PE components, which are geographically spread in the grid, and no PE component is considered as the master actuator. On the contrary, a centralized solution involves either only single PE component or more components with one acting as a control master.

1.2 Motivation of Development of Grid Operation Solutions with Power Electronics Components

The PE components have been widely installed in the grid. Previous researches have evaluated PE components' performance in operation aspects such as active power dispatch, reactive power management. The PE components can adjust the control actions within a time frame of tens of milliseconds, reinforcing the grid stability under disturbances with fast dynamic behaviors. On the contrary, conventional grid controllability enhancement solutions that employ passive regulation components, such as the on-load tap changer (OLTC) and capacitor banks, may not be capable of fast dynamic regulation. Consequently, the PE components based solutions are competitive options for distribution grid operation nowadays.

This thesis aims to develop innovative solutions, exploiting either the new intelligent algorithms or the innovative components differing from the existing ones. By regulating the power and voltage in the controlled grid, these solutions enhance the grid controllability to address the challenges introduced by the penetration of new actors.

The topologies and controller structures of the PE components should be studied as the first step to utilize the PE components in an optimal way. This study helps understand the functionalities that the PE components can provide and their limitations. As the next step, the behaviors of the components in the grid operation actions are analyzed. Depending on the grid connecting strategies, the PE component implements the regulation employing different

approaches, such as regulating the active/reactive power injection or regulating the voltage and frequency. It is crucial to analyze the performance of the connecting strategies since a significant impact on the operation performance can be observed with different connecting strategies. Based on the analysis, the essential factors for the PE components in grid operation, such as the controllability that PE components can gain with different strategies and selecting the proper power rating of the PE components, can be understood.

On the other hand, the impact of the grid on the PE components, while the components provide the grid operation actions, needs to be evaluated. The evaluation of impacts on the components helps identify the possible side effects of the grid support operation. Based on the evaluation, the controller of the PE components can be modified, minimizing the negative impact on the main functionalities for the PE components.

To systematically enhance the grid controllability with PE components, intelligent operation schemes are to be developed, coordinating the grid operation actions of the PE components. The operation schemes need to be optimized to fulfill the operation requirements. For instance, the schemes should have a considerable low computational burden to be capable of the online application; in the meantime, they should be practical, effective, and have high accuracy. For developing the proper schemes, analysis implemented through simulation in software and laboratory tests with hardware is required.

In this work, three PE components: fast charging station (FCS), energy storage static synchronous compensator (ES-STATCOM), and smart transformer (ST), are selected as actuators to provide grid controllability enhancement solutions. For coordinating the components, different intelligent operation schemes will be proposed, and the effectiveness of the proposed schemes will be evaluated by means of simulation and laboratory tests. Furthermore, the ST decouples the connected grids in some essential terms, such as phase angle, reactive power, and frequency, leaving only active power exchange. This feature enables some innovative grid operation concepts. The performance of the innovative operation concepts will be studied, respecting the conventional concepts. As the objectives, this thesis will develop a group of PE components based distributed and centralized solutions, enhancing the grid controllability in terms of power and voltage regulation, which promotes to host the increased penetration of the new actors such as DG and EVs.

1.3 Research Proposal

This thesis aims to investigate the distributed and centralized grid operation solutions based on PE components, which enhance the controllability in the distribution grid, increasing the grid's hosting capability for new actors. The thesis works on the development of operation solutions in three different aspects.

Target I: Developing a load-leveling approach

The first research objective is to develop a power regulation approach focusing on load-leveling. This approach aims to regulate the power consumption to track the demand forecast, alleviating the power mismatch between the demand forecast and the real-time consumption. By regulating the grid voltage, the approach eventually shapes the power demand of the voltage-sensitive loads to track the demand forecast. The voltage regulation is mainly implemented by the PE components, which exploits the spare capacity of the component to inject reactive power. The FCSs are selected as actuators since every FCS has a considerable aggregated power rating. The FCSs are geographically spread in the grid. Hence, the outcome of this target is a distributed solution for load-leveling using the FCSs as the actuators.

Target II: Developing a voltage regulation approach

The second objective is to develop a voltage regulation approach. This approach aims to reduce the average voltage deviation and mitigate the violation of voltage constraints that are emerged with the new actors. The regulation approach employs the voltage-correlation coefficients to compute the control references for the actuators, reducing the computation burden. The ES-STATCOM and the ST are selected as the actuators. By coordinating the ES-STATCOMs spread in the grid, a distributed solution for the voltage regulation can be formulated. In the MV grid, the ST based solution coordinates the actuators similar to the ES-STATCOMs. In the LV grid, the ST formulates a centralized solution since every ST is the single actuator for the connected grid.

Target III: Analyzing the meshed grid operation

The third objective is to investigate the application of an innovative grid reconfiguration concept: the meshed grid in the LV grid. The meshed grid concept represents a ring grid configuration. Compared to the widely used radial configuration, in which the loads are supplied from one upstream grid, the meshed grid enables the loads within the ring to be supplied from more upstream grids, achieving the improvements of grid operation and avoiding the overload issues of essential components. The ST is selected as the actuator for the meshed grid. The outcome of this target is an ST based centralized solution for meshed grid operation.

1.4 Structure of the Thesis

The structure of this thesis is shown in Fig. 1.1. A state-of-the-art review of the development and challenges of the contemporary distribution grid together with the existing grid reinforcement approaches is given in Chapter 2. This chapter also introduces the PE components, which are studied in this work. The topologies and the controller structure of the PE components to be analyzed are also explained in detail.

Chapter 3 introduces a power regulation approach, which focuses on load-leveling. This approach regulates the power demand of voltage-sensitive loads to track the demand forecast, alleviating the power mismatch arisen from the real-time demand. The primary actuators to implement the approach are the FCSs. The ancillary actuator is the OLTC of the transformer, which connects the testing network to the upstream grid, supporting more controllability. A two-stage scheme based on the optimization algorithm is developed to coordinate the actions of actuators under online operation condition. The scheme aims: (1) mitigation of the power mismatch; (2) minimization of the power transmission losses. The performance of the proposed approach will be evaluated by means of simulation and laboratory tests.

Chapter 4 presents the approach for the voltage regulation based on voltage-correlation coefficients, which minimizes the average voltage deviation and mitigates the violation of voltage constraints. Two components, the ES-STATCOM and the ST are selected as actuators to implement the approach. Due to the different grid connecting strategies of the two components, the approach for ES-STATCOMs regulates the voltage by means of reactive power injection, which exploits the spare capacity of the ES-STATCOMs. The approach for STs regulates the voltage similarly to the ES-STATCOMs in the MV grid, but in the LV grid, the ST directly forms the voltage. Consequently, the operation scheme of the ES-STATCOMs makes use of the reactive power-voltage correlation coefficients, and the scheme of the STs makes use of both power-voltage and voltage-voltage correlation coefficients. The performance of the proposed solutions will be evaluated by means of simulation. Moreover, a comparison of the two solutions will be performed to evaluate the impact of the grid connecting strategies.

The ST based operation approach for the meshed grid is discussed in Chapter 5. It is expected that the meshed grid can gain significant performance improvements on the grid operation, such as reducing voltage deviation and losses, respecting the radial grid configuration. An operation scheme based on the multi-objective optimization algorithm for the static state operation is developed, considering power supply unbalance, losses, and mean voltage deviation. By means of the Pareto optimality method, the non-dominated solutions of the proposed scheme can be derived, which allow every system operator selects the proper solution according to its individual preference. The performance of the proposed scheme will be analyzed and compared to the performance of the radial grid configuration. Moreover, a meshed grid based power quality conditioning scheme is also presented and evaluated in this chapter.

In Chapter 6, the results are summarized. The performance of various operation solutions is concluded before an outlook on future work is given.

1.5 Assignment of Publications to the Chapters of this Thesis

The following part shows how the publications related to this thesis are assigned to the different chapters, which is additionally visualized in Fig. 1.1. A complete list of the publications related to this thesis is given at the end.

- Chapter 2 addresses the topologies and controllers of the PE components, which is based on [C1], [C4], and [C6]
- Chapter 3 introduces the load-leveling with FCSs, employing the journal article of [J2] and conference article of [C7]
- Chapter 4 introduces voltage regulation, containing the information of journal article [J1] and [C2] plus the analysis methodology derived from the conference article [C3]
- Chapter 5 introduces the meshed grid operation, which involves the conference publications [C5] and [C8]

Journal publications

- J1 X. Gao, F. Sossan, K. Christakou, M. Paolone and M. Liserre, "Concurrent Voltage Control and Dispatch of Active Distribution Networks by Means of Smart Transformer and Storage." in IEEE Transactions on Industrial Electronics, vol. 65, no. 8, pp. 6657-6666, Aug. 2018.
- J2 X. Gao, G. De Carne, M. Andresen, S. Brüske, S. Pugliese and M. Liserre, "Voltage-Dependent Load-Leveling Approach by Means of Electric Vehicle Fast Charging Stations," in IEEE Transactions on Transportation Electrification, vol. 7, no. 3, pp. 1099-1111, Sept. 2021.

Conference publications

- C1 X. Gao, G. De Carne, M. Liserre and C. Vournas, "Increasing integration of wind power in medium voltage grid by voltage support of smart transformer," Wind Europe 2016, Hamburg, 2016.
- C2 F. Sossan, K. Christakou, M. Paolone, X. Gao and M. Liserre, "Enhancing the provision of ancillary services from storage systems using smart transformer and smart meters," 2017 IEEE 26th International Symposium on Industrial Electronics (ISIE), Edinburgh, 2017.
- C3 X. Gao, R. Zhu, G. De Carne and M. Liserre, "Comparison of voltage support services by means of STATCOM and smart transformer in medium voltage grid," 2018 13th IEEE Conference on Industrial Electronics and Applications (ICIEA), Wuhan, 2018, pp. 946-951.

-
- C4 L. Camurca, X. Gao, L. F. Costa and M. Liserre, "Design of a Medium Voltage DC Fast Charging Station with Grid Voltage Regulation and Central Modular Multilevel Converter," 2018 IEEE Energy Conversion Congress and Exposition (ECCE), Portland, OR, 2018, pp. 2798-2804.
- C5 C. Kumar, X. Gao and M. Liserre, "Smart Transformer Based Loop Power Controller in Radial Power Distribution Grid," 2018 IEEE PES Innovative Smart Grid Technologies Conference Europe (ISGT-Europe), Sarajevo, 2018.
- C6 X. Gao, G. De Carne, R. Zhu, M. Andresen and M. Liserre, "Mitigation of Disturbances by Means of Smart Transformer-based Storage Systems," 2019 IEEE 13th International Conference on Compatibility, Power Electronics and Power Engineering (CPE-POWERENG), Sonderborg, 2019.
- C7 X. Gao, G. De Carne, M. Langwasser and M. Liserre, "Online Load Control in Medium Voltage Grid by Means of Reactive Power Modification of Fast Charging Station," 2019 IEEE Milan PowerTech, Milan, 2019.
- C8 G. D. Carne, X. Gao, Z. Zou, M. Liserre, A. Kazerooni and M. Eves, "Smart Transformer requirements for integration in distribution grids and power quality improvement," 2019 IEEE Milan PowerTech, Milan, 2019.

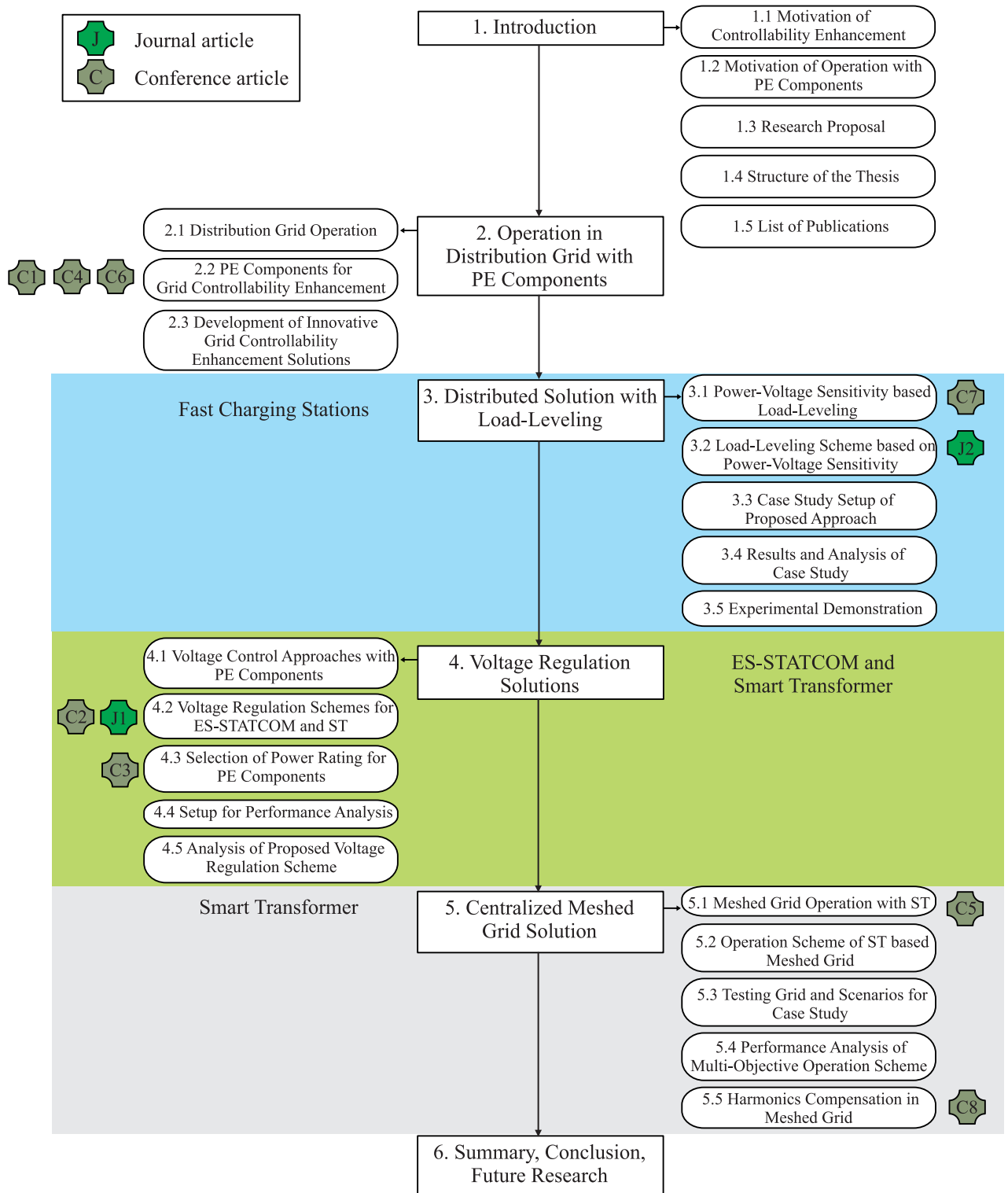


Fig. 1.1: Structure of the thesis and related publications.

2 Operation in Distribution Grid with Power Electronics Components

The power system has been evolving rapidly in the last decade. From the generation to the end-users, innovations with new components and operation concepts have been applied in all branches. Due to the increased penetration of new actors, such as renewable energy generation and electric vehicles (EVs), new operation challenges such as demand variability and decreased inertia have emerged in the distribution grid. The system operators must address these challenges to maintain the power supply's reliability and stability and to host the increased new actors.

The grid reinforcement solutions have drawn attention worldwide since they can address the challenges and defer the network infrastructure upgrade. Previous researches have evaluated various grid reinforcement solutions, targeting to address the emerging operation challenges, such as reversed power flow, degradation of grid stability, and the deterioration of power quality.

Power electronics (PE) technology has been developed rapidly in the last decades. The PE based grid operation components can provide fast response and various functionalities. In both the industry and academia, the PE components are considered as promising actuators to implement grid reinforcement. This thesis focuses on developing PE based solutions that enhance grid controllability and address the operation challenges in terms of power and voltage regulation. The components to be studied include the smart transformer, the energy storage static synchronous compensator, and the fast charging station.

This chapter presents a state-of-the-art review of the development and challenges in the contemporary distribution grid, and of the existing grid operation approaches from previous research. The PE components, which are involved in the further study, will be introduced following the review. Essential features of the components, such as the topologies and the controller's structures, will be explained in detail. In the end, some general characteristics of the grid enhancement solutions in this work will be explained.

2.1 Distribution Grid Operation: Development, Challenges, and Solutions

2.1.1 Development in distribution grid nowadays

Innovations in power systems have changed the conventional operation pattern in all branches, from generation to end-users. Conventional power generation relies on energy resources such as coal or nuclear power. Most generation units are installed in large scale power plants. The

energy generated from power plants is delivered via the transmission grid to the distribution grid, feeding the end-users.

Nowadays, renewable energy sources, including wind power and photovoltaic (PV), have been used more and more for electric power generation since these sources can benefit social issues such as environmental protection and sustainable development. Consequently, in the last decade, the penetration of renewable energy has been continuously increased, and this trend will continue in the following decades. Taking Germany as an example, about 35 % of electric energy was generated by renewable energy sources in the year 2020, and the federal government targets to increase the share of renewable energy production by up to more than 80 % till the year 2050 [3]. In the state of Schleswig-Holstein in northern Germany, which has a considerable share of wind power generation for the country, the number of wind generation units under operation has reached more than 3,000 with the cumulative capacity of power generation over 6700 MW [4].

The end-users are experiencing revolutions as well. Technical innovations have promoted electrification in different sectors, mainly having relied on non-electric energy before. For instance, the electrification of the transportation sector has recently gained renewed attention globally due to the emission-free feature of EVs. To promote transportation electrification, it is essential that the convenience of using EVs should be comparable to using fossil fuel vehicles. In material science, researches have been implemented to increase the lifetime of a fully charged battery. In electric power engineering, convenient access to charging facilities must be provided, and the charging duration should be reduced to be as competitive as refilling fossil fuel. As a consequence, more charging facilities have been installed, and the percentage of fast charging facilities is growing. There are already more than 20,000 facilities in Germany, and 3,000 among them are fast charging facilities [5, 6].

2.1.2 Challenges caused by innovations in distribution grid nowadays

With the benefits of renewable energy generation and electrification in different sectors, the new actors also have introduced some technical challenges for electric power system operators.

Challenges from distributed generation

A widely applied generation form of renewable energy is distributed generation (DG) of the small scale. The DG, mostly having a PE converter interface to the grid, has lower inertia than the conventional large scale power plants. A grid with a higher penetration of DG can suffer a higher frequency deviation and a more significant rate of change of frequency after a loss of generation, with respect to the case without or with lower penetration of DG

[1, 7, 8]. If the penetration of DG reaching a considerable level, the system operators must adopt solutions to avoid that the grid robustness under frequency disturbance is degraded.

Furthermore, power generation of conventional units such as thermal power plants can be fully dispatched upon demand. On the contrary, the power generation from renewable energy systems (RESs) depends strongly on the availability of resources, and the output can be highly intermittent [9]. The generation of RESs cannot always follow the generation dispatch plan, resulting in eventually load shedding in extreme operation conditions [10].

With the massive penetration of DG units at the end users' side in the distribution grid, the operation patterns could be utterly changed. If the DG based on renewable energy is sufficient to cover the power demand of the end users' side, reversed power flow is induced. The power will flow from the downstream grid to the upstream grid, which eventually changes the conventional direction of the power supply in the distribution grid. The reversed power flow can result in challenges in planning, operation, protection, and other operation aspects. [1, 8]. In the distribution grid at the medium voltage (MV) or low voltage (LV) levels, the reversed power flow can significantly increase voltage due to the unneglectable resistance of lines/cables of the grid, leading to eventually the violation of over-voltage constraint [11]. The undesirable over-voltage provokes irreversible damages to the devices in the grid.

Moreover, the voltage variations have a fast dynamic transition between a voltage rise and voltage drop. For instance, strong solar irradiation in a highly PV penetrated grid can cause the reversed power flow, leading to a voltage rise. If there is a cloud shadow suddenly passing by at this instant, the PV generation can be immediately decreased, resulting in a violation of the under-voltage constraint [12, 13, 14]. Study shows that the grid can experience a voltage variation of 3–4 % with a fast dynamic under high DG penetration [15]. Besides, the DG has also introduced challenges such as power quality degradation in terms of harmonics and unbalanced three-phase power.

Supposing the aforementioned challenges cannot be addressed appropriately, renewable energy generation must be curtailed to maintain grid stability, resulting in the waste of emission-free green energy. The curtailment also discourages the owners of DG units.

Challenges from new types of loads

With the growing penetration of new types of loads such as EVs, the power demand has been increased, leading to power congestion at some grid points. The grid components such as the line or transformer are under the pressure of overload. Moreover, those loads, such as customer-dependent charging of the EVs, behave with higher randomness. Consequently, the net-load demand (load minus generation from DG) becomes less forecastable than in the past, making it difficult to forecast accurately the demand [16, 17, 18]. This forecast error can result in power mismatch between the realtime demand and dispatch plan, increasing

the operation cost to balance the power. If the mismatch reaches a certain level, it can cause significant frequency deviations, endangering the grid's reliability and stability.

Additionally, the voltage drops appear much more severe in terms of both amplitude and duration with the new types of loads. A study has shown that 30 % of EV penetration is sufficient to result in a violation of voltage constraint of a grid that is regulated by the on-load tap changer (OLTC) [19].

The power supply has to be restricted to avoid undesirable grid behaviors such as violation of voltage constraints. In this case, the EV charging quality is degraded since the demand cannot be fulfilled. For instance, the charging facilities will have to prolong the charging duration, introducing inconvenience for the users of EVs.

2.1.3 Existing solutions to counter the operation challenges

To address the emerging grid operation challenges, which can result in the curtailment of renewable energy generation and prolonged charging durations, the system operator can upgrade the network infrastructure, e.g., installing new transformers and lines/cables of higher ampacity. However, for more practical issues, the Federal Network Agency of Germany has proposed the principle of "NOVA" (network optimization before enhancement before upgrading), which system operators have implemented in Germany. According to NOVA, the operators should update the operation schemes and components to cope with the operation challenges before they plan for upgrading the network infrastructure [20]. Similar principles have also been proposed in other countries, such as in UK [21]. Researches on different operation approaches for grid reinforcement have been implemented worldwide as a result.

This work focuses on the operation challenges of power and voltage regulation. Previously proposed solutions for power and voltage regulation have relied on the actuators, such as flexible loads (e.g., air conditions or EVs), energy storage systems (ESSs), and flexible ac transmission system (FACTS). The following part introduces power and voltage regulation to overcome challenges such as decreased inertia, power redispatch, and high voltage variability. Besides the solutions based on conventional concepts of grid configuration, solutions employing the concepts of grid reconfiguration are also discussed.

Power regulation

Power regulation aims to address the operation challenges such as the power mismatch or the decreased inertia, reducing the operation cost of power balance and increasing the grid frequency robustness and stability. Approaches have been proposed to act on the load power consumption by various categories to enhance the power controllability in the distribution grid.

One category of approaches employs the deferrable loads in domestic and commercial areas such as heating system, ventilation system, air conditioning system, and pool pumps system as the actuators [22, 23, 24, 25, 26]. Those deferrable loads have considerable thermal storage potential to provide ancillary power regulation to the grid operation. Meanwhile, the impact due to the provision of power regulation on the paramount service quality of the involved actuators, such as heating or cooling, is mostly not noticeable. Approaches for demand response have been developed for regulating the demand in short (in seconds) and long (in minutes) duration. The approaches regulate the deferrable loads to track predefined demand baseline or to provide substantial frequency regulation. Even though the effectiveness of all aforementioned approaches has been proven, the demand response approaches require an extensive monitoring/communication infrastructure to gain accurate data and estimate the availability and capability of the deferrable loads. Additionally, access to the deferrable loads is required in most demand response approaches, which can be an obstacle of implementation since the users have concerns about their privacy.

Besides the deferrable loads, EVs are the potential actuators for power regulation. Based on the vehicle-to-grid (V2G) concept, the EV's battery can be charged or discharged to provide energy to the grid if deemed necessary. Studies have proposed different approaches to exploit the V2G concept for power regulations in the last years. The approaches make use of the storage capability of the EVs for power regulation such as congestion management, peak load shaving, primary frequency control, and renewable energy integration [27, 28, 29, 30, 31, 32, 33, 34, 35]. The EV based approaches control the state-of-charge (SOC) of the batteries in the EVs. By means of charging and discharging actions, the power surplus from renewable energy generation can be absorbed, and the power deficit can be compensated. The V2G based approaches rely on massive EVs due to the limited capacity of a single EV's battery with respect to the grid energy demand. Besides, the time that EVs are connected to the grid has strong randomness. These features make the regulation of EVs much more complex than the deferrable loads based approaches. Last but not least, using the EVs as actuators, the EVs cannot always be charged during preferable charging time zones and with desirable SOC. The undesirable charging service can introduce extra costs to compensate for the discomfort of EV users.

Large scale ESSs such as battery energy storage system (BESS), super-capacitor, and fly-wheel can have the capacity to store hundreds of kWh energy or even more. The storage systems can act as adequate primary energy reserves. In the literature, several ESS-based approaches have been proposed to address the power regulation issues such as primary frequency control, dispatch of aggregated stochastic renewable generation, and load peak shaving [9, 36, 37, 38, 39, 40, 41, 42, 43, 44, 45, 46, 47, 48].

Fig. 2.1 shows the load behavior of an LV grid in which the BESS dispatches the power via the MV/LV transformer to track a predefined dispatch plan [J1]. Fig. 2.1 (a) is the schematic

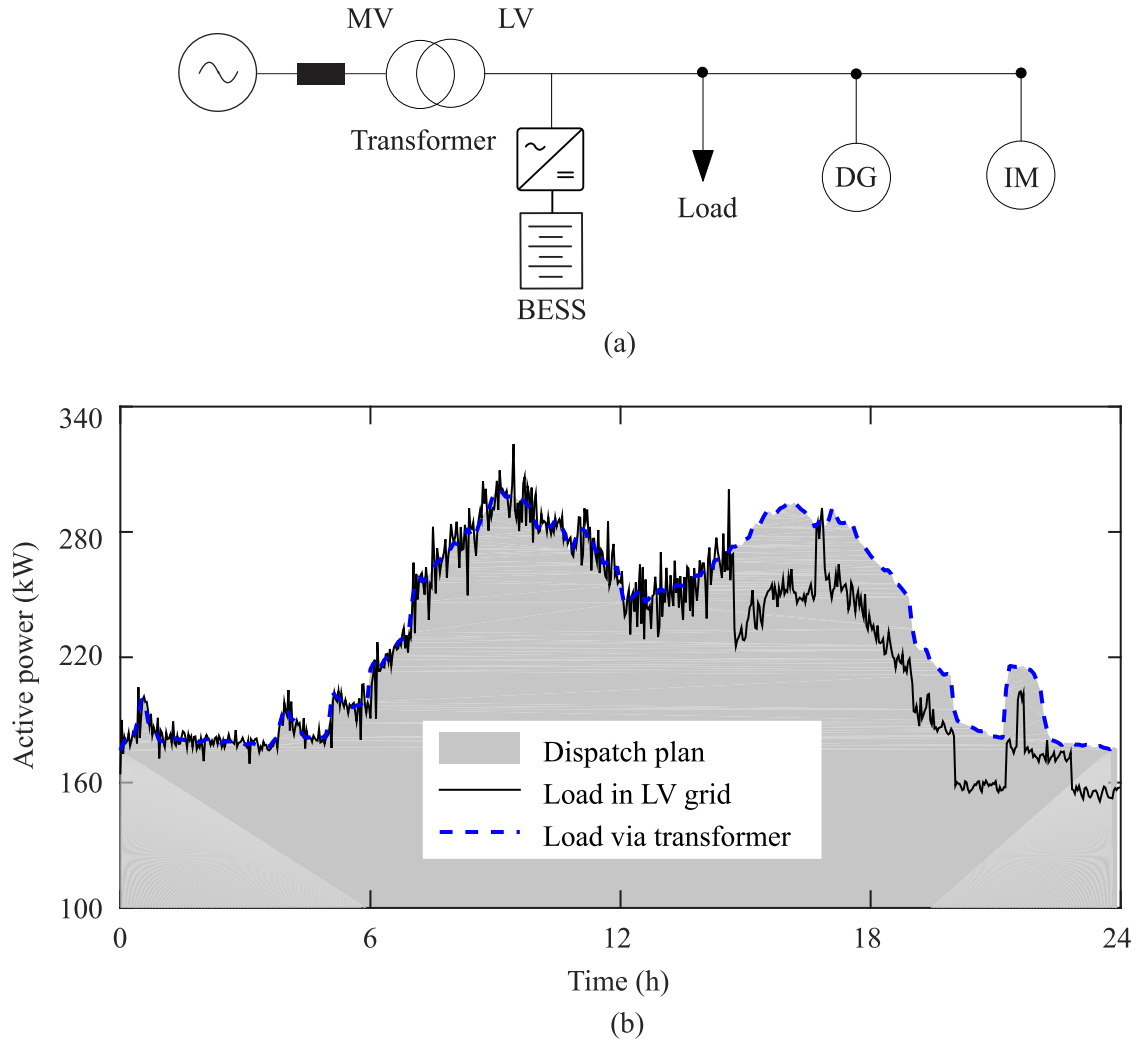


Fig. 2.1: Demand redispatch for tracking dispatch plan by means of BESS. (a) Schematic diagram of an LV grid (in BESS converter, '~': ac, '=': dc). (b) Power behavior of the LV grid without/with the regulation in respect to dispatch plan [J1].

diagram of an LV grid, which consists of an MV/LV transformer, battery, DG, induction machine (IM), and load. The power of dispatch plan, real-time load demand of the LV grid, and load via the transformer are shown in Fig. 2.1 (b). The mismatch between the dispatch plan and real-time load demand of the LV grid has been significantly alleviated by the BESS, resulting in the load via the transformer tracking the dispatch plan with tiny errors. However, the ESSs-based approaches require initial investment plus maintenance, increasing the cost of operation. Consequently, the ESSs must be only installed at some strategic points in the grid. In addition, repetitive power cycling can have impact on the lifetime of commonly used storage technologies, such as batteries, inducing rapidly reduced cycling operations [49].

Voltage regulation and reactive power management

Besides the power regulation, new actors have also introduced challenges in terms of voltage regulation. Different approaches to enhance the voltage controllability in the distribution grid

have been proposed and analyzed [50, 51, 52, 53, 54, 55, 56, 57, 58, 59, 60, 61, 62, 63, 64, 65, 66]. The actuators to implement the approaches can be classified into two categories: (1) the conventional technology based passive components such as the OLTC, shunt capacitor bank, or controllable load; (2) the PE technology based active components.

The passive components, including the OLTC and capacitor banks, are widely used for conventional grid operation such as voltage regulation and power factor correction [50, 51, 52]. To implement the control actions, the approaches based on passive components usually adjust the set-point of the actuators, e.g., the tap of the OLTC or the number of switched capacitor banks. Consequently, the control actions are impacted by the bandwidth of the set-points, resulting in not seamless control.

Moreover, there are approaches exploiting the active power of the controllable loads in voltage control. The active power is conventionally used for μ -grid voltage control [53], but can also be applied in the large scale distribution grid [54]. A much higher R/X ratio of lines/cables in the distribution grid than the ratio in the transmission grid is expected. Therefore, the active power based approaches can gain significant controllability in the distribution grid for voltage regulation.

For addressing the arisen challenges caused by the new actors, the conventional approaches, such as the ones based on passive components, show apparent drawbacks. The reversed power flow in the distribution grid nowadays is more harmful to the OLTC than the high current of the direction from the upstream grid to the downstream grid due to construction limitations [67]. Moreover, voltage violations can frequently vary between over-voltage and under-voltage within a short duration due to the intermittent generation of renewable energy based DG. For instance, if the cloud suddenly covers the photovoltaic (PV) units during a reversed power flow case, the voltage above the over-voltage constraint can immediately become below the under-voltage limit. This condition requires frequently adjusting the set-point of the OLTC, which wears its mechanical parts quickly, reducing its lifetime. Furthermore, the OLTC of the transformer influences the voltage of all downstream feeders connected to the transformer. A conventional grid without DG is not common to emerge conflict between the feeders by regulating the OLTC. However, conflicts can emerge if some feeders experience the voltage drop and others experience the voltage rise due to the DG. The regulation of OLTC can result in new voltage violations in some feeders while mitigating the violation of other ones. The severity and complexity of control issues have forced the grid operator to upgrade the passive component based voltage regulation approaches to cope with the new challenges with fast response in the distribution grid.

Due to the fact that the PE components can adjust their control actions seamlessly within a time scope of some tens of milliseconds, a desirable response for voltage regulation in the distribution grid can be achieved by the PE components.

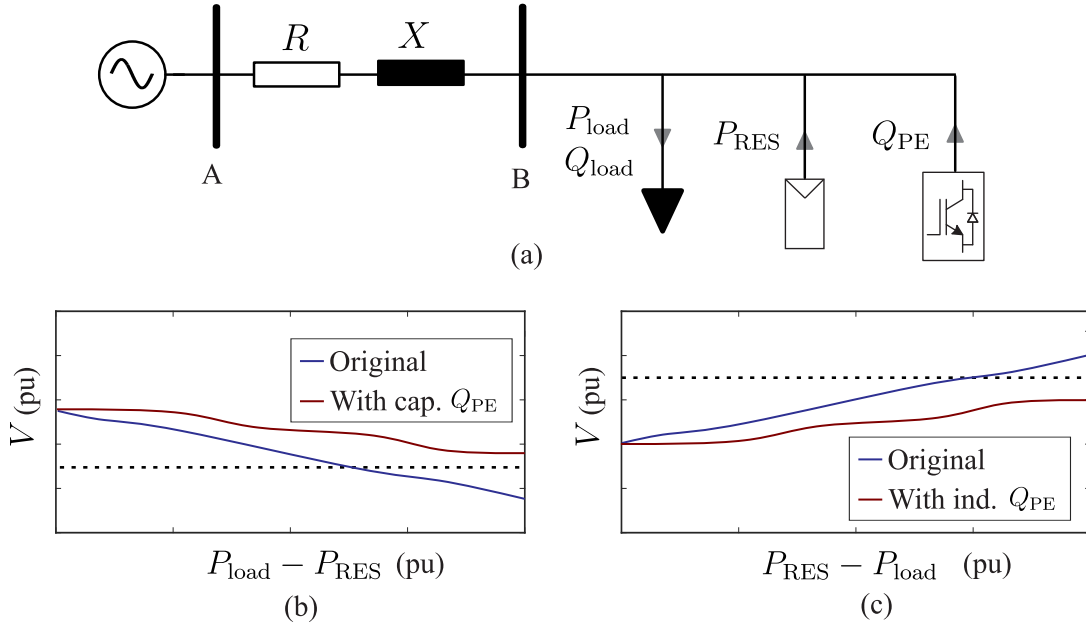


Fig. 2.2: Voltage regulation by reactive power injection with PE component. (a) Schematic diagram of a grid. (b) Voltage behavior without/with capacitive reactive power injection for an under-voltage condition. (c) Voltage behavior without/with inductive reactive power injection for an over-voltage condition.

The PE based components can regulate the voltage by means of various approaches. One widely applied principle exploits the relation between the voltage and reactive power, by which the PE components regulate the voltage by injecting reactive power. Fig. 2.2 (a) depicts a typical radial feeder for the distribution grid with load, RES, and PE component. The bus A voltage of the bulk grid is considered as constant. Voltage of bus B decreases with an increased net-load demand ($P_{load} - P_{RES}$), and the voltage increases with a decreased net-load demand ($P_{RES} - P_{load}$). Violation of voltage constraints can be expected without reactive power injection of the PE component, as shown in Fig. 2.2 (b) and (c). However, the violation can be mitigated with reactive power from the PE component Q_{PE} . Voltage deviations of the bus B with respect to the active/reactive power demand of the load, the generation of RES, and the reactive power injection of PE component can be estimated numerically as:

$$\Delta V = \frac{R(P_{RES} - P_{load}) + X(Q_{PE} - Q_{load})}{V} \quad (2.1)$$

where ΔV is the voltage deviation of the bus B, $P_{RES} - P_{load}$ is the active power difference between the generation of RES and the load demand, $Q_{PE} - Q_{load}$ is the sum of reactive power of the PE component and the load, and V is the voltage of the bus B. A positive (capacitive) injection of Q_{PE} increases the value of ΔV , reducing the voltage drop if ΔV is negative. Similarly, a negative (inductive) injection of Q_{PE} reduces the voltage rise in the case of positive ΔV . Compared to the OLTC, this reactive power injection based principle can focus on the voltage regulation at the problematic point in the grid, which avoids the maximal extent of introducing new violations to the grid.

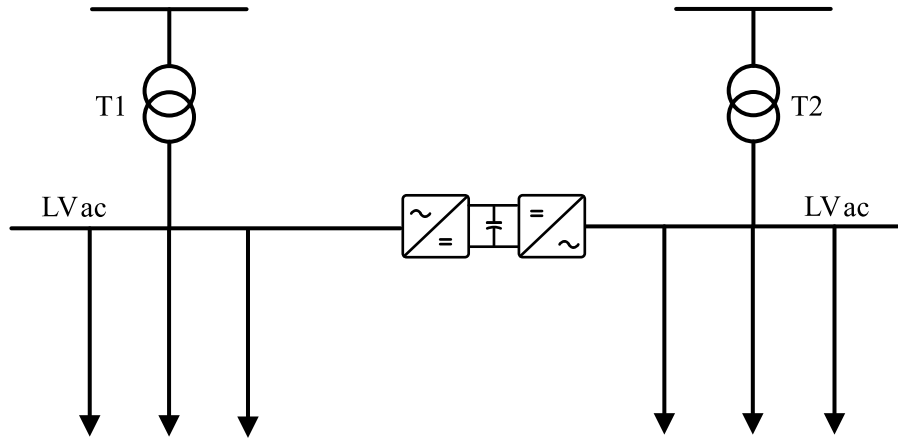


Fig. 2.3: LPC based approach for meshed grid application.

It is also possible to directly set the voltage amplitude at the bus, which the PE component is connected. Other than the previous principle that is reactive power injection based, this principle slightly impacts the power factor.

Application of new grid reconfigurations

Traditionally, in MV and LV distribution grids, the radial feeder has been widely applied since it is a solution of simplest and least expensive to construct [68, 69]. In this radial configuration, the loads are supplied from the sole upstream grid, leading that the power supply of the feeder is strongly dependent on the upstream grid. Besides, the loads are not evenly allocated in different feeders in most cases, resulting in challenges such as line congestion, voltage violation, and the lifetime reduction of the essential components such as the transformer.

With the application of innovative components, operation concepts that flexibly reconfigure the grid topologies have been proposed, aiming to address the aforementioned challenges. The concept of the meshed grid, which applies a ring reconfiguration of the radial feeders, has drawn interest by the researchers [70, 71, 72, 73, 74]. The loads in the meshed grid can be supplied by more than one upstream grid, increasing the flexibility of the power supply. This ring topology benefits the operation in the meshed grid, achieving, e.g., equally distributed power flow via the essential components, avoiding overload, and reducing voltage issues such as voltage rise.

Loop power controller (LPC) is one approach of the meshed grid application for the radial feeders [71, 72, 73]. The LPC is realized either with a combined set of tap changer and phase shifter transformers or a group of back-to-back (B2B) power converters situated between two radial feeders. The two feeders, which are connected at different sides of the LPC, can be operated with a ring configuration.

Fig. 2.3 depicts a LPC based meshed grid approach. The LPC, which is based on B2B converters, decouples the phase angles of two LVac feeders, solving the phase shift issue that is the main obstacle to meshed grid application. The LPC controls the power exchange between feeders. Assuming that the left feeder has a significantly large penetration of the DG and the right feeder has a heavy demand, the power generated from the DG in the left feeder can be directly delivered to the right feeder via the LPC. This solution reaches a balanced power flow via both transformers T1 and T2, decreasing the overload possibility of important components and increasing the robustness of the power grid [71, 72, 73]. The B2B converters can also control the reactive power in both feeders to maintain acceptable voltage magnitudes of the meshed grid and power factors level of the power exchange via the transformers T1 and T2.

2.2 Power Electronics Components for Grid Controllability

Enhancement

This thesis aims to exploit the PE components in grid controllability enhancement. The work evaluates three PE components, the smart transformer (ST), the energy storage static synchronous compensator (ES-STATCOM / ES-STA), and the fast charging station (FCS). The ST represents an innovative concept as a systematical grid reinforcement component other than the existing ones. The ES-STATCOM and the FCS are not widely applied components for grid controllability enhancement. However, with the continuous growth of the penetration of these components in the grid, it is worth exploiting the grid enhancement capability of the components as the ancillary tasks which they can provide. By providing the ancillary tasks, the spare capacity of the components can be exploited, maximizing the capability of the components. Details of the components' topologies and controllers' structures are given in the following part.

2.2.1 Smart transformer

Recently, power electronics based transformers have gained attention since they offer improved grid regulation performance than conventional low-frequency transformers (LFTs). Different topologies can be utilized for the power electronics based transformer. Fig. 2.4 (a) shows the three-stage solid-state-transformer (SST) based topology, and Fig. 2.4 (b) shows a B2B based topology. The voltage conversion of the SST is implemented by dc/dc stage via a high-frequency transformer so that the SST is directly connected to the MV grid. The B2B based topology, however, requires an LFT for the voltage conversion.

In comparison to the B2B based topology, the SST topology can offer several benefits. A 20–50 % reduction of volume and weight can be achieved by using the high-frequency trans-

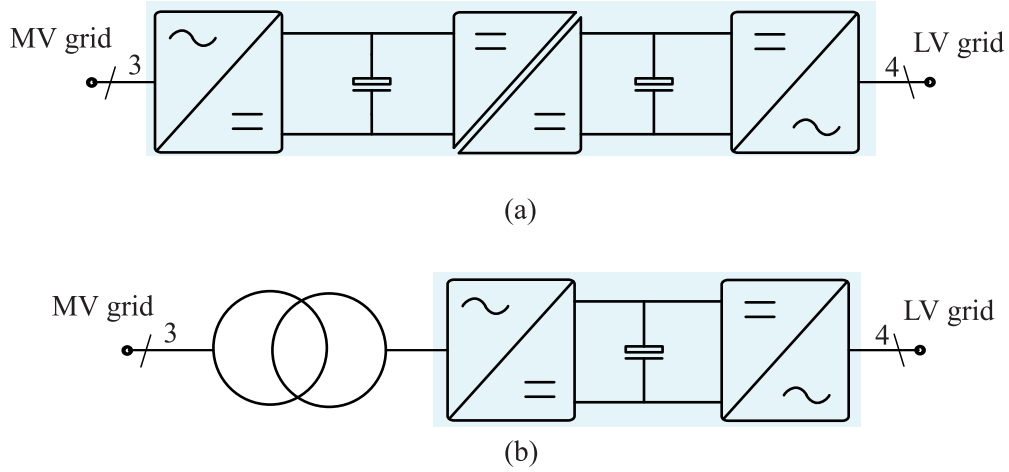


Fig. 2.4: Topologies of power electronics based transformer. (a) SST topology. (b) B2B topology.

former [8]. Moreover, it enables the dc links of ST at both MV and LV levels. Depending on the power rating, high power components such as wind turbines or fast charging stations can be connected to the MVdc link, while the LVdc link provides the connection for the photovoltaic (PV) units or small scale ESSs. The topology of double dc links has a better capability to maintain voltage stability. One dc link can also be used to damp the voltage oscillation, stabilizing the voltage of the other dc link, which connects the critical loads [75].

The already existing SST concept has more focus on the hardware aspects. The ST, however, represents the concept with more focus on the ancillary grid regulation aspects [76, 77, 78, 79]. Advanced communication infrastructures and intelligent grid management algorithms are also essential parts of the ST concept. Currently, the deployment of STs focuses on replacing the conventional iron low-frequency transformers at the points where the ancillary grid regulation can be enhanced significantly by providing the ST's grid management. Besides the basic operations such as voltage conversion like a conventional transformer in the distribution grid, the ST can provide several functionalities for improving the performance of the grid, such as resonance damping, load compensation, and voltage regulation [75]. It is a component providing a systematic approach to address the grid operation issues and to facilitate the management of the distribution grid [1, 8]. Analysis has demonstrated the effectiveness of the ST for its application in distribution grid regulation [75, 76, 77, 78, 79].

The architectures of every stage of the ST and its corresponding grid support functionalities vary from stage to stage. The details of each stage's architecture candidates and the corresponding controller structure will be explained in the following part.

The MV stage can be constructed by various architecture candidates, such as neutral-point clamped (NPC) converter, multilevel modular converter (MMC), and cascaded half bridge (CHB) converter. The details of the architectures are out of the scope of this work, which can refer to [75]. However, the corresponding controller structure of this stage can be represented in Fig. 2.5 highlighted in blue. This introduced controller structure is the fundamental one

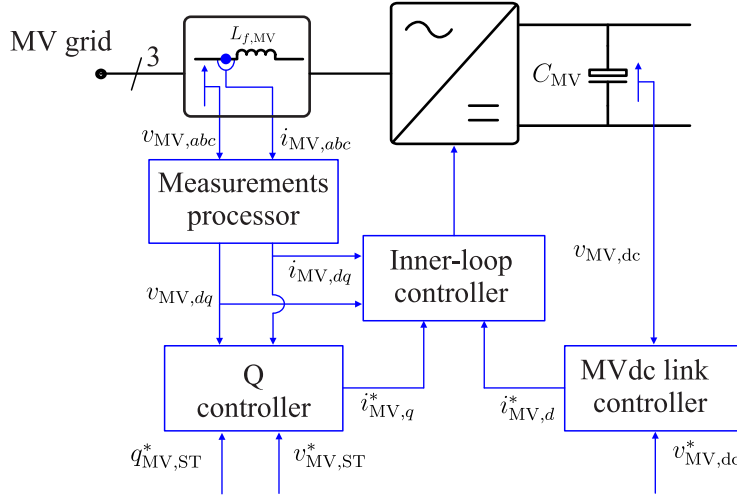


Fig. 2.5: Controller structure of ST's MV stage.

for the ST. Depending on the application, modifications can be implemented based on the fundamental structures, targeting the specified regulation tasks.

The controller of the MV stage has a double-loop controller structure. The outer-loop consists of a dc link controller and a reactive power (Q) controller. The dc link controller is responsible for the voltage control of the MVdc link. The voltage through the dc link $v_{MV,dc}$ is measured and sent to the controller. This controller controls the dc link voltage to follow the reference $v_{MV,dc}^*$, which can be a constant or a variable, depending on the control functionalities the dc link implements. The output of dc link controller is a current reference. In this work, the control of active/reactive power is decoupled by means of the Park's transformation, where the d/q-axis deals with active/reactive power control receptively. Consequently, the current reference generated from dc link controller is represented as $i_{MV,d}^*$. The Q controller is responsible for the reactive power injection to the MV grid. Using the reactive power reference $q_{MV,ST}^*$ or the voltage reference $v_{MV,ST}^*$ (which is usually the voltage reference of the MV bus ST connected), the controller generates the current reference $i_{MV,q}^*$, which controls the reactive power injection. The terminal voltage and output current of the MV stage $v_{MV,abc}$ and $i_{MV,abc}$, are converted into $v_{MV,dq}$ and $i_{MV,dq}$ in the measurements processor module, used as the feedback of controller. The inner-loop controller processes the references and feedback values to adjust the pulse-width-modulation (PWM) of the MV stage converter. Eventually, the required active power is exchanged between the MV stage and the ac grid, and the required reactive power is injected into the grid.

The active power of the MV stage flow must balance the power demand required by the loads connected to both the ST dc links and the LVac grid. Instead, the reactive power provision has a degree of freedom: the ST can work under the unity power factor or provide reactive power for ancillary grid operation. The reference $q_{MV,ST}^*$, can be generated by the local measurements. For example, a droop controller can generate the reference comparing the measured bus voltage, where ST is connected to, and the nominal voltage. The reference

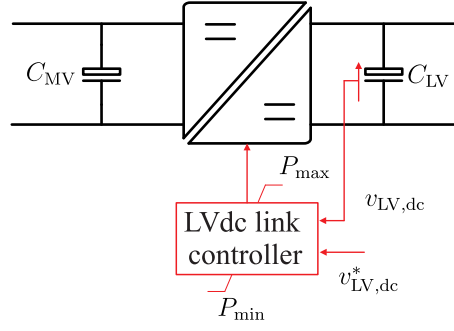


Fig. 2.6: Controller structure of ST's dc/dc stage.

$q_{MV,ST}^*$ can also receive from a control center, in which the value is computed according to the predefined algorithm. This stage can provide ancillary regulation to the ac grid at the MV level, such as voltage support or power factor correction by means of reactive power injection, enhancing the controllability in the MV grid. The capability of reactive power injection $Q_{ST,MV}$ is restricted by the power rating of this stage $S_{ST,MV}$ and the active power exchange $P_{ST,MV}$, as depicted in 2.2:

$$Q_{ST,MV}^2 \leq S_{ST,MV}^2 - P_{ST,MV}^2 \quad (2.2)$$

The dc stage is the isolation stage of the ST, which adapts the voltage levels between MV and LV via a high-frequency transformer. This stage usually can be constructed by means of two architecture candidates, which are the dual active bridge (DAB) and the series resonant converter (SRC) [75]. Besides the voltage conversion, this stage controls the voltage of the LVdc link, enabling a stable power supply to the LVac grid. The controller structure is presented in Fig. 2.6. $v_{LV,dc}^*$ is the reference voltage of the LVdc link, which can be a constant or a variable, depending on the operation requirements. The values of P_{max} and P_{min} are the maximal and minimal power that is allowed to transfer via this stage (Positive value in this work represents the power flow from the MV side to the LV side, and the negative value represents the opposite power direction). The value of P_{min} can be the opposite value of P_{max} . If the reversed power flow from LV to MV is restricted, the value can be varied between the $-P_{max}$ and 0. The dc stage decouples the MV and LV grids, enabling independent operation of both MV and LV grids connected to an ST.

The LV stage is responsible for the operation of the connected LVac grid. This stage usually can be constructed by means of various architecture candidates, such as NPC converter, T-type converter, and four-leg converter [1]. The grid regulation controller can have various modules, which the LV stage controller can select. If the power operation module is selected, the power references p_{LV}^* and q_{LV}^* will be sent as the input to the LV stage controller. If the voltage regulation module is selected, the voltage and frequency references $v_{LV,abc}^*$ and f^* will be used as the input. The values of these inputs can be the constant, which supplies a constant power or provides a stiff voltage to the LV grid, but it can also be variables to

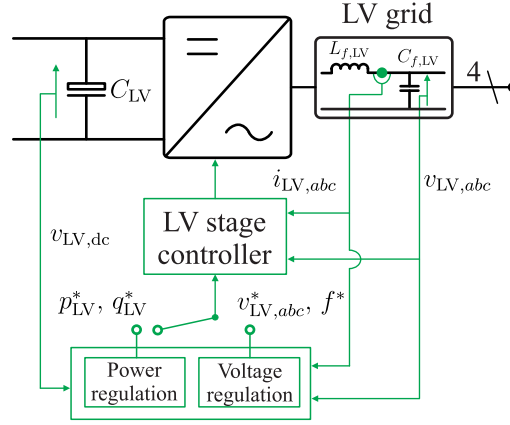


Fig. 2.7: Controller structure of ST's LV stage.

implement the regulation such as online load identification, soft load reduction, and overload limitation [1].

The LV stage controller processes the references together with the feedback, which are the measurements of voltage $v_{LV,abc}$, and current $i_{LV,abc}$ from the connected bus in the LV grid. This stage adjusts the PWM, modifying the output active/reactive power or the voltage amplitude/angle and frequency. The topology of the controller is presented in Fig. 2.7.

The power rating of the three stages can be identical. However, under specific sizing considerations, the power rating of each stage is treated independently, depending on the requirements of grid regulation [80]. The premises, unless specific sizing considerations are required, are that the MV and LV stages must be rated, taking into account the maximal power defined by the system operator that the stages need to operate during normal operation conditions [80]. During dynamic conditions caused by fault, on the opposite of DG, which the disconnection can be considered if the voltage/frequency violates the constraints, the ST shall remain operative during fault. However, a reduced operation capability shall be designed for this situation in order to not oversize the hardware [1].

2.2.2 Energy storage static synchronous compensator (ES-STATCOM)

The ESS, traditionally applied for μ -grid to store excess renewable generation and compensate for the energy deficit [39, 46], has gained increased focus for the operation of large interconnected power grids thanks to the technical progression of associated technologies, decreasing the cost but prolonging the life span [81, 82, 83]. In the literature, ESSs have been proposed in applications to grid controllability enhancement by providing regulation such as load peak shaving, dispatch of stochastic prosumption, and primary frequency support [37, 38, 40, 42, 48].

The STATCOM, on the other hand, is a fundamental component for the implementation of several operation functionalities, focusing on reactive power management and voltage

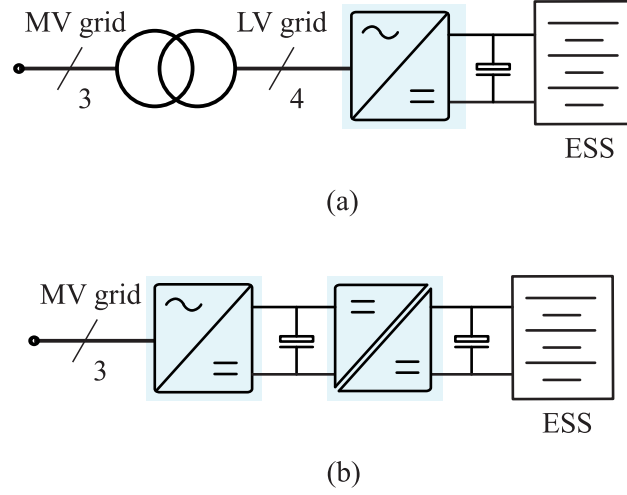


Fig. 2.8: Topologies of ES-STATCOM. (a) Conventional approach with an MV/LV transformer. (b) MMC based approach connected to MV grid.

regulation. For instance, the STATCOM has been employed to sustain the voltage in case of the disturbances such as voltage flicker, voltage sag/swell by the provision of reactive power [84, 85]. This component can also actively condition the power quality, such as reducing harmonics or damping the dynamic oscillation [57, 86].

A combination of ESS and STATCOM is expected to gain more grid controllability. Consequently, the ES-STATCOM has been proposed, which integrates the functions of STATCOM into the ESS. In this way, not only active power but also reactive power can be regulated to support the grid, providing more operation options to the grid. The ES-STATCOM has been evaluated in applications to provide ancillary frequency and voltage regulation to the grids [86, 87, 88]. In a distribution grid, where the R/X ratio of the lines/cables is higher than the transmission grid, coordinated actions of active/reactive power can be more effective than only active or reactive power regulation.

Various topologies can be utilized for ES-STATCOM. A conventional approach, as shown in Fig. 2.8 (a), employs an ac/dc stage to connect the ESS. This stage is installed in the LV grid, which requires an LFT to connect to the MV grid. The MMC approach, as shown in Fig. 2.8 (b), eliminates the LFT. Instead, it employs an ac/dc stage based on MMC, which directly connects to the MV grid. A dc/dc stage, following the ac/dc stage, converting the voltage to the level which the ESS requires. For every energy storage cell, a dc/dc converter is widely used to control the charging/discharging process. This converter is considered an internal component of the energy storage cell and not depicted in Fig. 2.8.

This work studies the conventional topology approach. The basic controller structure of the ES-STATCOM is presented in Fig. 2.9. The active power P_{ESS} is determined by the various charging/discharging algorithms, targeting such as mitigation of the demand deviation to track the dispatch plan [44]. The ac/dc stage controller structure is similar to the MV stage of ST, except the converter of ES-STATCOM is connected to the LV grid. The controller has a

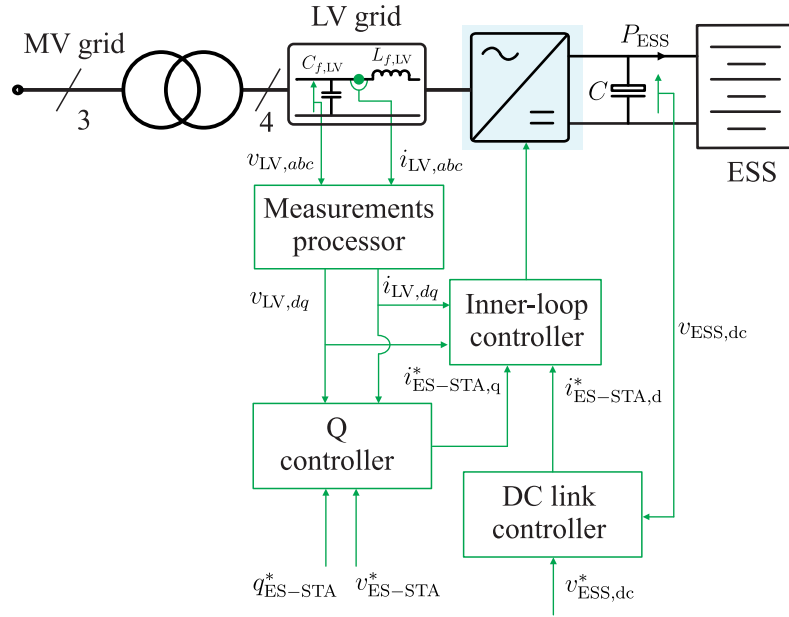


Fig. 2.9: Controller structure of conventional approach based ES-STATCOM.

double-loop structure. The outer-loop consists of a dc link controller and a Q controller. The dc link controller is responsible for a stable voltage of $v_{ESS,dc}$. The output of this controller is the current reference $i_{ES-STA,d}^*$ by applying the Park transformation. The Q controller is responsible for the reactive power exchange between the ES-STATCOM and the grid. Receiving the references q_{ES-STA}^* or v_{ES-STA}^* , this controller generates the current reference $i_{ES-STA,q}^*$. The current references are subjected to the inner-loop controller, which adjusts the PWM of the converter. Consequently, the required charging/discharging power can be exchanged between the ESS and the ac grid, and the required reactive power can be injected into the grid. The power rating of the converter S_{ES-STA} restricts the reactive power injection and charging/discharging power, similar to the MV stage of ST.

2.2.3 Fast charging station

The FCS can reduce the charging duration of the EVs, encouraging their use. The FCSs have been considered as controllable loads to conduct the grid support regulation, such as congestion management or renewable energy integration, by means of charging power control [28, 30, 33]. Charging power can be controlled by employing autonomous decentralized charging control or aggregated centralized charging control, depending on the communication architectures and charging algorithms.

The decentralized charging is that the individual EV performs as a mobile agent, which requires an EV to have onboard control [89, 90]. The decentralized charging control has less requirements on the communication infrastructure, and the control algorithm is easy to be implemented. The lack of an overall system view further requires a considerable safety mar-

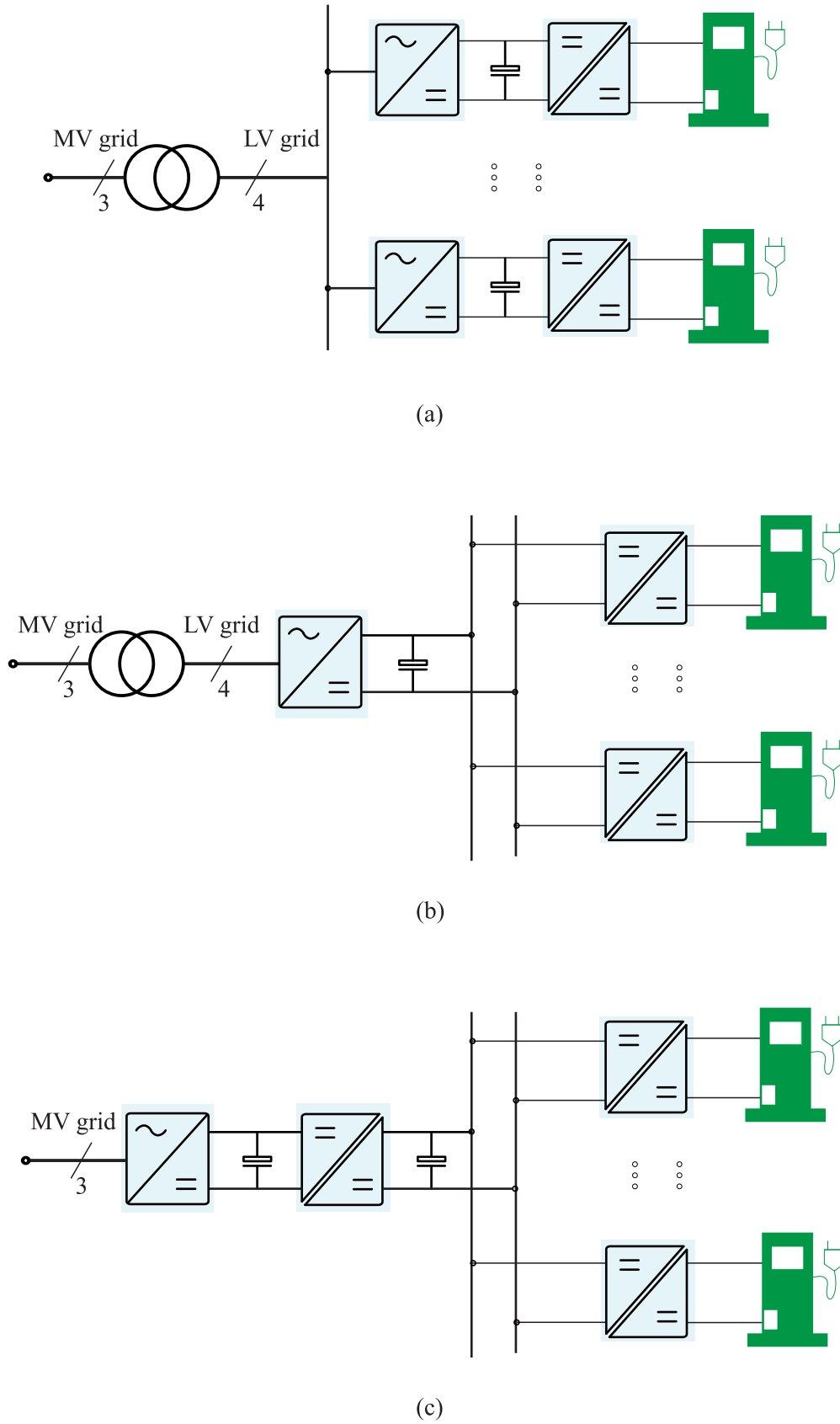


Fig. 2.10: Topologies of FCS. (a) Individual ac/dc stages based approach for LV grid connection. (b) Aggregated ac/dc stage based approach for LV grid connection. (c) MMC based approach for MV grid connection.

gin to maintain operating limits. Furthermore, neither overall optimization nor prioritization in the parallel operation mode is possible with the decentralized charging control.

The centralized charging control offers an overall system view. With the centralized charging controller, the grid capacity, defined as the ratio between charging rate and a voltage drop at the grid connection point, is better utilized. The centralized charging control gives the option to include state of charge weighting [89]. Therefore, intelligent prioritization in parallel operation mode is possible. Nevertheless, the central charging control requires a backup system of the central control logic to avoid station blackout [90].

Besides the charging power control, similar to other PE components, the FCS can inject a specified amount of reactive power to support the grid [91, 92]. The capability of reactive power injection is limited by the power rating of the charging facility and its charging power.

Topology of the FCS varies from manufacturer to manufacturer. A few common applied topologies are represented in Fig. 2.10 [93]. Fig. 2.10 (a) and (b) represent the topologies which the FCS is connected to the LV grid and an MV/LV transformer is required for the connection of the MV grid. The topology in Fig. 2.10 (b) uses an aggregated ac/dc stage as the interface between the charging facilities and the ac grid. On the contrary, there is no aggregated stage but individual ac/dc stage for every charging facility of the topology in Fig. 2.10 (a). Fig. 2.10 (c) represents an MMC based topology which eliminates the transformer for the connection of MV grid. A galvanic isolation between the EV battery and the electrical grid, however, is always required [94], which can be achieved by an LFT as depicted in Fig. 2.10 (a) and (b), or a high-frequency transformer, as depicted in Fig. 2.10 (c).

Without the aggregated ac/dc stage of a high power rating, it requires complex communication and coordination between the small ac/dc stages in Fig. 2.10 (a) to gain considerable capability of reactive power injection. On the other hand, the investment of the topology in Fig. 2.10 (b) is lower than the MMC one. This work studies consequently the topology of the FCS in Fig. 2.10 (b). The controller structure is depicted in Fig. 2.11, which is similar to the controller structure of the ES-STATCOM. A double-loop structure is applied. The outer-loop is responsible to generate the current references $i_{\text{FCS,d}}^*$ based on dc link voltage $v_{\text{FCS,dc}}^*$ and $i_{\text{FCS,q}}^*$ based on reactive power reference q_{FCS}^* or voltage reference v_{FCS}^* , respectively. The inner-loop controller is responsible for adjusting the converter's PWM so that the required charging power and reactive power can be exchanged from the ac grid. The charging power P_{FCS} is the summary of power from all charging facilities $P_{\text{EV},1}, \dots, P_{\text{EV},n}$. The power of every charging facility is decided by the charging algorithms, which can be exact the demand of the connected EV, or a value less than the demand to implement grid support such as congestion management or frequency support.

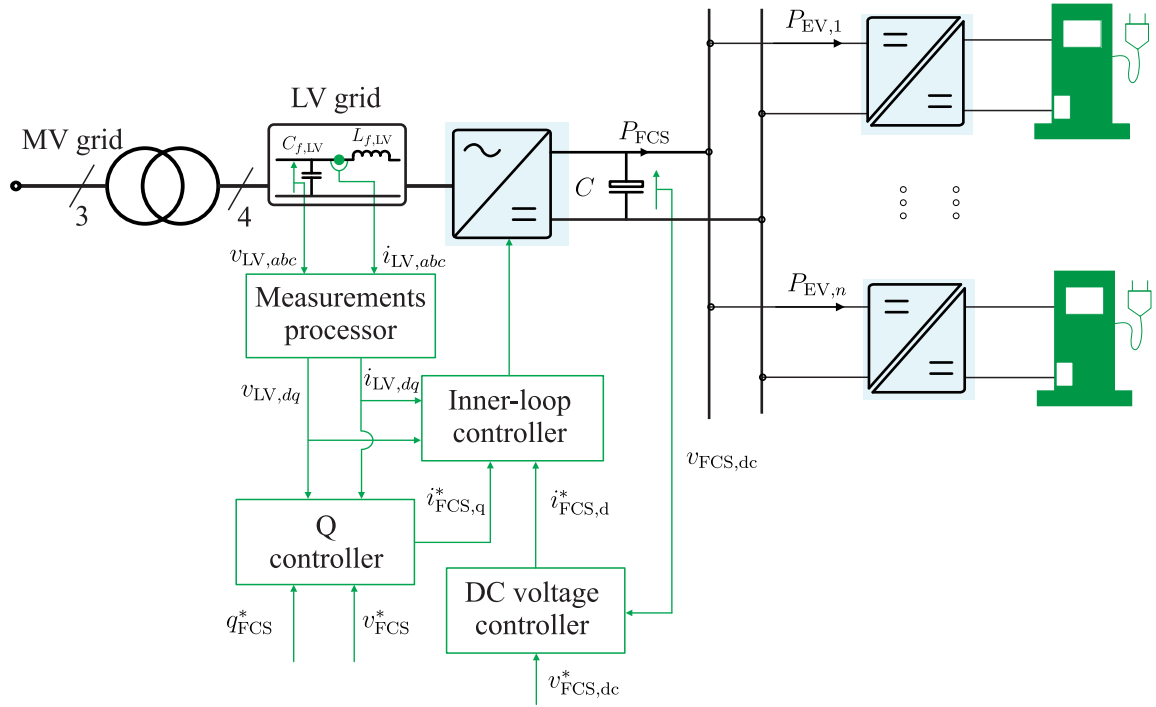


Fig. 2.11: Controller structure of aggregated ac/dc stage based FCS.

2.3 Development of Innovative Grid Controllability Enhancement Solutions based on Power Electronics Components

With the ST, the ES-STATCOM, and the FCS, this thesis aims to develop a group of grid controllability enhancement solutions, addressing the power and voltage operation challenges. The solutions will be developed either based on innovative operation concepts and schemes or based on innovative PE components. In this section, the common features of the proposed solutions, such as the grid connecting strategies, the coordination methods, are briefly introduced.

2.3.1 Grid connecting strategies

Grid connecting operation strategies have significant impacts on the operation schemes and controllability. Depending on the grid operation approaches, the grid connecting operation strategies can be categorized into grid-following and grid-forming, which target to regulate the active/reactive power injection and the voltage/frequency, respectively. It must point out that some types of grid-forming converters regulate the voltage and frequency by adjusting the active/reactive power injection. Furthermore, a PE component can flexibly adjust its grid connecting strategies according to the operators.

Grid-following strategy

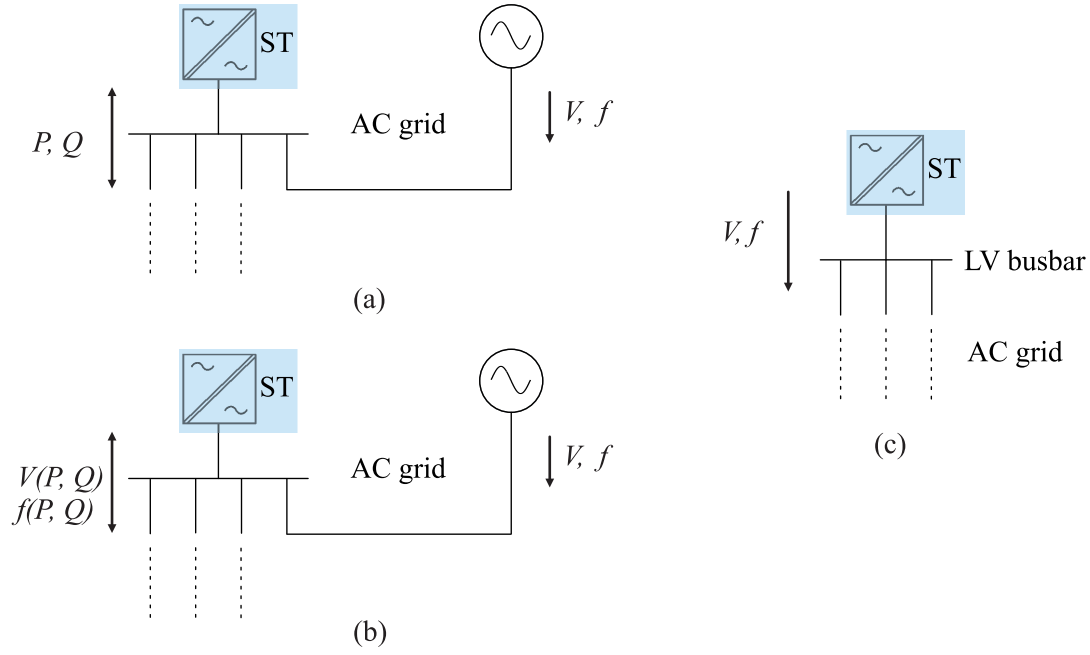


Fig. 2.12: Grid connecting strategies: (a) Grid-following strategy. (b) Grid-forming strategy in inter-connected grid. (c) Grid-forming strategy in islanded grid.

Grid-following is a widely used strategy for PE components [95]. Taking ST as an example, depicted in Fig. 2.12 (a), the ST injects the required amount of active/reactive power P and Q into the ac grid. Synchronization between the ST and the external grid is essential, which is normally achieved by a phase-lock-loop. With this strategy, the PE component works similarly to a distributed energy resource (DER).

Grid-forming strategy

In comparison to the grid-following strategy, the PE component in the grid-forming strategy does not aim to deliver the required amount of power into the grid. On the contrary, the PE component regulates the grid frequency and the voltage. As shown in Fig. 2.12 (b), the ST adjusts its power injection, targeting to regulate the voltage amplitude of the connected busbar and reduce the frequency deviation from the nominal value. In this case, the voltage waveform and the nominal frequency are defined by the ac grid, i.e., sinusoid waveform and in Europa 50 Hz frequency. The PE component, in this case, behaves similarly to a synchronous machine.

The ST can decouple its connected LV grid in terms of voltage and frequency, making the connected LV grid as 'a controlled island'. In this sense, the busbar voltage and LV grid frequency are formed by the ST, as depicted in Fig. 2.12 (c). Besides the conventional sinusoid voltage waveform and 50 Hz frequency, the ST can flexibly adjust the voltage waveform and frequency [75]. If voltage/frequency-dependent loads, e.g., constant impedance loads, are present, the power consumption of the LV grid can also be shaped to implement grid support

regulation, such as overload control or real-time frequency regulation [96, 97, 98, 99]. In this case, the PE component guarantees high power quality standards in the connected grid.

2.3.2 Distributed and centralized solutions

Grid regulation actions from PE components should be coordinated, optimizing the capability of the PE components. The developed solutions in this thesis can be categorized into the distributed and centralized solutions depending on the coordination approaches.

Distributed solution

As a distributed solution, multiple PE components geographically spread among the grid are coordinated, in which all components are regulated equally, i.e., no component behaves as a master.

Centralized solution

If only one PE component is involved in the solution, a centralized solution is formulated. For the solution that involves more than one component, a centralized solution can be formulated if one component behaves as a master actuator or if there is no interaction between the actuators.

2.3.3 Common features of the developed grid enhancement solutions

The solutions presented in the following chapters aim to regulate the power and voltage in the distribution grid, enhancing the grid controllability, addressing the operation challenges arising with the new actors. The proposed solutions must be in accordance with the involved PE components, making every solution have unique features. However, all solutions have some features that are in common. These common features are explained in the following text.

Exploitation of power electronics components' spare capacity

The ST is mainly responsible for voltage conversion of the MV and LV grids and supplies power demand to the connected LV grid; the ES-STATCOM is responsible for storing the energy surplus and compensating the energy deficit; the FCS has the main tasks to supply the EVs charging. The grid regulation, such as reactive power injection, is rather an ancillary regulation than the main task of the three components.

However, shown in Fig. 2.13, which is a grid with an ST, it can be noted that most time of the 24 h duration, the active power flow via the ST does not reach its power rating, leaving

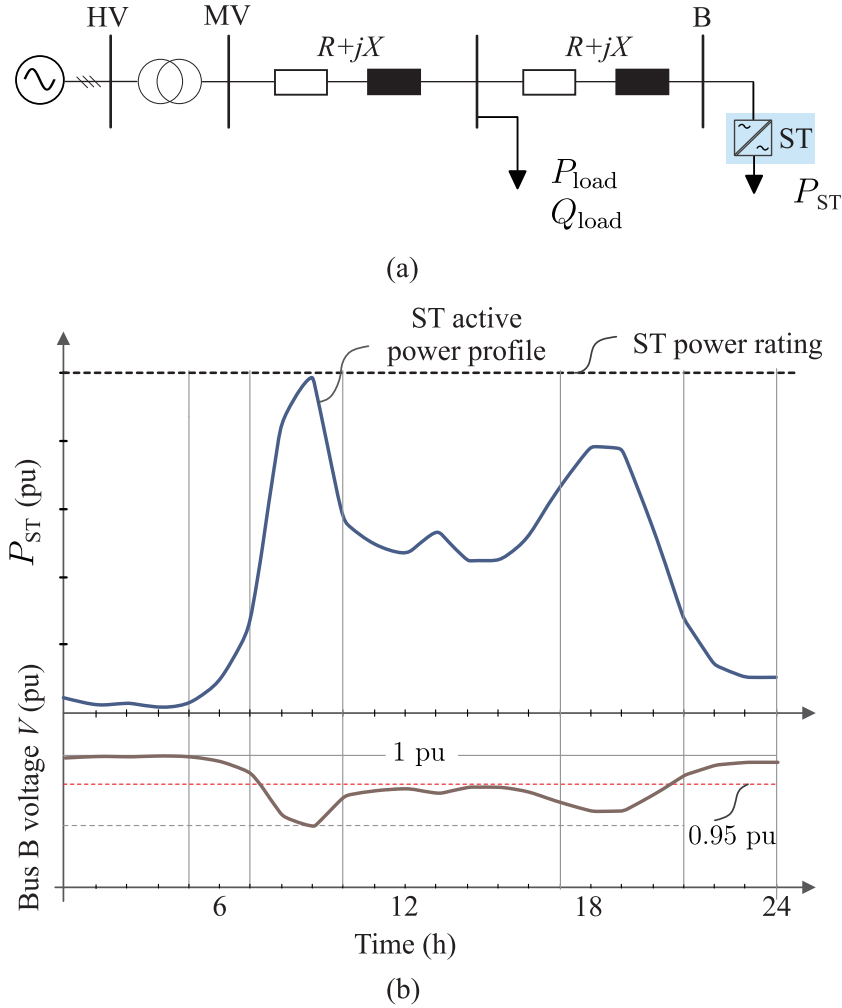


Fig. 2.13: Correlation of ST active power flow and ST-connected bus voltage behavior. (a) Topology of the grid. (b) Profiles of ST active power flow and bus B voltage.

significant spare capacity of reactive power injection. Most importantly, this figure shows that the voltage violation appears not always correlating to the peak active power flow via the ST. It is noted that the violation appears around 18h in Fig. 2.13 when the ST does have considerable spare capacity to provide reactive power to the grid. By providing the ancillary grid regulation, the installation of additional components to address the regulation challenges, such as the voltage violation in Fig. 2.13 can be avoided, decreasing the investment of grid enhancement. In the project "LV-ENGINE," which is funded by the Office of Gas and Electricity Markets of the UK, estimation shows that the ST can save up to GBP 60 Mio. in network infrastructure upgrade costs by the year 2030, and avoid the construction of 16 % new substations if it provides the ancillary grid regulation [100].

As mentioned before, the reactive power injection is limited by power rating and the active power of the converter. Taking FCS as an example, if an FCS injects a significant amount of reactive power, it will use a considerable portion of its converter's power rating. Consequently, the charging power can be eventually restricted, i.e., the FCS cannot fulfill its primary task. To avoid this issue, all the solutions proposed in this thesis make use of only

the spare capacity of the component. In this sense, the main tasks of the PE components can be impacted to a minimal extent.

Control center based solutions

To implement the control actions, the control references for different PE components, such as reactive power reference, can be derived either with the local controller or with the control center [101]. The local control approach focuses on controlling the grid to a small extent, which processes mainly the local measurements and requires only basic information and communication infrastructure. Moreover, the control algorithm is easy to be implemented. The local controllers implement autonomous control actions, and the coordination between the controllers is limited, e.g., only between the adjacent buses. Furthermore, there is no need to gain a global view of the entire grid. However, systematical coordination of all components to maximizing the gained controllability cannot be easily achieved with local controllers.

As an alternative, the control center approach collects the states of the power grid by the smart meters deployed in the entire grid. This approach requires an advanced communication system to gain a global view of the grid. Advanced communication systems, e.g., phasor measurement units (PMUs), have been more and more equipped in the grid nowadays [102, 103, 104]. It has become more realistic nowadays to achieve the approach based on a control center.

2.4 Summary

The distribution grid is undergoing transformation due to the increased penetration of new actors such as RESs and EVs, which introduce new operation challenges to system operators. Previous analysis has proposed several approaches for grid controllability enhancement in terms of power and voltage regulation. These approaches, relying on the components such as controllable loads, ESSs, OLTC, or STATCOM, show the capability to improve the grid operation, increasing the hosting capability of RESs and EVs.

This thesis aims to develop grid controllability enhancement solutions based on either the innovative operation schemes or the innovative components. Three PE components, ST, ES-STATCOM, and FCS, are involved in this work. For the ST, the possible topology candidates are the SST based topology and the B2B based topology. The three-stage SST based topology has been selected due to the advantages such as MV/LV dc links, less weight, smaller volume. The controller structures of different stages have been explained in detail. For the ES-STATCOM, a conventional ac/dc converter based topology and an MMC based one have been introduced, in which the conventional topology is selected for further evaluation. Its controller structure, which is similar to the ST MV stage, has been explained. For the FCS,

the multiple individual stages based topology, the aggregated stage based one, and the MMC based one have been introduced. The aggregated stage based topology is selected for the considerable power rating of the aggregated stage and lower cost than the MMC based one. The controller structure has been explained.

Depending on the coordination methods of the PE components, the developed solutions can be categorized into distributed and centralized. While injecting reactive power for the ancillary grid regulation, all solutions exploit only the spare capacity of the components, minimizing the negative impact on the main tasks. All solutions in this work are developed based on a control center to maximize the controllability that can be gained.

3 Distributed Load-Leveling Solution with Fast Charging Stations

Electrification in the private and public sectors increases not only the amount of power demand but also the uncertainty of the demand patterns. Different users have their individual demand patterns that the amount and the time have high randomness. The uncertainty of demand patterns, together with the intermittent power generation behaviors of the distributed generation (DG) units such as photovoltaic (PV), can lead to a considerable power mismatch between the demand forecast and real-time consumption. This power mismatch is one of the significant challenges for power system operators. Without appropriately addressing the mismatch, this issue can eventually affect the frequency stability. To alleviate the mismatch, the operators conventionally have to recur on either the balancing market or the energy storage systems (ESSs) [9, 29, 34, 47].

This chapter aims to develop a load-leveling approach exploiting the voltage-dependent loads to mitigate the power mismatch in the medium voltage (MV) grid. A controlled change of voltage magnitude can be achieved by reactive power injection of the power electronics (PE) components. Under these controlled voltage variations, the consumption of voltage-dependent loads in the grid can be shaped to achieve load-leveling. The fast charging stations (FCSs) for electric vehicles (EVs) are selected as the primary actuators to implement the approach due to their high aggregated power rating and limited utilization duration respecting to the full power rating. While the FCS fulfills the charging power demand of any connected EVs, reactive power can still be injected because of the sizeable spare capacity of its converter.

The proposed approach is schematically described in Fig. 3.1. The FCSs are distributed within the MV grid. Therefore, this load-leveling approach can be considered as a distributed solution. The approach is implemented by an optimization algorithm with two goals: (a) minimization of the power mismatch with respect to the demand forecast, (b) reduction of the power losses in the controlled grid. The performance of this approach will be evaluated based on the results from the simulation and laboratory tests.

3.1 Power-Voltage Sensitivity based Load-Leveling

The essential factor of the load leveling performance is the load's power-voltage sensitivity. This section explains some existing real-time sensitivity estimation methods. After that, the approach of the voltage-dependent load-leveling is briefly introduced, and an analysis of the controllability of this approach is performed under different grid parameters and sensitivity conditions. Furthermore, conservation voltage reduction (CVR), a conventional application

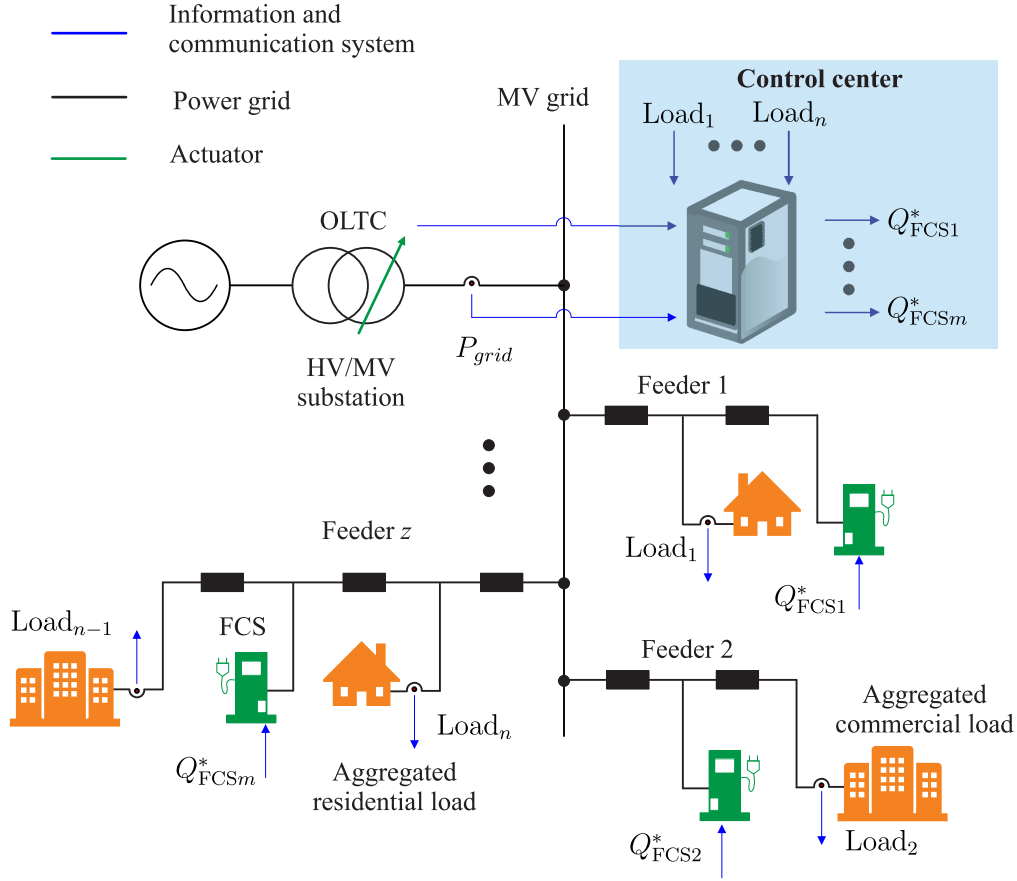


Fig. 3.1: Research focus of Chapter 3: Load-leveling approach in MV grid based on fast charging stations.

exploiting the power-voltage sensitivity, is described, demonstrating the feasibility of those voltage based load regulation approaches.

3.1.1 Power-voltage sensitivity

Power-voltage sensitivity is essential to the performance of the proposed approach. It is an inherent characteristic of the load, representing the dependency of the power consumption (both active power and reactive power) on voltage. Different models can represent the sensitivity, such as the constant impedance/current/power (ZIP) model and the exponential model [105, 106]. Both models have been employed to analyze the load voltage dependency in terms of static and dynamic behaviors.

ZIP model

ZIP model can be represented as:

$$\begin{aligned} P(t) &= P_0(t)[a_Z(V(t)/V_0)^2 + a_IV(t)/V_0 + a_P] \\ Q(t) &= Q_0(t)[b_Z(V(t)/V_0)^2 + b_IV(t)/V_0 + b_P] \end{aligned} \quad (3.1)$$

where $V(t)$ and V_0 are the measured and nominal voltage amplitudes, $P(t)$, $P_0(t)$, $Q(t)$, and $Q_0(t)$ are the measured and nominal active and reactive demand power of the load, respectively. a_Z , a_I , and a_P represent the coefficients of constant impedance load (Z-load), constant current load (I-load), and constant power load (P-load) of the active power. b_Z , b_I , and b_P represent the coefficients of Z/I/P load of reactive power. The coefficients must fulfill the requirement:

$$\begin{aligned} a_Z + a_I + a_P &= 1 \\ b_Z + b_I + b_P &= 1 \end{aligned} \quad (3.2)$$

Exponential model

The exponential model describes the load active and reactive power modification with voltage variation in the format of less parameters than the ZIP model:

$$\begin{aligned} P(t) &= P_0(t) (V(t)/V_0)^{k_p} \\ Q(t) &= Q_0(t) (V(t)/V_0)^{k_q} \end{aligned} \quad (3.3)$$

where k_p and k_q are power-voltage sensitivity coefficients of the active and reactive power, respectively.

The exponential model has only one parameter, i.e., k_p or k_q , to represent the active/reactive power-voltage sensitivity coefficient in each equation. On the contrary, the ZIP model has more dependent parameters in each equation. With more parameters, statistical assumptions have to be made, which can nullify the advantage of the real-time update of the sensitivity coefficients.

3.1.2 Online load identification

Traditionally, the prerequisite in applying the exponential model is that the nominal power is known. However, the voltage conditions are different from the nominal ones in most operation cases, resulting in difficulty to define the nominal power. For this reason, an online load identification method has been developed. This method lies in creating a controlled small voltage perturbation in the grid, and measuring the load power. To create the voltage variation, a commonly used way is the reactive power injection, which is suitable for any grid. If there is a grid-forming PE component such as the smart transformer, the identification can be implemented by directly changing the voltage reference at the grid forming point. The accuracy, effectiveness, and reliability of the online load identification have been demonstrated in previous researches [96, 97].

The steps to implement the online load identification are described as shown in Fig. 3.2. The PE component such as FCS, static synchronous compensator injects the reactive power Q_{PE}

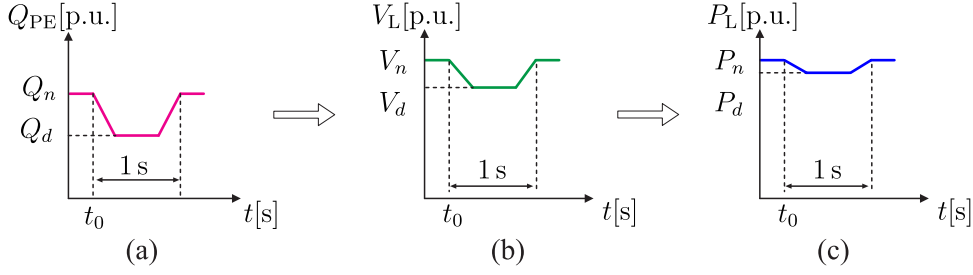


Fig. 3.2: Online load identification with reactive power injection from PE components. (a) Reactive power injection. (b) Voltage response. (c) Load active power reaction to corresponding voltage change.

in order to create the controlled 'perturbation' of the bus voltage V_{load} . As a consequence, the load of the bus changes its power P_{load} to respond to the voltage change. In the smart transformer case, the step of Fig. 3.2 (a) is not necessary. The load power-voltage sensitivity can be estimated by discretizing (3.3). For example, the estimation of k_p for any considered time step s_k can be expressed as:

$$k_p(s_k) = \frac{\frac{P_{load}(s_k) - P_{load}(s_{k-1})}{P_{load}(s_{k-1})}}{\frac{V_{load}(s_k) - V_{load}(s_{k-1})}{V_{load}(s_{k-1})}} \quad (3.4)$$

where $k_p(s_k)$ is the estimation of k_p at the time step s_k , $P_{load}(s_k)$ and $V_{load}(s_k)$ are the active power and voltage measurements of the corresponding time step. The estimated exponential sensitivity are only accurate around the voltage/power conditions in the computation.

The power-voltage sensitivity coefficients need to be updated periodical since the values can be influenced by grid conditions, weather, and composition of aggregated load. An updating periods of tens of minutes must be fulfilled [107, 108, 109]. The online sensitivity identification method allows a continuous update of the sensitivity coefficients, ensuring the accuracy of the estimation.

3.1.3 Power regulation with fast charging stations

The concept of the voltage-dependent load-leveling approach uses the actuators, i.e., FCSs, to inject reactive power, which regulates the demand of the voltage-dependent loads. The proposed approach uses the control center instead of different local controllers to determine the reactive power set-points of all FCSs.

As shown in Fig. 3.1, to implement the approach, all measurements are collected and processed by the control center. $Load_y(t)$ represents the measurement of each bus y , containing information of power-voltage sensitivity $k_{py}(t)$, $k_{qy}(t)$, voltage $V_{loady}(t)$, and load demand $P_{loady}(t)$, $Q_{loady}(t)$ of this bus. Additionally, the on-load tap changer (OLTC) is also used as a support actuator. Therefore, the tap position is also sent to the control center. After receiving

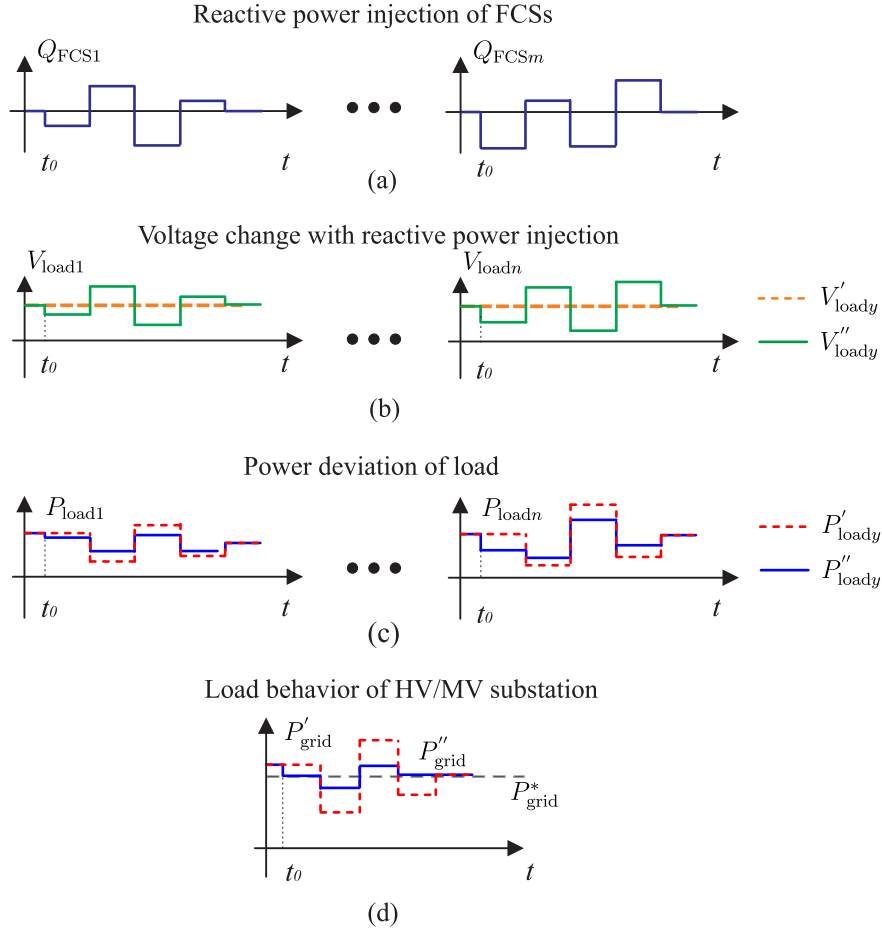


Fig. 3.3: Voltage and power behavior with reactive power injection from FCSs. (a) Reactive power injection from all FCSs. (b) Voltage response of different buses to reactive power from FCSs. (c) Active power reaction to voltage change. (d) Power behavior of the grid.

all information, the control center compares the real-time demand with the demand forecast $P^*_{grid}(t)$, which is derived from historical data, and determines the reactive power injection $Q_{FCSx}(t)$ ($x = 1, 2, \dots, m$) of FCS x .

Shown in Fig. 3.3 (a), all FCSs must inject the required reactive power computed by the control center. The voltage of each bus is regulated from $V'_{loady}(t)$ to $V''_{loady}(t)$ (the prime sign on symbols implies without load-leveling and the double prime sign represents with load-leveling), shown in Fig. 3.3 (b). The power of each load responds the voltage variation, adjusting its power consumption to $P''_{load,y}(t)$ (Fig. 3.3 (c)). The total power of entire grid $P''_{grid}(t)$ is controlled to track the grid demand forecast $P^*_{grid}(t)$, as shown in Fig. 3.3 (d).

The charging power supplying to the EVs is the first priority of all FCSs. Consequently, only the spare capacity of the FCSs after fulfilling the charging power is exploited for reactive power provision.

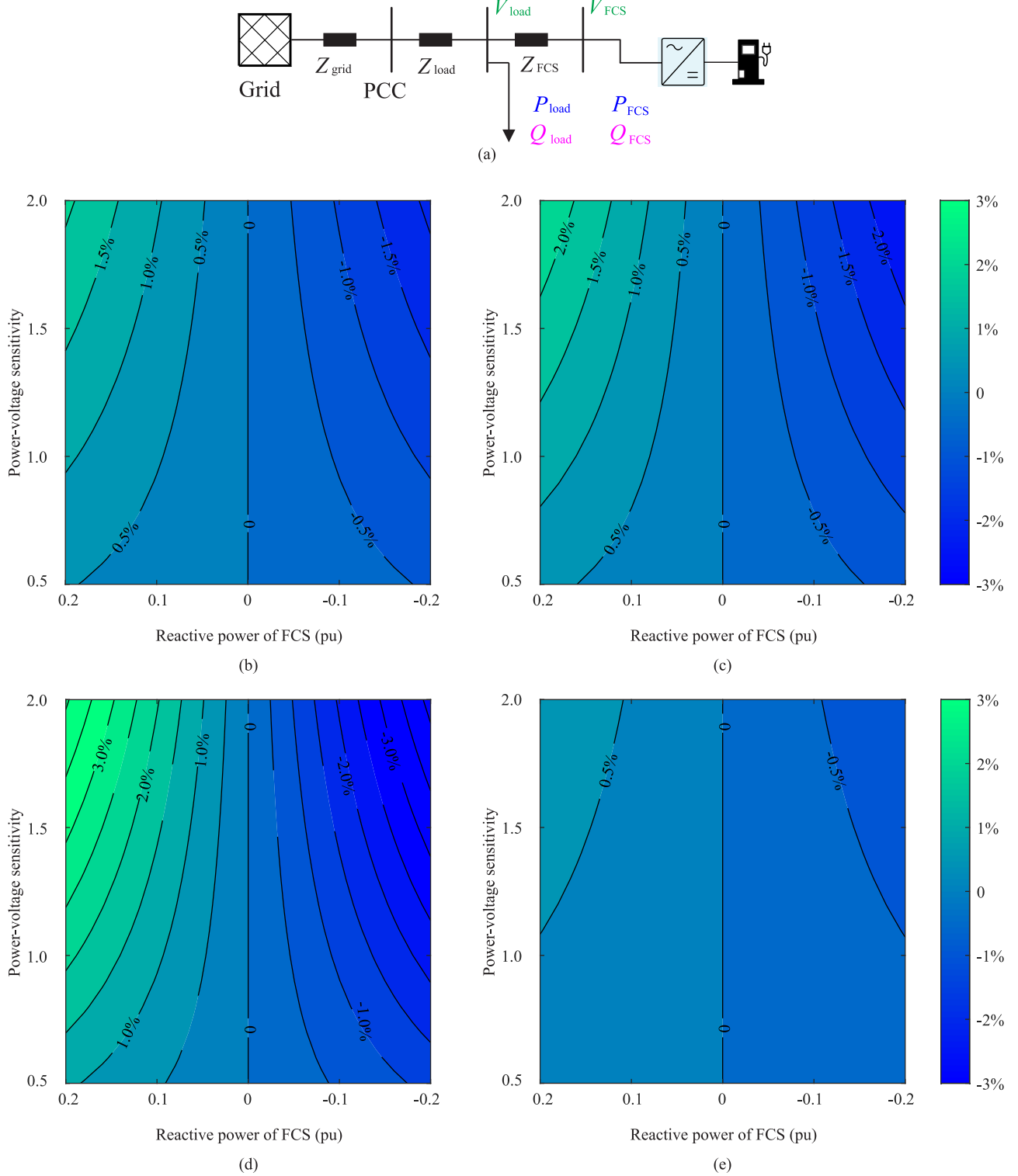


Fig. 3.4: Impact of reactive power injection on the load variation with different power-voltage sensitivity in a simplified feeder. (a) Topology of the simplified feeder. (b) Load variation of Group 1. (c) Load variation of Group 2. (d) Load variation of Group 3. (e) Load variation of Group 4.

Table 3.1: Parameters of simplified testing feeder in Fig. 3.4 (a)

Group No.	SCC ratio	P_{load} (pu)	Z (pu)	Power factor
1	20	2	0.005	1
2	20	2	0.005	0.9
3	10	2	0.005	1
4	50	2	0.005	1

3.1.4 Feasibility analysis with different grid conditions

The effectiveness in power controlling of voltage-dependent load with reactive power should be evaluated before further analysis. A simplified feeder, as shown in Fig. 3.4 (a), is modeled taking into account different grid conditions such as the short circuit capacity (SCC) (represented as Z_{grid}) and power factors. The impedance of every line is equal to Z with R/X ratio 4/3. Information of groups to be analyzed is listed in Table 3.1. The values are represented in per-unit (pu), which can be adjusted to the different voltage levels. To simplify the analysis without lacking in generality, it assumes that the FCS is only a reactive power source, i.e., it does not absorb any active power.

Fig. 3.4 (b)-(e) show the impact on the power consumption P_{load} due to the reactive power injection of FCS. Capacitive reactive power is represented as positive, and inductive reactive power is represented as negative. Fig. 3.4 (b) shows that an active power variation up to 2 % can be achieved with reactive power injection of 0.2 pu when the grid is with SCC of 20 pu and constant impedance load. If the power factor is reduced to 0.9, the control margin is increased to a bit more than 2 %, (Fig. 3.4 (c)). In a weaker grid of the SCC is 10 pu, the power variation of P_{load} can reach approximately 4 %, (Fig. 3.4 (d)). The value of load variation is almost twice it with the SCC of 20 pu. Fig. 3.4 (e) shows the load variation with a stronger grid (SCC 50 pu). Although the value on the power variation is lower than the previous conditions, a power deviation of more than 0.8 % can still be offered. It can be concluded that the load-leveling based on the reactive power provision of the FCS can be implemented under different grid conditions.

3.1.5 On-load tap changer based conservation voltage reduction

OLTC is a widely applied actuator to regulate voltage. Conventionally, the OLTC is controlled with a local controller to regulate the voltage of the bus equipped with OLTC, e.g., the MV busbar of the HV/MV substation. The control function can be represented as:

$$V_{\text{OLTC}}^* - \varepsilon \leq V_{\text{OLTC}}(t) \leq V_{\text{OLTC}}^* + \varepsilon \quad (3.5)$$

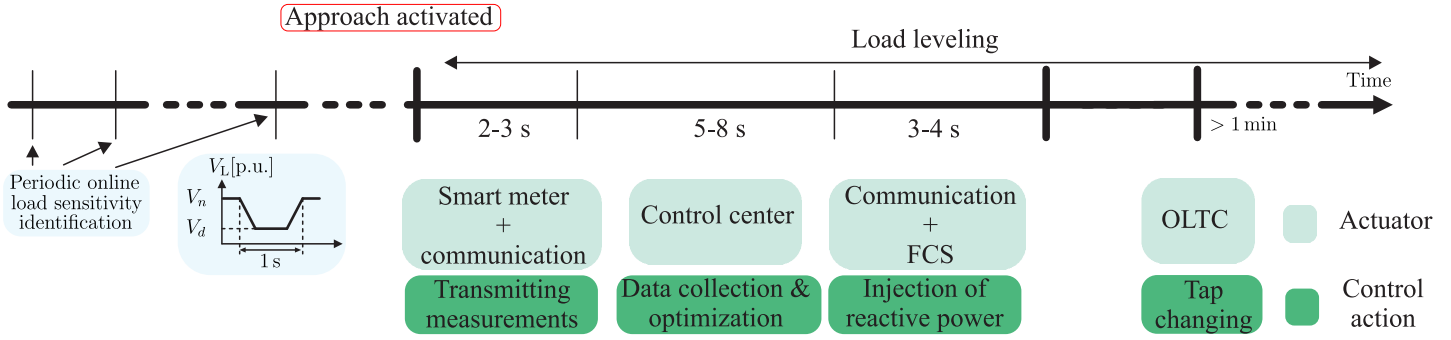


Fig. 3.5: Time-line for related actuators and actions of the proposed load-leveling approach.

where $V_{OLTC}(t)$ is the voltage of the bus with OLTC, V_{OLTC}^* is the voltage reference, and ε represents the voltage deadband of the OLTC controller, respectively.

The CVR by changing the OLTC position within the operator's defined permissible range, represents a well-known example of using OLTC in consumption regulation of voltage-dependent loads:

$$tap_{OLTC}(t) \in [tap_{OLTC,min}, tap_{OLTC,max}] \quad (3.6)$$

where $tap_{OLTC}(t)$ is the current tap position of OLTC, $tap_{OLTC,min}$ and $tap_{OLTC,max}$ are the lowest and highest positions of the OLTC, respectively. $tap_{OLTC} = 0$ in this work represents that the voltage conversion rate of the substation is 1:1 (pu). The CVR must respect the voltage operation constraints (e.g., $\pm 10\%$ of the nominal voltage).

Having been tested in different countries such as the USA, Australia, and Ireland, the CVR has been proven effectively in load control applications [110, 111]. However, due to the limited mechanical switching frequency, the CVR offers only slower control actions compared to the FCSs based load-leveling approach.

The proposed load-leveling approach also involves the OLTC to make the best use of equipment within the grid. As mentioned before, the OLTC actions in the HV/MV substation must be restricted to avoid unnecessary mechanical wear. In this work, the OLTC is activated in the load-leveling only if trigger signal a is 1. In order to trigger the OLTC, the following criteria must be fulfilled:

- No voltage in the grid exceeding $[V_{min}, V_{max}]$.
- A minimal time interval T_{tigger} is required since a is 1 for the last action.
- The power mismatch is higher than the threshold $\Delta\%$ with respect to the forecast.

3.1.6 Time-line for implementation of the proposed approach

Fig. 3.5 presents the overall time-line of load-leveling implementation. The power-voltage sensitivity is periodically estimated. The update of sensitivity is considerably less frequent

than implementing the proposed approach due to the much slower changes of sensitivity of the aggregated load. If the load-leveling approach is activated, approximately 10–15 s is taken to set the new reactive power set-points of FCSs. This delay takes into account the measurement communication delay, the execution time of the algorithm in the control center, and the transmission of the new set-point to each FCS. A communication delay has been estimated in the order of seconds, considering a communication infrastructure based on industrial protocols such as the ModBus (having a typically delay of 0.5–1.0 s). The signal to activate the OLTC for load-leveling is held by the control center at least one minute after the FCSs have adjusted the new reactive power set-points. If the power mismatch is still higher than a threshold value after the on hold duration, the control center will send to the OLTC an activation signal.

3.2 Load-Leveling Scheme based on Power-Voltage Sensitivity

In order to determine the set-points of all actuators, a multi-objective optimization algorithm is formulated. For every scheduled time (e.g., 5 or 15 minutes), the control center analyzes the grid conditions such as the grid demand forecast $P_{\text{grid}}^*(t)$, the measurements including the power, voltage, and load sensitivity coefficients from every bus of the grid, then it computes the new reactive power set-points of FCSs and the new OLTC position by means of nonlinear programming based optimization, aiming to mitigate the power mismatch of $P_{\text{grid}}(t)$ respecting the forecast $P_{\text{grid}}^*(t)$. The software GAMS (General Algebraic Modeling System) is used to implement the optimization. It is a type of high-level modeling software for mathematical optimization with solvers for different linear, nonlinear, and mixed-integer optimization problems.

The algorithm is a two-stage optimization, as described in Fig. 3.6. Stage 1 computes the reactive power injection set-points of the FCSs and the tap position of the OLTC, targeting minimization of the power mismatch $|P_{\text{grid}}(t) - P_{\text{grid}}^*(t)|$. If the mismatch can be fully mitigated by Stage 1, Stage 2 is activated to adjust the reactive power injection of all FCSs, minimizing total losses of the grid. The two stage optimization is developed since the multiple local minima can occur in Stage 1. Therefore, it is necessary to identify in Stage 2 the minimum, in which the minimum losses in the grid can be achieved. The two stages can be implemented with a group of optimization problems as described in the following part.

3.2.1 Stage 1: mitigation of power mismatch

Stage 1 of the algorithm is to minimize the difference between the forecast demand and real-time demand, as described in f_1 :

$$f_1 = \min(|P_{\text{grid}}(t) - P_{\text{grid}}^*(t)|) \quad (3.7)$$

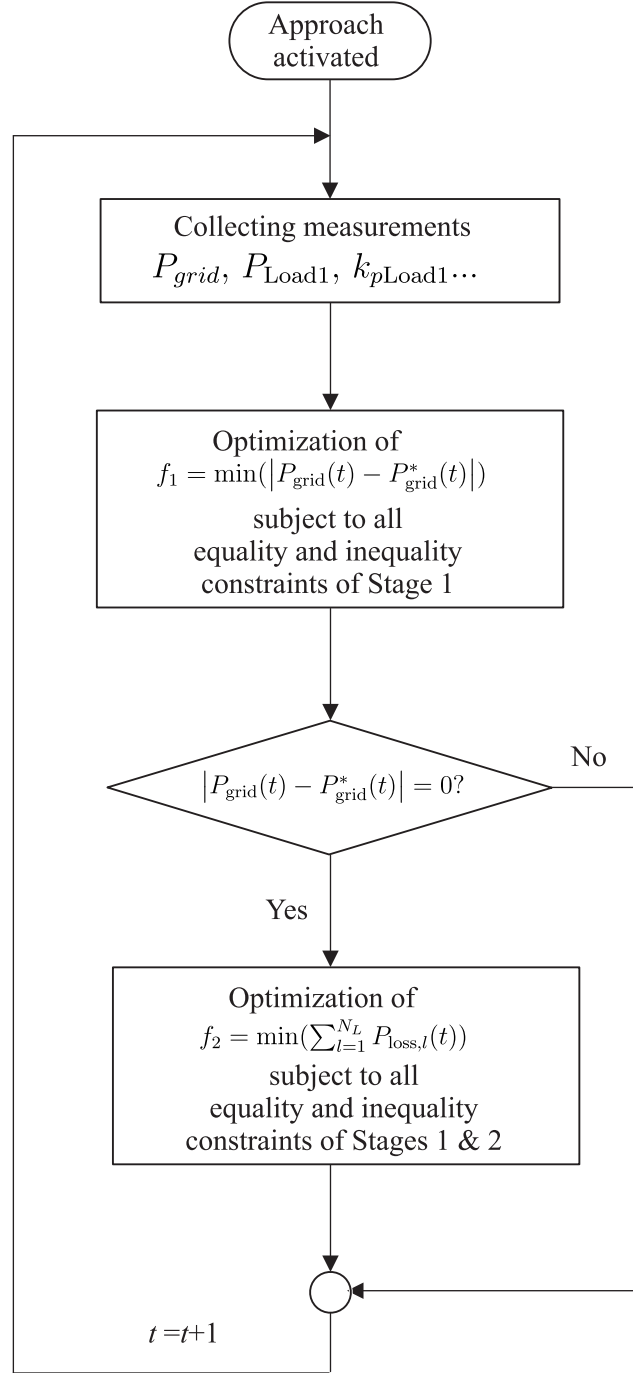


Fig. 3.6: Flow chart of the load-leveling scheme implementation.

Equality and inequality constraints must be subject to the optimization.

Equality constraints

The equality constraints include the load flow and the power-voltage sensitivity relation. They can be described as follows.

- Power flow constraint:

Power flow between different buses must respect the correlations between voltage amplitudes/angles and the impedance of branches (lines and transformers).

$$\begin{aligned} -P_{\text{load}k}(t) &= V_k(t) \sum_{j=1}^{N_B} V_j(t) [G_{kj} \cos(\delta_k(t) - \delta_j(t)) + B_{kj} \sin(\delta_k(t) - \delta_j(t))] \\ -Q_{\text{load}k}(t) &= V_k(t) \sum_{j=1}^{N_B} V_j(t) [G_{kj} \sin(\delta_k(t) - \delta_j(t)) - B_{kj} \cos(\delta_k(t) - \delta_j(t))] \end{aligned} \quad (3.8)$$

where the $N_B = m + n + 1$ is the number of buses of the controlled grid, including buses with loads m , buses with FCSs n , and substation, $P_{\text{load}k}(t)$ and $Q_{\text{load}k}(t)$ are the active and reactive power demand of the bus k ; $\delta(t)$ is the voltage angle; G_{kj} and B_{kj} are the conductance and susceptance of the admittance matrix Y_{kj} between the buses k and j .

- Load power-voltage sensitivity constraint:

Both active/reactive power demand of each load must respect the power-voltage sensitivity relation:

$$\begin{aligned} P_{\text{load}k}(t) &= P_{\text{load}k0} (V(t)_k / V_{k0})^{k_{pk}(t)} \\ Q_{\text{load}k}(t) &= Q_{\text{load}k0} (V(t)_k / V_{k0})^{k_{qk}(t)} \end{aligned} \quad (3.9)$$

where the $P_{\text{load}k0}/Q_{\text{load}k0}$ is the nominal power derived from online load identification, V_{k0} is the nominal voltage, and $k_{pk}(t)/k_{qk}(t)$ are the sensitivity coefficients derived from the online identification.

Inequality constraints

The inequality constraints include the operation constraints such as voltage, power rating of FCS, power factor. They can be described as follows.

- Voltage constraints:

The voltage of all buses must be within the voltage limits, which the operator defines.

$$V_{\min} \leq V_k(t) \leq V_{\max} \quad k = 1 \dots N_B \quad (3.10)$$

V_{\min} and V_{\max} are the under-/over-voltage limits. The constraints are identical to all buses.

- Power rating constraints of FCS:

The capability of reactive power injection of each FCS must respect the power rating of the FCS and the charging demand. The power rating is considered constant.

$$Q_{\text{FCS}_x}^2(t) \leq S_{\text{FCS}_x}^2 - P_{\text{FCS}_x}^2(t) \quad x = 1 \dots n \quad (3.11)$$

$Q_{\text{FCS}_x}(t)$ is the reactive power provision from FCS, and S_{FCS_x} and $P_{\text{FCS}_x}(t)$ are the power rating and charging power of FCS of bus x .

- Power factor constraints:

The operator has requirements on the power factor. In this work, the power factor of the power flow via the HV/MV substation must be maintained as:

$$\lambda_{\text{sub},\min} \leq \lambda_{\text{sub}}(t) \quad (3.12)$$

$\lambda_{\text{sub}}(t)$ represents the power factor of the substation.

- OLTC tap constraints:

The OLTC can be changed within the interval of its tap position:

$$\text{tap}_{\text{OLTC},\min} \leq \text{tap}_{\text{OLTC}}(t) \leq \text{tap}_{\text{OLTC},\max} \quad (3.13)$$

where, $\text{tap}_{\text{OLTC}}(t)$ is the current tap position of OLTC, $\text{tap}_{\text{OLTC},\min}$ and $\text{tap}_{\text{OLTC},\max}$ are the lowest and highest position of the OLTC, respectively.

- OLTC action constraints:

The actions of the OLTC must be restricted to protect the OLTC devices. Every time when the load-leveling approach changes the tap position of OLTC, the action must respect:

$$\begin{cases} \text{tap}_{\text{OLTC}}(t) = \text{tap}_{\text{OLTC}}^*(t) & a = 0 \\ \text{tap}_{\text{OLTC}}^*(t) - 1 \leq \text{tap}_{\text{OLTC}}(t) \leq \text{tap}_{\text{OLTC}}^*(t) + 1 & a = 1 \end{cases} \quad (3.14)$$

a is the binary trigger signal for the OLTC, $\text{tap}_{\text{OLTC}}^*(t)$ is the position from which the local controller of OLTC sets. If $a = 0$, the load-leveling approach is not allowed to change the position of OLTC; if $a = 1$, the proposed approach is allowed to change only one tap position.

- OLTC bus voltage constraints:

Different voltage constraints are imposed on the OLTC regulation. The applied constraint depends on whether the OLTC is regulated by the local controller or the control center for the load-leveling.

$$\begin{cases} V_{\text{OLTC}}^*(t) - \varepsilon \leq V_{\text{OLTC}}(t) \leq V_{\text{OLTC}}^*(t) + \varepsilon & a = 0 \\ V_{\min} \leq V_{\text{OLTC}}(t) \leq V_{\max} & a = 1 \end{cases} \quad (3.15)$$

$V_{\text{OLTC}}(t)$, $V_{\text{OLTC}}^*(t)$, and ε represents the same quantities as Eq. (3.5).

3.2.2 Stage 2: minimization of losses

Stage 2 is activated, if Stage 1 is able to fully mitigate the load mismatch, to optimize the reactive power output of the FCSs with the optimization objective:

$$f_2 = \min\left(\sum_{l=1}^{N_L} P_{\text{loss},l}(t)\right) \quad (3.16)$$

where:

$$P_{\text{loss},l}(t) = R_{kj} \cdot \frac{P_{kj}^2(t) + Q_{kj}^2(t)}{V_k^2(t)} \quad (3.17)$$

$P_{\text{loss},l}(t)$ are the losses on branch l , N_L is the number of branches of the controlled grid, R_{kj} is the resistance of impedance $Z_{kj} = \frac{1}{Y_{kj}}$, i.e. the impedance of branch between the nodes k and j .

The corresponding $P_{kj}(t)$ and $Q_{kj}(t)$ can be derived as:

$$\begin{aligned} P_{kj}(t) &= V_k^2(t)G_{kj} + V_k(t)V_j(t)[G_{kj}\cos(\delta_k(t) - \delta_j(t)) + B_{kj}\sin(\delta_k(t) - \delta_j(t))] \\ Q_{kj}(t) &= -V_k^2(t)B_{kj} + V_k(t)V_j(t)[G_{kj}\sin(\delta_k(t) - \delta_j(t)) - B_{kj}\cos(\delta_k(t) - \delta_j(t))] \end{aligned} \quad (3.18)$$

The same constraints as listed in Stage 1 remain in the optimization algorithms. An additional constraint must be imposed. This constraint ensures the mismatch to be fully mitigated by Stage 2:

$$\left|P_{\text{grid}}(t) - P_{\text{grid}}^*(t)\right| = 0 \quad (3.19)$$

3.3 Case Study Setup for Analysis

The evaluation of the proposed load-leveling approach is implemented in an MV grid. The grid is modeled following the indication of a German local distribution system operator. Different scenarios and cases are considered for evaluation. The grid state data is converted to per-unit (pu) with the base voltage of 11 kV and the base power of 1 MVA.

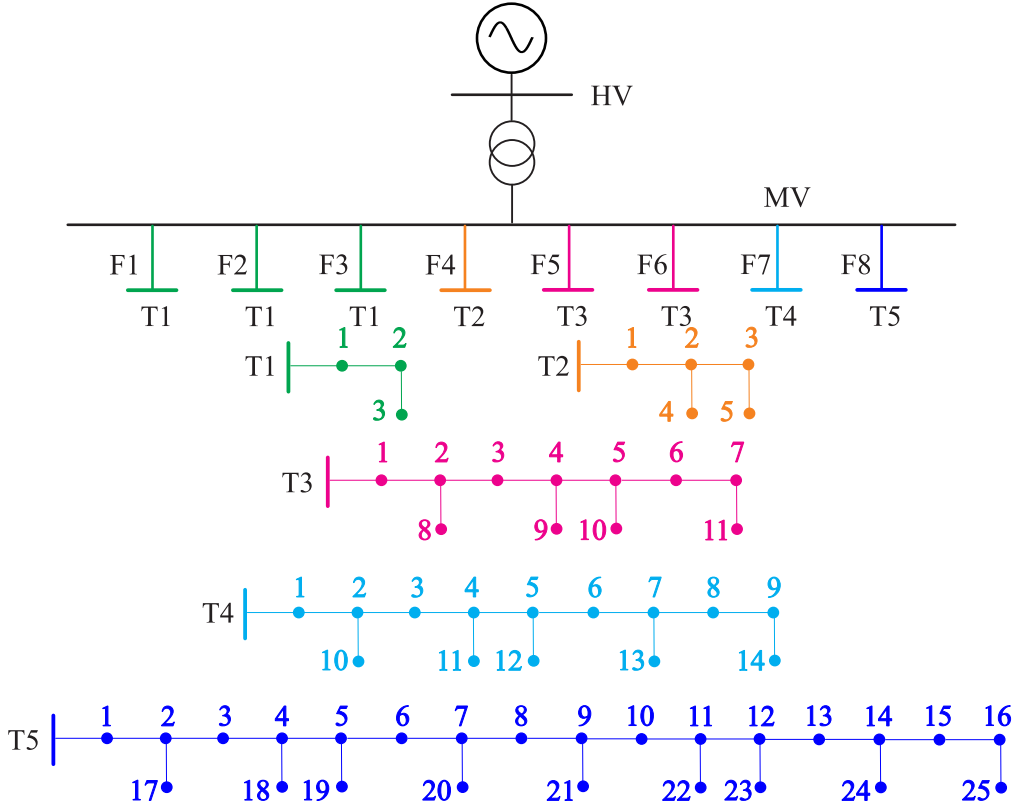


Fig. 3.7: Structure of MV grid for evaluation.

3.3.1 Grid under study

The structure of the grid under study is shown in Fig. 3.7. An HV grid with an SCC of 400 MVA, which is a common value from the German system operator, is used as the bulk grid. An HV/MV substation is used to connect the HV/MV grids with the equivalent impedance of $0.024 + j0.327\Omega$. The transformer of HV/MV substation is equipped with an OLTC of 11 positions, covering a voltage range between 0.95–1.05 pu. The original position of the OLTC is 1, i.e., 1.01 pu. The MV grid, which has 75 buses, consists of eight feeders (with lengths from 3 km to 10 km). One FCS is assumed to install in each feeder with power rating of 0.60 pu. Only one FCS per feeder is similar to the deployment of petrol stations. Normally, only one (or few) petrol station(s) is situated per small urban area.

Appendix 7.2 presents the types of loads or FCSs of buses in the MV grid. Loads/FCSs of the same type share identical 24 h demand profiles. Fig. 3.8 (a) shows the 24 h active power forecast profiles for single residential/commercial load. The power factor of residential/commercial load is constant and the peak apparent power $P_{load0} + jQ_{load0}$ is $0.35 + j0.05$ pu and $0.36 + j0.09$ pu of the residential load and the commercial one, respectively. To predict the EV charging profile is extremely important for load management [16]. The 24 h forecast of charging profiles of FCSs in residential area and commercial area are presented in Fig. 3.8 (b). Methods of the forecast can be referred to previous researches such as [17, 18]. The effectiveness and accuracy of those methods are outside the scope of this work to discuss.

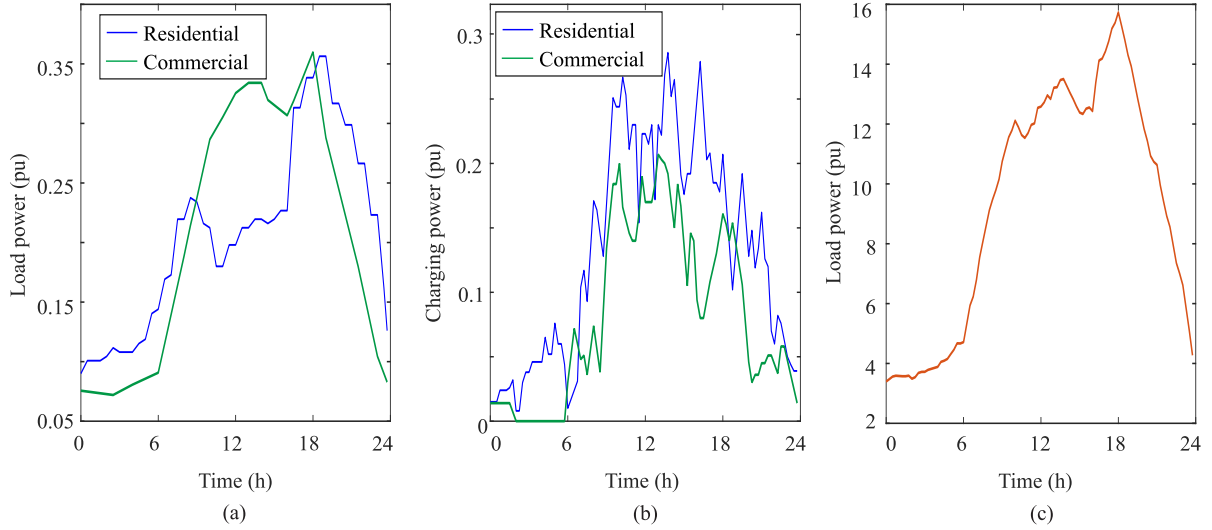


Fig. 3.8: 24 h active power profiles. (a) Profiles of residential/commercial load. (b) Profiles of FCS in residential/commercial areas. (c) Profile of power of the HV/MV substation.

Accordingly, the active power forecast of the HV/MV substation in a 24 h duration is computed with forecast profiles of the loads and FCSs within the grid together with the losses, as shown in Fig. 3.8 (c). The power demand forecast of the substation has a peak active power demand of approximately 16 pu.

The values of those constraints, which are used for the optimization algorithm, such as the maximum and minimum voltage and minimal power factor, are listed as follows:

- Voltage constraints:

$$\begin{aligned} V_{\min} &= 0.9 \text{ pu} \\ V_{\max} &= 1.1 \text{ pu} \end{aligned} \quad (3.20)$$

- Power factor constraints:

$$\lambda_{\text{sub},\min} = 0.9 \quad (3.21)$$

The proposed scheme defines a time interval restriction T_{trigger} and a threshold of power mismatch $\Delta\%$ to trigger the OLTC for load-leveling:

- Time interval:

$$T_{\text{trigger}} = 15 \text{ min} \quad (3.22)$$

- Threshold of power mismatch:

$$\begin{aligned} \Delta_1\% &= 5\% \\ \Delta_2\% &= 8\% \end{aligned} \quad (3.23)$$

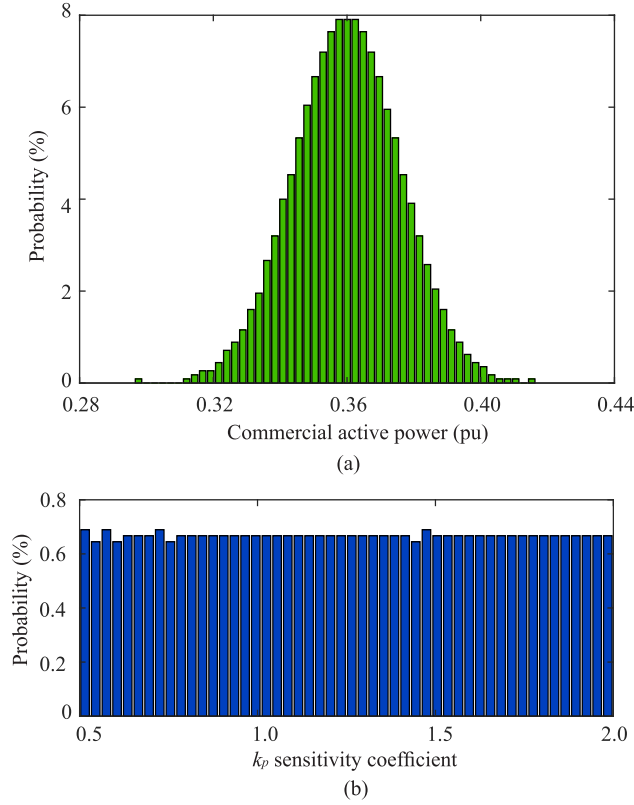


Fig. 3.9: Probability density of 1000 variation scenarios. (a) Probability density of power variation with respect to average power 0.36 pu following Gaussian distribution. (b) Probability density of sensitivity coefficients variation between (0.5–2.0) following uniform distribution.

3.3.2 Scenarios of Monte-Carlo analysis

The load or FCS consumption in real-time cannot follow the forecast perfectly due to the variable consumption patterns of the users, resulting in the power mismatch respecting the forecast demand power profiles in Fig. 3.8. However, previous study has confirmed that a considerable number of the power profiles shows some statistical characteristics [112, 113], which an average profile can be derived from the profiles. The Gaussian distribution can represent the possible variations of real-time demand from the average profile. The derived profiles in Fig. 3.8 (a) and (b) represent the average profiles. The variations of real-time demand follow the average profile with a standard deviation (SD) of 5 %.

The Monte-Carlo analysis is applied to take into account the variations. However, if each parameter requires M scenarios to ensure that the variations are properly considered, the total number of scenarios for N parameters is M^N , causing a huge computation burden. In order to reduce the computation burden, the Latin hypercube sampling (LHS) method is applied. The LHS increases the representative of each scenario by generating the scenarios with independent random permutations. Every scenario can be clearly distinguished from the others. The final sampling matrix is formed based on probability metrics. As a consequence, in each axis-aligned hyperplane, there are only M scenarios instead of M^N to be computed, reducing the computation burden. 1000 scenarios of 24 h profiles for single residential/commercial

load and single FCS in residential/commercial areas are generated, represent the uncertainty of variations. The same type of loads/FCSs shares the same Monte-Carlo scenario. The different loads are considered behaving without simultaneity. The probability density (PD) of the 1000 scenarios of a load with the power forecast of 0.36 pu is shown in Fig. 3.9 (a).

Despite the loads with power electronics interface are not voltage-dependent, by means of field experiments, previous researches have confirmed that a large amount of aggregated voltage dependent loads are still present in the power system [110, 114, 115]. The sensitivity coefficient is not constant. As demonstrated in recent study, the active power sensitivity varies in the range 1–2 pu [107, 108, 109, 115]. Considering some variability to extreme conditions, the sensitivity coefficients for residential and commercial load types in distribution grid due to the stochastic patterns are selected within the following range:

- Residential load: k_p (0.5–2.0); k_q (2.0–3.5)
- Commercial load: k_p (0.5–2.0); k_q (1.0–2.5)

To represent the variations of the sensitivity, 1000 groups of sensitivity coefficients have been developed using the LHS. The values of sensitivity in each group are randomly selected. However, the sensitivity values of 1000 groups show an uniform distribution, as depicted in Fig. 3.9 (b). It is noted that the low sensitivity coefficient, for instance, k_p is only 0.5, is also included in the evaluation. This approach ensures the generality of analysis.

It is expected that the proposed load-leveling approach can introduce only a few percent of voltage variation in the ac grid within a time frame of over tens of seconds. As a consequence, the impact of the proposed approach on the dc voltage of the FCS can be neglected. The charging demand of FCS is considered not sensitive to ac voltage variations.

3.3.3 Testing cases

Different cases have been defined to respect variety load-leveling conditions, in order to derive the generic and systematical conclusion from the analysis. Case O represents the case without any load-leveling action. It is used as the benchmark to evaluate other cases. In Case 1 and Case 2, only the OLTC is used for the load-leveling, with the threshold of $\Delta_1\%$ and $\Delta_2\%$, respectively. In Case 3, only the FCSs are involved in the load-leveling without involving the OLTC. The OLTC works with a local voltage controller (i.e., $a \equiv 0$). Case 4 and Case 5 denote the conditions in which both actuators of FCSs and OLTC are involved with the power mismatch threshold of each case $\Delta_1\%$ and $\Delta_2\%$, respectively. The power rating of FCS is identical for all FCSs. In Case 3-5, the power rating is 0.60 pu. The power rating of FCS is 0.40 pu in Case 6 and 0.80 pu in Case 7 instead of 0.60 pu, respectively. In Cases 6-7, except the power rating of FCSs, the rest conditions are identical to Case 5. A summary of all cases is listed in Table 3.2.

Table 3.2: Actuators and OLTC threshold values $\Delta\%$ for case study

Case	FCS	Power rating FCS (pu)	OLTC	$\Delta\%$
O	-	-	-	-
1	-	-	✓	$\Delta_1\%$
2	-	-	✓	$\Delta_2\%$
3	✓	0.60	-	-
4	✓	0.60	✓	$\Delta_1\%$
5	✓	0.60	✓	$\Delta_2\%$
6	✓	0.40	✓	$\Delta_2\%$
7	✓	0.80	✓	$\Delta_2\%$

3.4 Results and Analysis of Case Study

The results and analysis are presented in this section. First, one scenario in the time domain is selected to present the results in 24 h frame. The systematic analysis of all Monte-Carlo scenarios with both stages is presented afterward. Additionally, the impacts on OLTC actions, power factors, and voltage are presented in the last part.

3.4.1 Load-leveling performance in time domain

One of 1000 scenarios is selected, which its 24 h relative power mismatch of the HV/MV substation $\Delta P(t) = \frac{P_{\text{grid}}(t) - P_{\text{grid}}^*(t)}{P_{\text{grid}}^*(t)}$ in percentage is plotted in Fig. 3.10. The results show that the mismatch in Case 1 and Case 2 has no significant difference with respect to original mismatch without load-leveling (Case O). In the Fig. 3.10 (a) and (b), it shows only if the mismatch is higher than 5 % that small differences between Case 1 and Case 2 can be noted. In Case 3, the power mismatch can be fully compensated if the original mismatch is within the 2–3 % range. In Case 4 and Case 5, it is able to reduce further the mismatch with respect to Case 3 with a coordinated action of FCSs and OLTC. The results from this time-dependent scenario demonstrate the effectiveness of the proposed load-leveling approach that exploits the load regulation with both the FCSs and the OLTC.

Fig. 3.10 (c) shows the difference in Case 4 and Case 5. If the mismatch is between 5–8 %, e.g. around 13:00-15:00, the difference can be observed. Fig. 3.10 (d) shows the difference in Case 5, Case 6, and Case 7. For instance, around 11:00-13:00, the difference between the three cases can be observed. With a higher power rating of FCS, a smaller mismatch can be achieved.

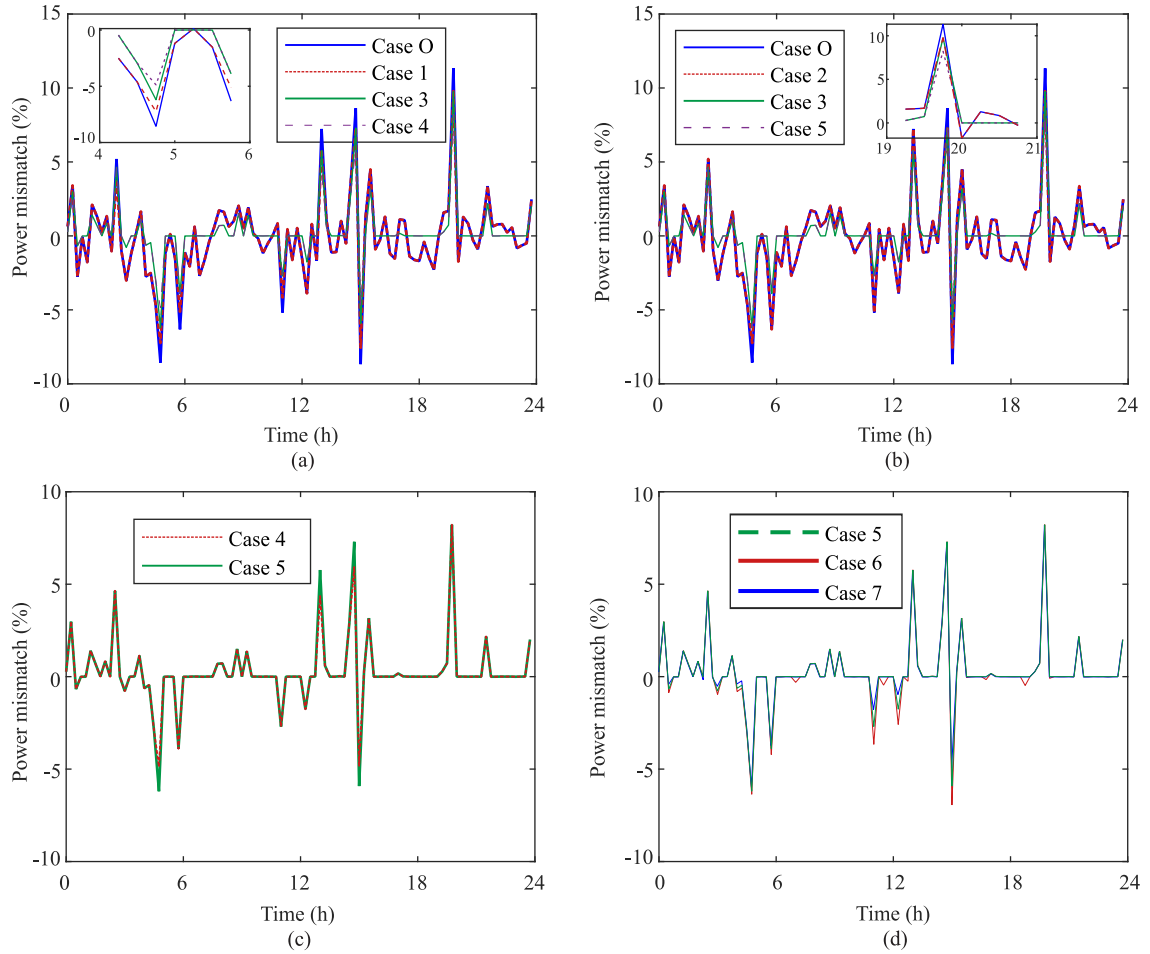


Fig. 3.10: 24 h demand power mismatch. (a) Power mismatch with respect to the power forecast of Case O, Case 1, Case 3, and Case 4. (b) Power mismatch with respect to the power forecast of Case O, Case 2, Case 3, and Case 5. (c) Power mismatch with respect to the power forecast of Case 4 and Case 5. (d) Power mismatch with respect to the power forecast of Case 5, Case 6, and Case 7.

The impact of the proposed scheme on the OLTC tapping actions is shown in Fig. 3.11 (a) and (b). In Case O and Case 3, the OLTC is not involved in load-leveling, leaving 4 times of tapping within 24 h. If the OLTC is involved, the tapping increases to 20 times and 12 times in Case 1 and Case 2, respectively. The threshold value to trigger the OLTC in Case 1 is 5 %, which is smaller than the threshold in Case 2 (8 %). Consequently, the tapping actions in Case 1 are 66 % more than the tapping actions in Case 2. Combining the FCS and OLTC, the tapping actions have been decreased to 14 times (Case 4) and 6 times (Case 5), respectively. The tapping actions in Case 4 are still twice more than the actions in Case 5. With the threshold of 5 %, the tapping actions in Case 4 are three times more than the actions in Case O. With the threshold of 8 %, the tapping actions in Case 5 are only 50 % more than the actions in Case O.

Fig. 3.12 shows the impact of the proposed scheme on the load and voltage change of the bus 25 in feeder F8 of Case 5. The power change with respect to the power without load-leveling in percentage is plotted in Fig. 3.12 (a). It can be observed that the power change

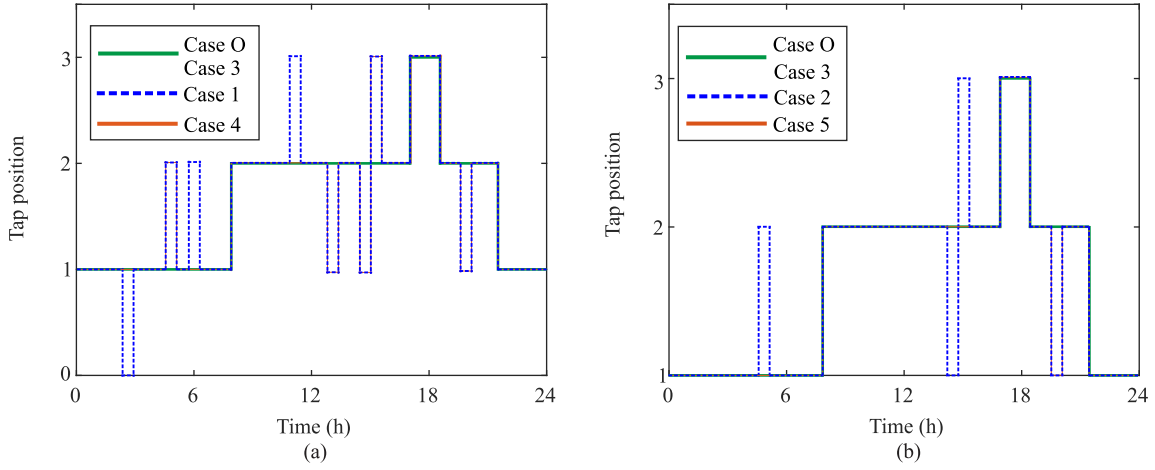


Fig. 3.11: 24 h change of OLTC tap positions. (a) Change of OLTC tap positions of Case O, 1, 3, and 4. (b) Change of OLTC tap positions of Case O, 2, 3, and 5.

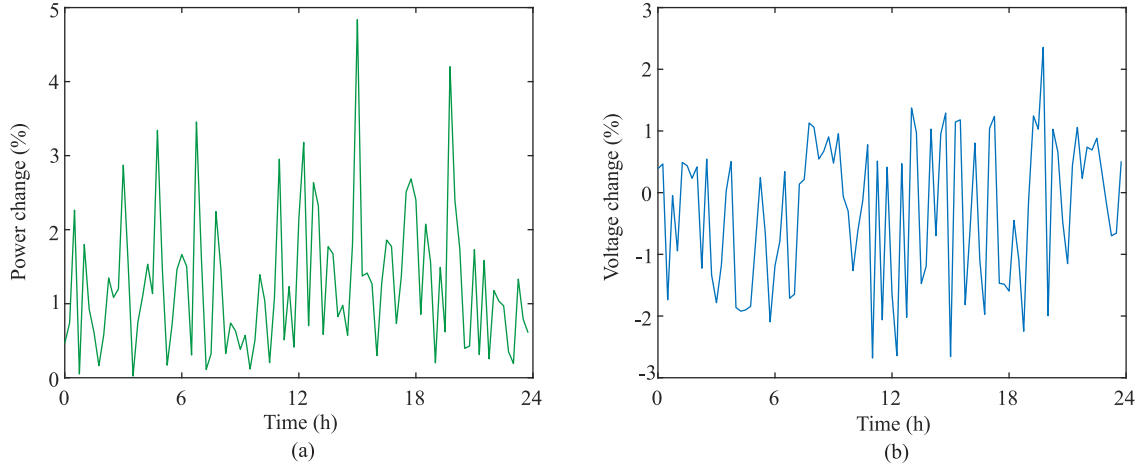


Fig. 3.12: 24 h power change and voltage behaviors of bus 25 in feeder F8. (a) Power changes with respect to uncontrolled power. (b) Voltage changes with respect to uncontrolled voltage.

has a confidence interval of 97 % within 4 %. Fig. 3.12 (b) shows voltage change with the voltage without load-leveling in percentage. Within a confidence interval of 91 %, the voltage variations are less than $\pm 2\%$. The CVR application has illustrated that this range of voltage variation doesn't negatively influence the quality of power supply to the residential and commercial users.

3.4.2 Load-leveling performance based on the Monte-Carlo analysis

The Monte-Carlo analysis is applied to analyze 1000 scenarios representing the uncertainty of load demand from the average profiles and power-voltage sensitivity to explore the load-leveling capability further. The PD of the power demand mismatch of all cases and their corresponding estimated normal distributions are presented in Fig. 3.13. As can be observed in Case 3, Case 4, and Case 5, the power mismatch has been compressed. The probability of mismatch in high percentage has been significantly reduced, and the probability of mismatch

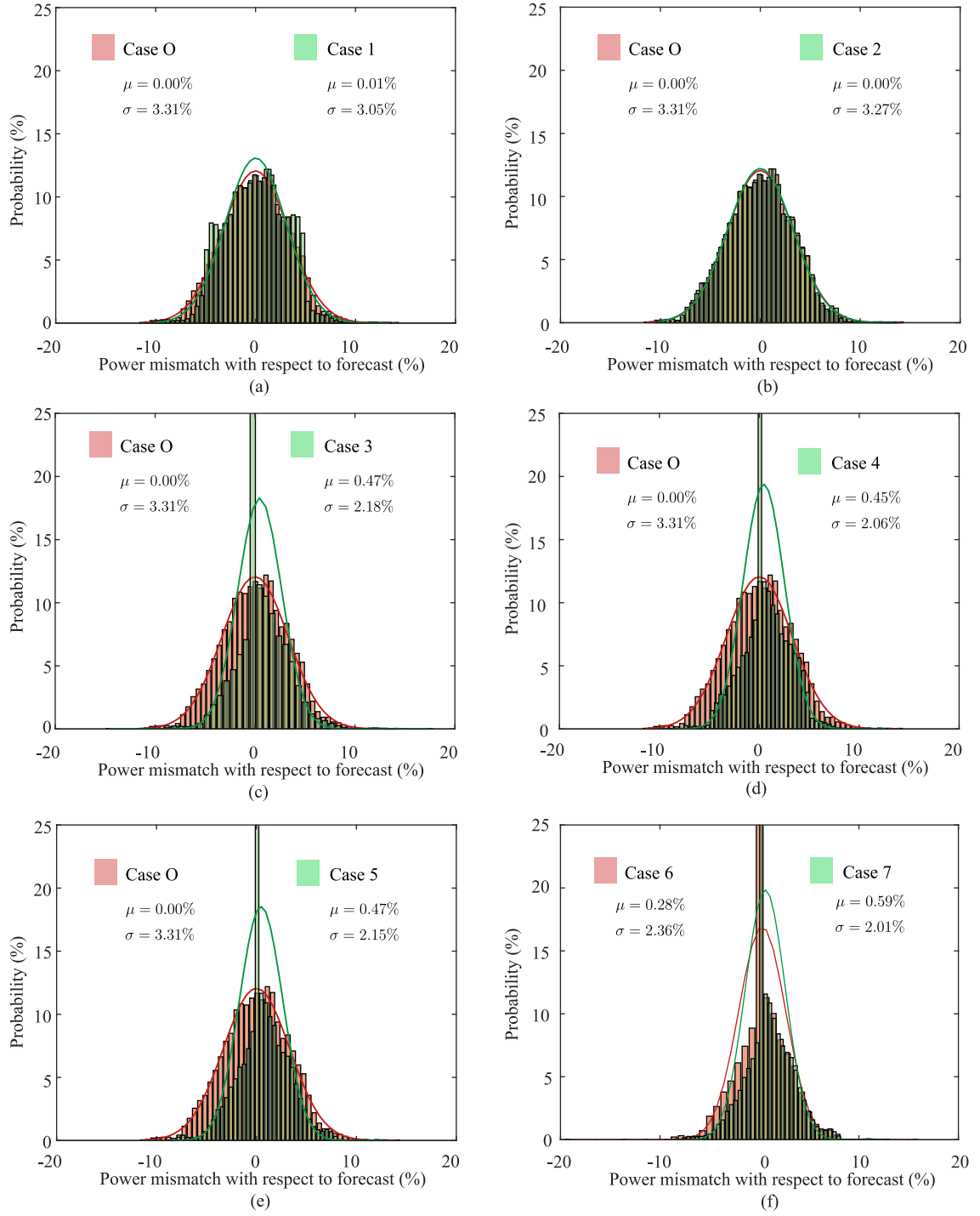


Fig. 3.13: Probability density of power mismatch of the testing grid. (a) Case O vs. Case 1. (b) Case O vs. Case 2. (c) Case O vs. Case 3. (d) Case O vs. Case 4. (e) Case O vs. Case 5. (f) Case 6 vs. Case 7.

Table 3.3: Mean value and standard deviation of the power mismatch from Monte-Carlo analysis

Case No.	Mean value μ %	SD σ %	SD with respect to case O
O	0.00	3.31	100%
1	0.01	3.05	92.15%
2	0.00	3.27	98.80%
3	0.47	2.18	65.86%
4	0.45	2.06	62.24%
5	0.47	2.15	64.95%
6	0.28	2.36	71.30%
7	0.59	2.01	60.73%

close to 0 reaches over 25 %. The difference between Case O and Case 1/Case 2 is slight.

Fitting the results into Gaussian Distribution, the standard deviation (SD) of power mismatch in the percentage of Case O, which is the case without the load-leveling, is 3.31 %. Summarized in Table 3.3, the value has been reduced to 3.05 % (Case 1) and 3.27 % (Case 2) using only OLTC as the actuator, respectively. The value of SD has been reduced to 2.18 % with FCSs as the actuator (Case 3) and has been further reduced to 2.06 % (Case 4) and 2.15 % (Case 5), respectively. The value of SD with respect to Case O has been reduced by 34 % of Case 3, 38 % of Case 4, and 35 % of Case 5, respectively. In Case 6 and Case 7, the values of SD have been decreased with the increased power rating of the FCSs. The value of SD with respect to Case O has been reduced by 29 % with FCS 0.40 pu, and 39 % with FCS 0.80 pu, respectively.

The absolute power mismatch $|\Delta P(t)|$ of all scenarios is plotted as cumulative distribution (CD) in Fig. 3.14. It is noted that the CD curves of Case O and Case 2 and the curves of Case 3 and Case 5 in Fig. 3.14 (a) have no significant difference, respectively. However, comparing the CD curves of Case O and Case 3, it can be observed that the probability of no mismatch in Case 3 has reached above 20 %. On the contrary, the probability of no mismatch in Case O is 9 %. Fig. 3.14 (b) shows the CD of Case 4 - Case 7. It is observed that the curves of Case 4 and Case 5 have no significant difference. Since the performance of load-leveling is mainly dependent on the reactive power from FCSs, if the power rating of the FCS changes, the performance is expected to change accordingly. Fig. 3.14 (b) shows that the probability of no power mismatch increases with a higher power rating of FCS. The values are 19 % of Case 6 (FCS 0.40 pu), 21 % of Case 5 (FCS 0.60 pu), and 23 % of Case 7 (FCS 0.80 pu).

The power mismatches in absolute values of Case O, Case 1, and Case 3 are presented in Fig. 3.15. Fig. 3.15 (a) shows that the proposed load-leveling scheme has reduced the

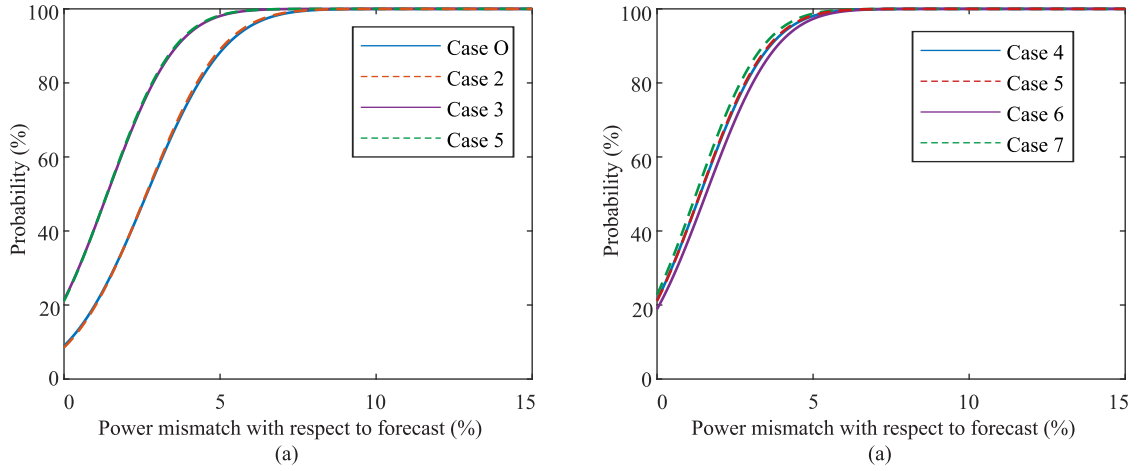


Fig. 3.14: Cumulative probability distribution of absolute power mismatch of 1000 Monte-Carlo scenarios. (a) Comparison of Case O, Case 2, Case 3, and Case 5. (b) Comparison of Case 4, Case 5, Case 6, and Case 7.

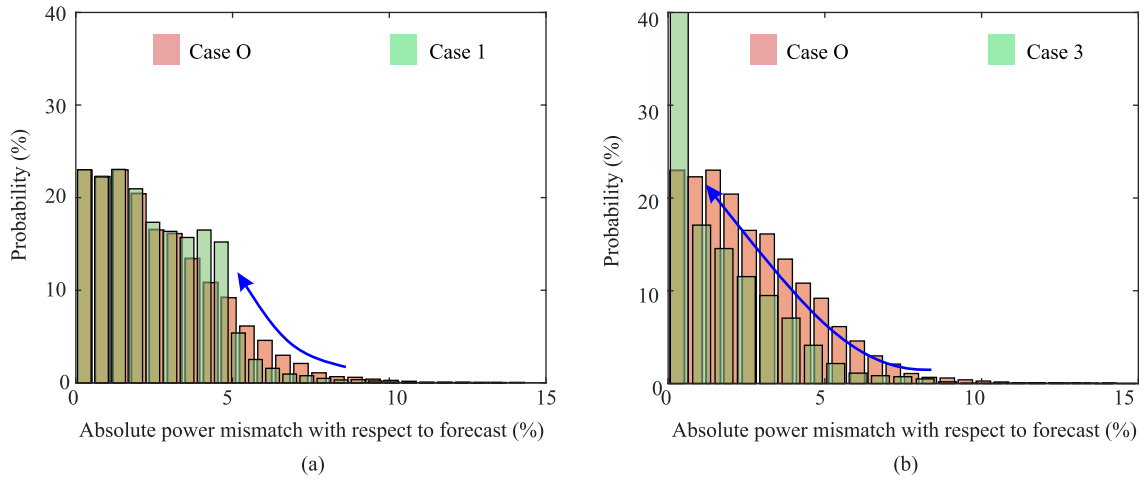


Fig. 3.15: Probability density of absolute power mismatch in Case O, Case 1, and Case 3.

probability of the mismatch in Case 1 if the mismatch is above 5 %, i.e., the threshold value to trigger the OLTC. Fig. 3.15 (b) shows the probability of mismatch has been reduced if the mismatch is above 0.5 %. The probability of mismatch, which is less than 0.5 %, has been increased to above 40 % in Case 3 instead of 22 % in Case O.

The results of the Monte-Carlo analysis have demonstrated that Stage 1 of the proposed load-leveling scheme can reduce the power mismatch, resulting in the decreased probability of large mismatch.

3.4.3 Analysis of the losses with load-leveling

The power losses in Case O, Case 3, Case 5, and Case 7 have been evaluated. The PD of the losses in Case O and Case 3 Stage 1 are shown in Fig. 3.16 (a). The comparison of PD between Case O and Case 5 Stage 1 is shown in Fig. 3.16 (b). It can be observed that the

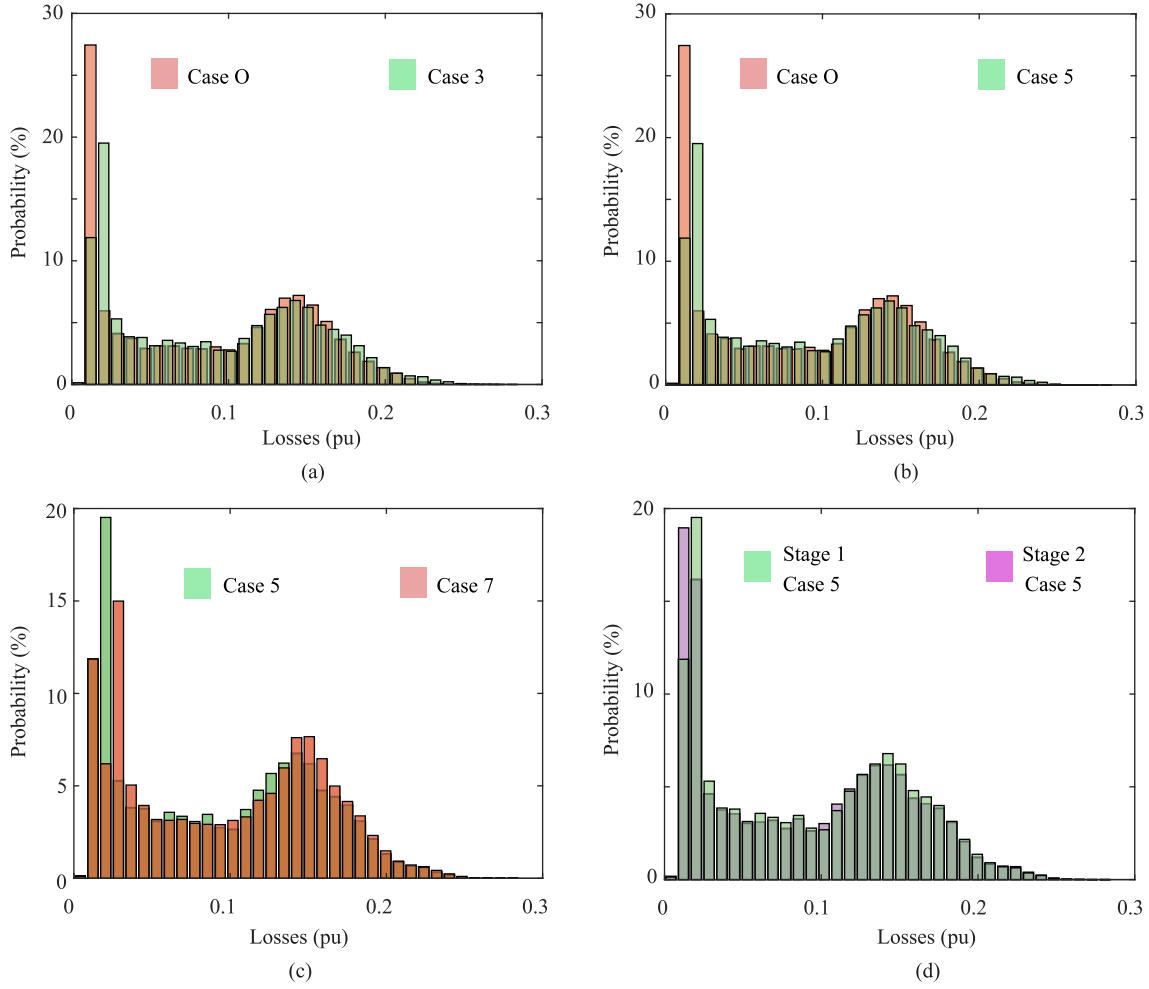


Fig. 3.16: Probability density of losses of 1000 Monte-Carlo scenarios. (a) Losses in Case O vs. losses in Stage 1 of Case 3. (b) Losses in Case O vs. Losses in Stage 1 of Case 5. (c) Losses in Stage 1 of Case 5 vs. Losses in Stage 1 of Case 7. (d) Losses in Stage 1 vs. Stage 2, Case 5.

proposed load-leveling scheme can increase the losses. As a consequence, the probability of losses smaller than 0.02 pu has been decreased by approximately 16 % in Case 3 and Case 5, respectively. There is no significant difference between Case 3 and Case 5, implying that the OLTC does not significantly impact the losses.

Comparing the losses in Stage 1 of Case 7 with respect to the losses in the same stage of Case 5, as shown in Fig. 3.16 (c), a significant difference in terms of PD can be observed when the losses are between 0.015 pu and 0.040 pu. The probability of losses less than 0.02 pu of Case 5 is approximately 13 % higher than the probability of Case 7 within the same losses range. Fig. 3.16 (d) shows the PD of losses in Stage 1 and Stage 2, both of Case 5. Although even in Stage 2, the probability of losses less than 0.02 pu is not as high as the probability of Case O. However, it is observed that the probability of losses higher than 0.02 pu has been decreased by Stage 2, resulting in that the probability of the losses less than 0.02 pu has been increased by 7 % by Stage 2 comparing Stage 1.

The reduction of losses in Stage 2 is achieved by resetting the reactive power injection of

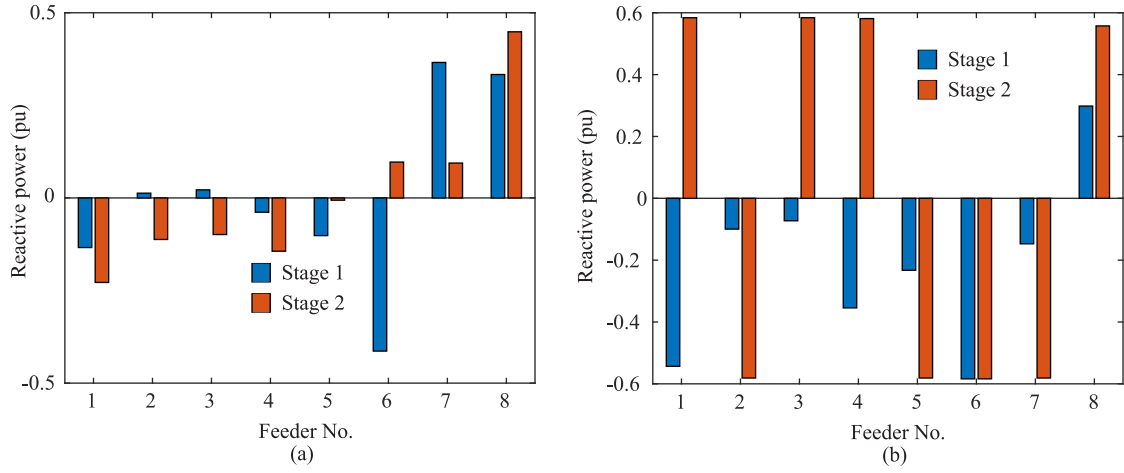


Fig. 3.17: Comparison of reactive power injection in Stage 1 and Stage 2 of Case 5. (a) One scenario at 09:00. (b) One scenario at 18:30.

the FCSs. Fig. 3.17 (a) shows the reactive power provision of the FCSs in each feeder at 09:00 with a scenario of Case 5. Stage 1 requires that the FCSs in the feeders F1, F4, F5, and F6 inject inductive reactive power (negative), and the rest FCSs inject capacitive reactive power (positive). The injection of reactive power in the feeder F6 is more than 0.4 pu. In the feeders F7 and F8, the FCSs inject the capacitive reactive power, which is also more than 0.3 pu. The FCSs inject significantly higher inductive reactive power from the feeders F1 to F4 in Stage 2 comparing their injection in Stage 1. In the feeder F5, the inductive reactive power from the FCS of Stage 1 has been reduced to approx 0 in Stage 2. In the feeder F6, the FCS injects capacitive reactive power in Stage 2 instead of inductive reactive power. As a result, the injection of the FCS in the feeder F7 has been reduced. On the contrary, the FCS in the feeder F8 injects more than 0.1 pu reactive power in Stage 2 with respect to Stage 1. At 09:00, with this scenario, the losses without the proposed load-leveling scheme are 0.095 pu. With Stage 1, the losses have been reduced to 0.094 pu. Stage 2 of the proposed scheme reduces the losses further to 0.092 pu, which is 2 % with respect to Stage 1.

Fig. 3.17 (b) shows the reactive power injection of the FCSs at 18:30 with a scenario of Case 5. Stage 1 of the proposed scheme requires all FCSs except the one in the feeder F8 inject inductive reactive power. The FCSs in the feeders F1 and F6 inject more than 0.5 pu inductive reactive power, where the FCS in the feeder F6 reaches its maximal injection capability. In Stage 2 of the scheme, the FCSs in the feeders F2, F5, F6, and F7 remain to inject inductive reactive power. The amount of injection in all the four feeders is more than 0.5 pu. The FCSs in feeders F1, F3, and F4 inject capacitive reactive power in Stage 2 instead. Moreover, the injection of the FCSs in the three feeders reaches the maximal injection capability. The FCS in the feeder F8 continuously injects the capacitive reactive power, but the amount has been increased. The losses without the proposed load-leveling scheme are 0.183 pu. With Stage 1 of the approach, the losses have been increased to 0.188 pu. If Stage 2 is imposed, the losses have been reduced to 0.173, an improvement of 8 % with respect to Stage 1.

Table 3.4: Average OLTC tapping actions of 1000 scenarios within 24 h

Case	O	1	2	4	5
Action number	5.948	24.364	7.971	12.446	7.044

The results show that the proposed load-leveling scheme can increase the losses in the grid under some conditions. However, Stage 2 of the approach is able to improve the losses issue introduced by Stage 1.

3.4.4 Analysis of the impacts on operation issues from the load-leveling

Impact on OLTC actions

The values of average tapping actions of OLTC within 24 h, which is derived from 1000 scenarios, are listed in Table 3.4. Without the load-leveling (i.e., Case O), the tapping actions of OLTC are 5.948 times within 24 h. The values in Case 1 and Case 2 have been increased to 24.364 times and 7.971 times, respectively. Using both actuators of FCSs and OLTC, the tapping actions of OLTC in Case 4 and Case 5 are 12.446 times and 7.044 times, respectively. With the threshold of $\Delta_1\%$ (5 %) to trigger the OLTC, the tapping actions of OLTC have been significantly increased. The tap-changer actions have increased more than 12 times within 24 h in Case 4, which is approximately double the actions in Case O. This can result in a considerable reduction of the lifetime of OLTC. However, the SD of mismatch probability estimation of Case 4, which is listed in Table 3.3, has been reduced by 3.62 % with respect to Case 3. In Case 5, the tapping actions have been increased by 17 % than the actions in Case O. It is a modest increment of the OLTC actions that does not affect its lifetime significantly. The threshold of OLTC must be set with a relatively high number to avoid unnecessary mechanical wear.

Impact on power factor

The PD of power factor in Case O and Case 5 has been plotted in Fig. 3.18. It shows in Fig. 3.18 (a) that the power factor of Case 5 can be improved with some scenarios and reduced with some other scenarios with respect to the power factor in Case O. The improvement of power factor is due to the injection of capacitive reactive power. The injection of inductive reactive power causes most of the decreased power factor. If the injection of capacitive reactive power leads that the MV grid provides capacitive reactive power back to the upstream grid, the power factor of the MV grid can also be decreased. The probability of a power factor close to its minimal restriction, i.e., 0.9, has been significantly increased. However, the power factor is controlled within the defined restriction. Fig. 3.18 (b) shows the PD of power factor of both stages in Case 5. It is noted that the probability of a higher

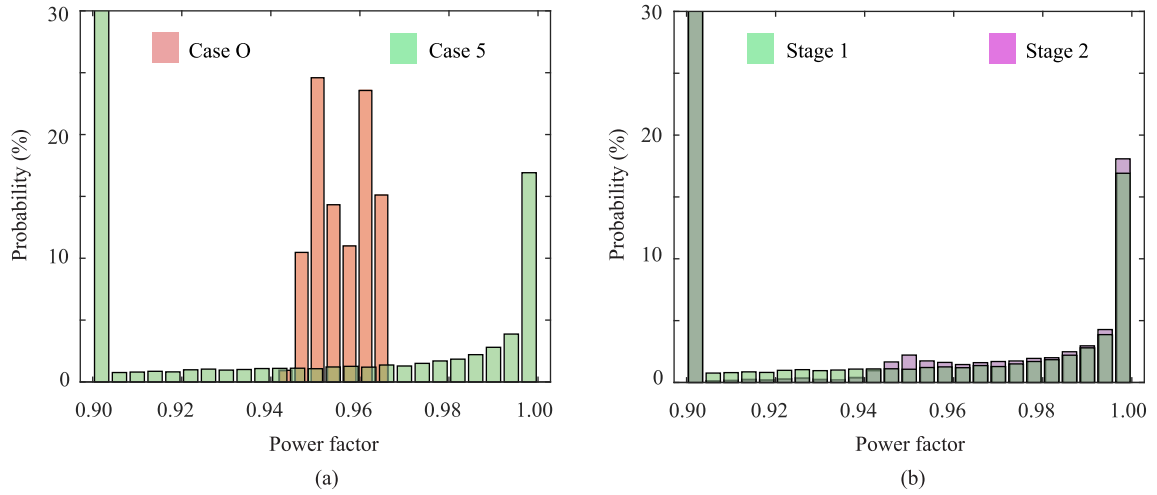


Fig. 3.18: Probability density of power factor of 1000 Monte-Carlo scenarios. (a) Probability density of power factor in Case O and Case 5. (b) Probability density of power factor in Stage 1 and Stage 2, Case 5.

power factor has been increased by the action of Stage 2, especially the probability close to the unity power factor.

Impact on voltage

The voltage amplitudes of the entire grid must be maintained within 0.90–1.10 pu. Based on the grid topology, node 25 of feeder 8 (F825) has the highest risk of voltage violation due to its largest electrical distance to the substation. Voltage of MV busbar from the HV/MV substation and the bus F825 is observed. The PD of the voltage of both buses is plotted in Fig. 3.19. Without the proposed load-leveling scheme, the voltage of MV busbar varies within 1.00–1.01 pu. Over 60 % the voltage lies close to 1.00 pu. With Stage 1 of the proposed approach, the voltage is distributed within 0.99–1.03 pu, as shown in Fig. 3.19 (a). Comparing the voltage in Stage 1 and Stage 2, it can be observed that the PD of the voltage in Stage 2 has been changed with respect to Stage 1, as shown in Fig. 3.19 (b).

Observing the voltage of the bus F825, without the proposed scheme, the PD of voltage is distributed around 0.97–1.00 pu. The PD of voltage is distributed around 0.95–1.02 pu in Stage 1, as shown in Fig. 3.19 (c). Stage 2 modifies the PD of voltage with respect to the Stage 1, as shown in Fig. 3.19 (d).

3.5 Analysis with Power-Hardware-In-the-Loop Test

Analysis with the setup of power-hardware-in-the-loop (PHIL) validates the feasibility and practicality of the proposed approach in the realistic conditions. It tests the interaction between the grid and the FCS hardware.

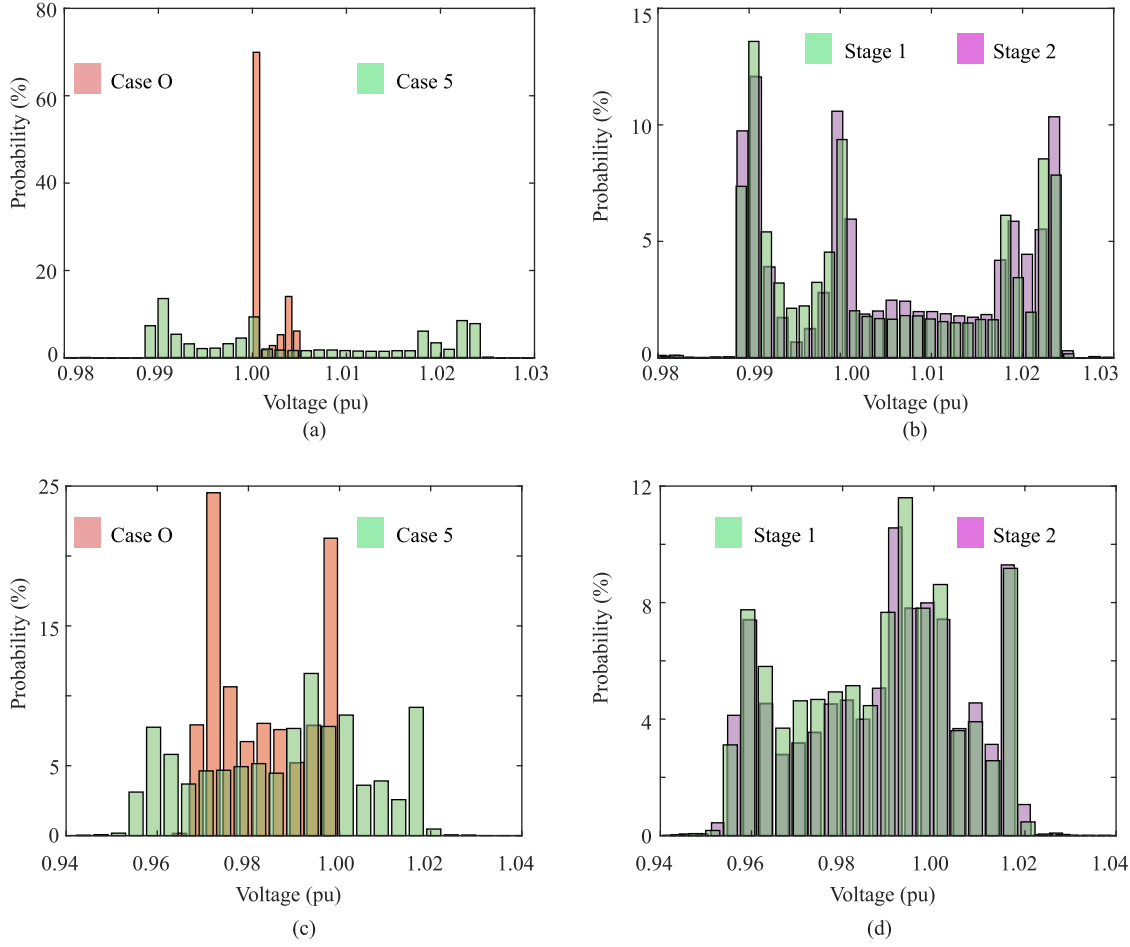


Fig. 3.19: Probability density of voltage of 1000 Monte-Carlo scenarios. (a) Voltage of MV busbar in Case O and Case 5. (b) Voltage of MV busbar in Stage 1 and Stage 2, Case 5. (c) Voltage of bus F825 in Case O and Case 5. (d) Voltage of bus F825 in Stage 1 and Stage 2, Case 5.

3.5.1 Concept of power-hardware-in-the-loop test

The PHIL setup, coupling the hardware under test (HuT) with a grid model in the real-time simulator, enables the analysis of the interaction of the FCS hardware and the grid. With PHIL setup, there is no need to realize the network in the laboratory. A schematic presentation of the setup and control loop is shown in Fig. 3.20. The grid and HuT, i.e., FCS converter, are modeled and simulated in the software of the digital real-time simulation system. The electrical quantities, such as voltage and current, are measured. The measurements of the bus that connects the HuT model are sent as input of the power amplifier (PA), which emulates the grid behavior for the hardware, i.e., the FCS converter. The reactions of hardware are tested with the emulated grid behavior by PA. The hardware measurements are sent back to the simulation system and used as input of the HuT model to emulate the FCS behavior in the grid. In this way, the loop of the PHIL setup is closed. Interactions of grid and hardware can be evaluated. With the PHIL setup, the testing conditions are flexible in terms of voltage level, the complexity of grid, and other aspects.

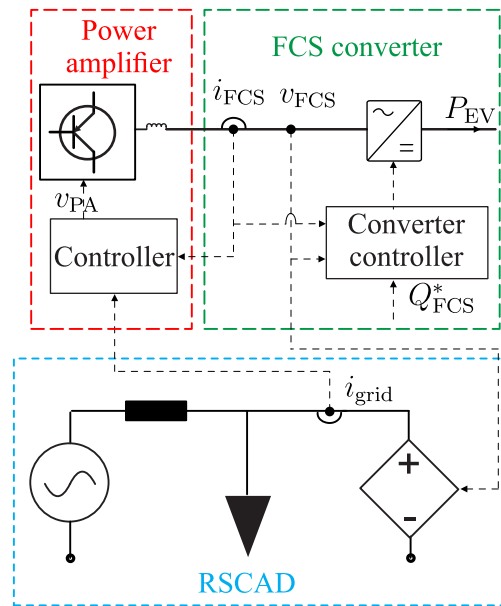


Fig. 3.20: Schematic presentation of the PHIL setup.

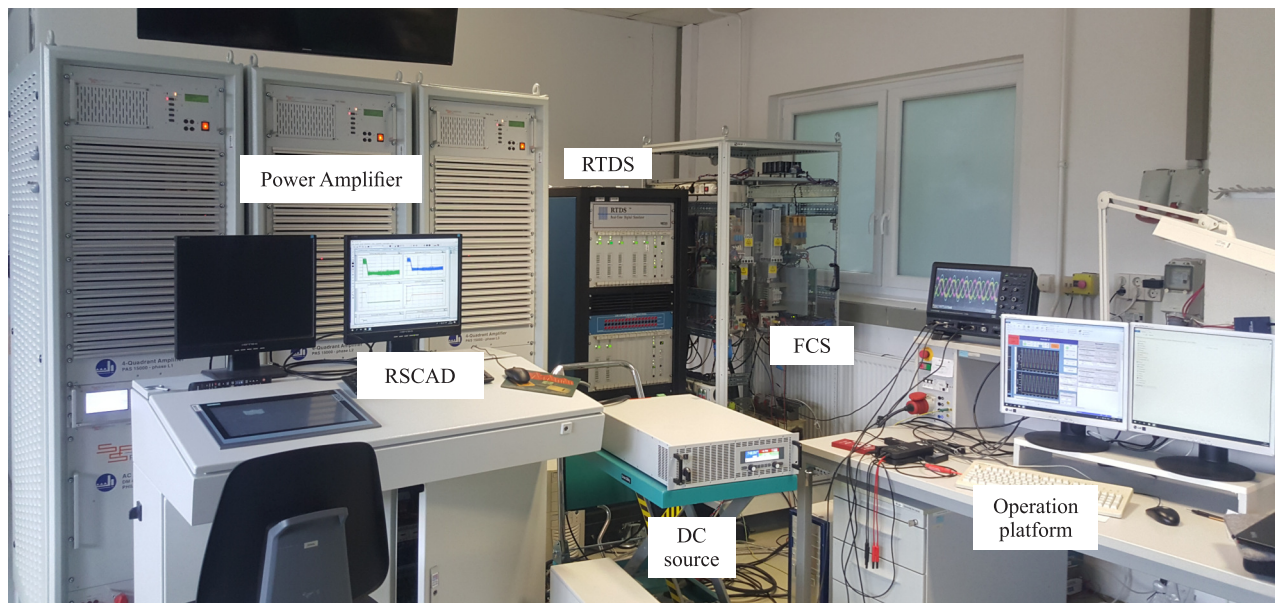


Fig. 3.21: Laboratory implementation of PHIL setup.

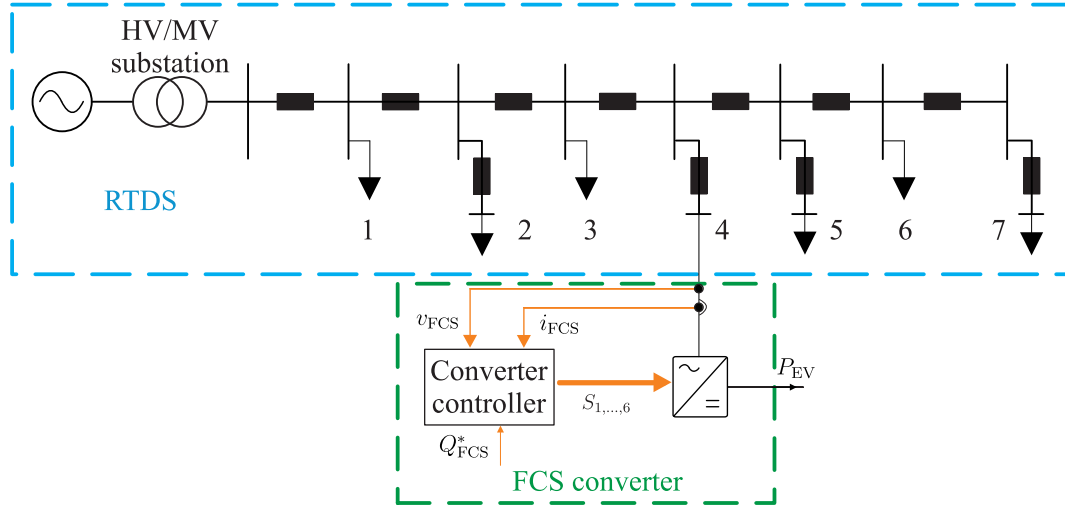


Fig. 3.22: Schematic presentation of the PHIL testing feeder.

Table 3.5: Summary of parameters of PHIL setup in laboratory

Parameters	Value	Parameters	Value
PA power rating	15kVA	RSCAD power scaling factor	137.5
FCS hardware power rating	4kVA	RSCAD FCS power rating	550kVA
DC source power rating	15kVA		

3.5.2 Setup in laboratory

The PHIL setup in the laboratory is shown in Fig. 3.21. The grid is realized in the software of RSCAD from Real Time Digital Simulator (RTDS) Technologies. The grid behavior is emulated under the actions of FCS reactive power provision. The FCS in RSCAD is modeled as a voltage source, which voltage reference (both amplitude and phase angle) is given by the terminal voltage of the hardware v_{FCS} . The active/reactive power of the hardware is reflected by the voltage and current output (amplitude and phase angle). In this sense, the impact of the hardware on the grid can be evaluated. An ideal transformer is modeled in the simulation to adjust the hardware voltage to the MV level. The PHIL test is controlled by means of a current type loop, in which the current in the RSCAD i_{grid} is sent to the PA controller, emulating the grid behavior from simulation in the hardware. With the reproduced grid behavior, the impact of the grid on the hardware can be evaluated. A Danfoss FC-302 converter represents the FCS. This converter is connected via the PA to the grid in RSCAD. The active power and reactive power consumption of the converter are determined by the load P_{EV} and the reactive power reference Q_{FCS}^* , respectively. A bidirectional dc source of the type EA-PSB is used to emulate the charging load P_{EV} . A scale factor of 137.5 is introduced between the power of hardware and the power of FCS in RSCAD. This factor copes with the limited power capability of the converter in the laboratory. The summary of the parameters of setup is listed as in Table 3.5.

Feeder F5 of Fig. 3.7 is implemented in RSCAD. A schematic presentation of the PHIL test grid is shown in Fig. 3.22. The loads are modeled as constant impedance loads.

3.5.3 Analysis of results

The PHIL tests have been implemented by means of two sets. In the first set, the concept of load-leveling with reactive power injection has been validated. The second set has evaluated the performance of the proposed load-leveling scheme with a 600 s profile.

Validation of the load-leveling approach concept

As first set of experiments, The nominal power of every load is $0.6 + j0.1$ MVA. The performance of the voltage-dependent load-leveling approach has been demonstrated in the simplified test case. Shown in Fig. 3.23 (a), starting from 1.5 s, the FCS injects 0.3 pu of inductive reactive power, with the goal to reduce the load power consumption. Consequently, the bus voltage of load 5 drops from 0.956 pu to 0.943 pu (Fig. 3.23 (b)), resulting in the decrease of the load consumption by 1.8 % (Fig. 3.23 (c)). The total feeder power consumption that includes the contribution from the FCS, drops from 3.62 pu to 3.54 pu, obtaining an overall 2.3 % power variation, as shown in Fig. 3.23 (d).

The FCS injects 0.3 pu of capacitive reactive power targeting to increase the active power consumption of voltage-dependent loads, shown in Fig. 3.23 (e). Starting from 1.5 s, as it can be seen in Fig. 3.23 (f), the bus voltage of load 5 increases from 0.956 pu to 0.969 pu, with a consequent increase of load consumption by 2.7 % (Fig. 3.23 (g)). The total power consumption of the feeder, including the contribution from the FCS, increases from 3.62 pu to 3.68 pu, obtaining an overall 1.7 % power variation, as shown in Fig. 3.23 (h).

These two tests have demonstrated the capability of the voltage-dependent load-leveling approach in regulating the load power consumption, enhancing the grid controllability in active power without installing any additional hardware.

Performance of load-leveling approach

In the second evaluation, a feeder demand forecast of 600 s (red line in Fig. 3.24 (a)) is defined, which is the target of load-leveling scheme. The blue and green lines represent the feeder's power without and with the load-leveling scheme, respectively.

As shown in Fig. 3.24 (a), the feeder power $P''_{\text{grid}}(t)$ obtained after the load-leveling scheme, has less deviation from the demand forecast $P^*_{\text{grid}}(t)$, showing an improvement with respect to feeder power profile without the load-leveling $P'_{\text{grid}}(t)$. This improvement can be seen with more details in Fig. 3.24 (b), where the power deviation to the feeder forecast is plotted. As can be noted, the maximal deviation is decreased from above 0.2 pu (appearing at 600 s when

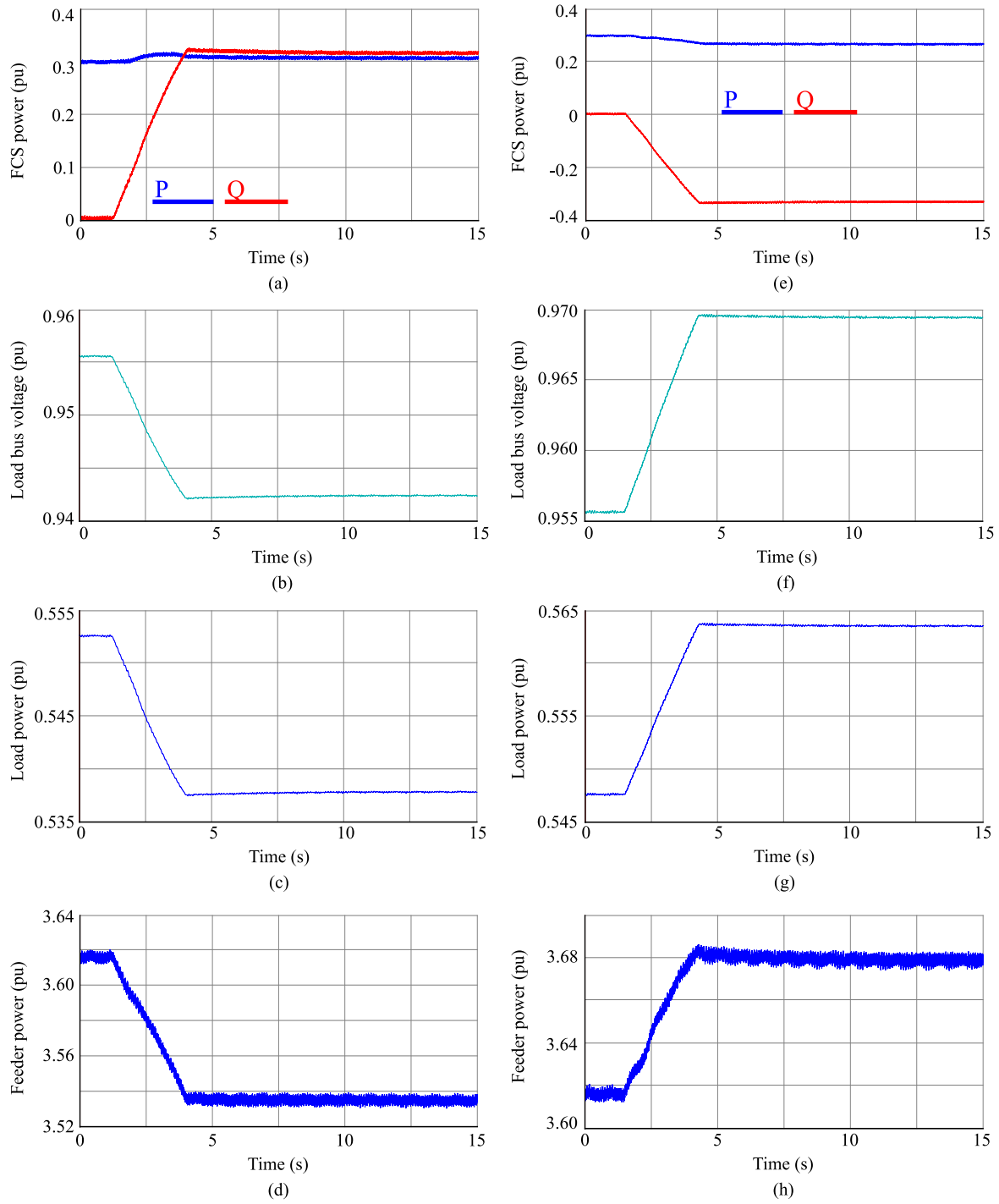


Fig. 3.23: Grid behavior with FCS reactive power injection. (a) Active/reactive power of FCS in RSCAD (blue line for active power, red line for inductive reactive power). (b) Voltage response of bus 5 to reactive power injection. (c) Demand behavior of load 5 to voltage response. (d) Power variation of the feeder to inductive reactive power injection. (e) Active/reactive power of FCS in RSCAD (blue line for active power, red line for capacitive reactive power). (f) Voltage response of bus 5 to reactive power injection. (g) Demand behavior of load 5 to voltage response. (h) Power variation of the feeder to capacitive reactive power injection.

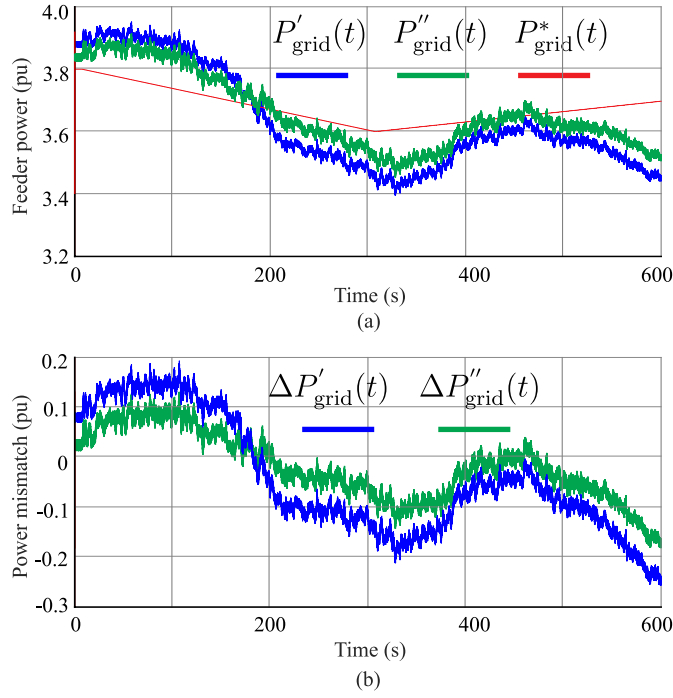


Fig. 3.24: 600 s load behavior from PHIL test. (a) Feeder power with/without load leveling respect to the demand forecast. (b) Power mismatch in relation to the demand forecast.

the power demand is below the forecast) to less than 0.2 pu (also at 600 s). The maximal mismatch is reduced by approximately 22 %.

The proposed approach can provide effectively the load leveling within 2–3 % as demonstrated in both experimental validations.

3.6 Summary

The uncertainty of users' patterns and the intermittent generation of the DG can lead to a more severe power mismatch between the power demand forecast and real-time consumption. To alleviate the power mismatch requires the operator to adopt new actuators and approaches. The FCS, exploiting the spare capacity of its converter, can regulate the loads with the voltage-dependent characteristic. This approach regulates voltage in the grid through reactive power injection of FCSs, shaping the voltage-dependent loads' power consumption. The OLTC is also considered in the approach. A two-stage scheme to mitigate the power mismatch in the MV grid has been developed. Based on the optimization algorithms, the scheme targets: (a) minimization of the power mismatch with respect to a load profile forecast; (b) reduction of the grid losses. Equality and inequality constraints related to the grid operation are imposed in the optimization algorithms. As all actuators are distributed in the grid and without any master actuator, this approach formulates a distributed solution to enhance the grid power controllability.

An MV distribution grid is modeled to evaluate the performance of the approach. The Monte-Carlo analysis has been performed, taking into account several grid conditions, including the statistical deviations of power consumption and load sensitivity to generalize the analysis of the load-leveling approach. The results from the simulation show that with the conventional CVR approach, which only OLTC implements, despite it has a neglectable impact on the losses and power factor, the power mismatch in terms of SD has only been decreased by 1.2–7.8 % with respect to the uncontrolled case. Using only the FCSs, Stage 1 of the proposed scheme is able to decrease the mismatch in terms of SD at least of 34.1 %. The reduction of SD can reach 35.0–37.8 % in cases combining the FCSs and OLTC. Stage 2 of the proposed scheme is able to limit the losses introduced by Stage 1 and improve the power factor at the MV/HV substation level. The impacts of the proposed approach on grid operations have been analyzed in terms of OLTC actions, power factor, and voltage. The results show that with an appropriate threshold value to trigger OLTC, a modest increment of OLTC actions can be achieved. Furthermore, by imposing the constraints in the load-leveling algorithm, the power factor and voltage can be maintained without violation of the operation limits. Two sets of PHIL validations have been performed, in both the short (15 s) and long time (600 s) range, confirming the potential of the load-leveling approach to alleviate the power mismatch without the additional component. The results of the analysis have proved the effectiveness of the proposed load-leveling approach, avoiding a cyclic intervention of other actuators, such as batteries.

4 Voltage Regulation Solutions with ES-STATCOM and Smart Transformer

The voltage regulation is also a crucial task of the distribution grid operation nowadays. The electrification in different sectors, such as electric vehicles (EVs) in the transportation sector, has increased the load demand, causing possible violations of the under-voltage constraint. On the other hand, the renewable energy systems (RESs), appearing as the distributed generation (DG) in the distribution grid, have led to the reversed power flow, causing possible violations of the over-voltage constraint. Furthermore, the uncertain demand patterns of users and the intermittent availability of renewable energy sources have changed voltage behaviors. The transitions of violations between the under-voltage and over-voltage constraints appear now more frequently and faster than before. The voltage regulation actuators and schemes need to be upgraded to cope with the voltage behaviors in the distribution grid.

Under such a circumstance, the power electronics (PE) components, which can fast adjust the control actions, have been proposed to implement the voltage regulation. This chapter evaluates the voltage regulation capability of two types of PE components, the energy storage static synchronous compensator (ES-STATCOM / ES-STA) and the smart transformer (ST). The ES-STATCOM is a combination of energy storage system (ESS) and STATCOM. Similar to STATCOM, it regulates the voltage by means of reactive power injection. The ST introduces some new features for grid operation. Its three-stage topology decouples the grids connected to different sides of ST, and its dc links can be used to connect the devices such as the photovoltaic (PV) unit. In the medium voltage (MV) grid, the ST can inject reactive power to provide ancillary grid regulations. In the connected low voltage (LV) grid, the LVac busbar can be directly regulated by the ST for grid regulation. A schematic depiction of the setup based on the two types of components is shown as in Fig. 4.1.

The ES-STATCOMs can be considered as actuators distributed in the grid, formulating a distributed voltage regulation solution. The STs formulate the same type of solution in the MV grid. In its connected LV grid, the ST formulates a centralized solution since it is the single actuator for the decoupled LV grid. An operation scheme to effectively coordinate the PE components is introduced, exploiting the voltage-correlation coefficients to gain a low computation burden. Depending on the components, the coefficients in the scheme must be adopted. The voltage regulation capability of the two components in both MV and LV grids will be evaluated and compared based on the simulation.

4.1 Voltage Control Approaches with Power Electronics Components

Introduced in Chapter 2, depending on the grid connecting strategies, the PE component can regulate the voltage by means of reactive power injection or by directly forming the voltage

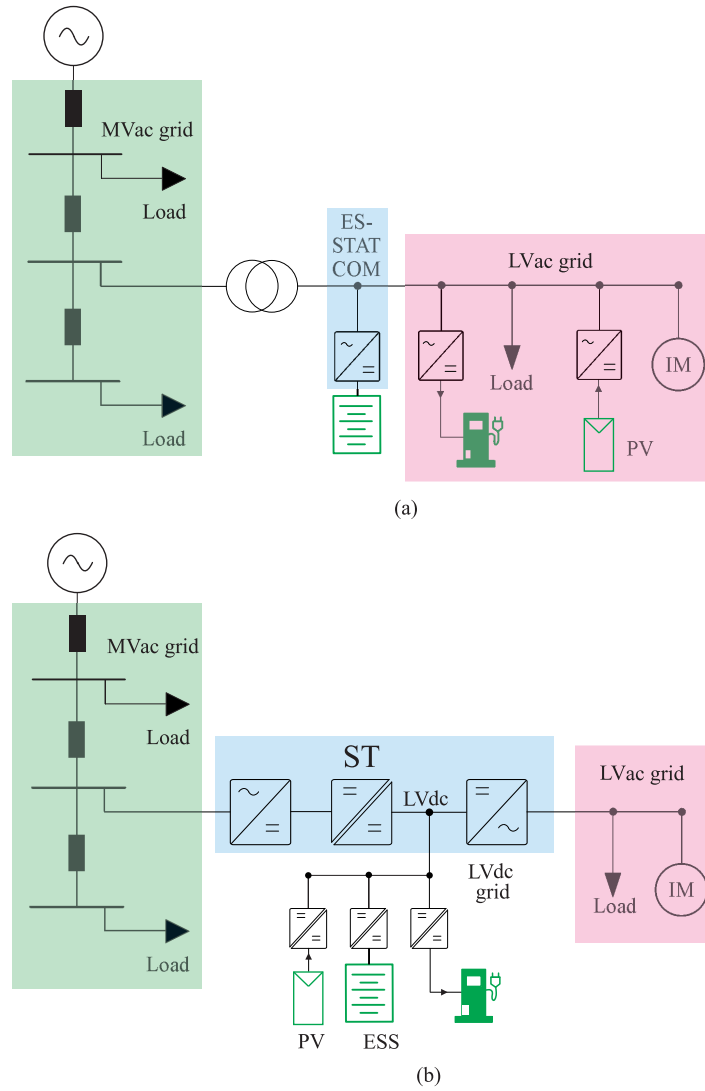


Fig. 4.1: Research focus of Chapter 4: Voltage regulation in distribution grid. (a). Solution with ES-STATCOM. (b) Solution with ST.

of a bus. The voltage regulation approach must be in accordance with the features of the PE components.

4.1.1 Voltage regulation by means of reactive power injection

The component, such as the ES-STATCOM, regulates the voltage by means of reactive power injection. Capacitive reactive power can increase the voltage and mitigate the voltage drop. Inductive reactive power, on the contrary, can decrease the voltage rise. Eq. (2.1) shows that the grid parameters, such as the impedance of the lines, the power factor, the R/X ratio as well as the short-circuit capacity (SCC) of the bulk grid, have a significant impact on the controllability of reactive power injection. A simplified feeder with one installed ES-STATCOM, shown in Fig. 4.2 (a), is used to evaluate the impact on the voltage amplitude from reactive power injection, considering various grid parameters.

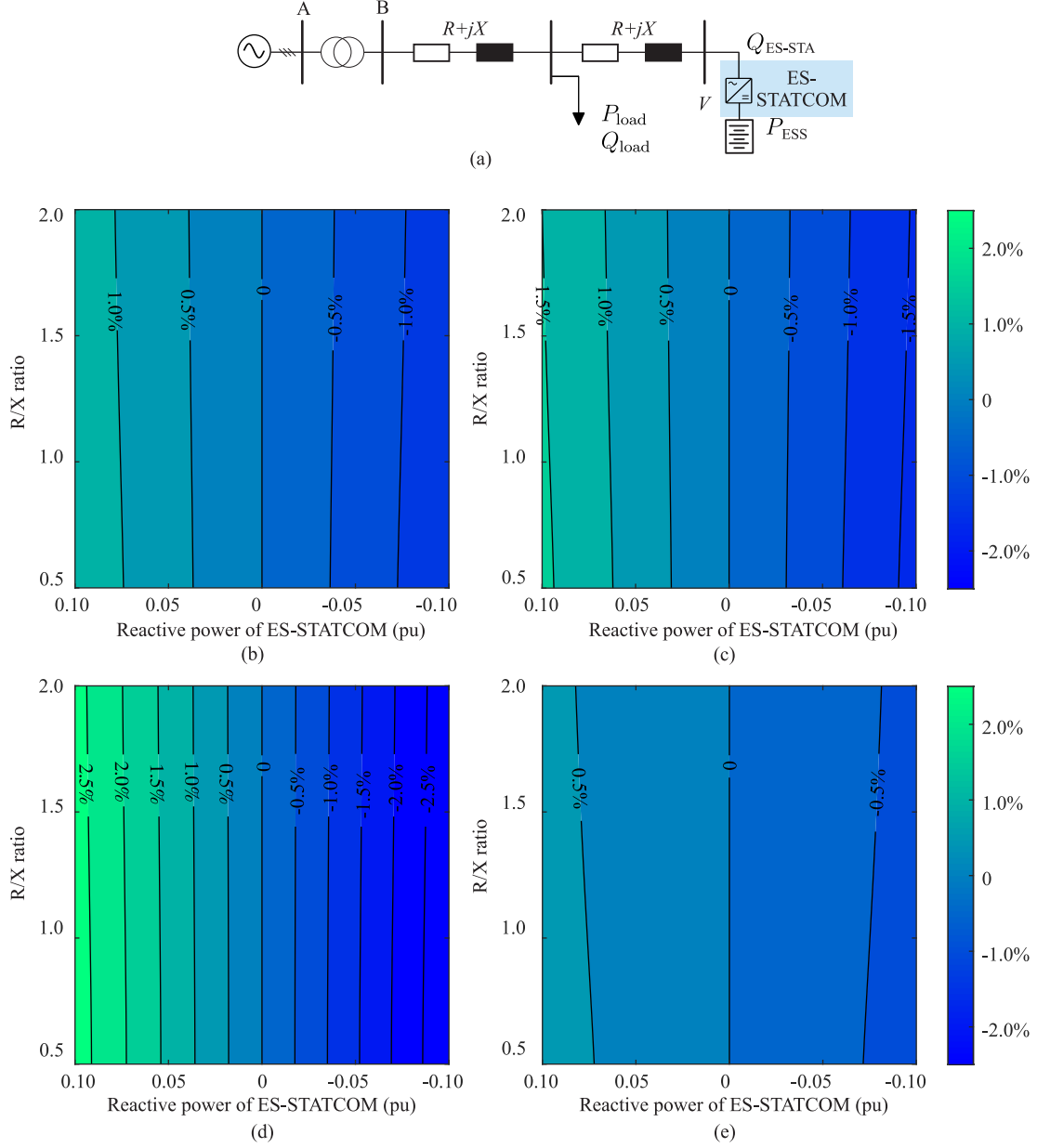


Fig. 4.2: Impact of reactive power injection on voltage deviation of ES-STATCOM bus, in a simplified radial feeder with different R/X ratios. (a) A simplified radial feeder with single load and single ES-STATCOM. (b) Voltage deviations of ES-STATCOM bus in group 1. (c) Voltage deviations of ES-STATCOM bus in group 2. (d) Voltage deviations of ES-STATCOM bus in group 3. (e) Voltage deviations of ES-STATCOM bus in group 4.

Table 4.1: Parameters of groups for analysis of voltage deviations with reactive power injection and R/X ratios

Group	SCC(pu)	S_{load} (pu)	Power factor	$ R + jX $ (pu)	P_{ESS} (pu)	X_T (pu)
1	10	1	1	0.01	0.3	0.01
2	10	1	0.9	0.01	0.3	0.01
3	5	1	1	0.01	0.3	0.01
4	25	1	1	0.01	0.3	0.01

The groups of different grid parameters are listed in Table 4.1. All values are represented by per-unit (pu), by which the evaluation can be adjusted with different voltage levels, keeping the generality of the evaluation. Groups 1 and 2 use a bulk grid with the SCC of 10 pu. The SCCs of groups 3 and 4 represent a weaker and a more robust bulk grid, respectively. In each group, the voltage deviations of the ES-STATCOM bus are compared with its voltage without reactive power injection, considering the different R/X ratios and power factors.

Fig. 4.2 (b)-(e) show the voltage deviations of ES-STATCOM bus in percentage. x axis represents the injection of reactive power (positive reactive power as capacitive and negative reactive power as inductive), and the y axis represents the R/X ratios. With the same R/X ratio, the voltage values without reactive power injection is the reference. Thus, at $x = 0$, the voltage deviations are 0. As can be noted in Fig. 4.2 (b), a voltage deviation within the range of approximately 1.3–1.4 % can be expected by means of reactive power injection of ± 0.1 pu from a single ES-STATCOM. The voltage deviation is larger with a smaller R/X ratio. The power factor in group 2 is 0.9, which is smaller than the power factor in group 1. As a consequence, the maximal voltage deviation reaches more than ± 1.5 %, as shown in Fig. 4.2 (c). The SCC in group 3 is half of the SCC in group 1. Accordingly, the maximal voltage deviation in group 3 is over 2.5 %, which is approximately 1.8 times higher than the maximal deviation in group 1, as shown in Fig. 4.2 (d). In group 4, the SCC is 2.5 times higher than the SCC in group 1. The maximal voltage deviation is less 0.7 %, i.e. approximately the half of the deviation in group 1, as shown in Fig. 4.2 (e). It can be concluded that it is feasible to use the reactive power from the PE components for voltage regulation with different grid parameters.

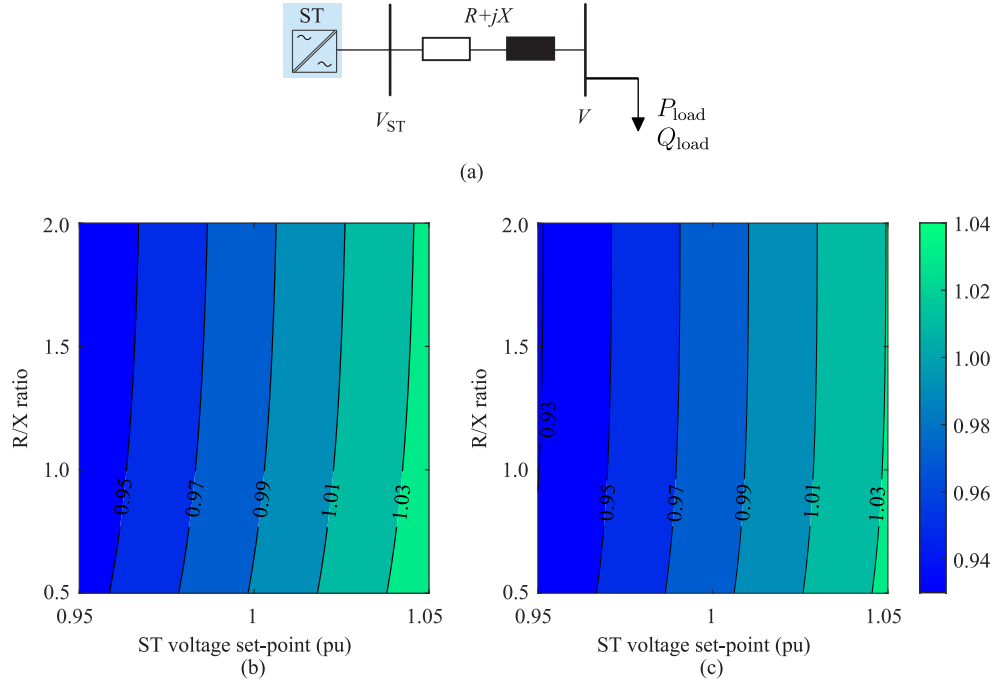
4.1.2 Voltage regulation by means of forming voltage

The ST decouples its connected LV grid from the MV one, thanks to its three-stage topology. Instead of reactive power injection, the ST can regulate the voltage of its LV grid by directly forming its LVac busbar voltage.

Fig. 4.3 (a) shows a simplified radial feeder, a typical topology for the LV grid. Once the

Table 4.2: Parameters of groups for analysis of load bus voltage with various ST voltage set-points and R/X ratios.

Group	$S_{\text{load}}(\text{pu})$	Power factor	$ R + jX (\text{pu})$
1	1	1	0.01
2	1	0.9	0.01

**Fig. 4.3:** Impact on load bus voltage from voltage set-points in an ST-fed feeder. (a) Simplified ST-fed radial LV feeder. (b) Voltage variations of load bus in group 1. (c) Voltage variations of load bus in group 2.

ST sets its LVac busbar voltage (V_{ST}), the load bus voltage V decreases with the increased impedance of the line or the increased load demand. Other parameters can affect the voltage deviations of the load bus, including the R/X ratios and the power factor of the load. Fig. 4.3 (b) and (c) show the load bus voltage with different parameters, which are listed in Table 4.2. By setting the ST voltage amplitude of 1.05 pu in group 1, the load bus voltage reaches approximately 1.04 pu with R/X ratio 0.5. The voltage drops with the increase of the R/X ratio. Its value reaches close to 1.03 pu with R/X ratio of 2.0. With the same voltage set-point of ST and the same R/X ratio, the load bus voltage decreases with the decreasing power factor. When the R/X ratio is 0.5, the difference of load bus voltage between groups 1 and 2 reaches approximately 0.01 pu. When the R/X ratio increases, the voltage of different power factors tends to get close to each other. The load bus voltage follows the change of the ST voltage, showing the effectiveness of this voltage regulation approach.

4.2 Voltage Regulation Schemes for ES-STATCOM and Smart Transformer

To effectively implement the voltage regulation with different types of PE components, operation schemes are developed to systematically compute the reference values for injecting reactive power and setting voltage amplitude. In order to reduce the computation burden, the schemes use the reactive power-voltage correlation coefficients and the voltage-voltage correlation coefficients.

As introduced in Chapter 2, the schemes are implemented with the control center. The control center gains a global view of the grid conditions by collecting measurements, such as the phase-to-ground voltage phasors, active/reactive power injection of buses, via an advanced communication system. It processes the measurements to estimate the grid states. Based on the grid states estimation, the control center calculates the references for all actuators, i.e., the ES-STATCOM or ST. The references are sent to the actuators via the communication system. Upon receiving the references, the actuators adjust their actions, e.g., the injection of reactive power, accordingly. The control center based schemes enable to make use of the actuators effectively. A framework of voltage regulation schemes for ES-STATCOM and ST is shown as in Fig. 4.4. Case 1 in the following part of this chapter refers to the case with the ES-STATCOM, and Case 2 refers to the case with the ST.

Case 1 shown as Fig. 4.4 (a): The MV grid is connected to a high voltage (HV) grid via a HV/MV substation. Conventional low-frequency transformers (LFTs) are used as the interfaces between the MV grid and the LV ones. The ES-STATCOM is installed at the LV side of the transformer with an ac/dc power converter. The control center collects all the necessary information and then computes reactive power injection references for each converter. The converters follow the references to adjust their reactive power injection, which regulates the voltage of both the MV and LV grids.

Case 2 shown as Fig. 4.4 (b) and (c): The grid structure is similar to Case 1. However, at the buses installed with ESSs, the STs replace the LFTs to interface the MV and LV grids. The voltage regulation in the MV grid is similar to that in Case 1. In the LV grid, the control center collects the voltage amplitudes of the LV grid and computes the voltage set-point of the ST's LVac busbar.

Schemes for both components aim to reduce the voltage rise and drop with fast response and to optimize the voltage profiles of the MV and LV grids. The details of voltage regulation schemes are introduced in the following part.

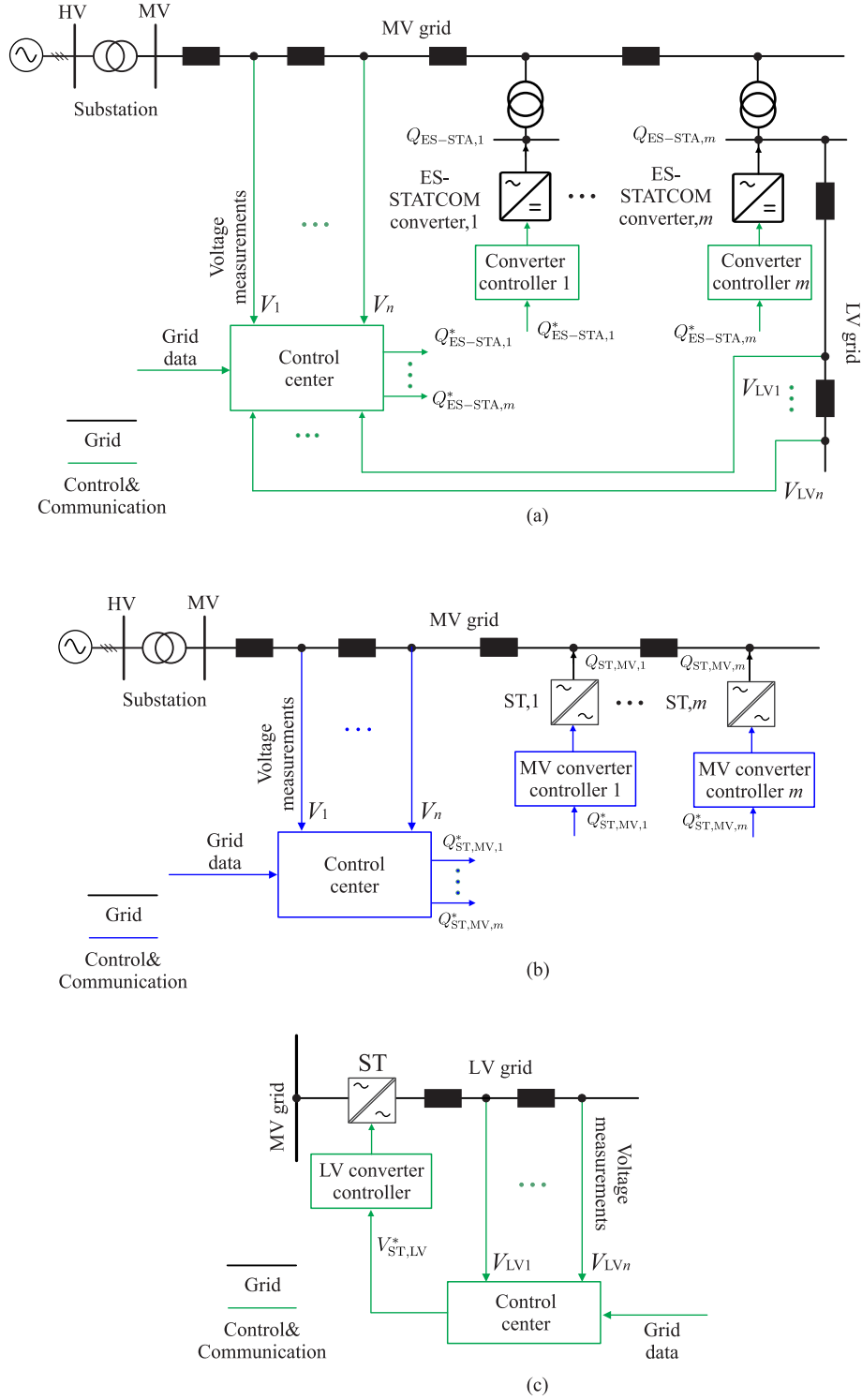


Fig. 4.4: Framework of voltage regulation schemes with PE components. (a) Framework with the ES-STATCOMs. (b) Framework with the STs: in MV grid. (c) Framework with the STs: in LV grid.

4.2.1 Voltage regulation scheme for ES-STATCOMs

Control variables of the scheme for the ES-STATCOMs are the reactive power injection $Q_{\text{ES-STA},i}(t)$ from corresponding converter, where i is the bus number of connected ES-STATCOM. The capability of injection $Q_{\text{ES-STA},i}(t)$ is restricted by the ES-STATCOM active power output $P_{\text{ESS},i}(t)$ and the power rating of the converter $S_{\text{ES-STA},i}$:

$$P_{\text{ESS},i}^2(t) + Q_{\text{ES-STA},i}^2(t) \leq S_{\text{ES-STA},i}^2 \quad (4.1)$$

where $P_{\text{ESS},i}(t)$ and $Q_{\text{ES-STA},i}(t)$ are time variant variables. The active power output $P_{\text{ESS},i}(t)$ is determined based on the dispatch plan of the ESS. This dispatch plan is computed according to the average aggregated power flow of the LV grid connected to the same MV/LV transformer with the ES-STATCOM. Details of dispatching the $P_{\text{ESS},i}(t)$ is out the scope of this work and can refer to [J1]. As a PE component, power rating $S_{\text{ES-STA},i}$ is dependent on the operation conditions, such as the terminal voltage. In the power grid analysis, the power rating can be considered a constant since the voltage deviation during the normal operation cannot significantly affect the power rating.

Once the active power injection $P_{\text{ESS},i}(t)$ of the ES-STATCOM i is determined, the reactive power injection $Q_{\text{ES-STA},i}(t)$ is controlled in order to provide voltage regulation to the MV and LV grids. The values of $Q_{\text{ES-STA},i}(t)$ are computed with an optimization problem that minimizes the total voltage deviations from the voltage reference V^* of the buses in the grid. The optimization exploits the reactive power-voltage correlation coefficients, which is derived from the grid operation conditions:

$$\begin{aligned} K_{Q,mi}(t) &= \frac{\partial |V_{\text{MV},m}(t)|}{\partial Q_{\text{ES-STA},i}(t)} \\ K_{Q,ni}(t) &= \frac{\partial |V_{\text{LV},n}(t)|}{\partial Q_{\text{ES-STA},i}(t)} \end{aligned} \quad (4.2)$$

where m and n are the bus in the MV and LV grids. The coefficients represent the voltage change at bus m or n as a response to the injection of reactive power at bus i .

At this stage, the optimal required injection of reactive power $Q_{\text{ES-STA},i}(t)$ is ready to be computed. The reactive power references of all converters to achieve a desirable voltage performance are derived via the following constrained optimization problem:

$$\begin{aligned} f_{\text{ES-STA}} = \min_{\Delta Q_{\text{ES-STA}}} & \left\{ \sum_{m=1}^{n_{\text{MV}}} \left(V_{\text{MV},m}(t) + \sum_{i=1}^{n_{\text{ES-STA}}} K_{Q,mi}(t) \Delta Q_{\text{ES-STA},i}(t) - V_m^* \right)^2 \right. \\ & \left. + \sum_{n=1}^{n_{\text{LV}}} \left(V_{\text{LV},n}(t) + \sum_{i=1}^{n_{\text{ES-STA}}} K_{Q,ni}(t) \Delta Q_{\text{ES-STA},i}(t) - V_n^* \right)^2 \right\} \end{aligned} \quad (4.3)$$

where $V_{MV,m}(t)$ is the voltage of bus m in the MV grid, $V_{LV,n}(t)$ is the voltage of bus n in the LV grid, $K_{Q,mi}$ and $K_{Q,ni}$ are the reactive power-voltage correlation coefficients of buses in the MV and LV grids with respect to the ES-STATCOM at bus i respectively, n_{ES-STA} is the number of the ES-STATCOM, n_{MV} and n_{LV} are the number of buses in the MV and LV grids respectively. The optimization problem aims to identify the best compromise in minimizing voltage deviations for both the MV and LV grids through reactive power injection.

When the voltage drop and the voltage rise appear simultaneously in the grid, the optimization scheme tends to increase the voltage of some buses and decreases the voltage of the other buses. Conflict can arise, resulting in the minimization of voltage deviations does not guarantee that there is no violation of voltage constraints. Therefore, the scheme must impose the voltage constraints:

$$\begin{aligned} V_{\min} &\leq V_{MV,m}(t) \leq V_{\max} \\ V_{\min} &\leq V_{LV,n}(t) \leq V_{\max} \end{aligned} \quad (4.4)$$

where V_{\min} and V_{\max} are the lower and upper voltage limits. With the constraints, the scheme makes some compromises in the optimization to ensure that no voltage constraints are violated. However, the average voltage deviations of the entire grid computed with Eq. (4.4) can be higher than the values, which are computed without the imposed voltage constraints.

It is noteworthy that in the formulation above, the energy constraints of ES-STATCOM are not enforced. The reason is that the scheme exploits only the spare capacity of the ES-STATCOM for reactive power injection. This scheme represents a conventional approach for voltage regulation with reactive power injection.

4.2.2 Voltage regulation scheme for smart transformers

Voltage regulation scheme for reactive power injection in MV grid

The voltage control schemes for the ST are different in the MV and LV grids. In the MV grid, the amount of reactive power $Q_{ST,i}(t)$ that can be injected into the grid must respect the power rating S_{ST} of the ST and the active power $P_{ST,i}(t)$ flowing through ST. In this chapter, the ST operates the active power of its connected LV grid, similar to the ES-STATCOM. Using the same dispatch plan as ES-STATCOM to control the ESS connected to the ST, the amount of $P_{ST,i}(t)$ is identical as $P_{ESS,i}(t)$. Once, the $P_{ST,i}(t)$ is determined, the reactive power availability of ST i can be represented as:

$$P_{ST,i}^2(t) + Q_{ST,i}^2(t) \leq S_{ST,i}^2 \quad (4.5)$$

By means of using the reactive power-voltage correlation coefficients, the injection of reactive power $\Delta Q_{MV,ST,i}(t)$ to optimize voltage patterns in the MV grid can be computed. This

amount of reactive power can regulate the voltage so that to minimize the voltage deviations from the voltage reference V^* :

$$f_{\text{ST,MV}} = \min_{\Delta Q_{\text{MV,ST}}} \left\{ \sum_{m=1}^{n_{\text{MV}}} \left(V_{\text{MV},m}(t) + \sum_{i=1}^{n_{\text{ST}}} K_{Q,mi}(t) \Delta Q_{\text{MV,ST},i}(t) - V_m^* \right)^2 \right\} \quad (4.6)$$

Voltage regulation scheme for voltage formation in LV grid

The ST allows providing voltage regulation to the LV grid by defining the voltage set-point reference $\Delta V_{\text{ST,LV}}$ at its LVac busbar. The ST assures suitable voltage levels of the buses along with the LV grid. In order to do so, the voltage-voltage coefficients of all buses in the LV grid must be computed:

$$K_{V^*,n}(t) = \frac{\partial |V_{\text{LV},n}(t)|}{\partial |V_{\text{ST,LV}}|} \quad (4.7)$$

The coefficient $K_{V^*,n}$ can be obtained by solving a linear system of equations, which is similar to the computation of correlation coefficients for the transformer's tap changer. Once the coefficients are known, the following optimization determines the suitable voltage reference of the ST:

$$f_{\text{ST,LV}} = \min_{\Delta V_{\text{ST,LV}}} \left\{ \sum_{n=1}^{n_{\text{LV}}} (V_{\text{LV},n}(t) + K_{V^*,n} \Delta V_{\text{ST,LV}} - V^*)^2 \right\} \quad (4.8)$$

where $V_{\text{LV},n}$ is the voltage of bus n without the voltage regulation.

4.2.3 Reactive power-voltage correlation coefficients

The control schemes make use of the reactive power-voltage and the voltage-voltage correlation coefficients. Reactive power-voltage coefficients are used for the schemes of the ES-STATCOMs, and the STs in the MV grid. The coefficients reflect the correlation of voltage amplitude as a response to the reactive power injection. Since the resistance of the distribution grid usually is not negligible, approaches used for calculating the coefficients in the transmission grid can cause accuracy issues when used to calculate the coefficients in the distribution grid. Furthermore, some conventional approaches for the distribution grid, such as the inverted Jacobian matrix based on the Newton-Raphson load flow formulation, also have some disadvantages. One of the disadvantages is that, for every change of the operation conditions in the grid, the Jacobian matrix needs to be updated based on the latest operation conditions [116]. As a result, a high computation burden for the implementation in real-time can arise.

This work uses the approach, which is developed for the distribution grid. Referring to a grid composed of X buses and \mathcal{X} is the set of buses, the relation between the voltage of each bus, admittance, and the current injection can be derived:

$$[\bar{\mathbf{I}}] = [\bar{\mathbf{Y}}] \cdot [\bar{\mathbf{V}}] \quad (4.9)$$

where $[\bar{\mathbf{I}}] = [\bar{I}^1, \dots, \bar{I}^X]^T$, $[\bar{\mathbf{V}}] = [\bar{V}^1, \dots, \bar{V}^X]^T$. The $[\bar{\mathbf{Y}}]$ matrix is formed by using the so-called compound admittance matrix as follows:

$$\begin{bmatrix} \bar{Y}_{11} & \cdots & \bar{Y}_{1X} \\ \vdots & \ddots & \vdots \\ \bar{Y}_{X1} & \cdots & \bar{Y}_{XX} \end{bmatrix} \quad (4.10)$$

The active/reactive power of each bus is considered independent of the voltage. Thus, for each separate perturbation of the power injection at one bus, the power of other buses does not change their set-points. Therefore, the computed correlation coefficients inherently account for the response of voltage in the whole grid to the active/reactive power change. Let the conjugate power of the bus i ($i \in \mathcal{X}$) be represented as:

$$\underline{S}_i = \underline{V}_i \sum_{l \in \mathcal{X}} \bar{Y}_{il} \bar{V}_l \quad (4.11)$$

\mathcal{S} is the subset of \mathcal{X} ($\mathcal{S} \subseteq \mathcal{X}$), which only contains all the slack buses. Thus:

$$\frac{\partial \bar{V}_i}{\partial Q_l} = 0, \quad \forall i \in \mathcal{S}, \quad l \in \mathcal{X} \quad (4.12)$$

The change of the power injection from non-slack buses with respect to the voltage of non-slack buses can be computed as:

$$\frac{\partial \underline{S}_i}{\partial Q_l} = \frac{\partial (P_i - jQ_i)}{\partial Q_l} \quad (4.13)$$

Eq. (4.13) can be rewritten by subjecting Eq. (4.11):

$$\frac{\partial \underline{S}_i}{\partial Q_l} = \frac{\partial \underline{V}_i}{\partial Q_l} \sum_{j \in \mathcal{X}} \bar{Y}_{ij} \bar{V}_j + \underline{V}_i \sum_{l \in \mathcal{X} - \mathcal{S}} \bar{Y}_{il} \frac{\partial \bar{V}_j}{\partial Q_l}, \quad \forall i, l \in \mathcal{X} - \mathcal{S} \quad (4.14)$$

The computation of the coefficients can referred to [116]. As a conclusion, the partial derivatives of the voltage magnitude can be expressed as:

$$\frac{\partial |\bar{V}_i|}{\partial Q_l} = \frac{1}{|\bar{V}_i|} \text{Re} \left(\underline{V}_i \frac{\partial \bar{V}_i}{\partial Q_l} \right) \quad (4.15)$$

The analysis can treat each phase of the grid separately. Thus, it can be applied to unbalanced grids.

4.2.4 Voltage-voltage correlation coefficients

The voltage-voltage correlation coefficients used by the ST in the LV grid can be obtained similar to the calculation of the voltage correlation for the tap changer variations [116]. Assuming that \mathcal{N} is the set of buses of the LV grid except for the bus connected to the ST, \mathcal{K} is the set of ST bus and $\bar{V}_i = |\bar{V}_i| e^{j\theta_i}$, the partial voltage derivatives of bus i with respect to the voltage magnitude $|\bar{V}_k|$ ($k \in \mathcal{K}$) are computed as:

$$-\underline{V}_i \bar{Y}_{ik} e^{j\theta_k} = \frac{\partial \underline{V}_i}{\partial |\underline{V}_k|} \sum_{j \in \mathcal{K} \cup \mathcal{N}} \bar{Y}_{ij} \bar{V}_j + \underline{V}_i \sum_{j \in \mathcal{N}} \bar{Y}_{ij} \frac{\partial \bar{V}_i}{\partial |\bar{V}_k|} \quad (4.16)$$

Taken into account that:

$$\frac{\partial}{\partial |\bar{V}_k|} \sum_{j \in \mathcal{K}} \bar{Y}_{ij} \bar{V}_j = \bar{Y}_{ik} e^{j\theta_k} \quad (4.17)$$

$$\frac{\partial \underline{S}_i}{\partial |\bar{V}_k|} = 0 \quad (4.18)$$

The coefficients can be computed as:

$$\frac{\partial |\bar{V}_i|}{\partial |\bar{V}_k|} = |\bar{V}_i| \operatorname{Re} \left(\frac{\partial \bar{V}_i}{\bar{V}_i \partial |\bar{V}_k|} \right) \quad (4.19)$$

Nevertheless, the calculation of voltage-voltage correlation is similar to the correlation of the tap-changer. The 'tap-changer' of ST is small enough to ensure the partial derivatives in the following analysis can represent the features of ST.

4.3 Selection of Power Rating for Power Electronics Components

A proper power rating is essential for the performance of the PE component. Insufficient power rating restricts the engagement of components in providing grid regulation. On the other hand, an impractical high power rating increases the investment of the component. It is essential to optimize the power rating of the components concerning both the grid regulation and the investment. This section introduces a scheme based on optimization algorithms to select the proper power rating for the ST. For other types of PE components, even though the unique features of the components must be respected with the optimization algorithms, the schemes of the power rating selection have no essential difference.

The selection of power rating is directly related to the power flow through the ST. The ST has a 3-stage topology. Power flow through the LV stage is active/reactive power demand $P_{LV,load}(t)$ $Q_{LV,load}(t)$ of the LV grid. The dc/dc stage operates the active power $P_{LV,load}(t)$ of the connected LV grid and the power of the LVdc bus of the ST, e.g., the generation of DG $P_{LVdc,DG}(t)$ and dc load demand $P_{LVdc,load}(t)$ (e.g. charging power demand). Since the MV grid and the LV one are decoupled in terms of reactive power flow, the MV stage is not responsible for the reactive power of the load, but it should provide reactive power $Q_{ST,MV}(t)$ to the MV grid. Furthermore, the MV stage must operate the active power of the connected LV grid and both MV and LV dc buses, e.g. the DG generation $P_{MVdc,DG}(t)$ and the demand $P_{MVdc,load}(t)$ of the MVdc bus. All power is time-variant. The power of the three stages can be represented as:

$$\begin{aligned} S_{ST,LV,PF}(t) &= P_{LV,load}(t) + jQ_{LV,load}(t) \\ P_{ST,dc}(t) &= P_{LV,load}(t) + P_{LVdc,load}(t) - P_{LVdc,DG}(t) \\ S_{ST,MV,PF}(t) &= P_{LV,load}(t) + P_{LVdc,load}(t) - P_{LVdc,DG}(t) + P_{MVdc,load}(t) - P_{MVdc,DG}(t) + jQ_{ST,MV}(t) \end{aligned} \quad (4.20)$$

The ST in this chapter uses the design that all three stages have the same power rating. On the LV side, the ST should supply the load demand to the connected LV grid. In this work, the 24 h load profiles of average power consumption are used for the analysis. Since the load consumption varies from day to day, the real load demand can be higher than the peak power of the average daily profile $\hat{S}_{LV,load}$. The previous analysis of historical power records shows that the power demand exists in a probabilistic manner and can be fitted with the normal distribution. As suggested in the study, the standard deviation (SD) of power deviations from the average power demand is estimated as σ of 5 % [113]. According to the features of normal distribution, the power within the range of 85–115 % ($100 \% \pm 3\sigma$) of the average power demand accounts for 99 % of the probability. Therefore, in this work, the power rating of ST LV stage $S_{ST,LV}$ must be no less than 115 % of the peak power of the average profile $\hat{S}_{LV,load}$. This power rating achieves a high confidential level to ensure no overload of ST when it delivers the power to the LV grid.

$$S_{ST,LV} = 115\% \cdot \hat{S}_{LV,load} \quad (4.21)$$

The power demands of different LV grids (i.e., different MV buses if seen from the MV grid) are not the same, which results in different peak power values. This work considers that all STs have an identical power rating. As a consequence, the peak power must be the largest one among the LV grids installed with STs:

$$\hat{S}_{LV,load} = \max(\hat{S}_{LV,load,i}) \quad (i \in N_{ST}) \quad (4.22)$$

where i is the number of LV grid, which ST is installed, $N_{ST} = 1 \dots n_{ST}$ is the set of the LV

buses with STs.

The daily profiles of the load and DG connected to the LVdc bus show the same statistic features as the LV load demand. Consequently, the peak power, which the dc/dc stage of the ST i must be able to operate, can be expressed as:

$$\hat{P}_{ST,dc,i} = (\hat{P}_{LV,load,i} + \hat{P}_{LVdc,load,i}) \quad (4.23)$$

where $\hat{P}_{LV,load,i}$ is the peak power of the average load demand profile in the LVac grid and $\hat{P}_{LVdc,load,i}$ is the peak power of the average load demand profile of the LVdc bus. The generation of the DG, such as PV, is set to be 0 in this calculation based on the assumption that the DG generation cannot induce significant reversed power flow.

All STs are considered to have the same power rating, resulting in:

$$S_{ST,dc} = 115\% \cdot \hat{P}_{ST,dc}, = 115\% \cdot \max(\hat{P}_{ST,dc,i}) \quad (i \in N_{ST}) \quad (4.24)$$

In the MV grid, the MV stage provides active power to the connected LV grid and dc buses. A similar calculation approach to determine the active power demand of the LV and dc stages can be used for this stage. Additionally, it must provide reactive power for the MV grid operation to mitigate the violations of voltage constraints with a maximal power consumption scenario. According to the analysis of load deviation in previous paragraphs, the maximal power consumption scenario is when the load demand of all buses is 15 % more than their average load profiles, and the generation of DG is 0.

The reactive power injection is calculated with this maximal power consumption scenario. To avoid the unnecessary high power rating of the ST, reducing the cost of components, the reactive power injection must be optimized as:

$$f_{ST}(t) = \min \left(\sum_{i=1}^{n_{ST}} Q_{ST,MV,i}(t) \right) \quad (4.25)$$

Optimization constraints are subjected to f_{ST} . The subjected constraints are listed as follows.

Equality constraints

The equality constraints to be respected are the power flow equations, defined as:

$$\begin{aligned} P_{Gm}(t) - P_{Dm}(t) &= V_m(t) \sum_{n=1}^{n_l} V_n(t) [G_{mn} \cos(\delta_m(t) - \delta_n(t)) + B_{mn} \sin(\delta_m(t) - \delta_n(t))] \\ Q_{Gm}(t) - Q_{Dm}(t) &= V_m(t) \sum_{n=1}^{n_l} V_n(t) [G_{mn} \sin(\delta_m(t) - \delta_n(t)) - B_{mn} \cos(\delta_m(t) - \delta_n(t))] \end{aligned} \quad (4.26)$$

where $m \in N_L$ and $m \notin N_{ST}$, which $N_L = (1 \dots n_l)$ is the set of all buses in the grid; $P_{Gm}(t)$ and $Q_{Gm}(t)$ are active and reactive power generation of bus m , respectively; $P_{Dm}(t)$ and $Q_{Dm}(t)$ are active and reactive power demand of bus m ; and G_{mn} and B_{mn} are transfer conductance and susceptance between bus m and bus n , which derived from admittance matrix.

If $m \in N_{ST}$, then the constraints are rewritten as:

$$\begin{aligned} P_{Gm}(t) - P_{Dm}(t) &= V_m(t) \sum_{n=1}^{n_l} V_n(t) [G_{mn} \cos(\delta_m(t) - \delta_n(t)) + B_{mn} \sin(\delta_m(t) - \delta_n(t))] \\ Q_{ST,MV,m}(t) &= V_m(t) \sum_{n=1}^{n_l} V_n(t) [G_{mn} \sin(\delta_m(t) - \delta_n(t)) - B_{mn} \cos(\delta_m(t) - \delta_n(t))] \end{aligned} \quad (4.27)$$

Inequality constraints

The inequality constraints imposed in the optimization of $f_{ST}(t)$ are the voltage constraints and power factor:

- Voltage constraints

$$V_{\min,m} \leq V_m(t) \leq V_{\max,m} \quad m \in N_L \quad (4.28)$$

where $V_{\min,m}$ and $V_{\max,m}$ are the minimal and maximal voltage of the corresponding bus.

- Power factor

$$\lambda_{\min} \leq \lambda \quad (4.29)$$

where λ_{\min} is the minimal power factor requirement of the HV/MV substation.

After calculation of the daily reactive power injection $Q_{ST,MV,i}(t)$ with the maximal power consumption scenario, the peak reactive power that the ST must inject is:

$$\hat{Q}_{ST,MV,i} = \max(Q_{ST,MV,i}(t)) \quad (4.30)$$

The peak power of every MV stage $\hat{S}_{ST,MV,i}$ can be computed by combining the active power of the ST from the maximal power consumption scenario:

$$\hat{S}_{ST,MV,i} = 115\% \cdot (\hat{P}_{LV,load,i} + \hat{P}_{LVdc,load,i} + \hat{P}_{MVdc,load,i}) + j\hat{Q}_{ST,MV,i} \quad (4.31)$$

Consequently, the power rating of MV stage is selected as:

$$S_{ST,MV} = \max(\hat{S}_{ST,MV,i}) \quad (i \in N_{ST}) \quad (4.32)$$

The power rating of ST should be able to fulfill the power demand in both MV and LV grid. Thus, the power rating is selected according to:

$$S_{ST} = \max(S_{ST,MV}, S_{ST,dc}, S_{ST,LV}) \quad (4.33)$$

4.4 Setup for Performance Analysis

The performance of the proposed voltage regulation schemes of the two cases is evaluated by means of simulation. The structure of the testing grid, the daily load/DG power profiles, and the scenarios to be evaluated are presented in this section.

4.4.1 Testing grid

The grid consists of both MV and LV ones, as shown in Fig. 4.5. An HV bulk grid with an SCC of 400 MVA is used as the upstream grid. This value of SCC is recommended by a German system operator. An HV/MV substation with two transformers is considered with the equivalent impedance of $0.024 + j0.327 \Omega$. The on-load tap changer is not involved in the analysis. The MV grid has the nominal voltage level of 11 kV, which the network consists of 8 radial feeders, with 75 buses in total, as shown in Fig. 4.5 (a). The LV grid connected to each bus is modeled as an aggregated load except at bus 1 in feeder 4 (bus F401). A detailed network is modeled for this grid with the nominal voltage 0.4 kV. Its structures with the conventional LFT and with the ST are shown in Fig. 4.5 (b) and (c). In Case 1, the charging facility and the ES-STATCOM are connected to bus A of the LV grid. One PV unit is connected to bus F. Case 2 uses the ST. The ESS, the charging facility, and the PV unit are connected to the LVdc grid of ST. The data of the line impedance is listed in Appendix 7.1.

Both residential load and commercial load are considered in the simulation. The charging facilities in the residential/commercial area also have corresponding daily load profiles. The PV units are connected to some buses. Details of the composition of the power components at different buses are listed in Appendix 7.3.

Each type of load and charging facility uses the same 24 h power profile of average power demand. All values are presented in pu with the base power 1 MVA. Both MV and LV grids use the nominal voltage as base values. The average active power demand profiles of the residential/commercial load for buses in the MV grid are shown in Fig. 4.6 (a). Both profiles have the peak power of 0.48 pu. However, the power factor of the residential load is 0.98 and of the commercial load is 0.95, respectively. All loads are constant power type. Fig. 4.6 (b) shows the charging power in the residential/commercial area. The charging facilities have a constant power factor of 1. The PV units have the maximal generation capacity 0.10 pu

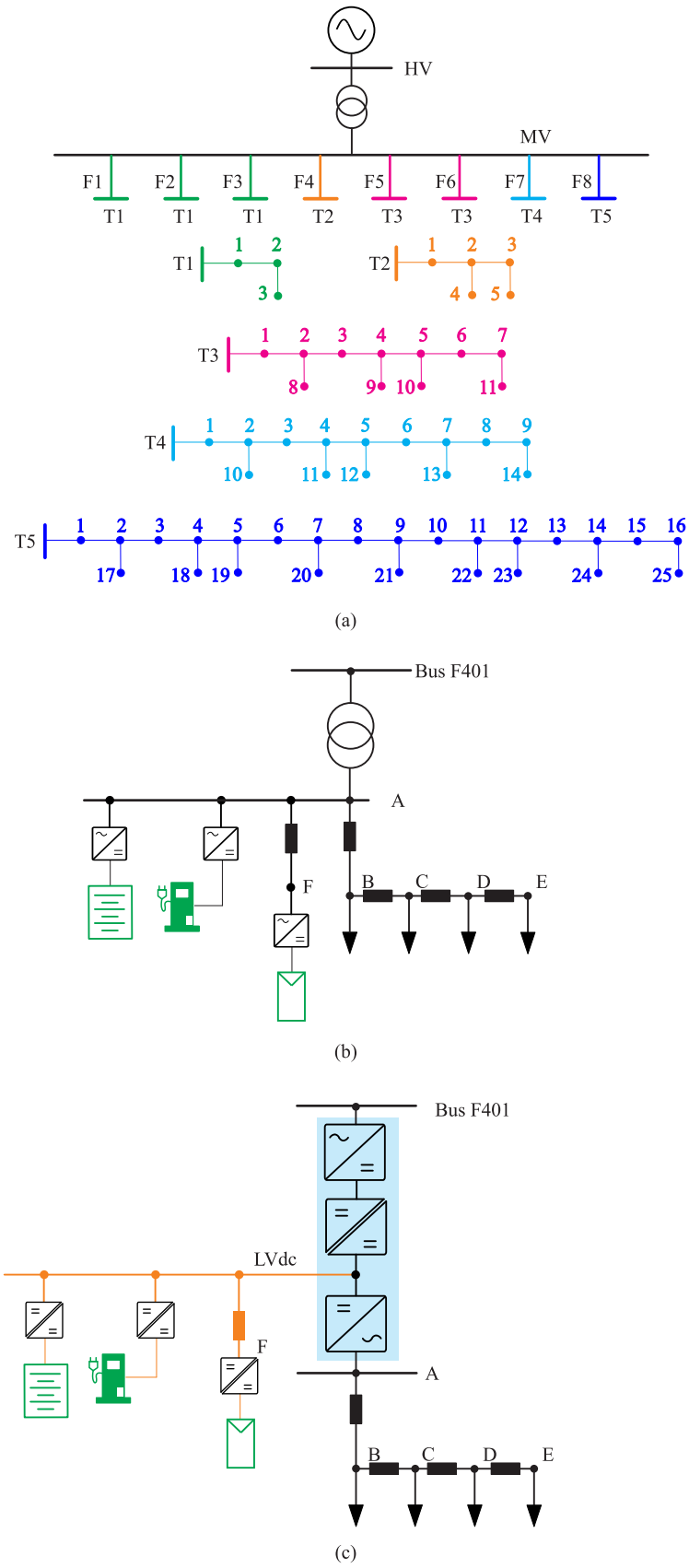


Fig. 4.5: Grid for evaluation of the proposed voltage regulation. (a) MV grid. (b) LV grid of Case 1. (c) LV grid of Case 2.

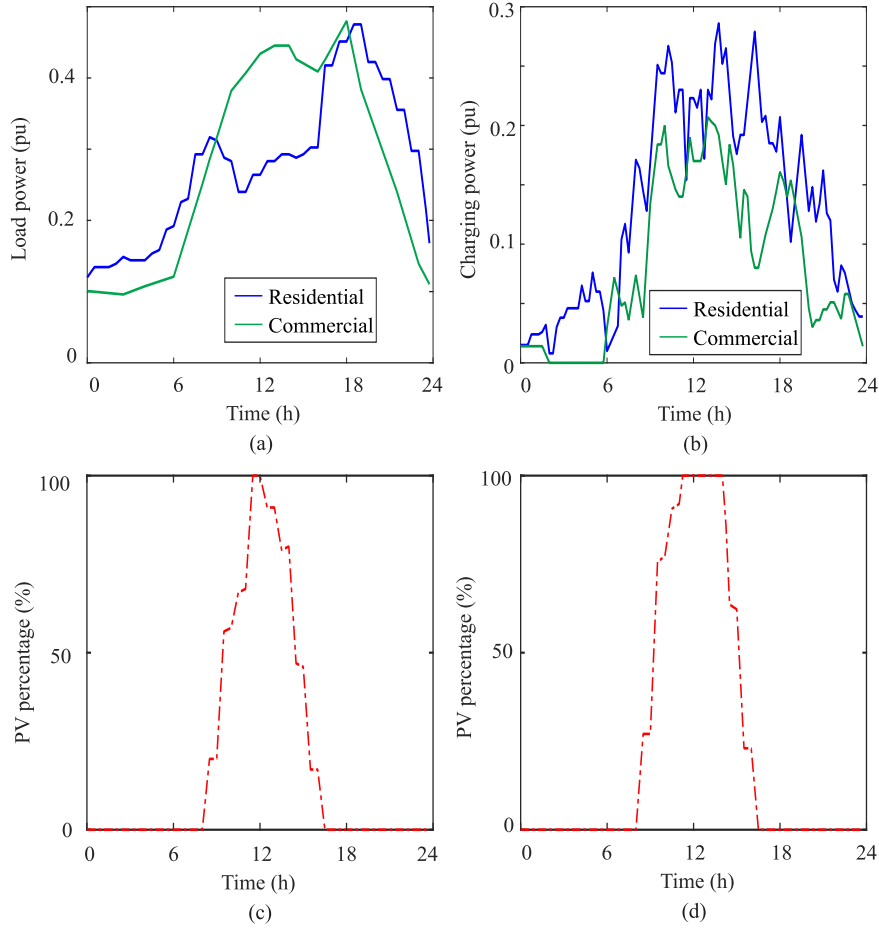


Fig. 4.6: 24 h profiles of power demand. (a) Average active power profiles for residential and commercial load of single MV bus. (b) Average charging power profiles for residential and commercial charging facility. (c) Average PV generation profile. (d) PV generation profile with 15 % increase.

except the one connected to the bus F401. All PV units share the same generation profile. The average profile is presented in Fig. 4.6 (c). The value of 100 % represents the PV unit reaching its generation capacity. Fig. 4.6 (d) shows the PV generation profile with a 15 % increase than the average profile. It is noticed that the maximal generation cannot exceed 100 %, since the generation capacity of the PV unit restricts it.

The charging facility of the LV grid in Fig. 4.5 (b) and (c) has the same load demand as other charging facilities in the residential area. The load demand seen from bus F401 is the same as the load demand of residential loads at other MV buses. The power demand along with the LV grid from bus B to E is equally distributed. The PV unit of bus F has the maximal generation capacity 0.20 pu.

4.4.2 Selection of power rating for power electronics components

The selection of ST power rating follows the approach introduced in Section 4.3. The ES-STATCOM uses the same power rating as the ST for a fair comparison.

Table 4.3: Possible groups of buses for ST installation

Group	Bus No.
1	F101 F203 F303 F401 F509 F603 F714 F817
2	F101 F203 F303 F401 F509 F603 F714 F825

The ST is installed at the buses, which connects the charging facility and PV unit. Every feeder of the MV grid has one ST. According to Appendix 7.3, from feeder 1 to feeder 7, only one bus in each feeder consists of a charging facility and a PV unit. Seven STs are installed at these buses. In feeder 8, the ST can be installed either at bus F817 or at bus F825. Therefore there are two possible groups of ST installation, as listed in Table 4.3.

For the LV stage of ST, according to Eq. (4.22), the value of $\hat{S}_{LV,load}$ can be computed with the peak load of commercial load:

$$\hat{S}_{LV,load} = |0.48 + j0.16| \approx 0.51 \quad (4.34)$$

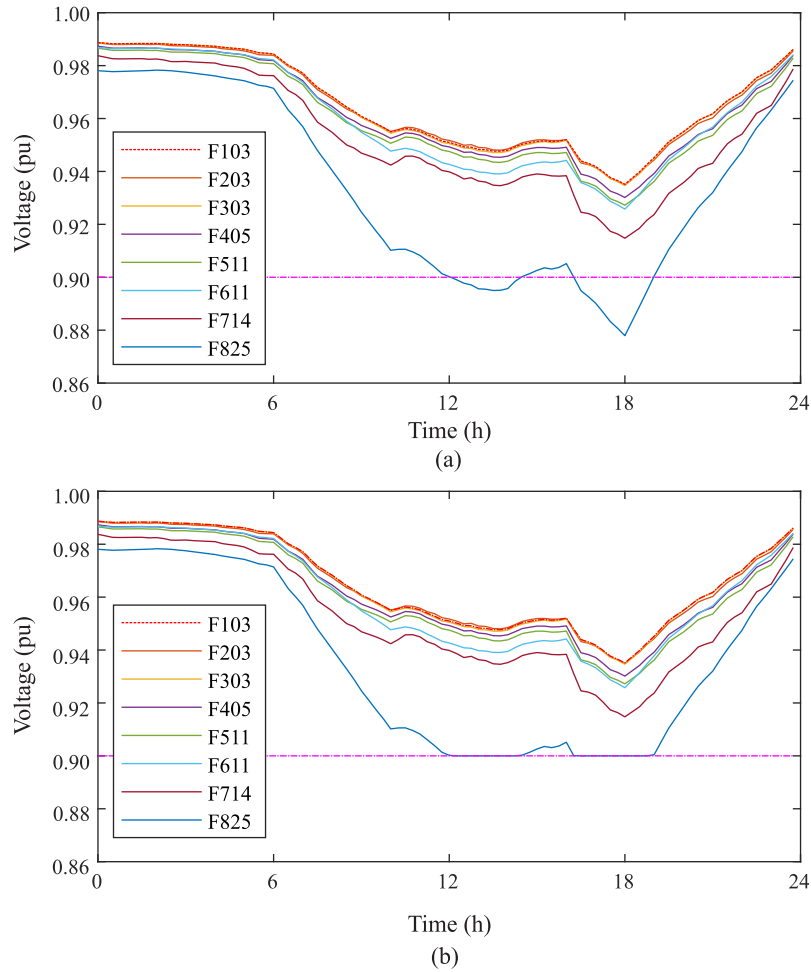


Fig. 4.7: 24 h voltage behaviors of buses in MV grid. (a) Without ST. (b) With injection of reactive power from ST according to Eq.(4.25).

Table 4.4: Peak reactive power injection $\hat{Q}_{ST,MV,i}$ of ST (pu)

Bus No.	F101	F203	F303	F401	F509	F603	F714	F817
$\hat{Q}_{ST,MV,i}$	0.264	0.264	0.264	0.264	0.265	0.265	0.265	0.307
Bus No.	F101	F203	F303	F401	F509	F603	F714	F825
$\hat{Q}_{ST,MV,i}$	0.163	0.163	0.163	0.163	0.164	0.164	0.164	0.372

Table 4.5: Peak power $\hat{S}_{ST,MV,i}$ for each ST (pu)

Bus	F101	F203	F303	F401	F509	F603	F714	F825
Apparent power	0.76	0.78	0.73	0.78	0.78	0.76	0.78	0.83

For the dc/dc stage, the peak power with the average profiles is 0.66 for the residential bus and 0.65 for the commercial bus, according to Eq. (4.23). As a consequence, the value of $\hat{P}_{ST,dc}$ is 0.66.

Using the maximal power consumption scenario, which is defined according to Section 4.3, the 24 h voltage behaviors of some buses in the MV grid without ST is shown in Fig. 4.7 (a). It is noted that the voltage of bus F825 violates the voltage constraint.

The mitigation of the violation is the task of the MV stage of ST. For the eight STs in each group, the first step to determine the power rating of the MV stage is to calculate the time-variant reactive power injection $Q_{ST,MV,i}(t)$, which is used to mitigate the violations according to Eqs. (4.25)-(4.29). The voltage constraints are 0.90–1.10 pu and the lowest power factor is 0.90. With the reactive power injection from STs, the new voltage behaviors can be derived, as shown in Fig. 4.7 (b). The STs have mitigated the voltage violations. 24 h injection of reactive power $Q_{ST,MV,i}(t)$ to achieve the voltage control has been calculated accordingly. The corresponding peak values of $\hat{Q}_{ST,MV,i}$ of every ST in the two installation groups are listed in Table 4.4.

According to Eq. (4.25), the total peak reactive power injection of group 2 is smaller than the peak injection of group 1, which implies better controllability of group 2. Therefore, the eight STs are installed at the buses of group 2.

Combining the 24 h active power demand of ST and the peak reactive power injection, the peak apparent power of each ST $\hat{S}_{ST,MV,i}$ can be computed, listed as in Table 4.5. The power rating of the ST is calculated using the peak power of all three stages with Eq. (4.33).

$$\begin{aligned}
 S_{ST,MV} &= 0.83 \\
 S_{ST,dc} &= 115\% \cdot \hat{P}_{ST,dc} \approx 0.76 \\
 S_{ST,LV} &= 115\% \cdot \hat{S}_{LV,load} \approx 0.59
 \end{aligned} \tag{4.35}$$

Table 4.6: Load condition coefficients of simulation scenarios

Scenario No.	Load condition coefficient of average load/charging profile	Load condition coefficient of average PV profile
1	115 %	0
2	100 %	0
3	100 %	100 %
4	85 %	115 %

The power rating of ST is 0.83 pu. To standardize the power rating for manufacture, the final value of S_{ST} uses 0.84 pu, i.e. each phase 0.28 pu.

The power rating of the ES-STATCOM S_{ES-STA} uses 0.84 pu as well. The ES-STATCOM is installed at the same buses as the STs, making both components the same amount.

4.4.3 Scenarios, evaluation criterion, and streams for analysis

The following scenarios are considered to represent the variation of load conditions in the testing grid. Based on the average profiles shown in Fig. 4.6, the scenarios are developed by multiplying a coefficient into the average profiles. The coefficients are listed in Table 4.6.

With scenarios 1 and 2, there is no generation of PV units. The PV profiles of scenarios 3 and 4 are represented in Fig. 4.6 (c) and (d).

The performance evaluation is separated for the MV and LV grids. With reference to the MV grid, a set \mathcal{D}_{MV} is denoted to evaluate voltage deviations with respect to reference, i.e. 1 pu for all the buses $l = 1, \dots, n_{MV}$ and time intervals $t = 1, \dots, T$:

$$\mathcal{D}_{MV} = \{(V_{MV,m}(t) - 1), m = 1, \dots, n_{MV}\}, t = 1, \dots, T \quad (4.36)$$

The formal definitions of two metrics for the voltage deviation evaluations are:

$$\bar{d}_{MV} = \frac{1}{T} \frac{1}{n_{MV}} \sum_{d \in \mathcal{D}_{MV}} |d| \quad (4.37)$$

$$d_{MV}^{\uparrow} = \max \{|d|, \forall d \in \mathcal{D}_{MV}\} \quad (4.38)$$

where \bar{d}_{MV} is the average voltage deviation of all buses and d_{MV}^{\uparrow} is the maximal voltage deviation of each case and each scenario.

For the LV grid, the computation is obtained by considering the voltage levels of all LV buses in the set \mathcal{D}_{LV} . The values are represented as \bar{d}_{LV} for the average voltage deviation of all buses and d_{LV}^{\uparrow} for the maximal voltage deviation.

There are three streams to be carried out in the analysis. The representation of streams A, B, and C are explained as:

- **Stream A** is used to evaluate the performance of the proposed voltage regulation schemes. Voltage constraints of 0.90–1.10 pu are imposed in the control schemes. The performance of the ES-STATCOMs (Case 1) and the STs (Case 2) are compared. All PE components have the identical power rating of 0.84 pu.
- **Stream B** implements similar voltage regulation schemes as the one in stream A. The PE components have the same power rating as stream A. However, as explained in 4.2, in order to mitigate the violations of under-voltage and over-voltage constraints simultaneously, compromise can arise. The mean voltage deviations \bar{d}_{MV} derived in stream A may not be the minimal ones that the scheme can gain. In stream B, the voltage constraints are not imposed to identify the possible compromise, which the schemes have made in stream A.
- **Stream C** uses the same voltage regulation schemes of Case 1 as stream A. Different power ratings of the ES-STATCOMs are tested. This stream aims to identify the power rating of the ES-STATCOMs, which can achieve comparable performance as the STs.

4.5 Analysis of Proposed Voltage Regulation Scheme

The analysis of the three streams is carried out based on the previously introduced grid and power profiles. The results are derived from the simulation, and the performance of the proposed voltage regulation schemes with different scenarios of different cases is evaluated.

4.5.1 Stream A

Stream A focuses on the comparison of performance between Case 1 (ES-STATCOM) and Case 2 (ST). The voltage constraints 0.90–1.10 pu are imposed. The ES-STATCOM and the ST have the same power rating of 0.84 pu.

Analysis in the MV grid

The values of \bar{d}_{MV} and d_{MV}^{\uparrow} with all four scenarios of both cases are listed in Table 4.7. The results show that the proposed schemes achieve no voltage violations with all scenarios of both cases. Both values of \bar{d}_{MV} and d_{MV}^{\uparrow} of Case 2 are smaller than the values of Case 1, with all scenarios. This is because the ST decouples the MV and LV grids, enhancing the controllability. \bar{d}_{MV} of Case 2 decreases of 15–28 % with respect the values of Case 1, depending on the scenarios. In Case 2, the \bar{d}_{MV} of scenario 3 is identical to scenario 2 due to the PV units are connected to the LVdc bus, which cannot impact the ac grid voltage.

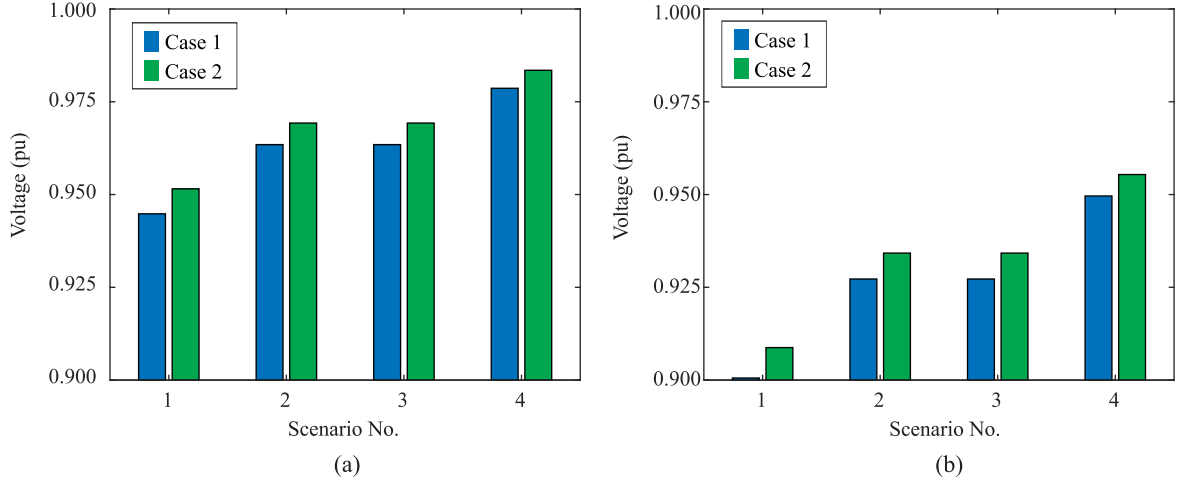


Fig. 4.8: Voltage amplitudes in MV grid at 18:00 of both cases with four scenarios, stream A. (a) Voltage amplitudes of bus F611. (b) Voltage amplitudes of bus F825.

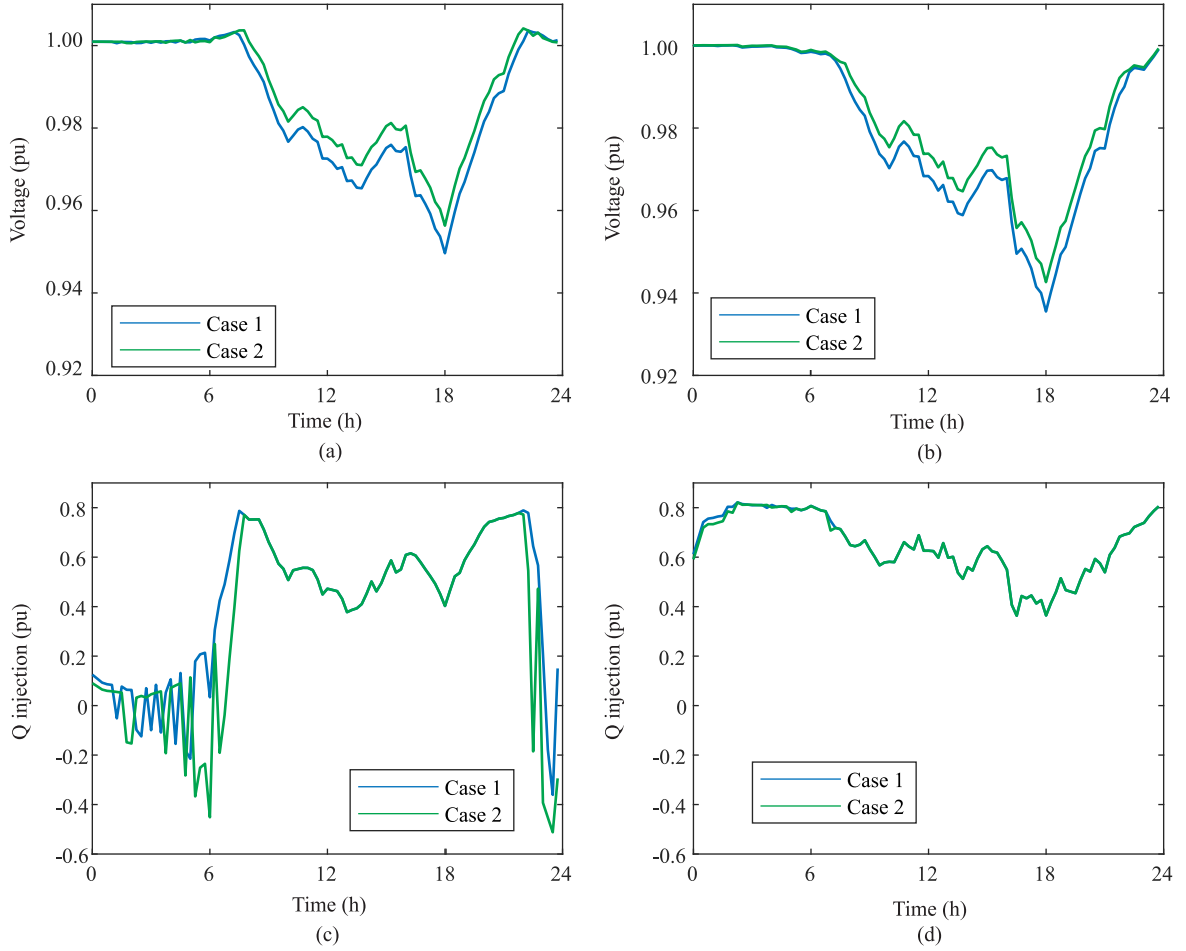


Fig. 4.9: 24 h voltage profiles of buses and corresponding injection of reactive power with scenario 1, stream A. (a) Voltage of bus F603. (b) Voltage of bus F714. (c) Injection of reactive power from PE components in feeder 6. (d) Injection of reactive power from PE components in feeder 7.

There is no voltage rise in the MV grid, and the voltage drop causes all the maximal voltage deviations. The maximal voltage drop happens at 18:00 h. With scenario 1, the d_{MV}^{\uparrow} of Case

Table 4.7: Voltage deviation in the MV grid, stream A

Case	1	2	1	2	1	2	1	2
Scenario	1		2		3		4	
\bar{d}_{MV} (pu)	0.020	0.017	0.013	0.010	0.012	0.010	0.007	0.005
d_{MV}^{\uparrow} (pu)	0.099	0.091	0.073	0.066	0.073	0.066	0.050	0.045

1 is 0.099 pu, which leads to the voltage is close to the under-voltage constraint. The value has decreased by 0.008 pu of Case 2, which is 0.091 pu. The PV has no generation at the time-step 18:00 h, resulting in the identical load conditions with scenarios 2 and 3 at this time point. Consequently, the values of d_{MV}^{\uparrow} are the same with both scenarios of Case 1 and Case 2, respectively. Comparing the performance among different scenarios of Case 1, both \bar{d}_{MV} and d_{MV}^{\uparrow} have the largest values with scenario 1 (heaviest load demand) and smallest values with scenario 4 (lightest load demand). The same tendency can also be observed among the four scenarios of Case 2.

Fig. 4.8 (a) and (b) show the voltage amplitudes of bus F611 in feeder 6 and bus F825 in feeder 8, respectively, both at time-step 18.00 h with all scenarios. 18.00 h is the time-step that the load demand reaches the peak. All voltage amplitudes of Case 2 are higher than the voltage amplitudes of Case 1. Comparing each scenario of the same case, the voltage amplitude of bus F611 is higher than bus F825. The lowest voltage amplitudes of both cases are 0.901 pu of Case 1 and 0.909 pu of Case 2, which appears at bus F825 with scenario 1 since this scenario has the heaviest load demand.

Fig. 4.9 shows the 24 h voltage profiles and reactive power injection with scenario 1. The voltage of Case 2 is no less than the voltage of Case 1 of both buses, as depicted in Fig. 4.9 (a) and (b). The reactive power injection varies between 0.4–0.7 pu within 24 h period (positive for capacitive and negative for inductive). From approximately 08:00 h to 20:00 h, the reactive power injection of both cases is identical, as shown in Fig. 4.9 (c) and (d). Taking into consideration the active power via ES-STATCOM or ST between approximately 08:00 h to 20:00 h, the reactive power injection of both components reaches the maximal capability during this period. Since the ST gains better controllability by decoupling the LV grid, the voltage of Case 2 is approximately 0.01 pu higher than the voltage of Case 1 if the reactive power injection is identical to both cases. It is observed from Fig. 4.9 (a) that the voltage of bus F603 is higher than 1 pu during approximately 00:00 h to 08:00 h. Accordingly, the reactive power injection in feeder 6 varies between inductive and capacitive during the same period, as shown in Fig. 4.9 (c). A similar phenomenon also appears between 22:00 h to 24:00 h. As shown in Fig. 4.9 (b), the voltage of bus F714 is under 1 pu with the entire duration. Consequently, the reactive power injection is always capacitive.

Fig. 4.10 shows the 24 h voltage profiles and reactive power injection with scenarios 2. The voltage of Case 2 is higher than it of Case 1 between approximately 08:00 h to 20:00 h, and

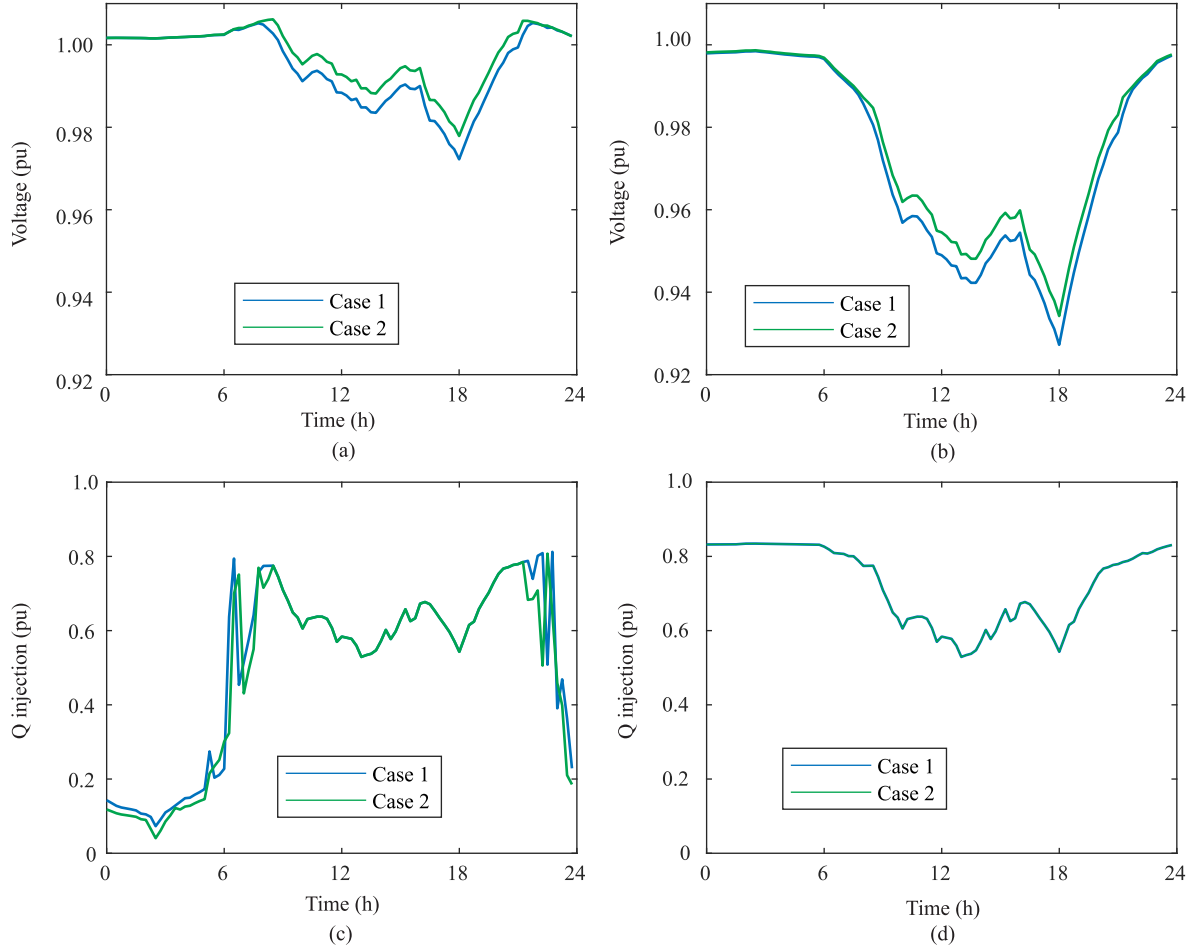


Fig. 4.10: 24 h voltage profiles of buses and corresponding injection of reactive power with scenario 2, stream A. (a) Voltage of bus F101. (b) Voltage of bus F825. (c) Injection of reactive power from PE components in feeder 1. (d) Injection of reactive power from PE components in feeder 8.

for the rest period, the voltage of both cases remains the same, as depicted in Fig. 4.10 (a) and (b). The reactive power injection is always capacitive in both cases, as shown in Fig. 4.10 (c) and (d). The voltage of bus F101 is above 1 pu during approximately 00:00 h to 08:00 h, as shown in Fig. 4.10 (a). At 18:00 h, the voltage of bus F825 reaches 0.927 pu of Case 1 and 0.934 pu of Case 2, which is the maximal voltage deviation of this scenario, as shown in Fig. 4.10 (b). Depicting in Fig. 4.10 (a) and (c), the voltage of both cases can be identical if the injection of reactive power has a difference. When the injection is different in both cases, mostly the injection of Case 1 is higher than in Case 2, as shown in Fig. 4.10 (c).

Fig. 4.11 shows the 24 h voltage profiles and reactive power injection with scenario 3. The voltage of Case 2 is no less than it of Case 1, as depicted in Fig. 4.11 (a) and (b). Fig. 4.11 (c) shows the reactive power injection of PE components in feeder 2 is identical between 08:00 h-20:00 h, and for the rest period, the reactive power injection of Case 1 is higher than Case 2. Fig. 4.11 (d) shows the injection in feeder 4 of Case 1 is higher than the injection of Case 2 from 00:00 h to 06:00 h, afterward, the injection of Case 2 starts to be no less than Case 1. Around 11:00 h to 13:00 h, the reactive power injection of Case 1 (ES-STATCOM)

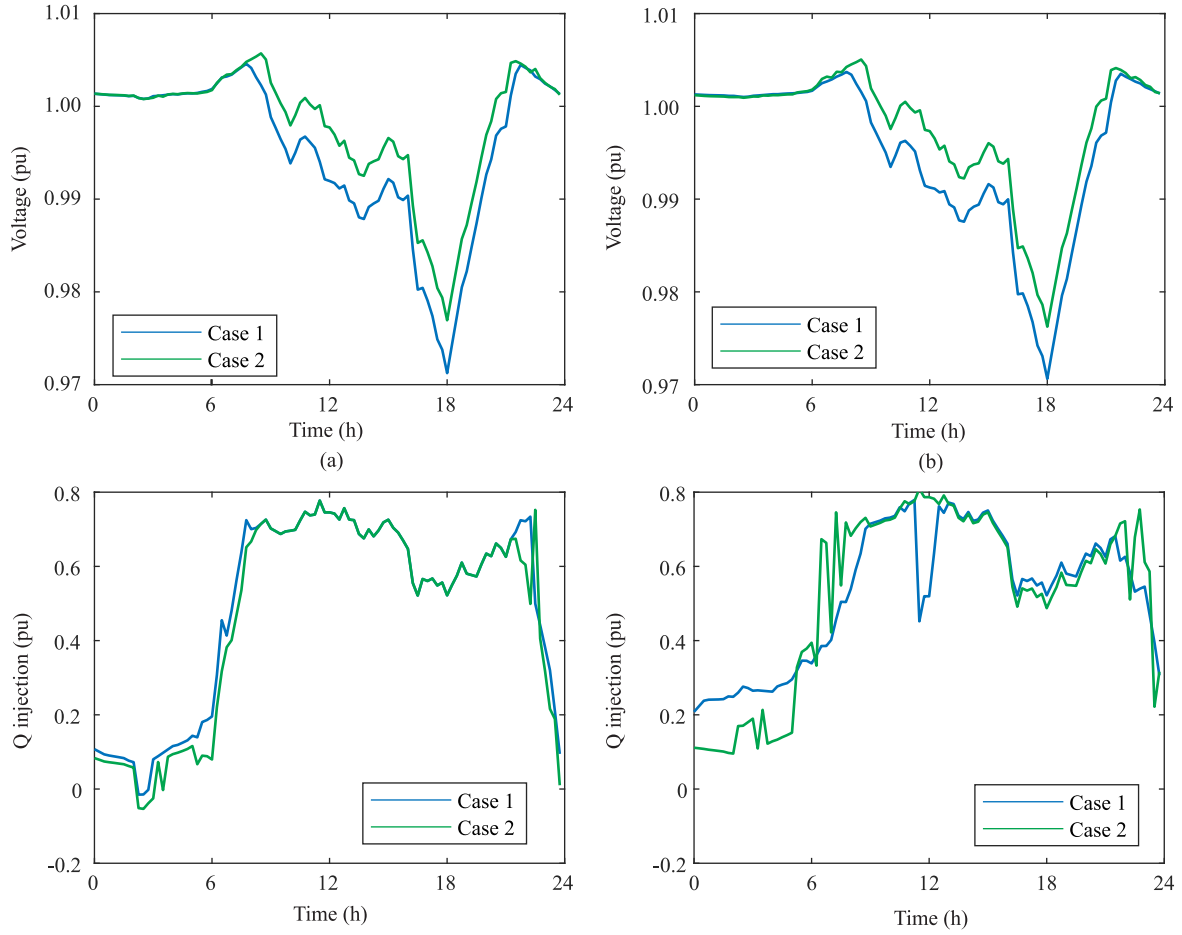


Fig. 4.11: 24 h voltage profiles of buses and corresponding injection of reactive power with scenario 3, stream A. (a) Voltage of bus F203. (b) Voltage of bus F401. (c) Injection of reactive power from PE components in feeder 2. (d) Injection of reactive power from PE components in feeder 4.

has a significant decrease. The ES-STATCOM cannot inject more reactive power during this period because of the voltage rise in the LV grid. The regulation schemes must make a compromise to mitigate the voltage rise and the voltage drop simultaneously. Furthermore, depicting in Fig. 4.11 (d), the reactive power injection in feeder 4 is capacitive (increasing voltage) even if there is a voltage rise in the LV grid.

Fig. 4.12 shows the 24 h voltage profiles and reactive power injection with scenario 4. The voltage behaviors of both cases have no significant difference with respect to other scenarios, as shown in Fig. 4.12 (a) and (b). Fig. 4.12 (c) shows the reactive power injection has a variation of Case 1 from 05:00 h to 07:00 h, and afterward, the injection of Case 1 is significantly higher than Case 2 till approximately 10:00 h. Fig. 4.12 (d) shows the reactive power injection of Case 1 in feeder 4 is lower than the injection of Case 2 from 08:00 h to 16:00 h. The difference can reach approximately 0.4 pu. This phenomenon is because the voltage rise in the LV grid restricted the injection of reactive power of Case 1.

Analysis in the LV grid

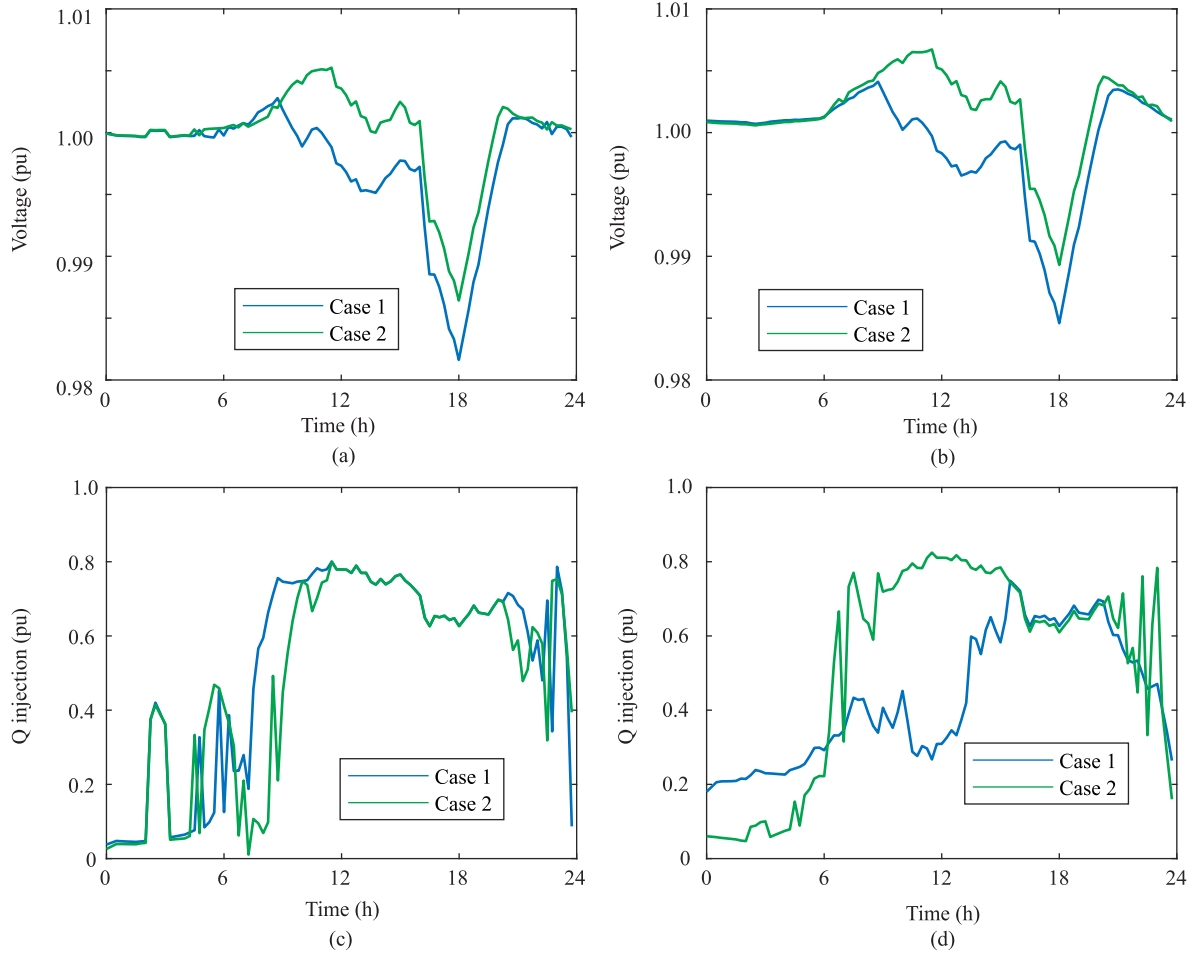


Fig. 4.12: 24 h voltage profiles of buses and corresponding injection of reactive power with scenario 4, stream A. (a) Voltage of bus F503. (b) Voltage of bus F401. (c) Injection of reactive power from PE components in feeder 5. (d) Injection of reactive power from PE components in feeder 4.

In the LV grid, Table 4.8 shows both \bar{d}_{LV} and d_{LV}^{\uparrow} values of Case 2 (ST) are smaller than Case 1 (ES-STATCOM), with all four scenarios. With scenario 1, it is noted that Case 1 is not able to mitigate the violation of under-voltage constraint, resulting in d_{LV}^{\uparrow} of 0.123 pu. However, Case 2 can mitigate the violation, demonstrating better controllability. Case 2 with scenarios 2 and 3 has the same \bar{d}_{LV} and d_{LV}^{\uparrow} values since the PV cannot impact ac grid voltage. With scenarios 3 and 4, the values of d_{LV}^{\uparrow} of Case 1 are 0.100 pu, i.e., the maximal allowed voltage deviation.

The voltage behaviors of all buses with scenarios 1 and 2 are plotted in Fig. 4.13. For every single bus, the voltage amplitudes of 24 h are represented in one point of the x-axis in the boxplot. The voltage amplitudes of Case 1 have significant variations. Especially the buses D and E with scenario 1, the voltage of both buses can be lower than 0.90 pu, as shown in Fig. 4.13 (a). The bus A voltage of Case 2 has the medium value of approximately 1.01 pu, and the voltage amplitudes of other buses of Case 2 are very close to 1 pu, illustrated in Fig. 4.13 (b) and (d).

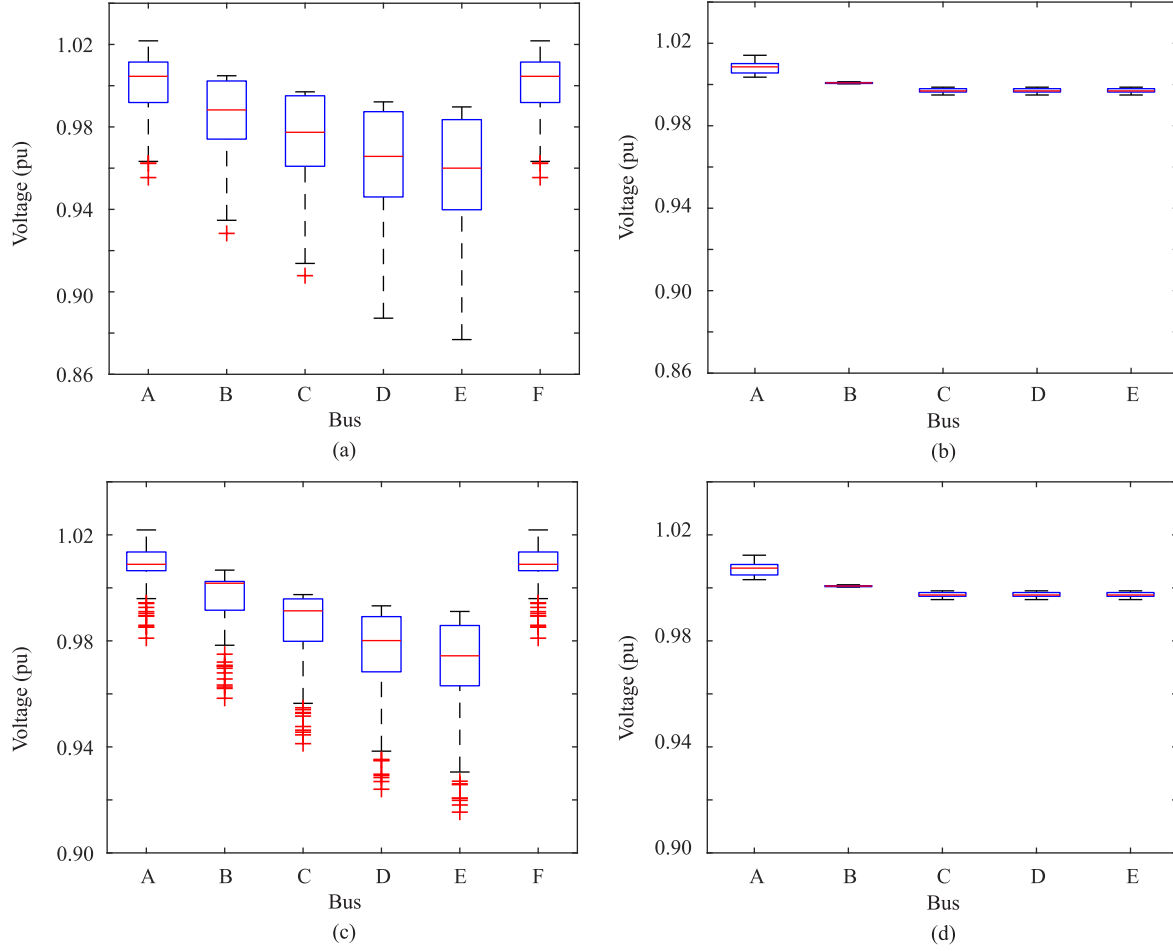


Fig. 4.13: Boxplot of voltage for all buses in the LV grid within 24 h, stream A. (a) Case 1, scenario 1. (b) Case 2, scenario 1. (c) Case 1, scenario 2. (d) Case 2, scenario 2.

Fig. 4.14 shows the voltage amplitudes of all buses with scenarios 3 and 4. With both scenarios, the voltage amplitudes at bus F of Case 1 can reach 1.10 pu, caused by the generation of PV, as shown in Fig. 4.14 (a) and (c).

In stream A, the voltage regulation schemes with the ES-STATCOMs (Case 1) and the STs (Case 2) have been evaluated. The coordination of ES-STATCOMs distributed in the grid forms a distributed solution for both MV and LV grids. However, since the ST decouples its connected MV and LV grids, despite the STs behave similarly to ES-STATCOMs in the MV grid, it provides a centralized solution for its LV grid. With the same power rating and active power dispatch plan, the smaller \bar{d} and d^\uparrow of ST based solution in both MV and LV grids can

Table 4.8: Voltage deviation in the LV grid, stream A

Case	1	2	1	2	1	2	1	2
Scenario	1		2		3		4	
\bar{d}_{LV} (pu)	0.026	0.004	0.017	0.003	0.020	0.003	0.016	0.003
d_{LV}^\uparrow (pu)	0.123	0.014	0.085	0.012	0.100	0.012	0.100	0.011

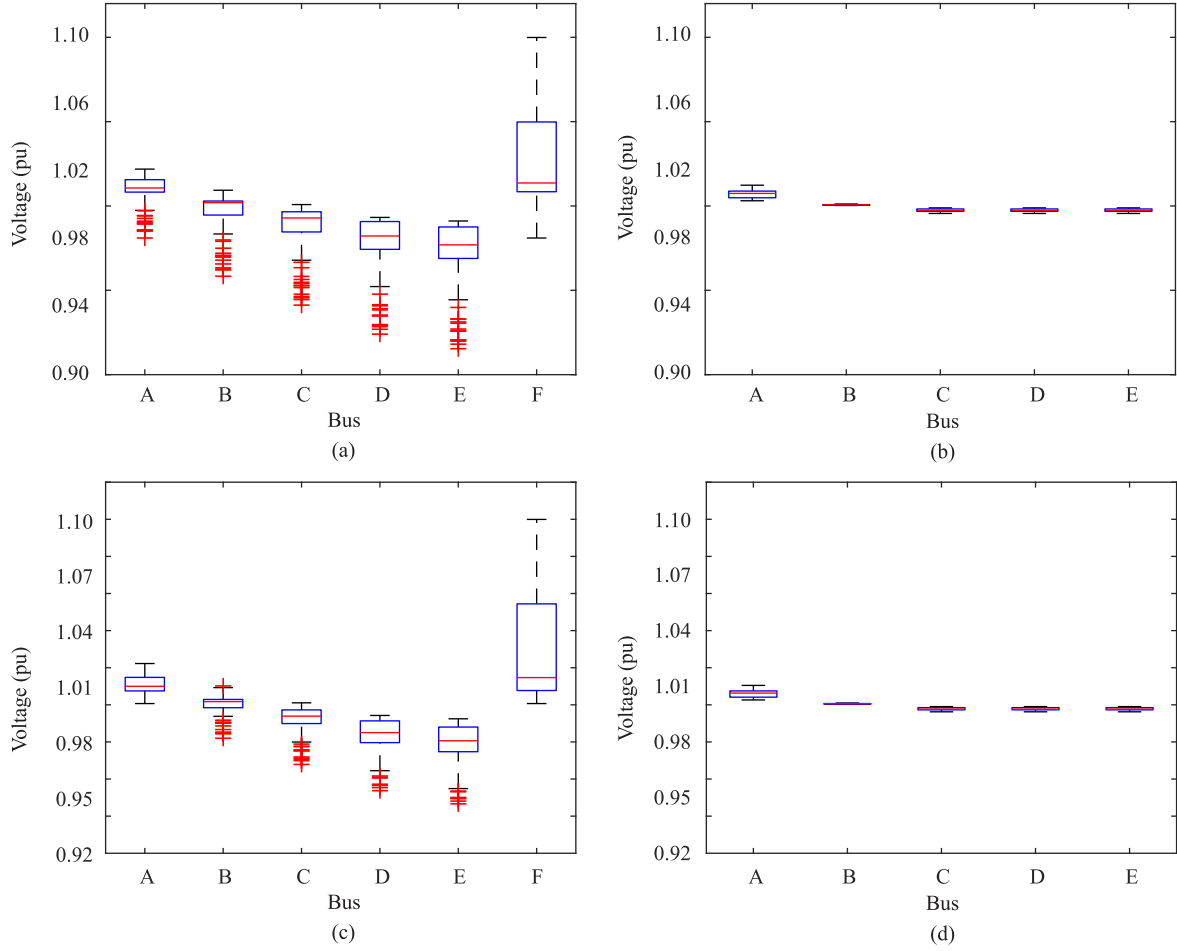


Fig. 4.14: Boxplot of voltage for all buses in the LV grid within 24 h, stream A. (a) Case 1, scenario 3. (b) Case 2, scenario 3. (c) Case 1, scenario 4. (d) Case 2, scenario 4.

be derived. In the LV grid, the ES-STATCOM based solution cannot mitigate the violation of under-voltage constraint with scenario 1.

4.5.2 Stream B

In order to mitigate the voltage rise, the proposed scheme tends to decrease the voltage of the MV busbar of the HV/MV substation. The opposite action is implemented to mitigate the voltage drop. When the voltage rise and drop appear simultaneously, to fulfill the voltage constraints, the proposed control scheme must make some compromises, resulting in the values of \bar{d} in stream A may not be the minimal ones. This stream examines the proposed scheme without the imposed constraints of voltage 0.90–1.10 pu in order to identify the compromise that has been made in stream A.

Analysis in the MV grid

The values of \bar{d}_{MV} and d_{MV}^{\uparrow} of the MV grid have been presented in Table 4.9 of stream B. Comparing the results with the values in Table 4.7, in the MV grid, the values from streams

Table 4.9: Voltage deviation in the MV grid, stream B

Case	1	2	1	2	1	2	1	2
Scenario	1		2		3		4	
\bar{d}_{MV} (pu)	0.020	0.017	0.013	0.010	0.012	0.010	0.007	0.005
d_{MV}^{\uparrow} (pu)	0.099	0.091	0.073	0.066	0.073	0.066	0.050	0.045

Table 4.10: Voltage deviation in the LV grid, stream B

Case	1	2	1	2	1	2	1	2
Scenario	1		2		3		4	
\bar{d}_{LV} (pu)	0.026	0.004	0.017	0.003	0.020	0.003	0.016	0.003
d_{LV}^{\uparrow} (pu)	0.123	0.014	0.085	0.012	0.113	0.012	0.107	0.011

A and B are identical with all four scenarios of both Cases.

Analysis in the LV grid

The values of \bar{d}_{LV} and d_{LV}^{\uparrow} of the LV grid have been presented in Table 4.10. Comparing the results with the values in Table 4.8 of stream A, the values of Case 2 with all scenarios in stream B are identical to those in stream A, thanks to the decoupling feature and the dc connection of the ST. The values with scenarios 1 and 2 of Case 1 are not changed from stream A. However, the values of d_{LV}^{\uparrow} with scenarios 3 and 4 are 0.113 pu and 0.107 pu, which violate the over-voltage constraint. Meanwhile, the values of \bar{d}_{LV} with scenarios 3 and 4 have a negligible decrease in stream B, leading to the values the same as the values in stream A with the precision of three decimal approximation.

The voltage behaviors of Case 1 are plotted in Fig. 4.15 with scenarios 3 and 4. For every bus, the voltage amplitudes of 24 h are represented in one point of the x-axis in the boxplot. The over-voltage violation can be observed at bus F with both scenarios.

With scenario 3, Fig. 4.16 (a) shows the voltage behaviors of bus A in the LV grid. It is observed from approximately 11:00 h to 13:00 h, there is a voltage decrease of approximately 0.01 pu in stream A, caused by the different reactive power injection of both streams. Fig. 4.16 (b) shows the injection from the ES-STATCOM at bus A. A difference of reactive power injection of approximately 0.3 pu during the same period can be observed. Fig. 4.16 (c) shows the voltage behaviors of the busbar of the HV/MV substation, with scenario 4. From approximately 11:00 h to 13:00 h, the MV busbar voltage of HV/MV substation have a slight difference between the streams A and B. Fig. 4.16 (d) shows that the reactive power injection at the bus F101 is identical in both streams. It is concluded that only the ES-STATCOM at bus A changes its reactive power injection in streams A and B, resulting in different values of d_{LV}^{\uparrow} .

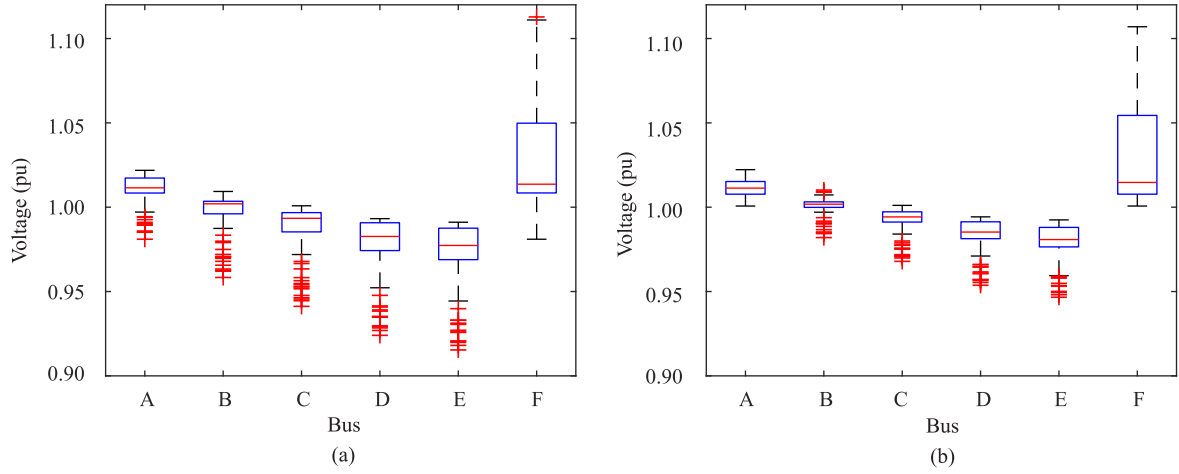


Fig. 4.15: Boxplot of voltage for all buses in the LV grid within 24 h, stream B. (a) Case 1, scenario 3. (b) Case 1, scenario 4.

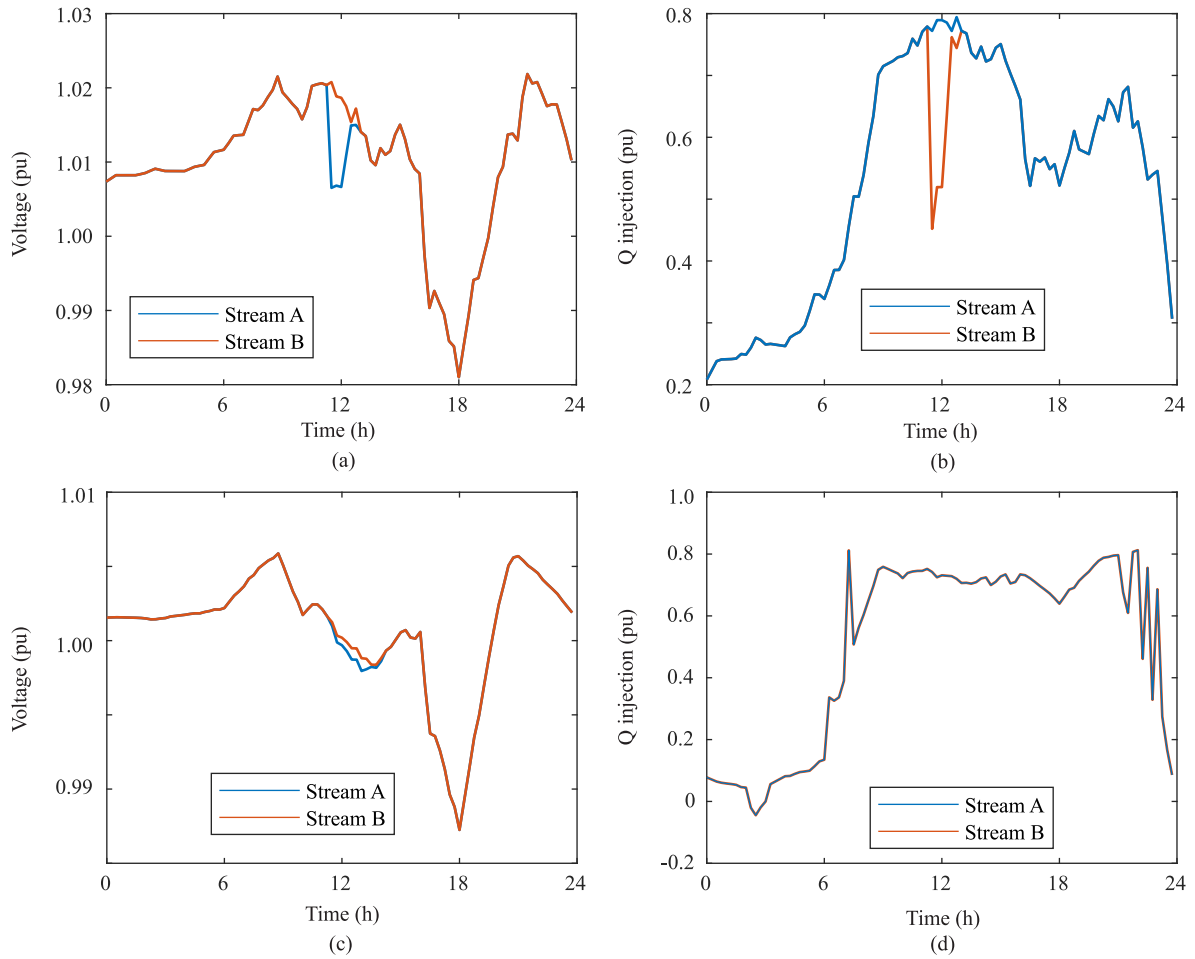


Fig. 4.16: 24 h voltage behavior and reactive power injection of Case 1 in streams A and B. (a) Voltage of bus A in the LV grid, scenario 3. (b) Injection of reactive power in feeder 4, scenario 3. (c) Voltage of substation busbar, scenario 4. (d) Injection of reactive power in feeder 1, scenario 4.

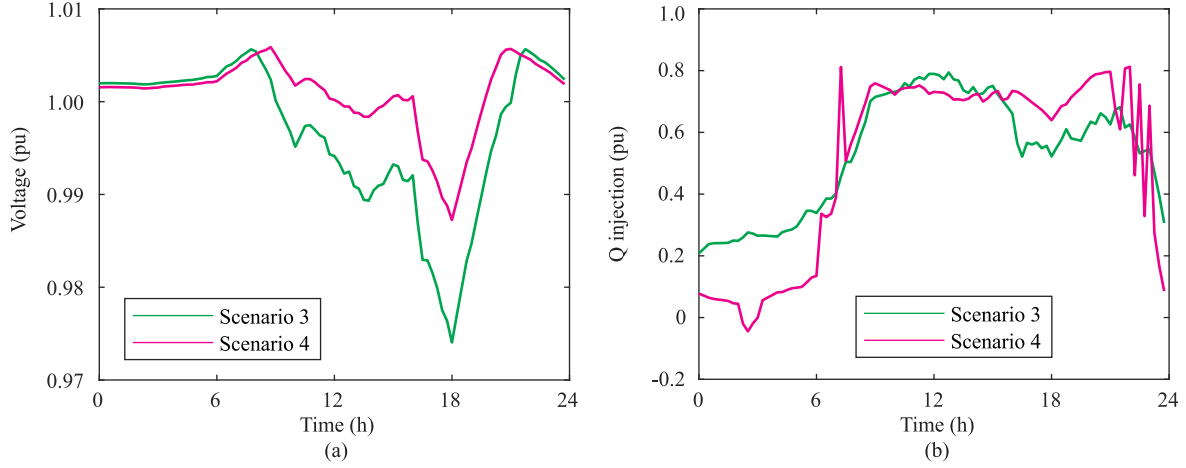


Fig. 4.17: 24 h behavior of voltage and reactive power injection of Case 1, stream B. (a) Voltage of substation busbar, scenarios 3 and 4. (b) Injection of reactive power in feeder 4, scenarios 3 and 4.

Furthermore, with scenario 4, the PV has a more significant generation, and the load demand is lighter with respect to scenario 3. A higher voltage rise is expected, but the value of d_{LV}^{\uparrow} with scenario 4 is smaller than the value with scenario 3. Fig. 4.17 (a) shows the voltage of the HV/MV substation busbar with the scenarios 3 and 4, both in the stream B. The voltage with scenario 3 is lower than the voltage with scenario 4 during 11:00 h to 13:00 h, as expected. However, Fig. 4.17 (b) shows the reactive power injection in feeder 4, in which the injection with scenario 3 is higher than scenario 4, resulting in eventually d_{LV}^{\uparrow} with scenario 3 is higher than it with scenario 4.

In stream A, the voltage constraints are imposed in the scheme. Consequently, the scheme can make some compromises to fulfill the imposed constraints. In order to analyze the possible compromises, in stream B, the proposed schemes do not take into account the imposed constraints. As a consequence, the violation of voltage constraints can appear, but the average voltage deviations \bar{d}_{MV} and \bar{d}_{LV} have only neglectable changes to stream A, suggesting the proposed schemes make only slight compromises to fulfill the imposed constraints.

4.5.3 Stream C

This stream aims to identify the power rating of the ES-STATCOM converter, which is able to achieve similar performance as the ST. Different power ratings of the ES-STATCOM converter are tested. Only scenarios 1 and 4 have been evaluated in this stream since the power conditions with the two scenarios can cause more critical voltage issues than the other two scenarios.

Identification of converter power rating in the MV grid

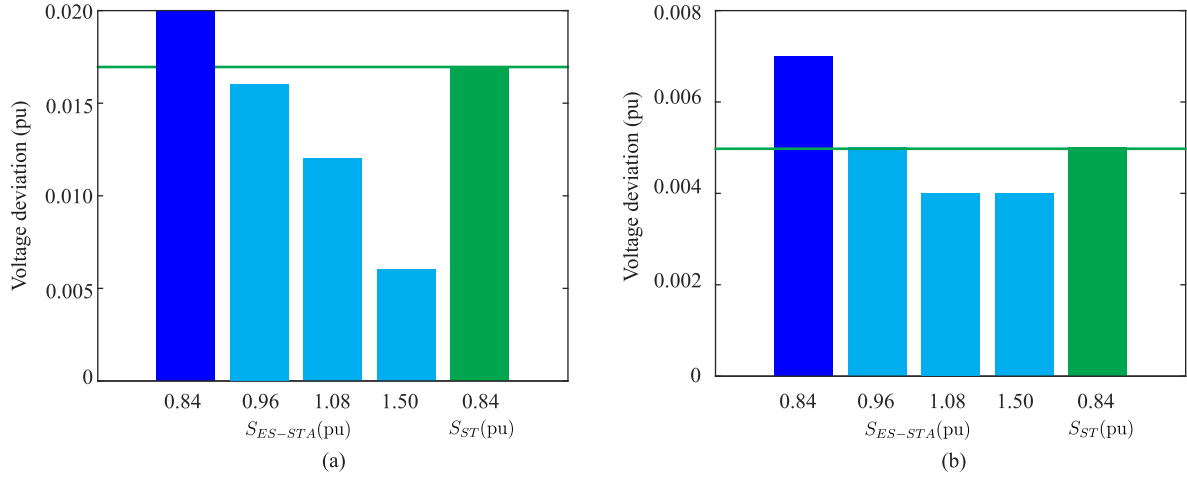


Fig. 4.18: \bar{d}_{MV} values of ES-STATCOM with different converter power ratings respecting the ST in the MV grid. (a) Scenario 1. (b) Scenario 4.

Table 4.11: \bar{d}_{MV} and d_{MV}^{\uparrow} values of ES-STATCOM with different converter power ratings respecting the ST in the MV grid

PE component power rating	ES-STATCOM (0.96 pu)	ES-STATCOM (1.08 pu)	ES-STATCOM (1.50 pu)	ST (0.84 pu)
Scenario	1			
\bar{d}_{MV} (pu)	0.016	0.012	0.006	0.017
d_{MV}^{\uparrow} (pu)	0.087	0.078	0.050	0.091
Scenario	4			
\bar{d}_{MV} (pu)	0.005	0.004	0.004	0.005
d_{MV}^{\uparrow} (pu)	0.043	0.035	0.024	0.045

The results of \bar{d}_{MV} and d_{MV}^{\uparrow} with different power ratings of the ES-STATCOM are listed in Table 4.11 and shown as in Fig. 4.18, with respect to the results of the ST.

In the MV grid, the results show that the \bar{d}_{MV} value of Case 1 can be improved to be smaller than the value of Case 2 by means of increasing the power rating of the ES-STATCOM converter. The power rating of the converter must be large enough to cover the reactive load, which the ST decouples. As a result, when increasing the power rating of the ES-STATCOM converter by 14 % to 0.96 pu, the performance of Case 1 is comparable with the performance of Case 2.

Identification of converter power rating in the LV grid

The results of \bar{d}_{LV} and d_{LV}^{\uparrow} with different power ratings of the ES-STATCOM are listed in Table 4.12 and shown as in Fig. 4.19, with respect to the results of the ST.

In the LV grid, both \bar{d}_{LV} and d_{LV}^{\uparrow} can be reduced by increasing the power rating of the ES-STATCOM converter. By increasing the power rating by 29 % to 1.08 pu, the violation

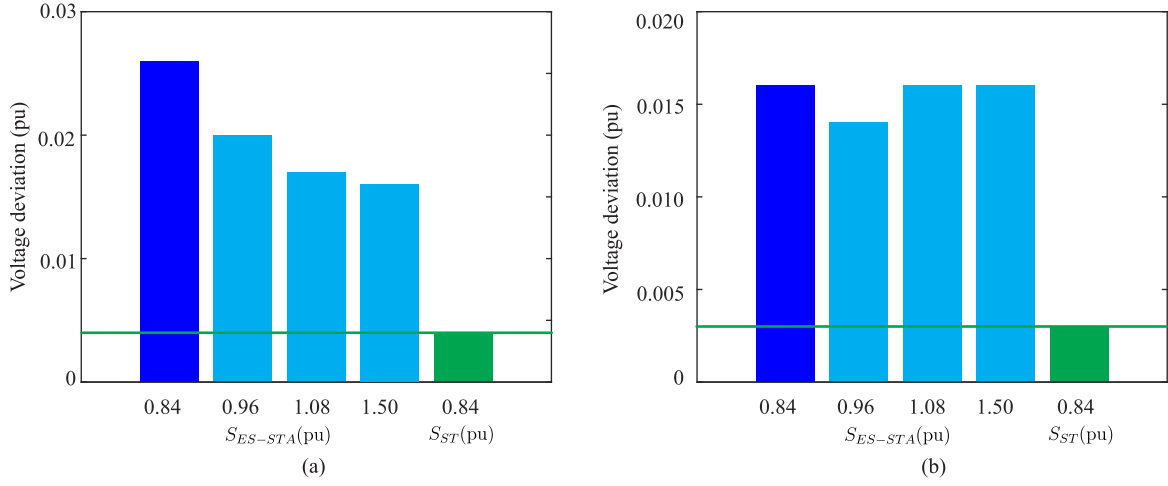


Fig. 4.19: \bar{d}_{LV} values of ES-STATCOM with different converter power ratings respecting the ST in the LV grid. (a) Scenario 1. (b) Scenario 4.

Table 4.12: \bar{d}_{LV} and d_{LV}^{\uparrow} values of ES-STATCOM with different converter power ratings respecting the ST in the LV grid

PE component power rating	ES-STATCOM (0.96 pu)	ES-STATCOM (1.08 pu)	ES-STATCOM (1.50 pu)	ST (0.84 pu)
Scenario	1			
\bar{d}_{LV} (pu)	0.020	0.017	0.016	0.004
d_{LV}^{\uparrow} (pu)	0.102	0.085	0.046	0.014
Scenario	4			
\bar{d}_{LV} (pu)	0.014	0.016	0.016	0.003
d_{LV}^{\uparrow} (pu)	0.100	0.096	0.094	0.011

of under-voltage constraint in scenario 1 can be mitigated by the ES-STATCOM, and the maximal voltage deviation d_{LV}^{\uparrow} in scenario 4 is reduced below 0.100 pu, i.e., the violation of over-voltage constraint in this scenario can be avoided without imposing an extra constraint 0.90–1.10 pu in the regulation scheme. However, by further increasing the power rating of ES-STATCOM to 1.50 pu, the reduction of \bar{d}_{LV} is no more than 0.001 pu of both scenarios. It can be concluded that the voltage regulation performance of the ES-STATCOM in the LV grid cannot reach as good as the ST since the ST forms the voltage of its connected LV grid.

4.6 Summary

The voltage regulation is an essential task for system operators. This chapter has discussed the voltage regulation implemented by the PE components. The ES-STATCOM and the ST are considered as actuators to implement the regulation. Depending on the grid connecting strategies, the ES-STATCOM regulates the voltage with reactive power injection. The ST,

behaving similarly to the ES-STATCOM in the MV grid, but regulates its connected LV grid by setting the voltage of its LV busbar. A method to select the proper power rating of the PE component has been presented, illustrated with the ST as an example. The regulation schemes with the same objective have been developed to coordinate the actuators. The regulation schemes exploit the voltage-correlation coefficients to reduce the computation burden. Different coefficients are adjusted for the ES-STATCOM and the ST schemes, depending on the voltage regulation features. The ES-STATCOMs distributed in the grid formulate a distributed solution. In the MV grid, the STs also formulate a distributed solution; in the LV grid, as the single actuator, the ST formulates a centralized solution.

The performance of the two types of PE components has been evaluated. Four scenarios have been taken into account, representing various load conditions. With the identical power rating of 0.84 pu, the ES-STATCOMs are not able to mitigate all of the violations with the given scenarios. However, the STs can mitigate all violations of under-voltage and over-voltage constraints, suggesting better controllability. As a consequence, with the same power rating, the STs have a better performance than the ES-STATCOMs both in the MV and LV grids. In the MV grid, the ST based solution gains some advantages due to it decouples the MV and LV grids in terms of voltage and reactive power exchange. Nevertheless, the advantages can be compensated by increasing the power rating of the ES-STATCOM converter, achieving the same performance in the MV grid respecting the ST. In the LV grid, by increasing the power rating of the ES-STATCOM converter to 1.08 pu, the violation of under-voltage constraint can be mitigated. However, by increasing the power rating to 1.50 pu, the performance with the ES-STATCOM has no significant difference with respect to the power rating of 1.08 pu. Conclusively, the distributed solution based on the ES-STATCOMs cannot reach the same performance as the ST based centralized solution in the LV grid.

5 Centralized Meshed Grid Solution based on Smart Transformer

The previous chapters have focused on the grid operation with radial network configuration. With this configuration, such as the two in parallel low voltage (LV) feeders shown in Fig. 5.1 (a), each feeder is supplied by one upstream grid of medium voltage (MV) via a transformer and is operated independently. In some cases, it can exist a normally open point (NOP) between the feeders. However, this point is switched off during the regular operation and can be switched on, for example, if one feeder loses its power supply from its connected upstream grid. The meshed grid represents the concept of a ring network configuration by switching on the NOP during regular operation [74]. The meshed configuration helps achieve an equal distribution of the load flow among the essential components such as transformers, avoiding the overload issues of such components.

One of the obstacles to apply the meshed grid concept is the voltage difference in terms of phase and amplitude at both sides of the NOP. Since the MV grid phase varies from one to another, a phase shift can arise between the feeders supplied by different MV grids. The network impedance and loads are not identical, resulting in a voltage amplitude difference at both sides of the NOP. Without a proper connection scheme, directly switching on the NOP between the feeders can lead to phenomena such as a significant power in-rush, endangering the system stability [117]. Thanks to the development of PE technology, components such as back-to-back (B2B) converter or smart transformer (ST) can decouple the phase angles and voltage amplitudes of grids connected at different sides of the component, leaving only active power exchange between the grids. The meshed grid concept is now possible to be implemented in grid operation, such as the "Flexible Urban Networks-Low Voltage" project in UK [118].

This chapter analyzes an ST-based solution for meshed grid operation. As shown in Fig. 5.1 (b), the ST replaces one conventional low-frequency transformer (LFT), enabling that the NOP can be switched on during the regular operation. Various ST-based meshed grid operation schemes can be implemented by controlling the output power of ST, optimizing the meshed grid's conditions in terms of losses, voltage. Furthermore, the ST can provide the power conditioning that prevents the harmonics in the meshed grid from spreading into the connected MV grid. Consequently, the power supply reliability and quality of the meshed grid can be improved. The grid's ability to cope with the issues such as the penetration of distributed generation (DG) can be enhanced.

As the single control point, the ST provides a centralized solution for the meshed grid operation. In the first part of this chapter, a static operation scheme based on multi-objective optimization is introduced. The scheme aims to provide operation solutions systematically that can fulfill the preferences of different grid operators. In the second part of this chapter,

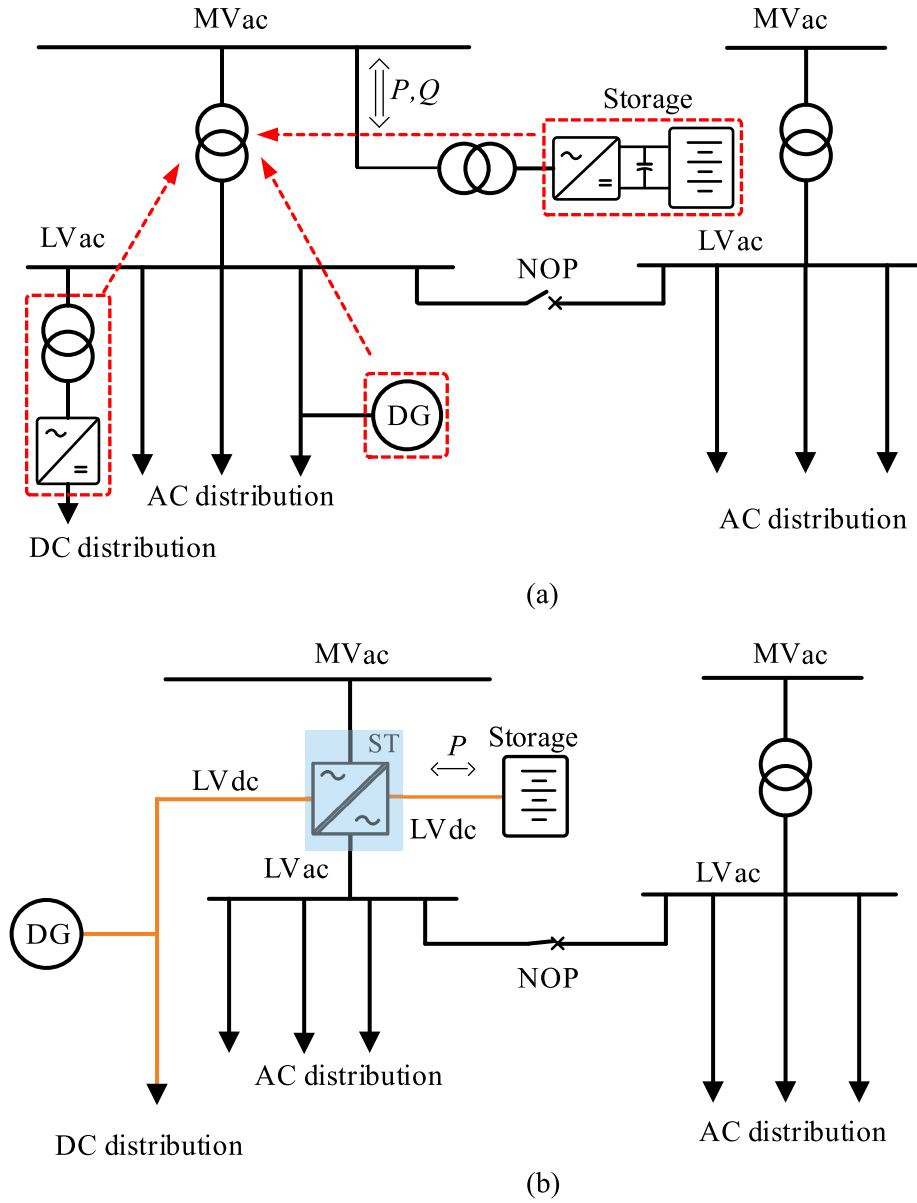


Fig. 5.1: Research focus of Chapter 5: Analysis of meshed grid operation. (a) Conventional operation of LV radial feeders. (b) ST base meshed grid solution.

a power conditioning scheme for harmonics control is introduced. The performance of both schemes will be evaluated based on the results from the simulation.

5.1 Meshed Grid Operation with Smart Transformer

To implement the ST-based meshed grid solution, at least one feeder must use ST instead of LFT. As shown in Fig. 5.2, the ST replaces the LFT of the feeder supplied by the external MV grid 1 (the left one). This feeder contains components such as the charging facility and photovoltaic (PV) unit that require the dc connection. By deploying the ST in this feeder can better exploit the capability of its dc links. The ST decouples the external MV grid 1 and the downstream LV feeder. The voltage and phase of MV grid 1 have no impact on the

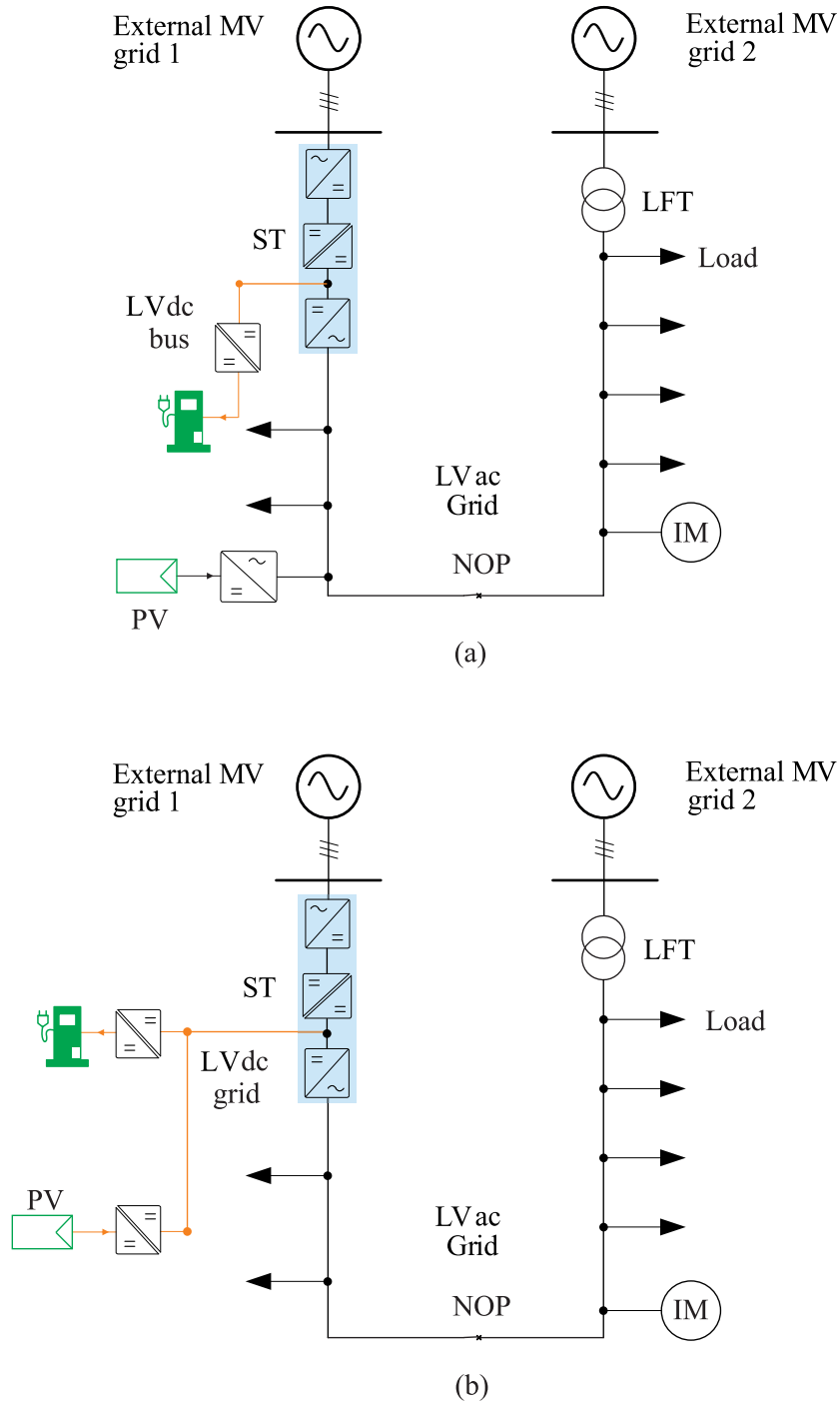


Fig. 5.2: Solutions for ST based meshed grid: (a) Solution with LVdc bus. (b) Solution with LVdc grid.

LV feeder. Consequently, the ST can regulate this feeder to be synchronized to the right side feeder supplied by MV grid 2, enabling the NOP to be switched on smoothly during regular operation [117].

Fig. 5.2 (a) shows the solution that ST provides the dc bus. The charging facility, which used to be connected to the ac grid via an ac/dc converter, is connected to this dc bus via a dc/dc converter. However, the PV unit, which is not directly connected to the LV busbar of ST, is still connected to the LVac grid via an ac/dc converter. When the dc bus of ST is expanded to some dc buses and eventually a dc grid, the PV unit can be connected directly to the dc grid as well, as shown in Fig. 5.2 (b).

The voltage control approach introduced in Chapter 4 exploits ST's capability, to which the grid-forming strategy is applied. In the meshed grid operation, however, the ST is operated with the grid-following strategy. With this strategy, the ST does not form the grid voltage in terms of waveforms, amplitude, and frequency. Instead, the ST implements all control actions by adjusting the injection of active and reactive power. The frequency is determined by the MV grid, which connects to the meshed grid via the LFT. For the meshed grid operation, the ST is the single control point.

5.2 Operation Scheme of Smart Transformer based Meshed Grid

As mentioned before, the meshed grid can achieve a balanced power supply through different MV grids, avoiding the overload of essential components. Furthermore, other operation aspects, such as minimization of the losses or minimization of the voltage deviation, can be achieved by adjusting the ST's power injection. However, improving the performance of one operation aspect commonly introduces degradation of performance of some other aspects. In order to maintain acceptable performance in all essential aspects, the operation schemes are required to take into account various aspects simultaneously, which the approaches with a single objective operation cannot fulfill this requirement.

The multi-objective optimization based scheme is developed to formulate the operation scheme, which overcomes the deficiency of those single-objective approaches. In this chapter, the operation scheme considers the power supply unbalance, the losses, and the voltage deviations. The operation scheme can be formulated as:

$$\min(f_{UB}, f_{losses}, f_{\Delta V}) \quad (5.1)$$

where f_{UB} , f_{losses} , and $f_{\Delta V}$ represent the objective of power supply unbalance, losses, and mean voltage deviations, respectively. It is noted that all objective functions are optimized with the minimization approach. The optimization is implemented by adjusting the ST's active/reactive power injection to the meshed grid. As the premise to implement the proposed

operation approach, the ST should gain a global view of the entire grid, which is achieved by employing measurements from the smart meters deployed in the grid.

A detailed introduction of every objective is given as followed.

- Objective of power supply unbalance:

This objective represents the extent of power supply difference from different MV grids by evaluating the active/reactive power supply from the external MV grids via the ST and the LFT. Its function can be represented as:

$$f_{UB} = \frac{|P_{ST}(t) - (P_{LFT}(t) + j \cdot Q_{LFT}(t))|}{|P_{ST}(t) + (P_{LFT}(t) + j \cdot Q_{LFT}(t))|} \cdot 100\% \quad (5.2)$$

where $P_{ST}(t)$ is the active power supply via the ST (noting the ST does not require reactive power from its connected external MV grid), $P_{LFT}(t)$ and $Q_{LFT}(t)$ are the active and reactive power supply via the LFT. The power is the time-variant variable.

- Objective of losses:

This objective represents the extent of losses of the entire meshed grid, i.e., the power consumption of the branches such as lines. The objective function can be represented as:

$$f_{losses} = \frac{\sum_{l=1}^r |P_{loss,l}(t)|}{P_{ST}(t) + P_{LFT}(t) + P_{DG}(t)} \cdot 100\% \quad (5.3)$$

where r is the number of branches of the grid, and $P_{DG}(t)$ is the DG generation in the meshed grid. $P_{loss,l}(t)$ are the power consumption over the branch l , which can be computed according to:

$$P_{loss,l}(t) = R_{kj} \cdot \frac{P_{kj}^2(t) + Q_{kj}^2(t)}{V_k^2(t)} \quad (5.4)$$

R_{kj} is the resistance of the branch between the buses k and j .

The corresponding $P_{kj}(t)$ and $Q_{kj}(t)$ can be derived as

$$\begin{aligned} P_{kj}(t) &= V_k^2(t)G_{kj} + V_k(t)V_j(t)[G_{kj}\cos(\delta_k(t) - \delta_j(t)) + B_{kj}\sin(\delta_k(t) - \delta_j(t))] \\ Q_{kj}(t) &= -V_k^2(t)B_{kj} + V_k(t)V_j(t)[G_{kj}\sin(\delta_k(t) - \delta_j(t)) - B_{kj}\cos(\delta_k(t) - \delta_j(t))] \end{aligned} \quad (5.5)$$

where k and j are the bus number, $P_{kj}(t)$ and $Q_{kj}(t)$ are the active and reactive power via branch between buses k and j ; $\delta(t)$ is the bus angle; G_{kj} and B_{kj} are the conductance and susceptance of the admittance matrix Y_{kj} between the buses k and j .

- Objective of voltage deviations:

This objective represents the extent of voltage deviations, which evaluates the deviations of all buses' voltage in the meshed grid. The objective function can be represented as:

$$f_{\Delta V} = \frac{\sum_{k=1}^N |(V_k(t) - V_k^*)|}{N \cdot (V_k^*)} \cdot 100\% \quad (5.6)$$

where $V_k(t)$ is the voltage of bus k and V_k^* is the corresponding reference, N is the number of buses in the grid. The voltage is a time-variant variable.

5.2.1 Operation constraints

All objective functions are computed with equality and inequality constraints, ensuring the meshed grid's safe and reliable operation. The constraints are listed as following:

- Power flow constraint:

Power flow between different buses must respect the correlations between voltage amplitudes/angles and branches' impedance.

$$\begin{aligned} -P_{\text{load}k}(t) &= V_k(t) \sum_{j=1}^N V_j(t) [G_{kj} \cos(\delta_k(t) - \delta_j(t)) + B_{kj} \sin(\delta_k(t) - \delta_j(t))] \\ -Q_{\text{load}k}(t) &= V_k(t) \sum_{j=1}^N V_j(t) [G_{kj} \sin(\delta_k(t) - \delta_j(t)) - B_{kj} \cos(\delta_k(t) - \delta_j(t))] \end{aligned} \quad (5.7)$$

where k and j are the bus number, $P_{\text{load}k}(t)$ and $Q_{\text{load}k}(t)$ are the active and reactive power at the bus k .

- Power rating constraint of ST:

The capability of active/reactive power injection of the ST must respect the ST's power rating.

$$P_{\text{ST}}^2(t) + Q_{\text{ST}}^2(t) \leq S_{\text{ST}}^2 \quad (5.8)$$

where $P_{\text{ST}}(t)$ and $Q_{\text{ST}}(t)$ are the active/reactive power injection from the ST, and S_{ST} is the power rating. It is noted that $P_{\text{ST}}(t)$ and $Q_{\text{ST}}(t)$ are time-variants. The power rating of the ST is considered constant in steady operation.

- Voltage constraint:

The voltage of each bus must lie within the voltage limits, which the system operator defines.

$$V_{\min} \leq V_k(t) \leq V_{\max} \quad k = 1 \dots N \quad (5.9)$$

where V_{\min} and V_{\max} are the under-/over-voltage limits.

- Power factor constraint:

Since the ST decouples the reactive power from the MV and LV grids, the MV grid connected to the ST supplies only active power to the meshed grid. The power factor of the power supply via the LFT in the meshed grid should be regulated as:

$$\lambda_{\min} \leq \lambda_{\text{LFT}}(t) \quad (5.10)$$

where λ_{\min} is the minimum limit of power factor, $\lambda_{\text{LFT}}(t)$ represents the power factor of power flow via the LFT.

- Reversed power flow constraint:

In this chapter, DGs' generation is not sufficient to cover the entire meshed grid's power demand. As a consequence, the reversed power flow of the ST and LFT should be avoided:

$$\begin{aligned} P_{\text{ST}}(t) &\geq 0 \\ P_{\text{LFT}}(t) &\geq 0 \end{aligned} \quad (5.11)$$

5.2.2 Derivation of solutions for multi-objective operation scheme

In deciding on the solutions of the multi-objective operation scheme, different objective functions might be in conflict, interdependent, or independent of each other. It is, in most cases, not possible to find a solution satisfying all objectives at once. A set of optimal solutions are mathematically equally good, i.e., the solutions cannot be mathematically preferred against each other, and a trade-off should be made for the selection.

There are some approaches to compute the solutions of multi-objective optimization. One conventional approach is the weighted sum approach, which converts the multi-objective optimization problems into a single objective one by defining a weight for every single objective. It can be represented for the example of minimization as:

$$\min \left\{ \alpha_1 f_1 + \alpha_2 f_2 + \dots + \alpha_M f_M \right\} \quad (5.12)$$

where α_1 to α_M are the weights of the corresponding objective functions. The weights must fulfill the requirements:

$$\alpha_1 + \alpha_2 + \dots + \alpha_M = 1 \quad (5.13)$$

$$\alpha_1 \geq 0 \quad \alpha_2 \geq 0 \quad \dots \quad \alpha_M \geq 0 \quad (5.14)$$

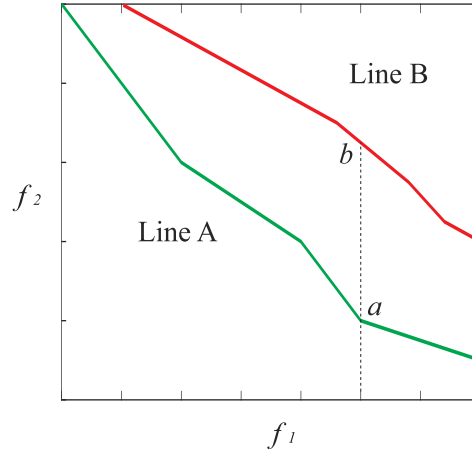


Fig. 5.3: Classification of dominated and non-dominated solutions.

However, this approach is not always applicable, especially in the following situations [119]:

- The objectives are mostly irrelevant, such as voltage deviation and power supply balance.
- The selection of weight coefficients depends highly on the system operators' preference, making it difficult to determine a group of weight coefficients with generality for all operators.

In order to overcome the shortcomings of the weighted sum approach, the Pareto optimality method is applied in this chapter. This method identifies a set of so-called non-dominated solutions, which means every objective's performance cannot be improved without degrading the performance of at least one of the other objectives. As shown in Fig. 5.3, the Line A (green) and Line B (red) are two sets of the solutions of a multi-objective optimization $\min(f_1, f_2)$. Along Line B, the f_2 value of solution b can be further minimized to solution a in Line A without increasing the f_1 value. The solution b is defined as being dominated by solution a . If it is not possible to find any solution dominating a , i.e., reducing the value f_2 of a always causes that the f_1 value will increase, solution a is considered as a non-dominated solution. The set of all non-dominated solutions is the Pareto optimality set. Line A represents the Pareto optimality set of $\min(f_1, f_2)$, it is observed that decreasing the f_2 value introduces always increasing the f_1 value.

The development of algorithms to compute the Pareto optimality set is out of the scope of this thesis. This chapter applies the algorithm explained in [119, 120]. The computed Pareto optimality set of the meshed grid's multi-objective operation scheme offers a group of non-dominated solutions with generality to the system operators, which the operators can select the solutions based on their preferences.

Table 5.1: NOP positions and dc connections of case study

Case	NOP position	DC connection
O	-	-
1	Buses E-K	One LVdc bus of ST
2	Buses F-K	One LVdc bus of ST
3	Buses E-K	One LVdc grid

5.3 Testing Grid and Scenarios for Case Study

5.3.1 Topology of testing grid

To evaluate the performance of the proposed operation scheme for the meshed grid, an LV grid model is developed, following the indication of a UK distribution system operator. The evaluation is implemented with the base voltage of 0.4 kV and the base power of 1 MVA.

The topology of the grid under analysis is shown in Fig. 5.4. Two external MV grids supply the LV feeders. The voltage of both MV grids is fixed with the value of 1 pu. In Case O, the LV feeders are operated separately without any NOP, as shown in Fig. 5.4 (a). In the left LV feeder, a charging facility is connected directly to the transformer's LV busbar. At bus F, there is a PV unit as DG. Buses B-E connect with the aggregated load. In the right LV feeder, the aggregated loads are connected to the buses H-K. Case O is a conventional case used as the benchmark to compare with the meshed grid operation. In Case 1, the meshed grid is modeled with an ST replacing the LFT1, and a NOP is installed between the buses E and K, as shown in Fig. 5.4 (b). The impedance of the line E-K is $0.0107 + j0.0032\Omega$. In Case 2, the NOP is installed between the buses F and K, and the line F-K has the same impedance as Case 1, as shown in Fig. 5.4 (c). In Case 3, buses E and K are connected as in Case 1. Unlike Case 1, the dc grid is considered in Case 3 instead of only the dc bus in Case 1, as shown in Fig. 5.4 (d). As a consequence, the PV unit is directly connected to the LVdc grid. The details of the case conditions are summarized in Table 5.1.

5.3.2 Testing scenarios

There are two testing scenarios, which are considered as the "typical cases", to be analyzed in the case study: the heavy load demand scenario and the peak DG generation scenario.

- Scenario 1: Heavy load demand scenario

In this scenario, the aggregated loads from bus B to bus E have the identical power demand of $0.10 + j0.02$ pu, and the aggregated loads from bus H to bus K have the

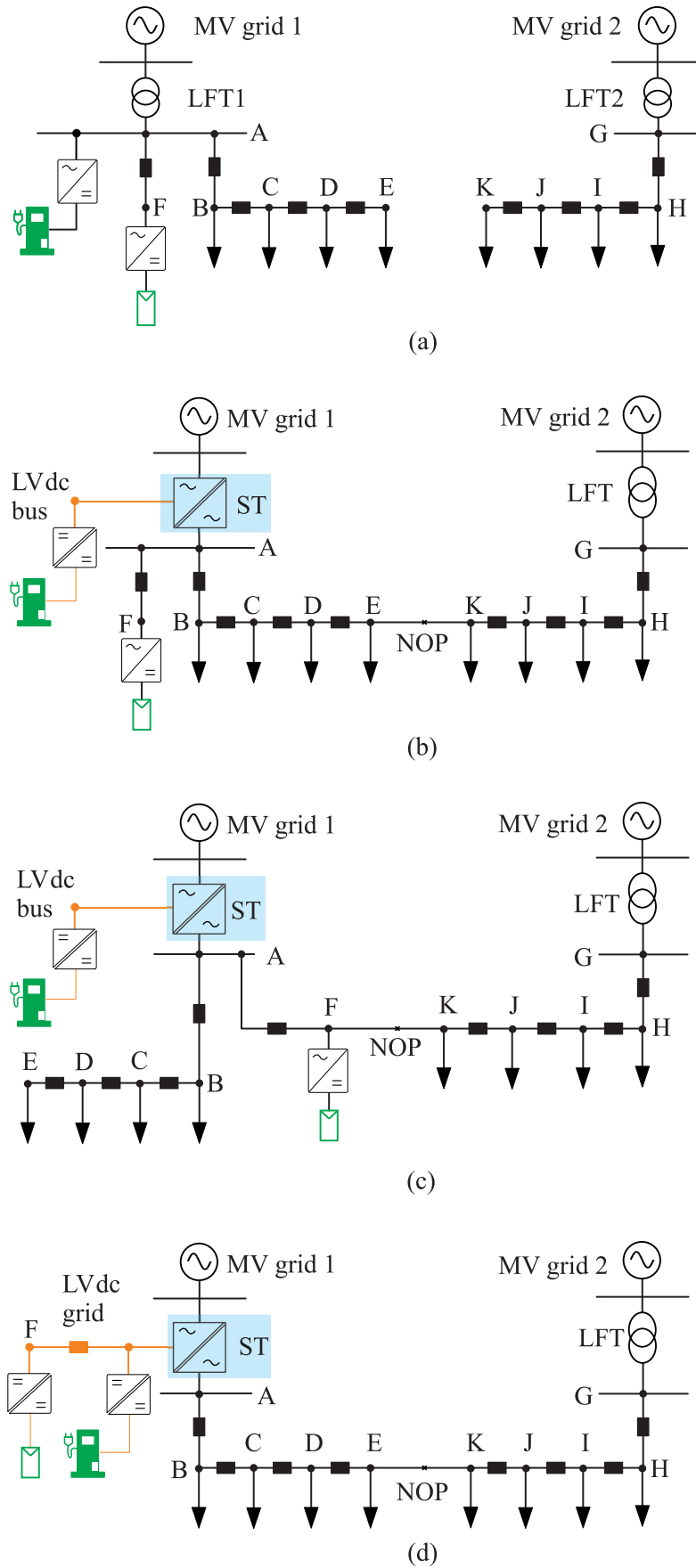


Fig. 5.4: LV grid under test. (a) Conventional operation of parallel feeders. (b) ST-based operation of the meshed grid with LVdc bus, topology 1. (c) ST-based operation of the meshed grid with LVdc bus, topology 2. (d) ST-based operation of the meshed grid with LVdc grid, topology 3.

identical power demand of $0.20 + j0.04$ pu. The charging facility has the power demand of 0.25 pu. This scenario corresponds to an evening peak demand condition, which can introduce the violation of the under-voltage constraint. The PV has no generation.

- Scenario 2: Peak DG generation scenario

In this scenario, the aggregated loads from bus B to bus E have the power demand of $0.05 + j0.01$ pu, and the aggregated loads from bus H to bus K have the power demand of $0.10 + j0.02$ pu. The charging power demand is 0.12 pu. This scenario corresponds to a condition with a peak generation of DG. The output of DG reaches its peak capacity, which is 0.30 pu. This scenario can introduce the violation of the over-voltage constraint.

5.3.3 Indices of performance evaluation and values of constraints

This chapter evaluates four aspects of the grid operation: power supply unbalance, power factor, losses, and voltage deviation. Each aspect is represented by an index to quantify the performance.

Index IDX_{UB} evaluates the level of power supply unbalance, which can be represented as:

$$IDX_{UB} = \frac{|(P_L(t) + j \cdot Q_L(t)) - (P_R(t) + j \cdot Q_R(t))|}{|(P_L(t) + j \cdot Q_L(t)) + (P_R(t) + j \cdot Q_R(t))|} \cdot 100\% \quad (5.15)$$

where $(P_L(t) + j \cdot Q_L(t))$ is the power flow of the MV grid 1 on the left side via the LFT/ST in Fig. 5.4 and $(P_R(t) + j \cdot Q_R(t))$ is the power flow of the MV grid 2 on the right side.

The power factors of the power flow via ST and LFT are evaluated. Only active power is exchanged between the ST and its connected MV grid in this chapter, making a constant unity power factor. Therefore, this chapter focuses on the power factor of power flow via LFT. Index IDX_λ is used to evaluate the performance:

$$IDX_\lambda = (1 - \lambda_{LFT}(t)) \cdot 100\% \quad (5.16)$$

Index IDX_{losses} evaluates the losses in percentage, which can be represented as:

$$IDX_{losses} = \frac{\sum_{l=1}^r |P_{loss,l}(t)|}{P_L(t) + P_R(t) + P_{DG}(t)} \cdot 100\% \quad (5.17)$$

Index $IDX_{\Delta V}$ evaluates the performance of voltage deviation, which is the mean voltage

deviation with respect to the nominal value, i.e., 1 pu:

$$IDX_{\Delta V} = \frac{\sum_{k=1}^N |(V_k(t) - V_k^*)|}{N \cdot (V_k^*)} \cdot 100\% \quad (5.18)$$

It is noted that all indices are represented in percentage, and a smaller value of every index implies a better performance in the corresponding aspect.

Besides the indices mentioned above, the maximal voltage deviation is also evaluated, which is defined as:

$$\Delta V_{\max} = \max(|(V_k(t) - V_k^*)| \cdot 100\% \quad k = 1 \dots N) \quad (5.19)$$

The operation constraints of ST power rating, voltage, and power factor are defined as:

$$\begin{aligned} S_{ST} &= 0.9 \text{ pu} \\ V_{\max} &= 1.1 \text{ pu} \\ V_{\min} &= 0.9 \text{ pu} \\ \lambda_{\min} &= 0.9 \end{aligned} \quad (5.20)$$

5.4 Performance Analysis of Multi-Objective Operation Scheme

5.4.1 Case O: conventional operation of parallel feeders

In Case O, the conventional operation for parallel LV feeders is evaluated. This case is used as a benchmark case to compare the performance of the meshed grid operation.

Scenario 1

Table 5.2 lists the indices of power supply unbalance, losses, and mean voltage deviation, as well as the maximal voltage deviation. The power flow via the left side LFT1 is $0.666 + j0.105$ pu (power factor 0.988), and the power flow via the right side LFT2 is $0.884 + j0.225$ pu (power factor 0.961). Consequently, the value of $IDX_{UB}\%$ is 15.7 %, the losses are 6.5 %, and the mean voltage deviation is 6.2 %, respectively. The maximal voltage deviation is 14.2 %, which violates the under-voltage constraint.

Scenario 2

Indices of this scenario are also listed in Table 5.2. The power flow via the LFT1 of the left side is $0.060 + j0.051$ pu (power factor 0.762, which violates the operation constraint), and the power flow via the LFT2 is $0.418 + j0.094$ pu (power factor 0.976). As a consequence,

Table 5.2: Performance indices of Case O

Scenario 1			
IDX_{UB} (%)	IDX_{losses} (%)	$IDX_{\Delta V}$ (%)	ΔV_{max} (%)
15.7	6.5	6.2	14.2
Scenario 2			
IDX_{UB} (%)	IDX_{losses} (%)	$IDX_{\Delta V}$ (%)	ΔV_{max} (%)
72.2	7.5	3.9	13.3

the power unbalanced index IDX_{UB} % is 72.2 %, the losses are 7.5 %, and the mean voltage deviation is 3.9 %, respectively. The maximal voltage deviation is 13.3 %, which violates the over-voltage constraint.

5.4.2 Case 1: Meshed grid topology 1

In this case, the NOP lies between bus E and bus K. With this topology, all power generation from DG (bus F) must be delivered first to the LV busbar of ST, i.e., bus A.

Scenario 1

Fig. 5.5 shows the Pareto optimality set derived from the proposed operation scheme. The two axes in the figure represent the indices of IDX_{UB} (power supply unbalance) and IDX_{losses} (losses in percentage). Fig. 5.5 (a) shows $IDX_{\Delta V}$ (mean voltage deviation) in colors. Fig. 5.5 (b) shows IDX_{λ} (power factor) in colors.

All solutions of the Pareto optimality set reach a reduced power supply unbalance than Scenario 1 in Case O (15.7 %), and a decreased mean voltage deviation as well (which is 6.2 % in Case O). Approximately 21 % of the solutions has the losses which are reduced respecting Case O (6.5 %).

Solution **a** in Fig. 5.5 reaches the lowest power supply unbalance (0), solution **b** reaches the smallest value of voltage deviation $IDX_{\Delta V}$ (3.9 %), and solution **c** reaches the lowest losses (5.7 %). The highest power supply unbalance (14.2 %) arises with solution **c**. Moreover, this solution reaches the largest value of $IDX_{\Delta V}$ (5.1 %). Solution **b** reaches the highest losses (9.7 %). The largest value of IDX_{λ} is about 2.5 %, which implies the minimal power factor of all solutions are around 0.975. All solutions are non-dominated. The grid operators can select the solutions depicted in the Pareto optimality set according to their preferences.

The correlation analysis shows that if one aspect's performance varies, what performance of other operation aspects can be expected. It helps the system operators understand the grid behavior and select the solutions. For instance, the evolution of colors in Fig. 5.5 depicts

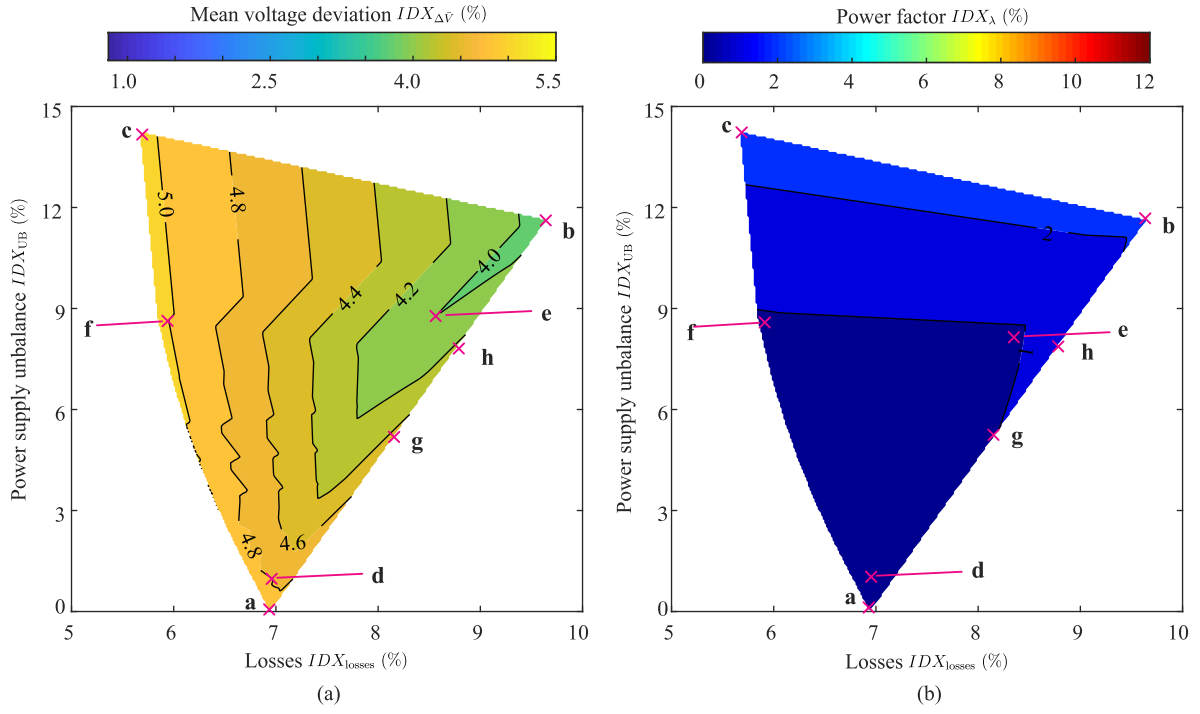


Fig. 5.5: Solutions of Pareto optimality set of proposed multi-objective operation scheme, Scenario 1 of Case 1. (a) Mean voltage deviation vs. power supply unbalance and losses. (b) Power factor vs. power supply unbalance and losses.

that with a decreased power supply unbalance, the value of IDX_{λ} becomes smaller until reaching the value of 0 (i.e., unity power factor) at solution **a**. The reason is that MV grid 1 does not supply any reactive power. Therefore, to reduce the power supply difference between MV grids 1 and 2, the reactive power flow of MV grid 2 must be reduced to a maximal extent. The frontier **a-g-h-b** is projected to the surface of power supply unbalance vs. mean voltage deviation and the surface of losses vs. mean voltage deviation, respectively, as shown in Fig. 5.6. It is noted that line a_1 - b_1 can be divided into three approximately linear segments. The slope of segment a_1 - g_1 is larger than it of g_1 - h_1 , implying that when the power supply unbalance varies the same amount, the voltage deviation changes more significantly within a_1 - g_1 than it within g_1 - h_1 . In other words, the voltage deviation is more sensitive to power supply unbalance variation within a_1 - g_1 . The slope of h_1 - b_1 is smaller than the other two segments, implying the voltage deviation in this segment is less sensitive to the power supply unbalance variation than the other two segments. However, it also means the

Table 5.3: Indices of solutions **d-f** on the Pareto optimality set in Fig. 5.5

Solution	IDX_{UB} (%)	IDX_{λ} (%)	IDX_{losses} (%)	$IDX_{\Delta V}$ (%)
d	0.8	0.1	7.0	4.8
e	8.2	0.8	8.3	4.0
f	8.6	0.8	5.9	5.0

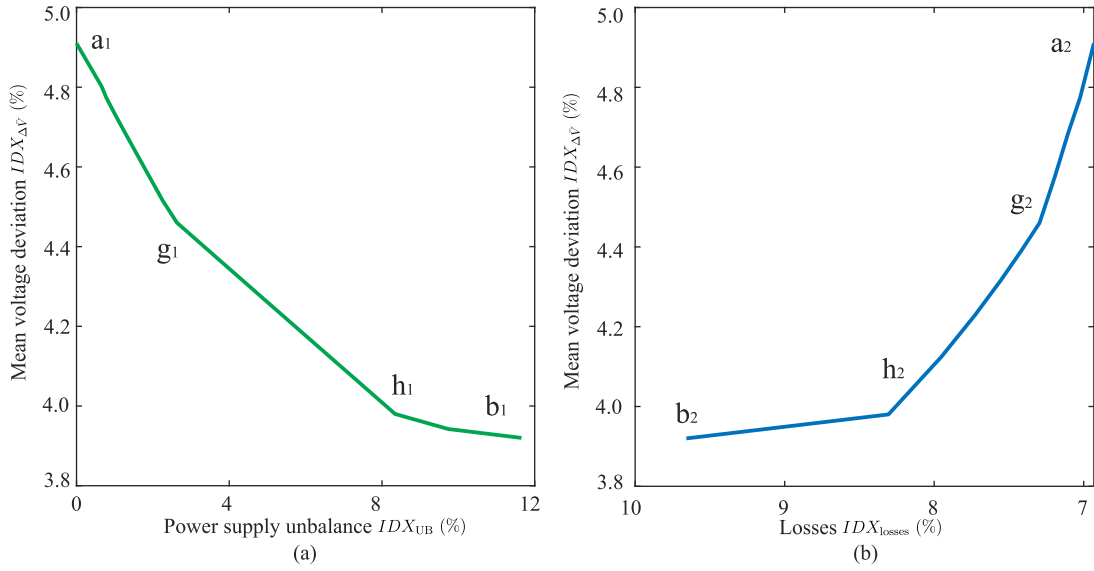


Fig. 5.6: Projection of frontiers **a-g-h-b** in Fig. 5.5. (a) Projection on the surface of power supply unbalance vs. mean voltage deviation. (b) Projection on the surface of losses vs. mean voltage deviation.

power supply unbalance more sensitive to voltage deviation variation. Line **a**₂-**b**₂ can also be divided into three approximately linear segments. The voltage deviation is more sensitive to losses variation in **a**₂-**g**₂ than it in other two segments, similar to line **a**₁-**b**₁.

Tradeoff between solutions can be observed in Fig. 5.5. For instance, to maintain the voltage deviation $IDX_{\Delta\bar{V}}$ smaller than 4 %, the losses larger than 8 % are expected, such as solution **e** in Table 5.3. Moreover, to get one solution of lower losses, for instance, solution **f**, a larger $IDX_{\Delta\bar{V}}$ and a higher power supply unbalance can be expected. The indices of solutions **d**, **e**, and **f** are listed in Table 5.3.

Solutions **d**, **e**, and **f** are compared in Fig. 5.7. In this figure, it is observed that solution **d** reaches the smallest indices of IDX_{UB} and IDX_{λ} . However, its $IDX_{\Delta\bar{V}}$ is larger than solution **e**, and its IDX_{losses} is larger than solution **f**, respectively. Solutions **e** and **f** have the smallest index of $IDX_{\Delta\bar{V}}$ and IDX_{losses} , respectively. Meanwhile, solution **e** has the largest IDX_{losses} and solution **f** has the largest IDX_{UB} and $IDX_{\Delta\bar{V}}$. Since the aspects such as power factor or voltage deviation are irrelevant, it is impossible to identify one solution that can be mathematically preferred. In order to provide the solutions with generality, the Pareto optimality method is required.

Table 5.4 lists values of the indices IDX_{losses} and $IDX_{\Delta\bar{V}}$, values of the power supply from MV grids, and values of the ST reactive power injection, for solutions **b** and **c**. The active power supply from MV grid 1 has no essential difference between solutions **b** and **c**. However, it is noted that the ST injects 0.482 pu reactive power into the meshed grid with solution **b**. As a consequence, the smallest $IDX_{\Delta\bar{V}}$ is achieved, and the meshed grid can support reactive power of 0.161 pu to MV grid 2. In the meantime, the ST's reactive power injection increases the current in the meshed grid, which eventually increases the losses. As a consequence, MV

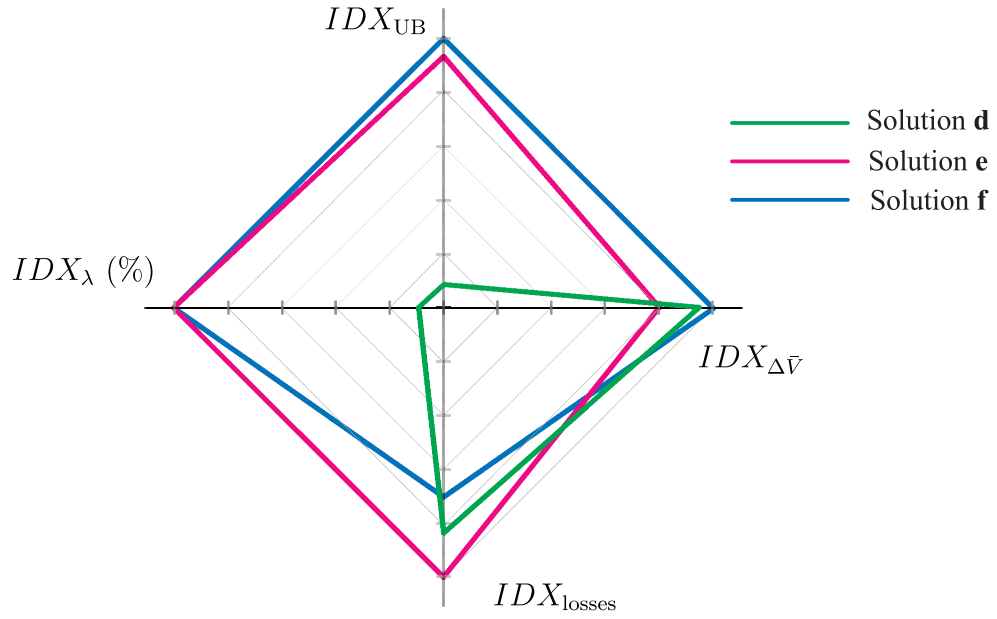


Fig. 5.7: Comparison of performance indices of solutions **d-f** in Fig. 5.5.

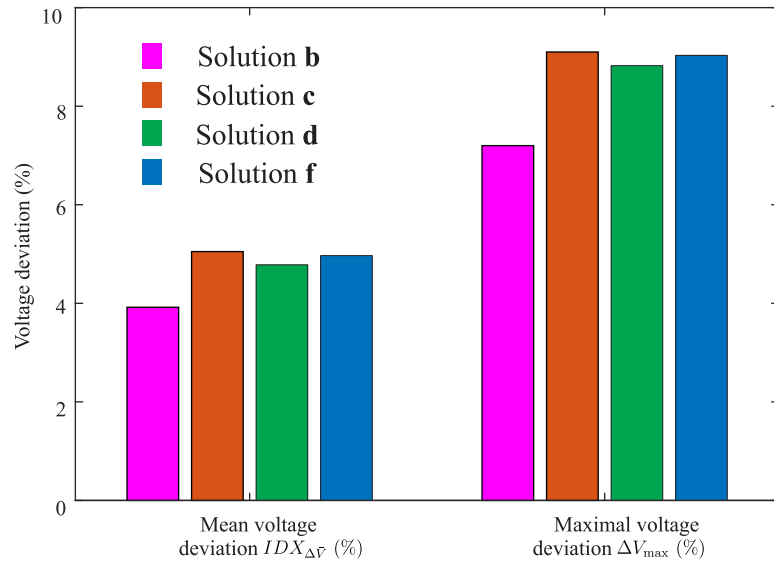


Fig. 5.8: Comparison of mean and maximal voltage deviations of solutions **b, c, d, and f** in Fig. 5.5.

Table 5.4: Indices IDX_{losses} and $IDX_{\Delta\bar{V}}$, power supply of both MV grids, and ST reactive power injection of solutions **b** and **c** in Fig. 5.5

Solution	IDX_{losses} (%)	$IDX_{\Delta\bar{V}}$ (%)	Power of MV grid 1 (pu)	Power of MV grid 2 (pu)	ST reactive power (pu)
b	9.7	3.9	0.851	0.754-j0.161	0.482
c	5.7	5.1	0.847	0.690+j0.155	0.139

grid 2 with solution **b** needs to supply active power of 0.754 pu to the meshed grid, which is 9 % higher than the active power from MV grid 2 with solution **c**. Among all solutions in the Pareto optimality set, the ST reactive power injection with solution **c** reaches the lowest one, and the highest ST reactive power injection arises with solution **b**.

Fig. 5.8 shows the mean and maximal voltage deviations of solutions **b**, **c**, **d**, and **f**. Both deviations correlate, i.e., a smaller mean voltage deviation corresponds to a smaller maximal voltage deviation.

Scenario 2

Fig. 5.9 shows the Pareto optimality set derived from the proposed operation scheme. The two axes in the figure represent the indices of IDX_{UB} (power supply unbalance) and IDX_{losses} (losses in percentage). Fig. 5.9 (a) shows $IDX_{\Delta\bar{V}}$ (mean voltage deviation) in colors. Fig. 5.9 (b) shows IDX_{λ} (power factor) in colors.

The solutions in which the power supply unbalance lower than Scenario 2 in Case O (72.2 %) take approximately 11 % of all solutions in the Pareto optimality set. All solutions have the increased losses and voltage deviation respecting Case O (IDX_{losses} 7.5 % and $IDX_{\Delta\bar{V}}$ 3.9 %). Nevertheless, it is noted that the violation of over-voltage constraint is mitigated in Case 1, and the power factor is maintained above 0.9.

Solution **a** in Fig. 5.9 has the lowest power supply unbalance, which is 65.6 %, solution **b** has the smallest value of mean voltage deviation $IDX_{\Delta\bar{V}}$ (5.1 %), and solution **c** has lowest losses (7.8 %). With the previous scenario, the index of IDX_{λ} decreases with a decreased power supply unbalance. However, with this scenario, the index of IDX_{λ} increases with a decreased power supply unbalance. The index IDX_{λ} reaches 10.0 % with solution **a** (i.e. power factor 0.900). This solution also has the largest value of $IDX_{\Delta\bar{V}}$, which is more than 5.4 %. With a decreased mean voltage deviation, the power supply unbalance is expected to be increased for all solutions until reaching the maximal unbalance at solution **b** (100 %). Similar to Scenario 1, solution **b** with the lowest voltage deviation has but the highest losses (10.1 %).

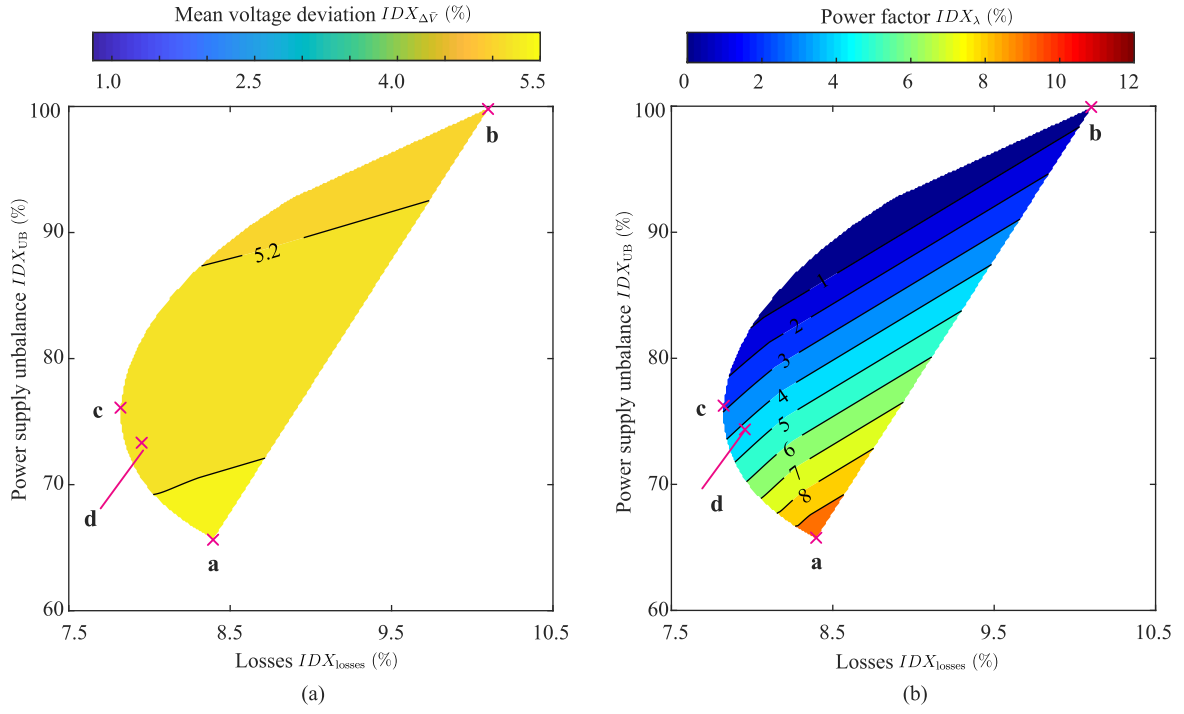


Fig. 5.9: Solutions of Pareto optimality set of proposed multi-objective operation scheme, Scenario 2 of Case 1. (a) Mean voltage deviation vs. power supply unbalance and losses. (b) Power factor vs. power supply unbalance and losses.

Table 5.5: Power supply of both MV grids and ST reactive power injection of solutions **a**, **b**, and **c** in Fig. 5.9

Solution	Power of MV grid 1 (pu)	Power of MV grid 2 (pu)	ST reactive power (pu)
a	0.100	0.386+j0.187	-0.040
b	0	0.501-j0.053	0.208
c	0.062	0.419+j0.105	0.040

Fig. 5.9 shows also the tradeoff between solutions. For instance, solutions close to **c** are expected having losses smaller than 8 %. In the meanwhile, those solutions are expected to have power supply unbalance within 70–80 % and mean voltage deviation approximately 5.3 %, such as solution **d** depicted in Fig. 5.9. The indices of solution **d** are: IDX_{UB} 73.0 %, IDX_{λ} 4.2 %, IDX_{losses} 7.9 %, and $IDX_{\Delta V}$ 5.3 %.

Fig. 5.10 (a) shows the mean and maximal voltage deviations of Case O and solutions **a**, **b**, **c**, and **d** in Case 1. The mean voltage deviation in Case O is the lowest one, but its maximal deviation is above 10 %. The mean voltage deviations of the solutions **a-d** are close to each other, and the maximal voltage deviations of all solutions are identical as 0.10 pu, which is the voltage deviation of bus F caused by the power injection of DG. Fig. 5.10 (b) shows the voltage profiles of buses A-E and buses G-K of Case O (bus E and K of Case O is not connected), and the profiles of the same buses of solutions **a** and **b**. The three voltage

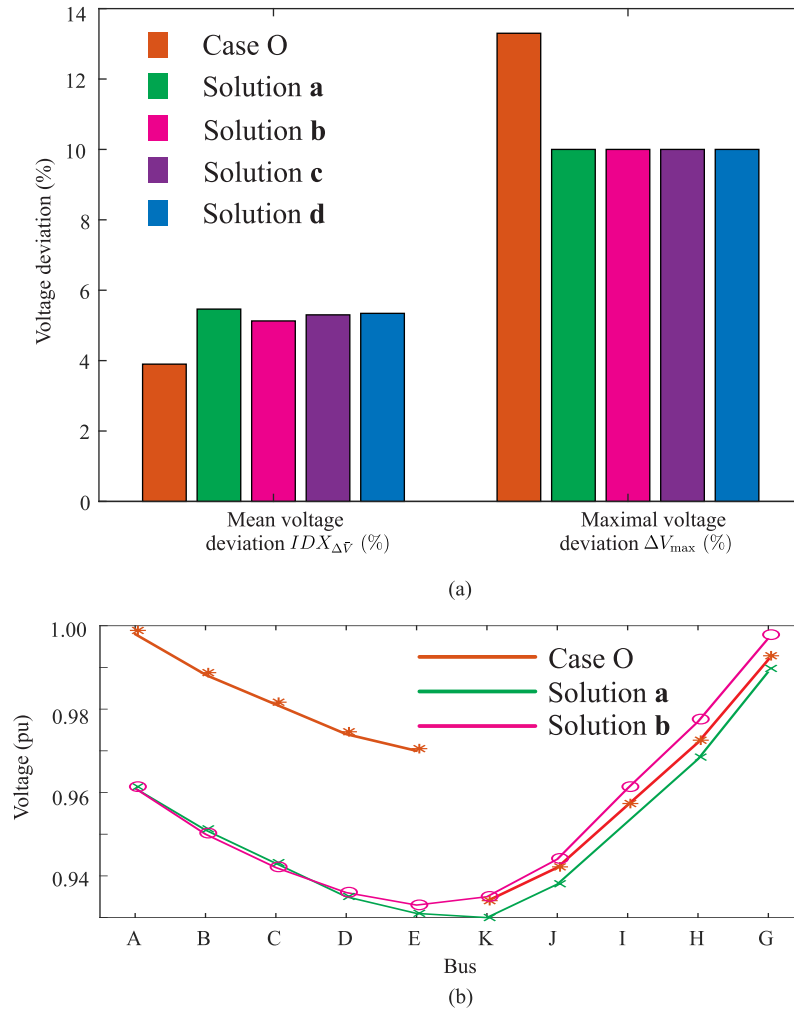


Fig. 5.10: Voltage behaviors of Scenario 2, Case O and Case 1. (a) Comparison of mean and maximal voltage deviations of Case O and solutions **a**, **b**, **c**, and **d** in Case 1. (b) Voltage profiles of Case O, solutions **a** and **b** in Case 1.

profiles of buses G-K have no significant difference. Reducing the voltage of bus A is the only method to mitigate the violation of over-voltage constraint at bus F in this ST based meshed grid. Consequently, the ST consumes reactive power with solution **a**, as listed in Table 5.5. MV grid 1 does not supply active power, and the ST injects a considerable amount of reactive power, making MV grid 2 consume reactive power with solution **b**. As a result, voltage amplitudes of bus A of solutions **a** and **b** are approximately 0.04 pu lower than it of Case O. Even with solution **c**, the usage of ST is low, as listed in Table 5.5. Among all Pareto optimality set solutions, the highest amount of ST reactive power injection arises with solution **b**, similar to Scenario 1.

Summary of Case 1

Case 1 has analyzed the meshed grid topology shown in Fig. 5.4 (b). This topology enables loads of buses A to E and H to J to be supplied by both MV grids, which can mitigate the under-voltage constraint violation. The DG power generation of bus F must be first

delivered to the LV busbar of ST, i.e., bus A. In this sense, if a violation of voltage constraint appears at bus F, the only way to mitigate the violation is to regulate bus A voltage. The performance of the proposed multi-objective operation scheme is evaluated in aspects of power supply unbalance, power factor, losses, and voltage deviation, for which the Pareto optimality method is applied to derive the solutions with generality. All solutions in the set are non-dominated so that the system operators can select the solutions according to their individual preferences.

With Scenario 1, all solutions derived from the proposed operation scheme reach a reduced power unbalance, and a reduced voltage deviation, comparing the results in Case O. 21 % of the solutions has lower losses than Case O. Furthermore, the violation of under-voltage constraint is avoided. The lowest power factor of all solutions is around 0.975. The Pareto optimality set depicted in Fig. 5.5 enables the analysis of the correlation between different aspects. For instance, with a lower power supply unbalance, a smaller value of IDX_{λ} is always expected. The sensitivity of mean voltage deviation to the variation of power supply unbalance can be observed in Fig. 5.6 (a). The Pareto optimality set shows the tradeoff between different aspects, which helps the system operators understand the grid behaviors and select the solutions.

With Scenario 2, voltage rise arises at bus F as the consequence of the DG power generation. With this topology, bus A voltage must be reduced to regulate bus F voltage, avoiding violation of the over-voltage constraint. Consequently, the controllability of the meshed grid has been restricted. However, all operation constraints such as voltage and power factor are appropriately respected with the meshed grid operation. It must point out that the meshed grid offers flexibility to grid operation, which the grid operators can not only select the preferred solutions from the Pareto optimality set but also decide the switching status of the NOP based on the grid load/DG conditions.

5.4.3 Case 2: Meshed grid topology 2

In this case, the NOP lies between bus F and bus K. With this topology, the loads of buses B-E can only be supplied via bus A (the LV busbar of the ST), but the generation of DG can directly supply loads of buses H-K without via bus A.

Scenario 1

Fig. 5.11 shows the Pareto optimality set derived from the proposed operation scheme. The two axes in the figure represent the indices of IDX_{UB} (power supply unbalance) and IDX_{losses} (losses in percentage). Fig. 5.11 (a) shows $IDX_{\Delta V}$ (mean voltage deviation) in colors. Fig. 5.11 (b) shows IDX_{λ} (power factor) in colors.

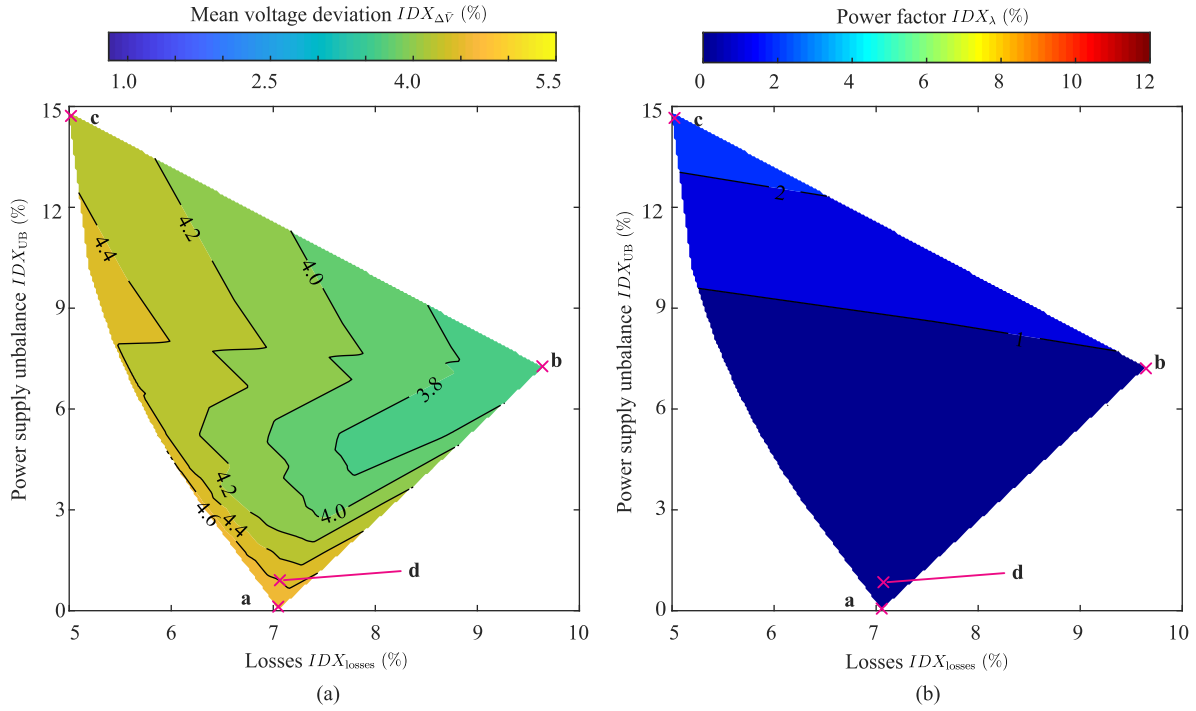


Fig. 5.11: Solutions of Pareto optimality set of proposed multi-objective operation scheme, Scenario 1 of Case 2. (a) Mean voltage deviation vs. power supply unbalance and losses. (b) Power factor vs. power supply unbalance and losses.

All solutions of the Pareto optimality set have a lower power supply unbalance than Scenario 1 in Case O (15.7 %) and a smaller value of mean voltage deviation $IDX_{\Delta V}$ than Case O (6.2 %), respectively. The solutions, which the losses are lower than Case O (6.5 %), take approximately 34 %. The percentage is higher than the value in Case 1 (21 %).

Solution **a** in Fig. 5.11 has the lowest power supply unbalance (0) but the largest value of $IDX_{\Delta V}$ (4.8 %), solution **b** has the smallest value of $IDX_{\Delta V}$ (3.6 %) but the highest losses (9.7 %), and solution **c** has the lowest losses (5.0 %) but the highest power supply unbalance (14.5 %). The largest value of IDX_{λ} arises with solution **c**, which is approximately 2.5 %, similar to Case 1. With a decreased power supply unbalance, the value of IDX_{λ} becomes smaller and smaller. The tradeoff between solutions can be observed in the figure. For

Table 5.6: Power supply of both MV grids, and ST reactive power injection of solutions **a**, **b**, **c**, and **d** in Fig. 5.11

Solution	Power of MV grid 1 (pu)	Power of MV grid 2 (pu)	ST reactive power (pu)
a	0.780	0.780	0.302
b	0.828	0.777-j0.105	0.418
c	0.846	0.680+j0.157	0.130
d	0.790	0.766+j0.002	0.299

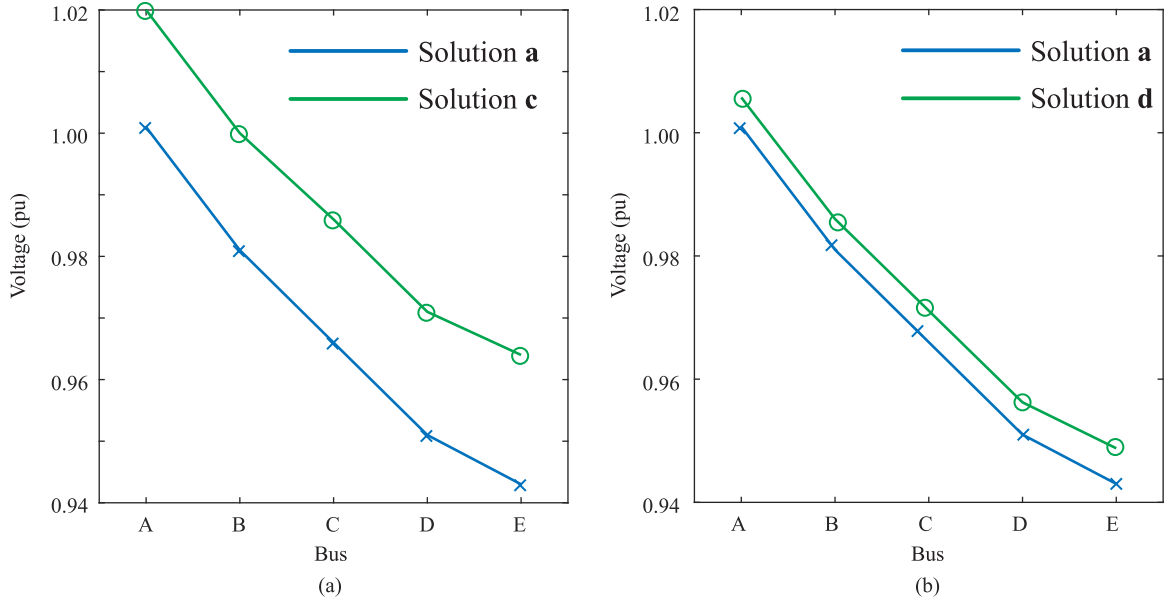


Fig. 5.12: Voltage profiles of buses A-E. (a) Voltage profiles of solutions **a** and **c**. (b) Voltage profiles of solutions **a** and **d**.

instance, in order to get one solution with the power supply unbalance smaller than 5 %, it is expected that the losses are within 6–8 % and the voltage deviation is above 4.5 %, such as solution **d** (IDX_{UB} 1.1 %, IDX_{λ} 0.0 %, IDX_{losses} 7.0 %, and $IDX_{\Delta V}$ 4.6 %).

The voltage profiles of buses A-E of solutions **a**, **c**, and **d** are depicted in Fig. 5.12. Fig. 5.12 (a) shows that the voltage profiles of solutions **a** and **c**, and Fig. 5.12 (b) shows the voltage profiles of solutions **a** and **d**. It can be noted that the bus A voltage of solutions **c** and **d** is higher than it of solution **a**. As listed in Table 5.6, the ST reactive power injection of solutions **a** and **d** has no essential difference. However, the power supply of MV grid 1 of solution **a** is 0.010 pu less than it of solution **d**, resulting in that bus A voltage of solution **a** is lower than solution **d**. The ST reactive power injection is increased by 0.172 pu from solution **c** to **a**, in which a higher bus A voltage of solution **a** is expected. However, due to the power supply from MV grid 1 of solution **a** is 0.066 pu less than it of solution **c**, eventually, the bus A voltage of solution **a** is lower than it of solution **c**. Since the meshed grid lines have a high R/X ratio, the active power is expected to more significantly impact voltage than the reactive power, which is confirmed by the voltage behavior. Among all solutions of the Pareto optimality set, the highest ST reactive power injection arises with solution **b**, but the lowest one arises with solution **c**, as listed in Table 5.6.

Scenario 2

Fig. 5.13 shows the Pareto optimality set derived from the proposed operation scheme. The two axes in the figure represent the indices of IDX_{UB} (power supply unbalance) and IDX_{losses} (losses in percentage). Fig. 5.13 (a) shows $IDX_{\Delta V}$ (mean voltage deviation) in colors. Fig. 5.13 (b) shows IDX_{λ} (power factor) in colors.

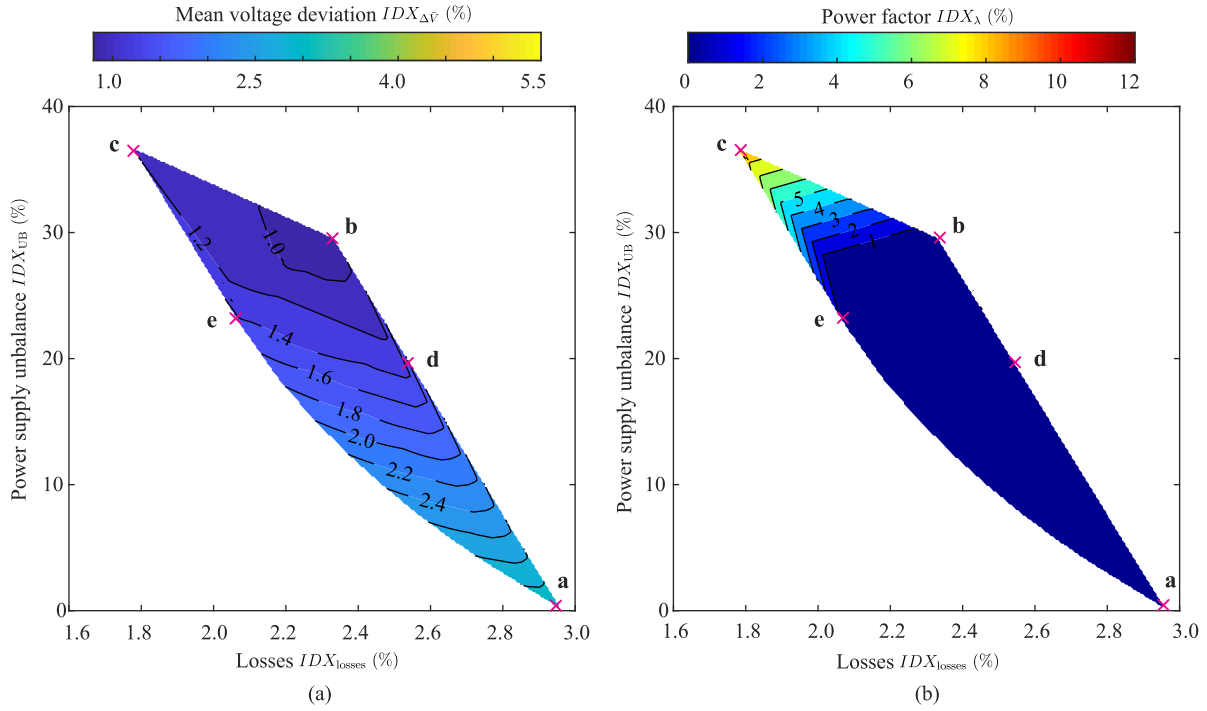


Fig. 5.13: Solutions of Pareto optimality set of proposed multi-objective operation scheme, Scenario 2 of Case 2. (a) Mean voltage deviation vs. power supply unbalance and losses. (b) Power factor vs. power supply unbalance and losses.

The power supply unbalance, losses, and mean voltage deviation of the solutions are 100 % lower than the ones in Case O, which the values in Case O are 72.2 %, 7.5 %, and 3.9 %, respectively. All violations of power factor and voltage constraint are mitigated. It is also noted that the index IDX_{λ} around solution **c** is approaching 10 %, i.e., the power factor approaching 0.90. However, the power factor lower than 0.95 takes only approximately 4 % of the solutions.

Solution **a** in Fig. 5.13 has the lowest power supply unbalance (0), solution **b** has the smallest $IDX_{\Delta V}$ (0.9 %), and solution **c** has lowest losses (1.8 %). The index of IDX_{λ} decreases together with the power supply unbalance. Solution **a** has the largest voltage deviation (3.2 %) and highest losses (3.0 %). Solution **c** has the highest power supply unbalance (37.0 %). Unlike other cases where reducing the losses can increase the voltage deviation significantly, all solutions within the area **b-c-e-d** have a similar mean voltage deviation. All solutions reach the decreased voltage deviation and losses respecting solution **a**.

Fig. 5.14 (a) and (b) show the projections of the frontiers **a-d-b** and **a-e-c**, respectively, to the same surface of power supply unbalance vs. mean voltage deviation. It is observed that IDX_{UB} increases from 0 (**a**₁ and **a**₂) to approximately 20 % (**d**₁ or **e**₂), where the slopes of line **a**₁-**d**₁ and **a**₂-**e**₂ have no clear difference. The voltage deviations of both lines reach approximately 1.3–1.4 pu at **d**₁ or **e**₂, respectively. Afterwards, the voltage deviation in **d**₁-**b**₁ is decreased below 1 % but keeping the power supply unbalance below 30 %. In segment **e**₂-**c**₂, the power supply unbalance increases to more than 35 % but keeping the voltage deviation

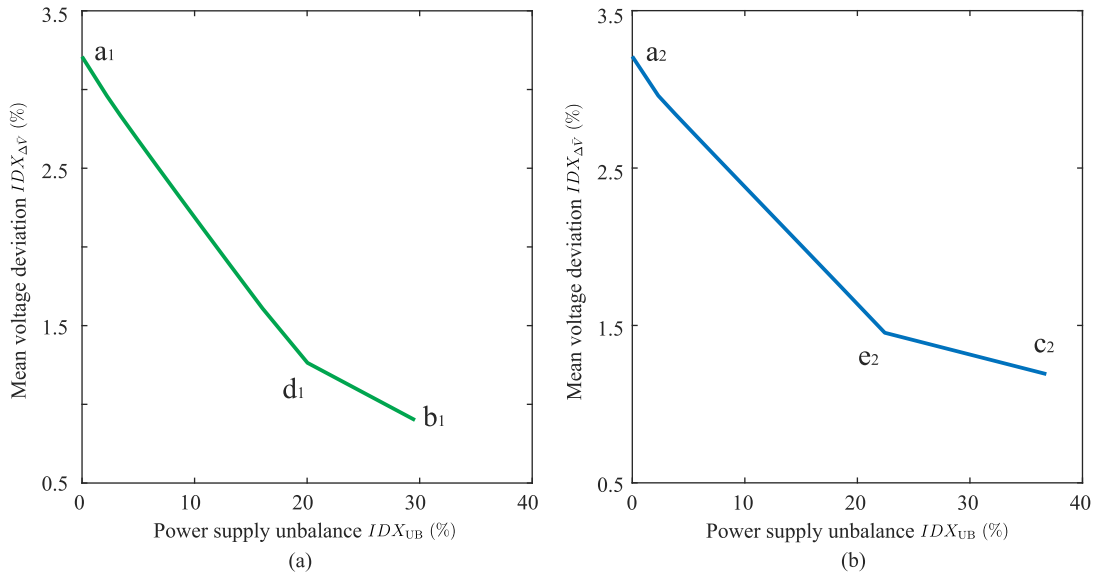


Fig. 5.14: Projection of frontiers in Fig. 5.13 to the surface of power supply unbalance vs. mean voltage deviation. (a) Projection of frontier **a-d-b**. (b) Projection of frontier **a-e-c**.

Table 5.7: Power supply of both MV grids and ST reactive power injection of solutions **a-e** in Fig. 5.13

Solution	Power of MV grid 1 (pu)	Power of MV grid 2 (pu)	ST reactive power (pu)
a	0.221	0.221	0.129
b	0.283	0.154-j0.009	0.135
c	0.290	0.143+j0.066	0.059
d	0.263	0.175-j0.013	0.140
e	0.266	0.169+j0.016	0.110

above 1 %.

Listed in Table 5.7, between solutions **b** and **d**, the ST reactive power injection has no essential difference, but power supply of MV grid 1 increases from 0.263 pu to 0.283 pu, which results in a reduced voltage deviation as shown in Fig. 5.14 (a). The power supply of MV grid 1 with solution **c** is 0.007 pu larger than it with solution **b**, as listed in Table 5.7. Meanwhile, the ST reactive power injection with solution **c** is 0.076 pu smaller than solution **b**, resulting in the voltage deviation of solution **c** is higher than solution **b**. Solution **c** also has the lowest ST reactive power injection.

Unlike the other cases, in which the solution with the lowest voltage deviation corresponds to the one with the highest losses, the highest losses appear here with solution **a**, which has the lowest power supply unbalance. Fig. 5.15 shows for solutions **a** and **b** the voltage profile of bus A via bus F and bus K to bus G and the profile of buses A-E, respectively. It can be noted that the voltage of all buses of solution **b** is higher than solution **a**. Accordingly, the

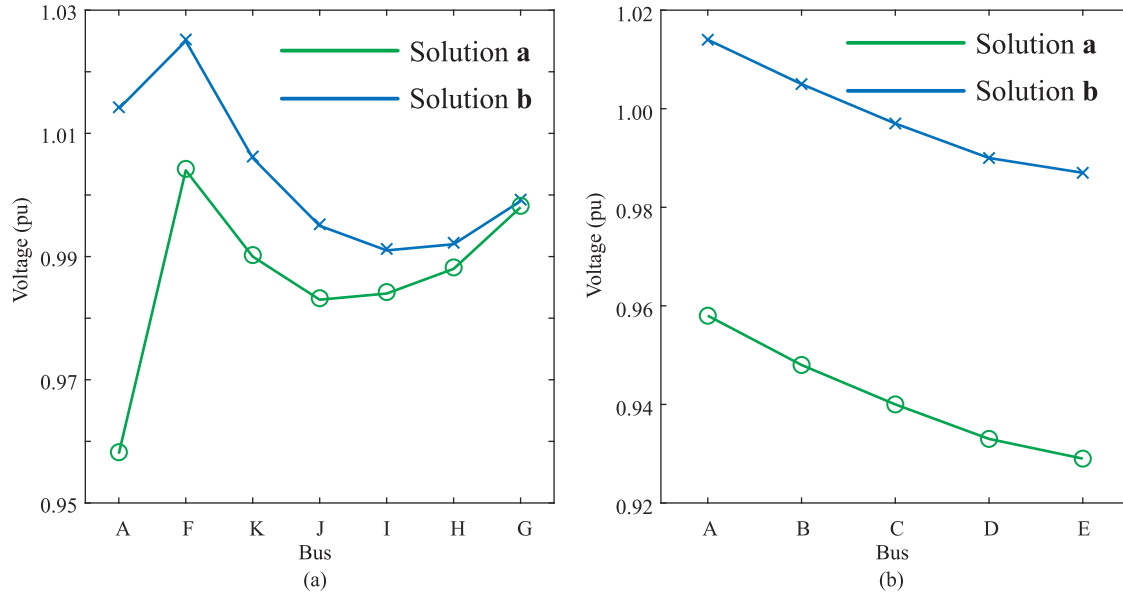


Fig. 5.15: Voltage behaviors of Scenario 2, Case 2. (a) Voltage profiles of bus A to bus G. (b) Voltage profiles of bus A to bus E.

current flow of solution **b** is smaller than solution **a** if delivering the same amount of power, which reduces the losses. For example, the losses of power flow over the line bus A-bus F are 0.010 pu with solution **a** and 0.005 pu with solution **b**, respectively. The losses of solution **a** are twice the losses of solution **b**.

Summary of Case 2

Case 2 has analyzed the meshed grid topology shown in Fig. 5.4 (c). This topology enables the DG generation to be directly delivered to loads of buses H to K without via the ST's LV busbar. Even without DG generation, loads of buses H-K can be supplied by both MV grids. As a consequence, violation of either under-voltage or over-voltage constraints can be mitigated. The performance of the proposed multi-objective operation scheme is evaluated in all four aspects using the Pareto optimality method.

With Scenario 1, all solutions derived from the Pareto optimality set of the proposed scheme reach a reduced power unbalance, and a reduced mean voltage deviation comparing the results in Case O. 34 % of the solutions has lower losses than Case O. The lowest power factor of the solutions is around 0.975.

With Scenario 2, the DG power generation of bus F can be directly delivered to loads of buses H to K. Unlike Case 1, in Case 2, power supply unbalance, losses, and voltage deviations of all solutions are smaller than the ones in Case O. The lowest power factor is 0.90, but only 4 % of the solutions has a power factor smaller than 0.95.

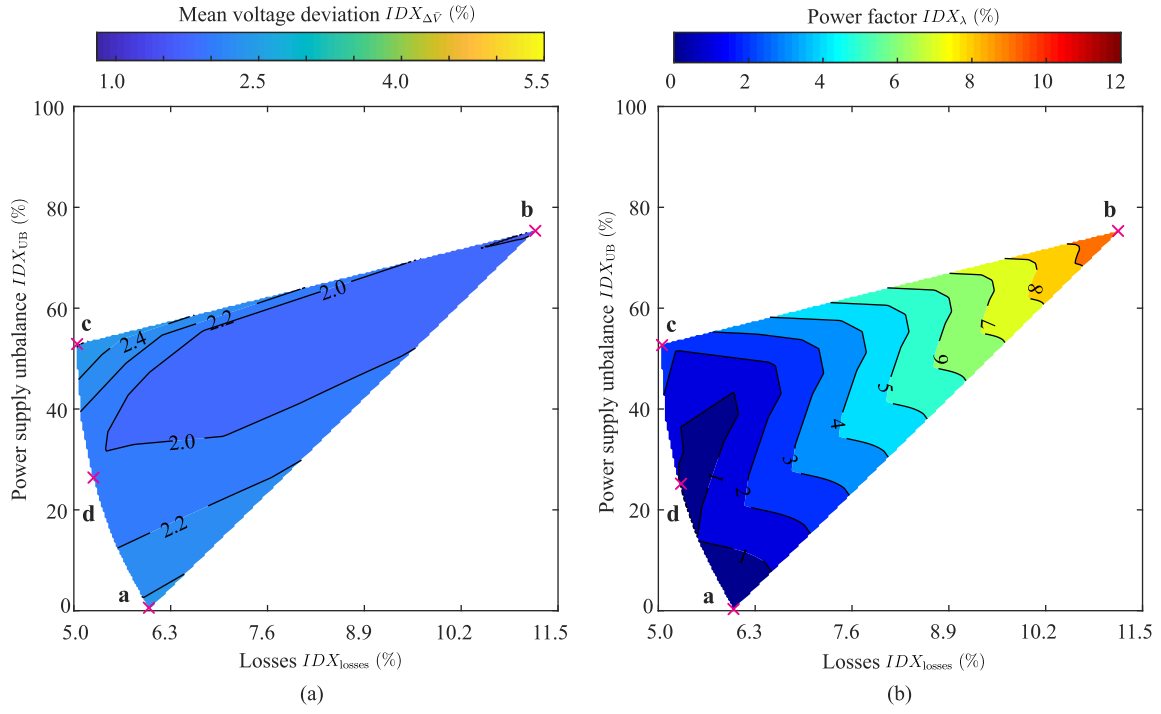


Fig. 5.16: Solutions of Pareto optimality set of proposed multi-objective operation scheme, Scenario 2 of Case 3. (a) Mean voltage deviation vs. power supply unbalance and losses. (b) Power factor vs. power supply unbalance and losses.

5.4.4 Case 3: Meshed grid topology 3

Similar to case 1, the NOP lies between bus E and bus K in this case. However, the DG is connected to the dc grid instead of the ac grid. Bus F has been isolated from the ac grid so that its voltage rise issue due to DG power's penetration has no impact on the ac grid operation.

Scenario 1

Since the DG does not inject power into the grid, the performance of Scenario 1 is identical to it of Case 1.

Scenario 2

Fig. 5.16 shows the Pareto optimality set derived from the proposed operation scheme. The two axes in the figure represent the indices of IDX_{UB} (power supply unbalance) and IDX_{losses} (losses in percentage). Fig. 5.16 (a) shows $IDX_{\Delta V}$ (mean voltage deviation) in colors. Fig. 5.16 (b) shows IDX_{λ} (power factor) in colors.

All solutions of the Pareto optimality set have a lower mean voltage deviation than Case O (3.9 %). Approximately 99 % of the solutions reaches a lower power supply unbalance to Case O (72.2 %). Unlike Case 1, the balanced power supply (i.e., IDX_{UB} is 0) can be

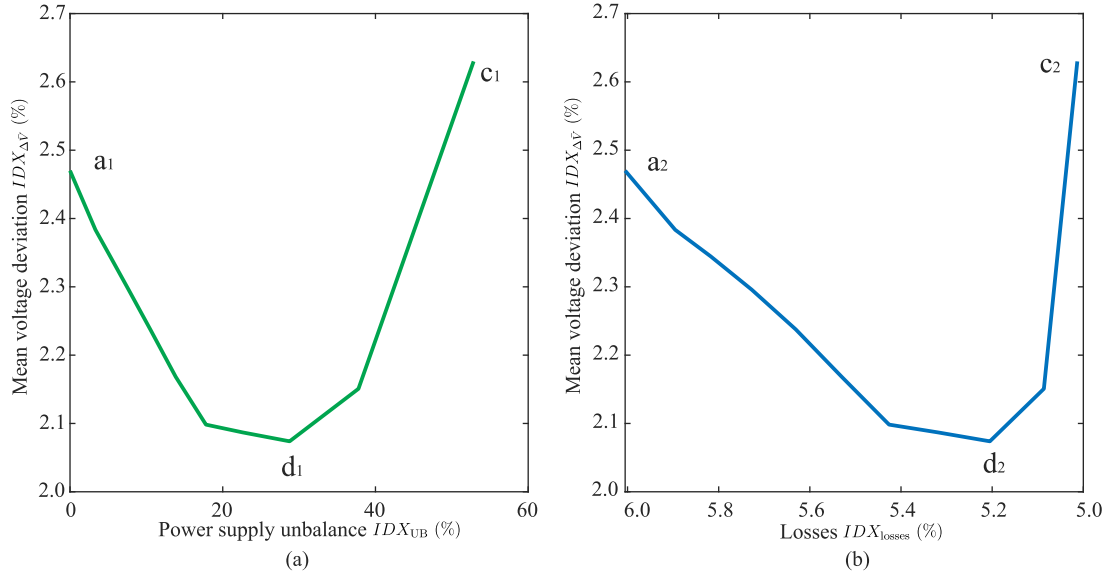


Fig. 5.17: Projection of frontier **a-d-c** in Fig. 5.16. (a) Projection to the surface of power supply unbalance vs. mean voltage deviation. (b) Projection to the surface of losses vs. mean voltage deviation.

achieved in Case 3. The solutions of lower losses to Case O (7.5 %) take approximately 59 %.

Solution **a** in Fig. 5.16 reaches the lowest power supply unbalance (0), solution **b** reaches the smallest voltage deviation (1.8 %), and solution **c** reaches lowest losses (5.0 %). The highest power supply unbalance (75.6 %) and highest losses (11.2 %) appear with solution **b**. In Case 1, solution **b** has the lowest value of IDX_{λ} , on the contrary, solution **b** in Case 3 has the maximal value of IDX_{λ} , i.e., power factor 0.900. The solutions, which the value of IDX_{λ} is larger than 5 %, take approximately 27 %. From all three Cases, it is noted that if the power supply unbalance IDX_{UB} can be reduced to 0, the index IDX_{λ} increases or decreases together with IDX_{UB} , and reaches the value of 0 when IDX_{UB} becomes 0. Solution **c** has the largest voltage deviation (2.6 %). The system operators can select the solutions according to Fig. 5.16. For instance, if the operator wants a solution with losses below 6 %, solutions around **d** in Fig. 5.16 can be suitable for the operator since solutions there keep power supply unbalance within 25–35 % and voltage deviation around 2 %.

Fig. 5.17 shows the frontier **a-d-c** projected to different surfaces. Fig. 5.17 (a) is the frontier projected to the surface of power supply unbalance vs. mean voltage deviation. The voltage deviation decreases from a_1 , reaching the smallest value d_1 , and starting to increase till c_1 , while the power supply unbalance continuously increases. Fig. 5.17 (b) is the frontier projected to the surface of losses vs. mean voltage deviation, which the losses continuously decreases from a_2 to c_2 .

Fig. 5.18 (a) shows the mean and maximal voltage deviations of solutions **a**, **b**, **c**, and **d**. It is noticed that the largest value of mean voltage deviation appearing with solution **c**, but the largest value of maximal voltage deviation appearing with solution **a**. The meshed ac grid's

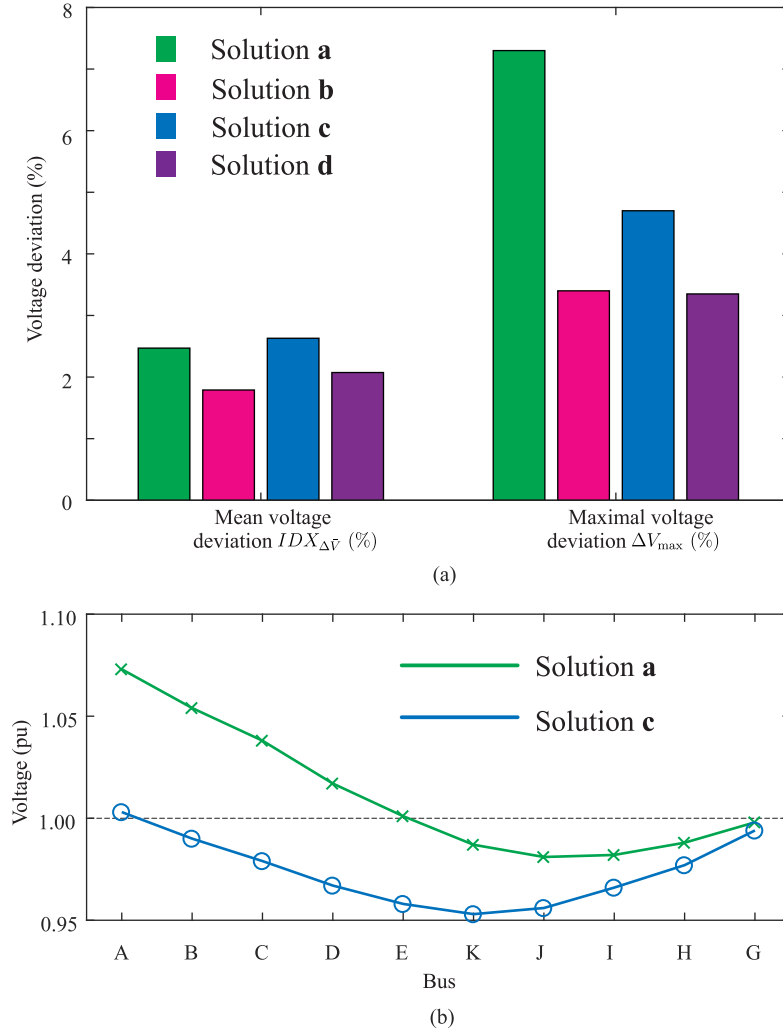


Fig. 5.18: Voltage behaviors of Scenario 2, Case 3. (a) Comparison of mean and maximal voltage deviations of solutions **a**, **b**, **c**, and **d** in Fig. 5.16. (b) Bus voltage profiles of solutions **a** and **c**.

voltage profiles with solutions **a** and **c** are depicted in Fig. 5.18 (b). The bus A voltage of solution **a** is increased to 1.073 pu due to the active power of MV grid 1 and reactive power injection of ST as listed in Table 5.8. On the contrary, bus A voltage with solution **c** is close to 1 pu. However, starting from bus D, the voltage profile of solution **a** is closer to 1 pu than the profile of solution **c**, resulting in a smaller value of mean voltage deviation of solution **a**.

The active power supply of both MV grids and the ST reactive power injection of solutions **a**, **b**, and **c** are listed in Table 5.8. Similar to most cases, the highest ST reactive power injection arises with solution **b**. The lowest arises with **c**.

Summary of Case 3

Case 3 has analyzed the meshed grid topology shown in Fig. 5.4 (d). This topology enables loads of buses A to E and H to J can be supplied by both MV grids. The DG power generation

Table 5.8: Power supply of both MV grids and ST reactive power injection of solutions **a**, **b**, and **c** in Fig. 5.16

Solution	Power of MV grid 1 (pu)	Power of MV grid 2 (pu)	ST reactive power (pu)
a	0.233	0.233	0.133
b	0.075	0.436-j0.211	0.366
c	0.112	0.346+j0.073	0.059

of bus F is delivered to the LV busbar of ST, i.e., bus A, via the dc grid. The voltage rise issue of bus F due to the DG power penetration has no impact on the ac voltage.

With Scenario 1, since the DG has no power injection, the performance is identical in Case 1.

With Scenario 2, due to the voltage rise of bus F has no impact on the voltage operation for ac grid, all solutions of the proposed scheme reach a lower voltage deviation than Case O. Moreover, the solutions, which have a lower power supply unbalance or lower losses than Case O, take 99 % and 59 %, respectively. The proposed operation scheme mitigates the violations of power factor and voltage in Case O. 73 % of the solutions has a power factor higher than 0.95.

5.4.5 Summary of performance analysis

With the ST, different meshed grid topologies can be applied. This work has proposed a meshed grid operation scheme, which is based on multi-objective optimization. The Pareto optimality method has been exploited to compute the solutions of the proposed scheme, achieving that the derived set of solutions can fulfill the preferences of different system operators. The performance of the proposed scheme with the two scenarios, which represent different load conditions, has been evaluated.

The analysis has evaluated the meshed grid's performance in terms of four aspects. Compared to the performance of conventional radial feeder topology, the meshed grid with the proposed scheme has achieved improvement in most cases. With Scenario 1, solutions of all three topologies reach a lower power supply unbalance and a smaller value of mean voltage deviation than radial feeder topology (Case O). 21 % of the solutions of Case 1 and Case 3, and 34 % of the solutions of Case 2 have reached lower losses than Case O. The lowest power factor of the meshed grid is around 0.975. With Scenario 2, solutions of three topologies cases reach no violation of voltage or power factor constraint. Comparing Case 2 to Case O, all solutions of Case 2 have better performance in terms of power supply unbalance, losses, and mean voltage deviation. Comparing Case 3 to Case O, all solutions achieve a

Table 5.9: Percentage of meshed grid solutions with reduced indices IDX_{UB} , IDX_{losses} , and $IDX_{\Delta\bar{V}}$ respecting Case O

Pareto set of Case 1			
Scenario	Reduced IDX_{UB} in percentage (%)	Reduced IDX_{losses} in percentage (%)	Reduced $IDX_{\Delta\bar{V}}$ in percentage (%)
1	100	21	100
2	11	0	0
Pareto set of Case 2			
Scenario	Reduced IDX_{UB} in percentage (%)	Reduced IDX_{losses} in percentage (%)	Reduced $IDX_{\Delta\bar{V}}$ in percentage (%)
1	100	34	100
2	100	100	100
Pareto set of Case 3			
Scenario	Reduced IDX_{UB} in percentage (%)	Reduced IDX_{losses} in percentage (%)	Reduced $IDX_{\Delta\bar{V}}$ in percentage (%)
1	100	21	100
2	99	59	100

smaller mean voltage deviation; 99 % of the solutions has lower power supply unbalance; 59 % of the solutions has lower losses. 95 % of the solutions of Case 2 and 73 % of Case 3 have a power factor above 0.95. The results are summarized in Table 5.9. The meshed grid operation can significantly improve the grid's conditions, reducing the power supply unbalance, the losses, and the voltage deviation.

The meshed grid's topologies can significantly impact the controllability that can be gained. For the topology in Case 1, the only way to mitigate the over-voltage at bus F is to regulate the voltage at bus A. Consequently, the bus A voltage of Scenario 2 has to be around 0.96 pu, which restricted the proposed scheme's controllability. For the topology in Case 2, the generation of DG can directly supply loads of buses H-K without via bus A, the voltage rise issue is solved. All solutions with this topology achieve a better performance in power supply unbalance, losses, and mean voltage deviation. For the topology in Case 3, with the introduction of the dc grid between bus A and bus F, bus F's voltage rise issue cannot impact the ac grid operation. As a result, 100 % of solutions with this topology reach a smaller voltage deviation than Case O, and 59 % of the solutions has lower losses.

It is also noticed that if the power supply unbalance can be reduced to 0, the value of IDX_{λ} decreases or increases together with the power supply unbalance. Furthermore, in most cases, the highest ST reactive power injection corresponds to the solutions with the lowest voltage deviation, and the lowest injection corresponds to the solutions with the lowest losses.

5.5 Harmonics Compensation in Meshed Grid

Non-linear loads can introduce harmonics currents into the grid. In the LV grid, home appliances like refrigerators, washing machines, or televisions are typical non-linear loads with a high presence of low order harmonics current [121]. Photovoltaic converters can also contribute to the harmonic content [122]. The harmonics lead to the distortion of the current and voltage waveforms, eventually violating grid operation constraints.

The ST has demonstrated its capability as the active power filter in both MV and LV grids [123]. In the meshed grid, the ST can also provide power conditioning that improves the power quality and avoids the propagation of harmonics. Fig. 5.19 (a) shows a simplified meshed grid with non-linear load. Since the ST decouples the LV grid with its upstream MV grid, the harmonics cannot be spread into this MV grid, but they can be spread into the external MV grid 2 connecting the LFT. To prevent the harmonics from flowing into MV grid 2, besides injecting current $i_{ST,load}$ to supply the loads with fundamental frequency, the ST should generate the harmonics compensation (HC) current $i_{hc,m}$ (m for the order of harmonic). The HC current compensates the harmonics parts of the current $i_{LFT,load}$. Consequently, the current from MV grid 2 via the LFT i_{LFT} can be conditioned to be less distorted. The principle of harmonics compensation are shown in Fig. 5.19 (b). As a premise to implement this compensation, accurate and simultaneous information exchange between the LFT and ST is required, which requires high-frequency metering systems and advanced communication infrastructure.

5.5.1 Generation of harmonics compensation reference in smart transformer

In order to generate the harmonics compensation reference $i_{hc,k}$, the $p-q$ theory based method is applied. The LV grid is usually a three-phase four-wire grid. As the first step, the proposed scheme applies the Clark transformation to convert the three-phase measurements, such as current and voltage, into the $\alpha\beta 0$ reference frame [124]. The conversion between three-phase measurement into $\alpha\beta 0$ reference frame is represented as:

$$\mathbf{a}_{\alpha\beta 0} = \mathbf{T}_{\alpha\beta 0} \mathbf{a}_{abc} \quad (5.21)$$

where the \mathbf{a}_{abc} are the measurements, $\mathbf{a}_{\alpha\beta 0}$ are the quantities after Clark transformation, and $\mathbf{T}_{\alpha\beta 0}$ is the transformation matrix.

After converting the voltage and current from the abc phases into $\alpha\beta 0$ frame, the instantana-

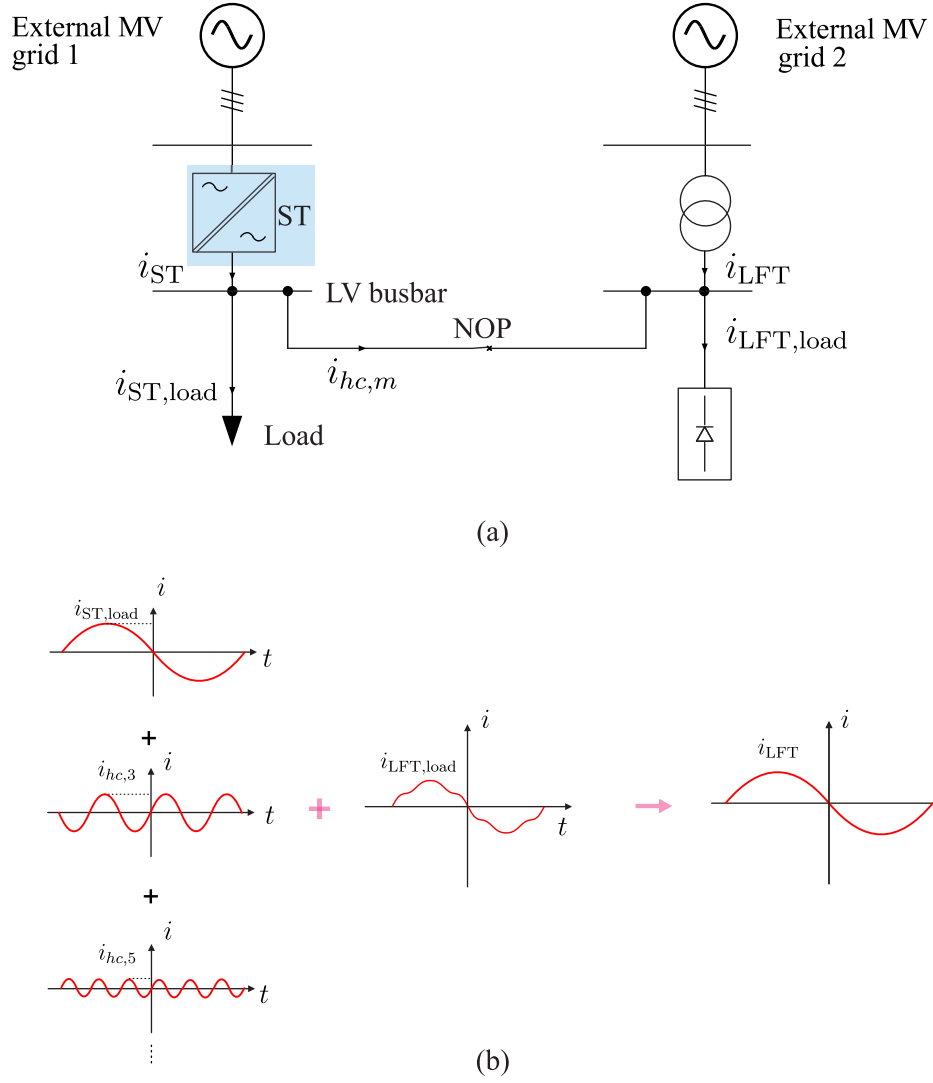


Fig. 5.19: Principle of harmonics compensation in meshed grid. (a) Meshed grid with non-linear load. (b) Principle of harmonics compensation with ST.

neous active power p and reactive power q can be represented as:

$$\begin{bmatrix} p_{\alpha\beta} \\ q_{\alpha\beta} \\ p_0 \end{bmatrix} = \mathbf{M}_{\alpha\beta 0} \begin{bmatrix} i_{\alpha} \\ i_{\beta} \\ i_0 \end{bmatrix} = \begin{bmatrix} v_{\alpha} & v_{\beta} & 0 \\ -v_{\beta} & v_{\alpha} & 0 \\ 0 & 0 & v_0 \end{bmatrix} \begin{bmatrix} i_{\alpha} \\ i_{\beta} \\ i_0 \end{bmatrix} \quad (5.22)$$

where $p_{\alpha\beta}$ and $q_{\alpha\beta}$ are the instantaneous active and reactive power, p_0 is the instantaneous zero-sequence power.

Defining the three phases power $p_{3\phi}$, which is the sum of $p_{\alpha\beta}$ and p_0 , the instantaneous active power delivered collectively by the three phases can be represented as:

$$p_{3\phi} = p_{\alpha\beta} + p_0 \quad (5.23)$$

where

$$\begin{aligned} p_{\alpha\beta} &= v_{\alpha}i_{\alpha} + v_{\beta}i_{\beta} \\ p_0 &= v_0i_0 \end{aligned} \quad (5.24)$$

Accordingly, the instantaneous reactive power can be defined as:

$$q_{\alpha\beta} = v_{\alpha}i_{\beta} - v_{\beta}i_{\alpha} \quad (5.25)$$

The instantaneous active/reactive power consists of a constant quantity and an oscillatory quantity, which can be represented as:

$$\begin{aligned} p_{\alpha\beta} &= \bar{p}_{\alpha\beta} + \tilde{p}_{\alpha\beta} \\ q_{\alpha\beta} &= \bar{q}_{\alpha\beta} + \tilde{q}_{\alpha\beta} \\ p_0 &= \bar{p}_0 + \tilde{p}_0 \end{aligned} \quad (5.26)$$

The constant quantities of instantaneous power p and q represented as \bar{p} and \bar{q} are originated if the voltage/current have the same frequency and sequence. The oscillatory quantities \tilde{p} and \tilde{q} are originated if there is a frequency or sequence difference in voltage/current, e.g., load's harmonics components.

When the p and q are known, the corresponding current reference can be computed by inverting the matrix $\mathbf{M}_{\alpha\beta 0}$ in (5.22):

$$\begin{bmatrix} i_{\alpha}^* \\ i_{\beta}^* \\ i_0^* \end{bmatrix} = \mathbf{M}_{\alpha\beta 0}^{-1} \begin{bmatrix} p_{\alpha\beta} \\ q_{\alpha\beta} \\ p_0 \end{bmatrix} \quad (5.27)$$

where

$$\mathbf{M}_{\alpha\beta 0}^{-1} = \frac{1}{v_{\alpha}^2 + v_{\beta}^2} \begin{bmatrix} v_{\alpha} & v_{\beta} & 0 \\ -v_{\beta} & v_{\alpha} & 0 \\ 0 & 0 & \frac{1}{v_0} \end{bmatrix} \quad (5.28)$$

In three-phase four-wire system, the unbalanced three-phase current can cause the zero-sequence component to flow via the neutral wire. Removing the row and column of $[\mathbf{M}_{\alpha\beta 0}]^{-1}$, which is related to the zero sequence, to force the zero-sequence current to zero, a two-row two-column matrix $[\mathbf{M}_{\alpha\beta}]^{-1}$ can be derived.

Assuming that the instantaneous active/reactive power injection of the ST to feed the load is $\bar{p}_{\text{ST},\alpha\beta}^*$, and $\bar{q}_{\text{ST},\alpha\beta}^*$, the current references of the ST for the controller can be derived as:

$$\begin{bmatrix} \bar{i}_{\alpha}^* \\ \bar{i}_{\beta}^* \end{bmatrix} = \mathbf{M}_{\alpha\beta}^{-1} \begin{bmatrix} \bar{p}_{\text{ST},\alpha\beta}^* \\ \bar{q}_{\text{ST},\alpha\beta}^* \end{bmatrix} = \frac{1}{v_{\text{ST},\alpha\beta}^2 + v_{\text{ST},\alpha\beta}^2} \begin{bmatrix} v_{\text{ST},\alpha\beta} & -v_{\text{ST},\alpha\beta} \\ v_{\text{ST},\alpha\beta} & v_{\text{ST},\alpha\beta} \end{bmatrix} \begin{bmatrix} \bar{p}_{\text{ST},\alpha\beta}^* \\ \bar{q}_{\text{ST},\alpha\beta}^* \end{bmatrix} \quad (5.29)$$

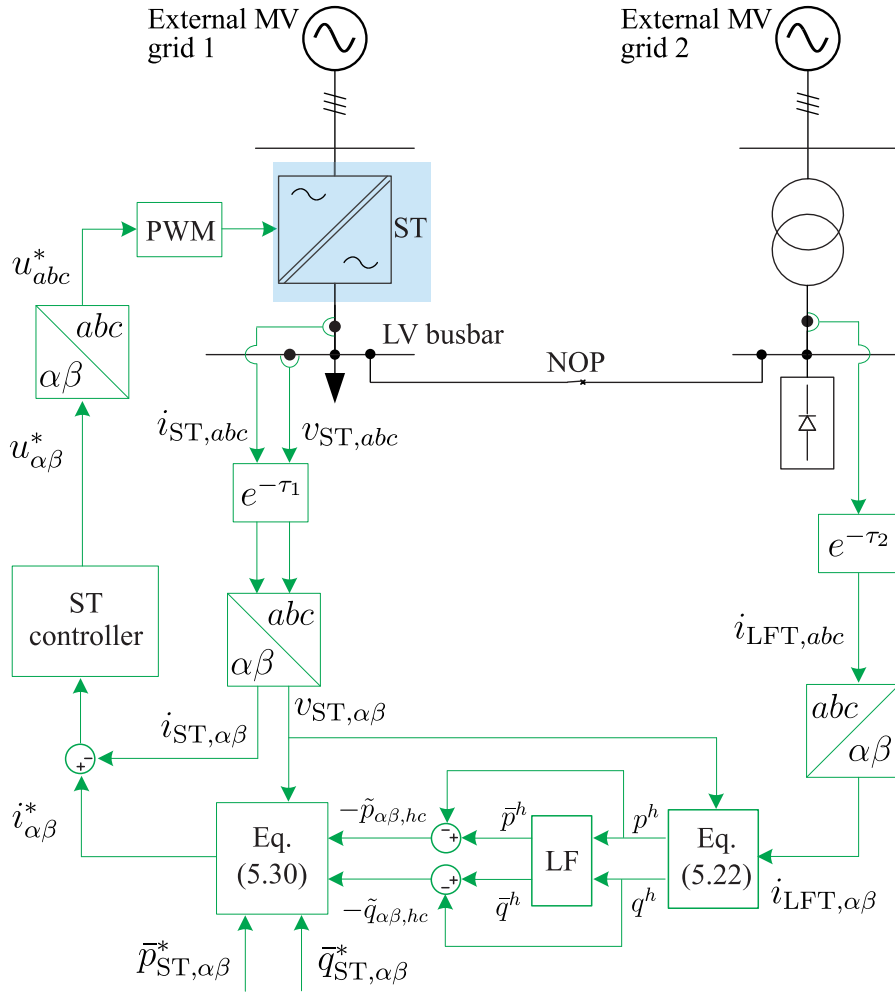


Fig. 5.20: Control scheme of ST with HC functionality in meshed grid.

In order to compensate the harmonics current, the current of the control point, e.g., LV busbar of the LFT, is sent to the ST. Using the measurements, the ST generates the compensation power references $\tilde{p}_{\alpha\beta,hc}$ and $\tilde{q}_{\alpha\beta,hc}$ according to (5.22). By adding the compensation power references into the ST power references $\bar{p}_{ST,\alpha\beta}^*$ and $\bar{q}_{ST,\alpha\beta}^*$, the current references of the ST can be computed as:

$$\begin{bmatrix} \tilde{i}_{\alpha}^* + \tilde{i}_{\alpha}^* \\ \tilde{i}_{\beta}^* + \tilde{i}_{\beta}^* \end{bmatrix} = \frac{1}{v_{ST,\alpha\beta}^2 + v_{ST,\alpha\beta}^2} \begin{bmatrix} v_{ST,\alpha\beta} & -v_{ST,\alpha\beta} \\ v_{ST,\alpha\beta} & v_{ST,\alpha\beta} \end{bmatrix} \begin{bmatrix} \bar{p}_{ST,\alpha\beta}^* - \tilde{p}_{\alpha\beta,hc} \\ \bar{q}_{ST,\alpha\beta}^* - \tilde{q}_{\alpha\beta,hc} \end{bmatrix} \quad (5.30)$$

It is noted that the compensation power references should be minus in the ST power references. Using the derived current references $\tilde{i}_{\alpha}^* + \tilde{i}_{\alpha}^*$ and $\tilde{i}_{\beta}^* + \tilde{i}_{\beta}^*$, the ST can inject the current to compensate the targeted harmonics.

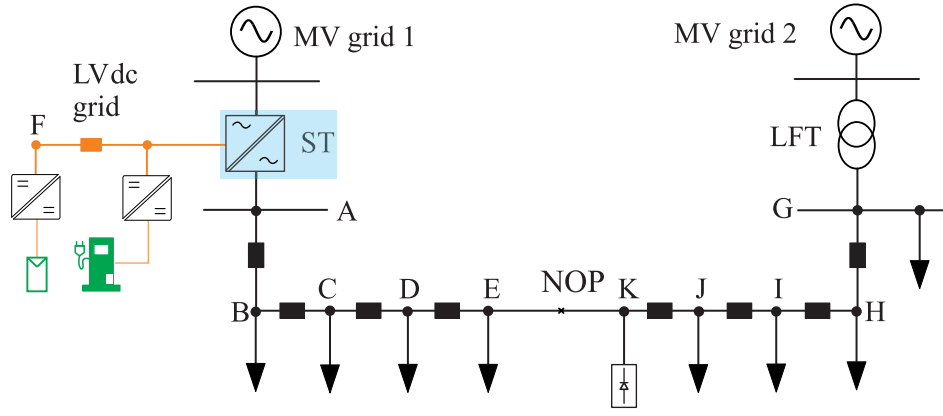


Fig. 5.21: Grid for analysis of harmonics compensation.

5.5.2 Control scheme of smart transformer for harmonics compensation

The control scheme of ST to implement the HC is illustrated in Fig. 5.20. The controller receives the voltage and current from the LV busbar of ST and the current from the LV busbar of LFT. Delays such as the algebraic-digital conversion and the data transmitting are represented with τ_1 for ST and τ_2 for LFT. The measurements, once converted into $\alpha\beta$ frame, are used to compute the instantaneous power according to (5.22). With the help of lowpass filter (LF), the required HC power $\tilde{p}_{\alpha\beta, hc}$ and $\tilde{q}_{\alpha\beta, hc}$ are derived. Together with the power of the ST $\bar{p}_{ST, \alpha\beta}$ and $\bar{q}_{ST, \alpha\beta}$, the current reference for the ST controller is generated according to (5.30). Inside the ST controller, the ST output current are controlled to track the current reference by generating the voltage reference $u_{\alpha\beta}^*$ used for the pulse-width-modulation (PWM) of the ST.

5.6 Performance Evaluation of Harmonics Compensation in Meshed Grid

5.6.1 Setup of testing grid

The performance of harmonics compensation in the ST based meshed grid is analyzed by means of simulation in the PSCAD. The grid is shown in Fig. 5.21. Two load scenarios, which are defined in Section 5.3.2, are used in the evaluation. A three-phase diode rectifier with a resistor has replaced the three-phase balanced load of bus K. The resistance is 1Ω .

The harmonics of low orders are of main interests for the compensation [125]. In this work, the harmonics of 5^{th} , 7^{th} , 11^{th} and 13^{th} are analyzed. Those orders of harmonics are normally the dominant components to affect the power quality.

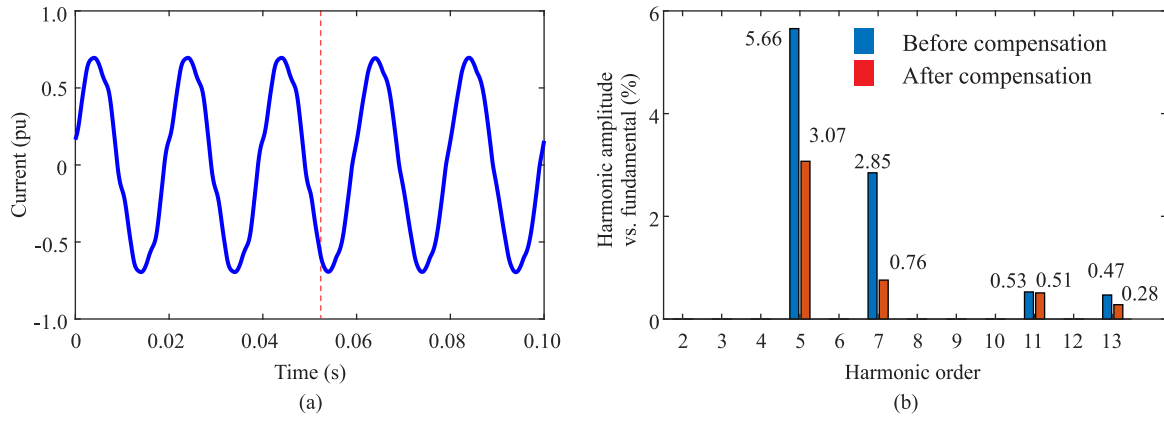


Fig. 5.22: Analysis of current waveform via the LFT with Scenario 1. (a) Current waveform before and after compensation. (b) Harmonic spectrum of the current waveform.

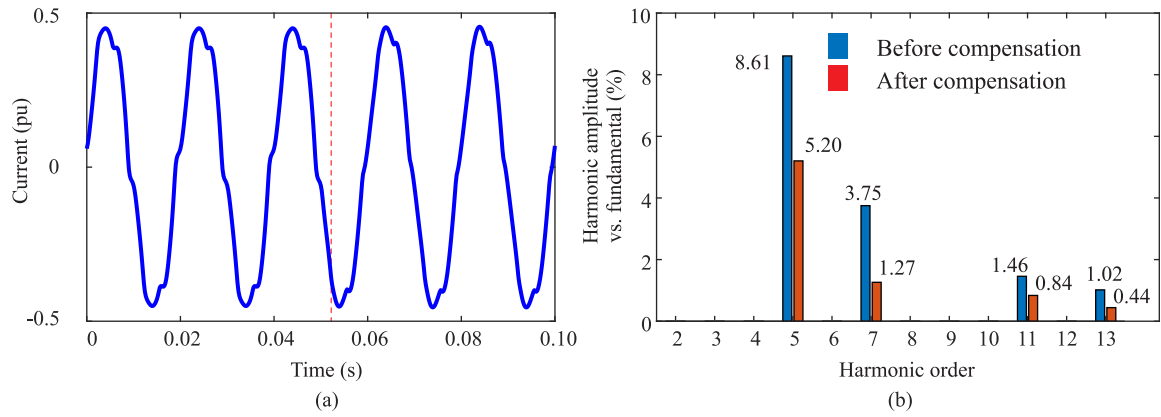


Fig. 5.23: Analysis of current waveform via the LFT with Scenario 2. (a) Current waveform before and after compensation. (b) Harmonic spectrum of the current waveform.

5.6.2 Simulation results and analysis

The waveforms and harmonic spectrum of the current flowing via the LFT are depicted in Fig. 5.22 for Scenario 1 and Fig. 5.23 for Scenario 2, respectively. From 0.55 s, the ST starts to compensate the harmonics for both scenarios. In Fig. 5.22 (a), the distortion of the current waveform after 0.55 s (time to trigger the harmonics compensation) has been reduced. Depicted in Fig. 5.22 (b), the corresponding harmonic spectrum based on fast Fourier transform (FFT) analysis shows that harmonics of all orders have been reduced. The 7th harmonic has the largest reduction of 72 %, which the value is decreased from 2.85 % to 0.76 %.

In Fig. 5.23 (a), the harmonics components have been reduced after 0.55 s, but the distortion of the current waveform can still be observed. Depicted in Fig. 5.23 (b), the corresponding harmonic spectrum shows that all orders' harmonics have been reduced. The 7th harmonic, similar to Scenario 1, has the largest reduction of 66 %, which the value is decreased from 3.75 % to 1.27 %.

With Scenario 1, the total harmonics distortion (THD) of the current via the LFT is 6.37 % before the compensation and 3.22 % after the compensation. The reduction is 49 %. Accord-

Table 5.10: THD of current and voltage of the LFT with both scenarios

Scenario 1			
Measurement	THD before compensation (%)	THD after compensation (%)	Reduction of THD (%)
Current	6.37	3.22	49
Voltage	1.05	0.52	50
Scenario 2			
Measurement	THD before compensation (%)	THD after compensation (%)	Reduction of THD (%)
Current	9.57	5.46	43
Voltage	1.05	0.57	46

ingly, the THD of the voltage of the LV busbar of the LFT is reduced from 1.05 % to 0.52 %. With Scenario 2, the THD of the current via LFT is 9.57 % before the compensation and 5.46 % after the compensation. The reduction is 43 %. The THD of the voltage is reduced from 1.05 % to 0.57 %. The results are listed in Table 5.10.

5.7 Summary

The ST decouples the connected MV and LV grids in terms of phase angle and voltage, enabling the operation of the meshed grid on the LV side. Furthermore, the ST enhances the controllability of its connected grid by providing the dc bus and even the dc grid. In this chapter, the ST based centralized solution for the meshed grid operation has been proposed. The performance of static state operation and power conditioning is evaluated.

An operation scheme based on multi-objective optimization has been developed to exploit the advantages of the meshed grid in the static state. The scheme takes into account the three operation aspects, i.e., power supply unbalance, losses, and voltage deviation. By means of the Pareto optimality method, the non-dominated solutions of the proposed scheme are derived, allowing each system operator can select the solution according to its individual preference. The performance of the proposed scheme has been evaluated with three meshed grid topologies. Two scenarios have been studied to respect different load conditions. With Scenario 1, all solutions of the three topologies reach a lower power supply unbalance and a smaller value of mean voltage deviation than Case O. 21 % of the solutions in Case 1 and Case 3, and 34 % of the solutions in Case 2 have lower losses. The lowest power factor is around 0.975. With Scenario 2, solutions of all three topologies reach no violation of voltage or power factor constraints. Different topologies can impact the meshed grid performance. For instance, with the topology in Case 1, the power from DG must be first delivered to the

LV busbar of the ST, which restricts the controllability. With other topologies, the meshed grid achieves a significant improvement of grid conditions than the conventional operation of radial feeders. With the topology in Case 2, 100 % of the solutions achieves a better performance in terms of power supply unbalance, losses, and mean voltage deviation. With the topology in Case 3, the dc grid between bus A to bus F isolates bus F from ac grid voltage regulation. As a result, 100 % of the solutions reach a lower voltage deviation than Case O, and 59 % of the solutions has lower losses.

Moreover, the ST-based meshed grid operation can mitigate harmonics, which prevents the harmonics from spreading into the MV grids. The results show that the THD of the current can be reduced by 43–49 %, depending on the load conditions.

6 Summary, Conclusion, and Future Research

6.1 Summary and Conclusion

The contemporary power system is experiencing significant changes in different branches, from the generation to the end-users. Due to the emerging renewable energy generation in the generation branch, electricity production gradually shifts from concentrated large scale power plants into small scale distributed generation (DG) installed locally in the distribution grid. From the operation point of view, the broad installation of DG can introduce some benefits, for instance, reducing the power losses. On the end-user side, electrification in different sectors, e.g., electric vehicles (EVs), has been promoted due to social benefits such as net-zero emissions. Nevertheless, the increasing penetration of these new actors has introduced grid operation issues because of their intermittent energy production feature, the randomness of power demand, and some other features. The issues have arisen the grid operation challenges, including reversed power flow, decreased grid inertia, high unforeseeable power demand, and fast voltage transients. Previous researches have proposed a group of solutions to address the operation challenges.

This thesis, based on the previous researches, has proposed a group of power electronics (PE) components based solutions to enhance grid controllability, overcoming the challenges that the new actors have brought. Three components: the smart transformer (ST), the energy storage static synchronous compensator (ES-STATCOM), and the fast charging station (FCS), have been evaluated as the primary actuators of the proposed solutions. The ST provides a systematical solution for grid regulation. The ES-STATCOM and FCS can achieve the benefits by providing grid regulation as ancillary functionalities. To well understand the features of these components, in Chapter 2, the topologies of the three PE components have been introduced, as well as the corresponding controller structures. This chapter also defines the concept of distributed and centralized solutions in this thesis. Furthermore, the typical characteristics of the solutions have been explained.

This thesis has focused on the grid regulation issues in terms of power and voltage. Since the new actors have introduced intermittent generation and high randomness demand, real-time consumption can deviate significantly from the demand forecast. The increased power mismatch introduces a high cost for power balancing and can eventually endanger the grid frequency stability without proper alleviation. A load-leveling approach that exploits the FCSs to alleviate the mismatch has been proposed in Chapter 3. This approach exploits the loads' voltage-dependent characteristics. By means of reactive power injection from FCSs, which uses the spare capacity of FCSs, the grid voltage can be regulated, shaping as a consequence the voltage-dependent loads' power consumption. The on-load tap changer of the transformer, which connects the network to the upstream grid, is employed as an additional actuator of this approach. A two-stage load-leveling scheme has been developed,

targeting: (a) minimization of the power mismatch with respect to the demand forecast; (b) reduction of the losses. This load-leveling scheme systematically employs all actuators with equal status. Consequently, the proposed approach formulates a distributed solution of grid controllability enhancement. The performance of this solution has been analyzed by means of simulation and laboratory tests. Results of the analysis have confirmed the effectiveness of the solution in alleviating the power mismatch.

To address the voltage issues introduced by the new actors, Chapter 4 has proposed a voltage regulation approach, exploiting the voltage-correlation coefficients to reduce the computation burden. This approach can be implemented with various PE components, such as the ES-STATCOMs and the STs. The coefficients must be adopted according to the grid connecting strategies of the components, which can eventually impact the gained controllability of the proposed approach. For the ES-STATCOMs, a scheme has been developed which employs the reactive power-voltage correlation coefficients. The coordination of the ES-STATCOMs is similar to Chapter 3, which formulates the ES-STATCOMs based solution as a distributed one. The scheme for the STs exploits the reactive power-voltage correlation coefficients in the medium voltage (MV) grid; however, it exploits the voltage-voltage correlation coefficients in the low voltage (LV) grid. Consequently, the STs based solution is a distributed and centralized combined one. The performance of the two solutions has been analyzed, and a comparison between the solutions has been conducted. The results from the simulation have confirmed the effectiveness of the voltage regulation approach in mitigating the voltage violation and minimizing the average voltage deviation. Furthermore, the difference of performance between the ES-STATCOM and the ST based solutions has been compared, showing the impact of the grid connecting strategies.

Besides the power and voltage regulation with the unchanged grid configuration, Chapter 5 has analyzed the regulation approach based on grid reconfiguration. By means of the ST, two parallel-operated radial feeders in the LV grid can be meshed upon the requirement, making a ring configuration. This configuration can benefit the operation, e.g., to achieve a balanced power flow via the essential components such as transformer in different feeders. Different possible meshed topologies have been taken into account in the analysis. In order to systematically implement the power and voltage regulation, a scheme based on multi-objective optimization has been developed. By means of the Pareto optimality method, the non-dominated solutions of the proposed scheme are determined, which allow every system operator to select the proper solution according to its individual preference. The evaluation has been conducted to analyze the meshed grid performance in terms of power supply unbalance, losses, voltage deviation, and power factors. The results show that in most cases, the meshed grid operation has achieved improved performance in terms of power and voltage regulation respecting the radial feeder operation, confirming the effectiveness of the meshed grid operation concept. Furthermore, a power conditioning scheme to reduce the harmonics current has been discussed. Its effectiveness has been confirmed by the corresponding

analysis.

6.2 Research Contribution

Contribution to the load-leveling approach

- A load-leveling approach, exploiting the spare capacity of the FCSs, has been proposed. This approach injects reactive power to alleviate the power mismatch between the demand forecast and the real-time consumption.
- The application of the voltage-dependent loads in the power regulation has been analyzed. By means of voltage regulation from the reactive power injection of the FCSs, and under some conditions from the on-load tap-changer of the transformer, the power demand of the voltage-dependent loads can be shaped to track the demand forecast.
- A distributed solution employing actuators of the FCSs and the on-load tap-changer in the grid has been formulated. A two-stage load-leveling scheme has been developed. Stage 1 minimizes the power mismatch. Based on Stage 1, if the power mismatch is fully mitigated, stage 2 is activated to minimize the losses.

Contributions to the voltage regulation approach

- A voltage regulation approach, which PE components with different grid connecting strategies such as the ES-STATCOMs or the STs can implement, has been proposed. The approach exploits the spare capacity of the PE components for reactive power injection, while the active power is not impacted.
- The scheme to implement the approach exploits the voltage-correlation coefficients to reduce the computation burden. The coefficients vary between reactive power-voltage correlation coefficients and voltage-voltage correlation coefficients, adopting the grid connecting strategies of the PE components.
- A distributed solution for voltage regulation based on the ES-STATCOMs has been proposed. The scheme to coordinate the ES-STATCOMs employs the reactive power-voltage correlation coefficients. For the STs, in the MV grid, a distributed solution has been formulated, whose scheme employs the same coefficients as ES-STATCOMs; in the LV grid, the ST formulates a centralized solution that employs voltage-voltage correlation coefficients.
- A comparison of the performance of the two components has been conducted to evaluate the impact of the grid connecting strategies.

Contributions to the meshed grid operation approach

- The meshed grid concept, which makes ring reconfiguration for the parallel operated radial feeders, has been evaluated. Different possible meshed grid configurations have been studied.
- A meshed grid operation scheme based on the multi-objective optimization has been developed, taking into account minimizing power supply unbalance, minimizing losses, and minimizing voltage deviation.
- The Pareto optimality method is employed to solve multi-objective optimization, which derives the non-dominated solutions, ensuring the various system operators can select optimal solutions according to their individual preferences.
- A scheme for the power quality conditioning, i.e., the mitigation of harmonics, has been discussed.

6.3 Future Research

Various PE components based grid controllability enhancement solutions have been proposed. Those solutions are targeted at grid reinforcement, overcoming the emerging grid operation challenges introduced by new actors such as renewable energy generation, increasing the grid capability to host more new actors, and eventually deferring network infrastructure upgrade.

In the author's opinion, the challenges that the future research must address are:

- Most analyses of the proposed solutions are based on the simulation. The laboratory tests have been implemented with the grid model of a radial structure. To further develop and optimize the proposed solutions, laboratory tests with complex grid structures are essential. Laboratory demonstrators with complex grid structures are to be developed. Besides, field tests in a real grid must be considered if possible.
- The solutions proposed in this thesis focus mainly on the grid static operation. The PE components are also capable of providing grid controllability enhancement for transient operations. To develop the solutions for transient operation, researchers must further analyze, modify, and optimize the controller of the PE components, making the controller capable of transient operation. The schemes to implement the transient grid operations are to be developed. Communication issues, like delay, data loss, and jitter, play a more critical role in the transient operation, which are to be deeply studied.
- The control center is required for the proposed solutions. However, the grid and communication infrastructure cannot always fulfill the requirements of control center based

solutions. Consequently, local controllers based solutions are to be developed and evaluated. For the local controller based solutions, the interactions and conflicts of different local controllers are to be identified. The coordination issues of local controllers, such as communication and information exchanges, is to be studied.

- Despite the proposed grid enhancement solutions that can enhance the grid controllability, deferring the upgrade of network infrastructure, the investment in implementing these solutions such as installation of the PE components and the possible maintenance cost, must be analyzed. Furthermore, the solutions must be optimized to avoid overuse and to prolong the lifetime of the PE components, eventually reducing the operation cost. Studies are needed to quantify the remuneration of the ancillary grid operation offered by the PE components and put it in relation to the investment of the proposed solutions. Consequently, the financial benefits of the proposed solutions can be compared with the upgrade of network infrastructure. The financial analysis assists system operators in optimizing their network development plan, allocating the appropriate and adequate investment on the grid controllability enhancement solutions and the infrastructure upgrade.

7 Appendix

7.1 Line Impedance of MV and LV Grids

The MV grid has 5 different types of feeders. The impedance of each line in each feeder is listed in Table 7.1-Table 7.5. Each line is represented by bus No. (bus No.x-bus No.y), to which the two terminals of the line are connected. All feeders have 1 terminal connected to the MV busbar of the HV/MV substation.

Table 7.1: Parameters of line impedance for feeder type 1

Line	Z (Ω)	Line	Z (Ω)	Line	Z (Ω)
MV-1	0.2038+j0.1056	1-2	0.2038+j0.1056	2-3	0.0624+j0.017

Table 7.2: Parameters of line impedance for feeder type 2

Line	Z (Ω)	Line	Z (Ω)	Line	Z (Ω)
MV-1	0.266+j0.1378	1-2	0.266+j0.1378	2-3	0.266+j0.1378
2-4	0.0663+j0.018	3-5	0.0663+j0.018		

Table 7.3: Parameters of line impedance for feeder type 3

Line	Z (Ω)	Line	Z (Ω)	Line	Z (Ω)
MV-1	0.0745+j0.0574	1-2	0.0745+j0.0574	2-3	0.0745+j0.0574
3-4	0.0745+j0.0574	4-5	0.0745+j0.0574	5-6	0.0745+j0.0574
6-7	0.0745+j0.0574				
2-8	0.0542+j0.0147	4-9	0.0542+j0.0147	5-10	0.0542+j0.0147
7-11	0.0542+j0.0147				

Table 7.4: Parameters of line impedance for feeder type 4

Line	Z (Ω)	Line	Z (Ω)	Line	Z (Ω)
MV-1	0.0917+j0.0706	1-2	0.0917+j0.0706	2-3	0.0917+j0.0706
3-4	0.0917+j0.0706	4-5	0.0917+j0.0706	5-6	0.0917+j0.0706
6-7	0.0917+j0.0706	7-8	0.0917+j0.0706	8-9	0.0917+j0.0706
2-10	0.0571+j0.0155	4-11	0.0571+j0.0155	5-12	0.0571+j0.0155
7-13	0.0571+j0.0155	9-14	0.0571+j0.0155		

Table 7.5: Parameters of line impedance for feeder type 5

Line	Z (Ω)	Line	Z (Ω)	Line	Z (Ω)
MV-1	0.0665+j0.0512	1-2	0.0665+j0.0512	2-3	0.0665+j0.0512
3-4	0.0665+j0.0512	4-5	0.0665+j0.0512	5-6	0.0665+j0.0512
6-7	0.0665+j0.0512	7-8	0.0665+j0.0512	8-9	0.0665+j0.0512
9-10	0.0665+j0.0512	10-11	0.0665+j0.0512	11-12	0.0665+j0.0512
12-13	0.0665+j0.0512	13-14	0.0665+j0.0512	14-15	0.0665+j0.0512
15-16	0.0665+j0.0512				
2-17	0.0729+j0.0198	4-18	0.0729+j0.0198	5-19	0.0729+j0.0198
7-20	0.0729+j0.0198	9-21	0.0729+j0.0198	11-22	0.0729+j0.0198
12-23	0.0729+j0.0198	14-24	0.0729+j0.0198	16-25	0.0729+j0.0198

Table 7.6: Parameters of line impedance in LV grid

Line	Z (Ω)	Line	Z (Ω)
A-B	0.0070+j0.0032	B-C	0.0070+j0.0032
C-D	0.0107+j0.0032	D-E	0.0107+j0.0032
A-F	0.0821+j0.0198		

The LV grid has 4 ac lines to connect the loads and one ac/dc line to connect the PV unit. The ac line impedance details are listed in Table 7.6.

In mesh grid operation, an additional LV feeder is modeled. This feeder consists of 4 lines. The line impedance details are listed in Table 7.7. The line impedance between the buses E/F and K is $0.0107 + j0.0032\Omega$.

If the PV unit is connected to the dc grid, the resistance of the line AF between the PV unit and the ST is 0.063Ω .

Table 7.7: Parameters of line impedance in the additional LV feeder of mesh grid

Line	Z (Ω)	Line	Z (Ω)
G-H	0.0070+j0.0032	H-I	0.0070+j0.0032
I-J	0.0107+j0.0032	J-K	0.0107+j0.0032

7.2 Composition of Load Components in MV Grid of Chapter 3

The details of load type and charging facilities of each bus in the MV grid are listed in Table 7.8-Table 7.15. The residential/commercial load is represented by RL/CL, respectively, and the charging facility in the residential/commercial area is represented by RC/CC, respectively.

Table 7.8: Load components in feeder 1

Bus	Load type	Bus	Load type
F101	CC	F103	CL

Table 7.9: Load components in feeder 2

Bus	Load type	Bus	Load type
F201	RL	203	RC

Table 7.10: Load components in feeder 3

Bus	Load type	Bus	Load type
F301	CL	F303	CC

Table 7.11: Load components in feeder 4

Bus	Load type	Bus	Load type
F401	RC	F404	RL
F405	RL		

Table 7.12: Load components in feeder 5

Bus	Load type	Bus	Load type
F501	RL	F503	RL
F506	RL	F508	RL
F509	RC	F510	RL
F511	RL		

Table 7.13: Load components in feeder 6

Bus	Load type	Bus	Load type
F601	CL	F603	CC
F606	CL	F608	CL
F609	CL	F610	CL
F611	CL		

Table 7.14: Load components in feeder 7

Bus	Load type	Bus	Load type
F701	RL	F703	RL
F506	RL	F508	RL
F710	RL	F711	RL
F712	RL	F713	RL
F714	RC		

Table 7.15: Load components in feeder 8

Bus	Load type	Bus	Load type
F801	CL	F803	CL
F806	CL	F808	CL
F810	CL	F813	CL
F815	CL	F817	CL
F818	CL	F819	CL
F820	CL	F821	CL
F822	CL	F823	CL
F824	CL	F825	CC

7.3 Composition of Power Components in MV Grid of Chapter 4

The details of power components, e.g., load type, charging facilities, and PV generation, of each bus in the MV grid are listed in Table 7.16-Table 7.23. The residential/commercial load is represented by RL/CL, respectively, and the charging facility in the residential/commercial area is represented by RC/CC, respectively.

Table 7.16: Power components in feeder 1

Bus	Power components	Bus	Power components
F101	CL+CC+PV	F103	CL

Table 7.17: Power components in feeder 2

Bus	Power components	Bus	Power components
F201	RL	203	RL+RC+PV

Table 7.18: Power components in feeder 3

Bus	Power components	Bus	Power components
F301	CL	F303	CL+CC+PV

Table 7.19: Power components in feeder 4

Bus	Power components	Bus	Power components
F401	RL+RC+PV	F404	RL
F405	RL		

Table 7.20: Power components in feeder 5

Bus	Power components	Bus	Power components
F501	RL	F503	RL
F506	RL	F508	RL
F509	RL+RC+PV	F510	RL
F511	RL		

Table 7.21: Power components in feeder 6

Bus	Power components	Bus	Power components
F601	CL	F603	CL+CC+PV
F606	CL	F608	CL
F609	CL	F610	CL
F611	CL		

Table 7.22: Power components in feeder 7

Bus	Power components	Bus	Power components
F701	RL	F703	RL
F506	RL	F508	RL
F710	RL	F711	RL
F712	RL	F713	RL
F714	RL+RC+PV		

Table 7.23: Power components in feeder 8

Bus	Power components	Bus	Power components
F801	CL	F803	CL
F806	CL	F808	CL
F810	CL	F813	CL
F815	CL	F817	CL+CC+PV
F818	CL	F819	CL
F820	CL	F821	CL
F822	CL	F823	CL
F824	CL	F825	CL+CC+PV

References

- [1] G. D. Carne, “Analysis of smart transformer features for electric distribution,” Ph.D. dissertation, Kiel University, 2018.
- [2] J. Lopes, N. Hatziaargyriou, J. Mutale, P. Djapic, and N. Jenkins, “Integrating distributed generation into electric power systems: A review of drivers, challenges and opportunities,” *Electric Power Systems Research*, vol. 77, no. 9, pp. 1189 – 1203, 2007, distributed Generation.
- [3] Statistisches-Bundesamt-Germany, accessed on Jan.31.2021. [Online]. Available: https://www.destatis.de/DE/Themen/Branchen-Unternehmen/Energie/Erzeugung/_inhalt.html
- [4] State-Schleswig-Holstein, “Windenergie,” accessed on Jan.31.2021. [Online]. Available: <https://www.schleswig-holstein.de/DE/Landesregierung/Themen/Energie/Windenergie/windenergie.html>
- [5] Statistisches-Bundesamt-Germany, “Anzahl der ladestationen für elektrofahrzeuge in deutschland,” accessed on Jan.31.2021. [Online]. Available: <https://de.statista.com/statistik/daten/studie/460234/umfrage/ladestationen-fuer-elektroautos-in-deutschland-monatlich/>
- [6] BMWK-Germany, “Masterplanladeinfrastruktur der bundesregierung,” accessed on Jan.31.2021.
- [7] P. Tielens and D. Van Hertem, “The relevance of inertia in power systems,” *Renewable and Sustainable Energy Reviews*, vol. 55, pp. 999–1009, 2016.
- [8] Z.-X. Zou, “Control of smart transformer-fed distribution grid,” Ph.D. dissertation, Kiel University, 2019.
- [9] Q. Jiang, Y. Gong, and H. Wang, “A battery energy storage system dual-layer control strategy for mitigating wind farm fluctuations,” *IEEE Transactions on Power Systems*, vol. 28, no. 3, pp. 3263–3273, Aug 2013.
- [10] H. Xu, U. Topcu, S. H. Low, C. R. Clarke, and K. M. Chandy, “Load-shedding probabilities with hybrid renewable power generation and energy storage,” in *2010 48th Annual Allerton Conference on Communication, Control, and Computing (Allerton)*, 2010, pp. 233–239.
- [11] N. Dinic, B. Fox, D. Flynn, L. Xu, and A. Kennedy, “Increasing wind farm capacity,” *IEE Proceedings - Generation, Transmission and Distribution*, vol. 153, no. 4, pp. 493–498, July 2006.

-
- [12] N. R. Tummuru, M. K. Mishra, and S. Srinivas, "Dynamic energy management of renewable grid integrated hybrid energy storage system," *IEEE Trans. Ind. Electron.*, vol. 62, no. 12, pp. 7728–7737, Dec 2015.
 - [13] P. Khamphakdi, M. Nitta, M. Hagiwara, and H. Akagi, "Zero-voltage ride-through capability of a transformerless back-to-back system using modular multilevel cascade converters for power distribution systems," *IEEE Trans. Power Electron.*, vol. 31, no. 4, pp. 2730–2741, April 2016.
 - [14] L. Wang, F. Bai, R. Yan, and T. K. Saha, "Real-time coordinated voltage control of pv inverters and energy storage for weak networks with high pv penetration," *IEEE Transactions on Power Systems*, vol. 33, no. 3, pp. 3383–3395, 2018.
 - [15] A. Woyte, V. Van Thong, R. Belmans, and J. Nijs, "Voltage fluctuations on distribution level introduced by photovoltaic systems," *IEEE Transactions on Energy Conversion*, vol. 21, no. 1, pp. 202–209, 2006.
 - [16] L. Calero, A. Thingvad, K. Suzuki, and M. Marinelli, "Grid loading due to ev charging profiles based on pseudo-real driving pattern and user behavior," *IEEE Transactions on Transportation Electrification*, vol. 5, no. 3, pp. 683–694, 2019.
 - [17] A. Ashtari, E. Bibeau, S. Shahidinejad, and T. Molinski, "Pev charging profile prediction and analysis based on vehicle usage data," *IEEE Transactions on Smart Grid*, vol. 3, no. 1, pp. 341–350, 2012.
 - [18] F. Ahmad, M. S. Alam, S. M. Shariff, and M. Krishnamurthy, "A cost-efficient approach to ev charging station integrated community microgrid: A case study of indian power market," *IEEE Transactions on Transportation Electrification*, vol. 5, no. 1, pp. 200–214, 2019.
 - [19] G. A. Putrus, P. Suwanapingkarl, D. Johnston, E. C. Bentley, and M. Narayana, "Impact of electric vehicles on power distribution networks," in *2009 IEEE Vehicle Power and Propulsion Conference*, 2009, pp. 827–831.
 - [20] Bundesnetzagentur-Germany, "Monitoringbericht 2019," accessed on Jan.31.2021.
 - [21] E. A. Martinez Cesena and P. Mancarella, "Distribution network reinforcement planning considering demand response support," 02 2015.
 - [22] J. L. Mathieu, S. Koch, and D. S. Callaway, "State estimation and control of electric loads to manage real-time energy imbalance," *IEEE Transactions on Power Systems*, vol. 28, no. 1, pp. 430–440, 2013.
 - [23] F. Elghitani and E. El-Saadany, "Smoothing net load demand variations using residential demand management," *IEEE Transactions on Industrial Informatics*, vol. 15, no. 1, pp. 390–398, 2019.

-
- [24] H. Hao, Y. Lin, A. S. Kowli, P. Barooah, and S. Meyn, "Ancillary service to the grid through control of fans in commercial building hvac systems," *IEEE Transactions on Smart Grid*, vol. 5, no. 4, pp. 2066–2074, 2014.
- [25] Y. Lin, P. Barooah, S. Meyn, and T. Middelkoop, "Experimental evaluation of frequency regulation from commercial building hvac systems," *IEEE Transactions on Smart Grid*, vol. 6, no. 2, pp. 776–783, 2015.
- [26] Y. Lin, P. Barooah, and J. L. Mathieu, "Ancillary services through demand scheduling and control of commercial buildings," *IEEE Transactions on Power Systems*, vol. 32, no. 1, pp. 186–197, Jan 2017.
- [27] J. Hu, C. Si, M. Lind, and R. Yu, "Preventing distribution grid congestion by integrating indirect control in a hierarchical electric vehicles management system," *IEEE Transactions on Transportation Electrification*, vol. 2, no. 3, pp. 290–299, Sep. 2016.
- [28] O. Hafez and K. Bhattacharya, "Integrating ev charging stations as smart loads for demand response provisions in distribution systems," *IEEE Transactions on Smart Grid*, vol. 9, no. 2, pp. 1096–1106, March 2018.
- [29] K. Knezovic, S. Martinenas, P. B. Andersen, A. Zecchino, and M. Marinelli, "Enhancing the role of electric vehicles in the power grid: Field validation of multiple ancillary services," *IEEE Transactions on Transportation Electrification*, vol. 3, no. 1, pp. 201–209, March 2017.
- [30] Y. Liao and C. Lu, "Dispatch of ev charging station energy resources for sustainable mobility," *IEEE Transactions on Transportation Electrification*, vol. 1, no. 1, pp. 86–93, June 2015.
- [31] H. Kikusato, K. Mori, S. Yoshizawa, Y. Fujimoto, H. Asano, Y. Hayashi, A. Kawashima, S. Inagaki, and T. Suzuki, "Electric vehicle charge discharge management for utilization of photovoltaic by coordination between home and grid energy management systems," *IEEE Transactions on Smart Grid*, vol. 10, no. 3, pp. 3186–3197, 2019.
- [32] D. Zhang, L. Y. Wang, J. Jiang, and W. Zhang, "Load prediction and distributed optimal control of on-board battery systems for dual-source trolleybuses," *IEEE Transactions on Transportation Electrification*, vol. 3, no. 1, pp. 284–296, 2017.
- [33] S. F. Aliabadi, S. A. Taher, and M. Shahidehpour, "Smart deregulated grid frequency control in presence of renewable energy resources by evs charging control," *IEEE Transactions on Smart Grid*, vol. 9, no. 2, pp. 1073–1085, March 2018.

-
- [34] A. Malhotra, G. Binetti, A. Davoudi, and I. D. Schizas, "Distributed power profile tracking for heterogeneous charging of electric vehicles," *IEEE Transactions on Smart Grid*, vol. 8, no. 5, pp. 2090–2099, Sep. 2017.
- [35] A. S. Masoum, S. Deilami, P. S. Moses, M. A. S. Masoum, and A. Abu-Siada, "Smart load management of plug-in electric vehicles in distribution and residential networks with charging stations for peak shaving and loss minimisation considering voltage regulation," *IET Generation, Transmission Distribution*, vol. 5, no. 8, pp. 877–888, August 2011.
- [36] L. Wang, D. H. Liang, A. F. Crossland, P. C. Taylor, D. Jones, and N. S. Wade, "Coordination of multiple energy storage units in a low-voltage distribution network," *IEEE Transactions on Smart Grid*, vol. 6, no. 6, pp. 2906–2918, Nov 2015.
- [37] M. Bahramipanah, D. Torregrossa, R. Cherkaoui, and M. Paolone, "A decentralized adaptive model-based real-time control for active distribution networks using battery energy storage systems," *IEEE Transactions on Smart Grid*, vol. 9, no. 4, pp. 3406–3418, 2018.
- [38] S. J. Lee, J. H. Kim, C. H. Kim, S. K. Kim, E. S. Kim, D. U. Kim, K. K. Mehmood, and S. U. Khan, "Coordinated control algorithm for distributed battery energy storage systems for mitigating voltage and frequency deviations," *IEEE Transactions on Smart Grid*, vol. 7, no. 3, pp. 1713–1722, May 2016.
- [39] Y. S. Kim, E. S. Kim, and S. I. Moon, "Frequency and voltage control strategy of standalone microgrids with high penetration of intermittent renewable generation systems," *IEEE Transactions on Power Systems*, vol. 31, no. 1, pp. 718–728, Jan 2016.
- [40] C. A. Hill, M. C. Such, D. Chen, J. Gonzalez, and W. M. Grady, "Battery energy storage for enabling integration of distributed solar power generation," *IEEE Transactions on Smart Grid*, vol. 3, no. 2, pp. 850–857, June 2012.
- [41] X. Li, D. Hui, and X. Lai, "Battery energy storage station (bess)-based smoothing control of photovoltaic (pv) and wind power generation fluctuations," *IEEE Transactions on Sustainable Energy*, vol. 4, no. 2, pp. 464–473, April 2013.
- [42] H. Rahimi-Eichi, U. Ojha, F. Baronti, and M. Y. Chow, "Battery management system: An overview of its application in the smart grid and electric vehicles," *IEEE Industrial Electronics Magazine*, vol. 7, no. 2, pp. 4–16, June 2013.
- [43] M. A. Abdullah, K. M. Muttaqi, D. Sutanto, and A. P. Agalgaonkar, "An effective power dispatch control strategy to improve generation schedulability and supply reliability of a wind farm using a battery energy storage system," *IEEE Transactions on Sustainable Energy*, vol. 6, no. 3, pp. 1093–1102, July 2015.

-
- [44] F. Sossan, E. Namor, R. Cherkaoui, and M. Paolone, "Achieving the dispatchability of distribution feeders through prosumers data driven forecasting and model predictive control of electrochemical storage," *IEEE Transactions on Sustainable Energy*, vol. 7, no. 4, pp. 1762–1777, 2016.
- [45] H. H. Abdeltawab and Y. A. I. Mohamed, "Mobile energy storage scheduling and operation in active distribution systems," *IEEE Transactions on Industrial Electronics*, vol. 64, no. 9, pp. 6828–6840, 2017.
- [46] Q. Wei, D. Liu, F. L. Lewis, Y. Liu, and J. Zhang, "Mixed iterative adaptive dynamic programming for optimal battery energy control in smart residential microgrids," *IEEE Transactions on Industrial Electronics*, vol. 64, no. 5, pp. 4110–4120, May 2017.
- [47] S. Negarestani, M. Fotuhi-Firuzabad, M. Rastegar, and A. Rajabi-Ghahnavieh, "Optimal sizing of storage system in a fast charging station for plug-in hybrid electric vehicles," *IEEE Transactions on Transportation Electrification*, vol. 2, no. 4, pp. 443–453, Dec 2016.
- [48] E. Stai, L. Reyes-Chamorro, F. Sossan, J. Le Boudec, and M. Paolone, "Dispatching stochastic heterogeneous resources accounting for grid and battery losses," *IEEE Transactions on Smart Grid*, vol. 9, no. 6, pp. 6522–6539, 2018.
- [49] L. K. Gan, J. K. H. Shek, and M. A. Mueller, "Analysis of tower shadow effects on battery lifetime in standalone hybrid wind-diesel-battery systems," *IEEE Transactions on Industrial Electronics*, vol. 64, no. 8, pp. 6234–6244, Aug 2017.
- [50] Z. Yang, A. Bose, H. Zhong, N. Zhang, Q. Xia, and C. Kang, "Optimal reactive power dispatch with accurately modeled discrete control devices: A successive linear approximation approach," *IEEE Transactions on Power Systems*, vol. 32, no. 3, pp. 2435–2444, 2017.
- [51] J. Choi and S. Moon, "The dead band control of ltc transformer at distribution substation," *IEEE Transactions on Power Systems*, vol. 24, no. 1, pp. 319–326, 2009.
- [52] A. Ulinuha, M. A. S. Masoum, and S. M. Islam, "Optimal scheduling of ltc and shunt capacitors in large distorted distribution systems using evolutionary-based algorithms," *IEEE Transactions on Power Delivery*, vol. 23, no. 1, pp. 434–441, 2008.
- [53] T. L. Vandoorn, B. Renders, L. Degroote, B. Meersman, and L. Vandeveld, "Active load control in islanded microgrids based on the grid voltage," *IEEE Transactions on Smart Grid*, vol. 2, no. 1, pp. 139–151, 2011.

-
- [54] P. J. Douglass, R. Garcia-Valle, J. Østergaard, and O. C. Tudora, "Voltage-sensitive load controllers for voltage regulation and increased load factor in distribution systems," *IEEE Transactions on Smart Grid*, vol. 5, no. 5, pp. 2394–2401, Sep. 2014.
- [55] P. M. S. Carvalho, P. F. Correia, and L. A. F. M. Ferreira, "Distributed reactive power generation control for voltage rise mitigation in distribution networks," *IEEE Transactions on Power Systems*, vol. 23, no. 2, pp. 766–772, May 2008.
- [56] M. Badoni, A. Singh, and B. Singh, "Variable forgetting factor recursive least square control algorithm for dstatcom," *IEEE Trans. Power Del.*, vol. 30, no. 5, pp. 2353–2361, Oct 2015.
- [57] P. Dong, L. Xu, Y. Lin, and M. Liu, "Multi-objective coordinated control of reactive compensation devices among multiple substations," *IEEE Transactions on Power Systems*, vol. 33, no. 3, pp. 2395–2403, May 2018.
- [58] H. D. Nguyen and K. Turitsyn, "Voltage multistability and pulse emergency control for distribution system with power flow reversal," *IEEE Transactions on Smart Grid*, vol. 6, no. 6, pp. 2985–2996, Nov 2015.
- [59] K. Christakou, D.-C. Tomozei, M. Bahrampianah, J.-Y. Le Boudec, and M. Paolone, "Primary voltage control in active distribution networks via broadcast signals: The case of distributed storage," *IEEE Transactions on Smart Grid*, vol. 5, no. 5, pp. 2314–2325, 2014.
- [60] H. Yi, M. H. Hajiesmaili, Y. Zhang, M. Chen, and X. Lin, "Impact of the uncertainty of distributed renewable generation on deregulated electricity supply chain," *IEEE Transactions on Smart Grid*, vol. 9, no. 6, pp. 6183–6193, Nov 2018.
- [61] C. Kumar and M. K. Mishra, "A voltage-controlled dstatcom for power-quality improvement," *IEEE Trans. Power Del.*, vol. 29, no. 3, pp. 1499–1507, June 2014.
- [62] S. Stankovic and L. Söder, "Analytical estimation of reactive power capability of a radial distribution system," *IEEE Transactions on Power Systems*, vol. 33, no. 6, pp. 6131–6141, 2018.
- [63] A. Spring, G. Wirth, G. Becker, R. Pardatscher, and R. Witzmann, "Grid influences from reactive power flow of photovoltaic inverters with a power factor specification of one," *IEEE Transactions on Smart Grid*, vol. 7, no. 3, pp. 1222–1229, 2016.
- [64] A. Safavizadeh, G. R. Yousefi, and H. R. Karshenas, "Voltage variation mitigation using reactive power management of distributed energy resources in a smart distribution system," *IEEE Transactions on Smart Grid*, vol. 10, no. 2, pp. 1907–1915, 2019.

-
- [65] M. Brenna, E. De Berardinis, L. Delli Carpini, F. Foiadelli, P. Paulon, P. Petroni, G. Sapienza, G. Scrosati, and D. Zaninelli, "Automatic distributed voltage control algorithm in smart grids applications," *IEEE Transactions on Smart Grid*, vol. 4, no. 2, pp. 877–885, June 2013.
- [66] M. A. Elshaharty, A. Luna, J. I. Candela, and P. Rodriguez, "A unified power flow controller using a power electronics integrated transformer," *IEEE Transactions on Power Delivery*, vol. 34, no. 3, pp. 828–839, 2019.
- [67] L. Cipcigan and P. Taylor, "Investigation of the reverse power flow requirements of high penetrations of small-scale embedded generation," *Renewable Power Generation, IET*, vol. 1, pp. 160 – 166, 10 2007.
- [68] E. Schweitzer, A. Scaglione, A. Monti, and G. A. Pagani, "Automated generation algorithm for synthetic medium voltage radial distribution systems," *IEEE Journal on Emerging and Selected Topics in Circuits and Systems*, vol. 7, no. 2, pp. 271–284, 2017.
- [69] S. Abdelrahman and J. V. Milanovic, "Practical approaches to assessment of harmonics along radial distribution feeders," *IEEE Transactions on Power Delivery*, vol. 34, no. 3, pp. 1184–1192, 2019.
- [70] M. Saradarzadeh, S. Farhangi, J. L. Schanen, P. O. Jeannin, and D. Frey, "The benefits of looping a radial distribution system with a power flow controller," in *2010 IEEE International Conference on Power and Energy*. IEEE, Nov 2010, pp. 723–728.
- [71] S. K. Chaudhary, J. M. Guerrero, and R. Teodorescu, "Enhancing the capacity of the ac distribution system using dc interlinks - a step toward future dc grid," *IEEE Trans. Smart Grid*, vol. 6, no. 4, pp. 1722–1729, July 2015.
- [72] C. Chen, C. Tsai, C. Lin, W. Hsieh, and T. Ku, "Loading balance of distribution feeders with loop power controllers considering photovoltaic generation," *IEEE Transactions on Power Systems*, vol. 26, no. 3, pp. 1762–1768, 2011.
- [73] N. Okada, "Verification of control method for a loop distribution system using loop power flow controller," in *2006 IEEE PES Power Systems Conference and Exposition*. IEEE, Oct 2006, pp. 2116–2123.
- [74] R. Zhu, M. Liserre, M. Langwasser, and C. Kumar, "Operation and control of the smart transformer in meshed and hybrid grids: Choosing the appropriate smart transformer control and operation scheme," *IEEE Industrial Electronics Magazine*, vol. 15, no. 1, pp. 43–57, 2021.

-
- [75] M. Liserre, G. Buticchi, M. Andresen, G. De Carne, L. F. Costa, and Z.-X. Zou, "The smart transformer: Impact on the electric grid and technology challenges," *IEEE Industrial Electronics Magazine*, vol. 10, pp. 46–58, 2016.
- [76] S. Bhattacharya, "Transforming the transformer," *IEEE Spectrum*, vol. 54, no. 7, pp. 38–43, 2017.
- [77] D. Shah and M. L. Crow, "Online volt-var control for distribution systems with solid-state transformers," *IEEE Trans. Power Del.*, vol. 31, no. 1, pp. 343–350, Feb 2016.
- [78] X. She, A. Q. Huang, S. Lukic, and M. E. Baran, "On integration of solid-state transformer with zonal dc microgrid," *IEEE Trans. Smart Grid*, vol. 3, no. 2, pp. 975–985, June 2012.
- [79] A. Q. Huang, "Medium-voltage solid-state transformer: Technology for a smarter and resilient grid," *IEEE Ind. Electron. Mag.*, vol. 10, no. 3, pp. 29–42, Sept 2016.
- [80] L. Costa, G. De Carne, G. Buticchi, and M. Liserre, "The smart transformer: A solid-state transformer tailored to provide ancillary services to the distribution grid," *IEEE Power Electronics Magazine*, vol. 4, no. 2, pp. 56–67, June 2017.
- [81] F. Xue, R. Yu, and A. Q. Huang, "A 98.3," *IEEE Transactions on Industrial Electronics*, vol. 64, no. 11, pp. 9094–9103, 2017.
- [82] R. Palma-Behnke, C. Benavides, F. Lanas, B. Severino, L. Reyes, J. Llanos, and D. Saez, "A microgrid energy management system based on the rolling horizon strategy," *IEEE Transactions on Smart Grid*, vol. 4, no. 2, pp. 996–1006, June 2013.
- [83] N. Korada and M. K. Mishra, "Grid adaptive power management strategy for an integrated microgrid with hybrid energy storage," *IEEE Transactions on Industrial Electronics*, vol. 64, no. 4, pp. 2884–2892, April 2017.
- [84] Z. Deng, M. Liu, Y. Ouyang, S. Lin, and M. Xie, "Multi-objective mixed-integer dynamic optimization method applied to optimal allocation of dynamic var sources of power systems," *IEEE Transactions on Power Systems*, vol. 33, no. 2, pp. 1683–1697, March 2018.
- [85] M. El-Moursi and A. Sharaf, "Novel reactive power controllers for the statcom and sssc," *Electric Power Systems Research*, vol. 76, no. 4, pp. 228 – 241, 2006.
- [86] Z. Yang, C. Shen, L. Zhang, M. L. Crow, and S. Atcitty, "Integration of a statcom and battery energy storage," *IEEE Transactions on Power Systems*, vol. 16, no. 2, pp. 254–260, May 2001.

-
- [87] F. Hahn, L. Camurca, and M. Liserre, "Investigation of modular multilevel converters for e-statcom applications," in *2020 IEEE 29th International Symposium on Industrial Electronics (ISIE)*, 2020, pp. 1028–1032.
- [88] A. F. Cupertino, W. C. S. Amorim, H. A. Pereira, S. I. Seleme Junior, S. K. Chaudhary, and R. Teodorescu, "High performance simulation models for es-statcom based on modular multilevel converters," *IEEE Transactions on Energy Conversion*, vol. 35, no. 1, pp. 474–483, 2020.
- [89] P. Richardson, D. Flynn, and A. Keane, "Local versus centralized charging strategies for electric vehicles in low voltage distribution systems," *IEEE Transactions on Smart Grid*, vol. 3, no. 2, pp. 1020–1028, 2012.
- [90] J. Garcia-Villalobos, I. Zamora, J. San Martin, F. Asensio, and V. Aperribay, "Plug-in electric vehicles in electric distribution networks: A review of smart charging approaches," *Renewable and Sustainable Energy Reviews*, vol. 38, no. C, pp. 717–731, 2014.
- [91] M. Kesler, M. C. Kisacikoglu, and L. M. Tolbert, "Vehicle-to-grid reactive power operation using plug-in electric vehicle bidirectional offboard charger," *IEEE Transactions on Industrial Electronics*, vol. 61, no. 12, pp. 6778–6784, Dec 2014.
- [92] H. Valizadeh Haghi and Z. Qu, "A kernel-based predictive model of ev capacity for distributed voltage control and demand response," *IEEE Transactions on Smart Grid*, vol. 9, no. 4, pp. 3180–3190, 2018.
- [93] F. Hoffmann, L. Camurca, and M. Liserre, "Modular ev fast charging station architectures based on multiphase-medium-frequency transformer," in *IECON 2018 - 44th Annual Conference of the IEEE Industrial Electronics Society*, 2018, pp. 1327–1332.
- [94] *Konduktive Ladesysteme für Elektrofahrzeuge*, Standard E DIN EN 61 851-23.
- [95] W. Du, F. Tuffner, K. P. Schneider, R. H. Lasseter, J. Xie, Z. Chen, and B. P. Bhattarai, "Modeling of grid-forming and grid-following inverters for dynamic simulation of large-scale distribution systems," *IEEE Transactions on Power Delivery*, 2020.
- [96] G. De Carne, M. Liserre, and C. Vournas, "On-line load sensitivity identification in lv distribution grids," *IEEE Transactions on Power Systems*, vol. 32, no. 2, pp. 1570–1571, March 2017.
- [97] G. D. Carne, G. Buticchi, M. Liserre, and C. Vournas, "Load control using sensitivity identification by means of smart transformer," *IEEE Transactions on Smart Grid*, vol. 9, no. 4, pp. 2606–2615, July 2018.

-
- [98] G. De Carne, G. Buticchi, Z. Zou, and M. Liserre, "Reverse power flow control in a st-fed distribution grid," *IEEE Transactions on Smart Grid*, vol. 9, no. 4, pp. 3811–3819, July 2018.
- [99] J. C. Vasquez, R. A. Mastromauro, J. M. Guerrero, and M. Liserre, "Voltage support provided by a droop-controlled multifunctional inverter," *IEEE Transactions on Industrial Electronics*, vol. 56, no. 11, pp. 4510–4519, 2009.
- [100] "Lv engine," accessed on Jan.31.2021. [Online]. Available: https://www.spenergynetworks.co.uk/pages/lv_engine.aspx
- [101] Z. Zou, G. Buticchi, and M. Liserre, "Control and communication in the smart transformer-fed grid," in *2016 IEEE 21st International Conference on Emerging Technologies and Factory Automation (ETFA)*. IEEE, Sept 2016.
- [102] Y. Zhang, Y. Xu, and Z. Y. Dong, "Robust ensemble data analytics for incomplete pmu measurements-based power system stability assessment," *IEEE Transactions on Power Systems*, vol. 33, no. 1, pp. 1124–1126, Jan 2018.
- [103] X. Wang, D. Shi, J. Wang, Z. Yu, and Z. Wang, "Online identification and data recovery for pmu data manipulation attack," *IEEE Transactions on Smart Grid*, vol. 10, no. 6, pp. 5889–5898, Nov 2019.
- [104] S. Sarri, M. Paolone, R. Cherkaoui, A. Borghetti, F. Napolitano, and C. A. Nucci, "State estimation of active distribution networks: Comparison between wls and iterated kalman-filter algorithm integrating pmus," in *2012 3rd IEEE PES Innovative Smart Grid Technologies Europe (ISGT Europe)*. IEEE, 2012.
- [105] "Load representation for dynamic performance analysis (of power systems)," *IEEE Transactions on Power Systems*, vol. 8, no. 2, pp. 472–482, 1993.
- [106] J. V. Milanovic and S. Mat Zali, "Validation of equivalent dynamic model of active distribution network cell," *IEEE Transactions on Power Systems*, vol. 28, no. 3, pp. 2101–2110, 2013.
- [107] Y. Wan, M. A. A. Murad, M. Liu, and F. Milano, "Voltage frequency control using svc devices coupled with voltage dependent loads," *IEEE Transactions on Power Systems*, vol. 34, no. 2, pp. 1589–1597, 2019.
- [108] L. M. Korunovic, J. V. Milanovic, S. Z. Djokic, K. Yamashita, S. M. Villanueva, and S. Sterpu, "Recommended parameter values and ranges of most frequently used static load models," *IEEE Transactions on Power Systems*, vol. 33, no. 6, pp. 5923–5934, 2018.

-
- [109] D. P. Stojanovic, L. M. Korunovic, and J. Milanovic, "Dynamic load modelling based on measurements in medium voltage distribution network," *Electric Power Systems Research*, vol. 78, no. 2, pp. 228 – 238, 2008.
- [110] A. Ballanti and L. F. Ochoa, "Voltage-led load management in whole distribution networks," *IEEE Transactions on Power Systems*, vol. 33, no. 2, pp. 1544–1554, 2018.
- [111] Z. Wang and J. Wang, "Review on implementation and assessment of conservation voltage reduction," *IEEE Transactions on Power Systems*, vol. 29, no. 3, pp. 1306–1315, 2014.
- [112] F. Neves, A. C. Finamore, S. C. Madeira, and R. Henriques, "Mining actionable patterns of road mobility from heterogeneous traffic data using biclustering," *IEEE Transactions on Intelligent Transportation Systems*, 2021.
- [113] R. Bo and F. Li, "Probabilistic Imp forecasting considering load uncertainty," *IEEE Transactions on Power Systems*, vol. 24, no. 3, pp. 1279–1289, Aug 2009.
- [114] A. Ballanti, L. N. Ochoa, K. Bailey, and S. Cox, "Unlocking new sources of flexibility: Class: The world's largest voltage-led load-management project," *IEEE Power and Energy Magazine*, vol. 15, no. 3, pp. 52–63, 2017.
- [115] A. Bokhari, A. Alkan, R. Dogan, M. Diaz-Aguilo, F. de Leon, D. Czarkowski, Z. Zabbar, L. Birenbaum, A. Noel, and R. E. Uosef, "Experimental determination of the zip coefficients for modern residential, commercial, and industrial loads," *IEEE Transactions on Power Delivery*, vol. 29, no. 3, pp. 1372–1381, June 2014.
- [116] K. Christakou, J.-Y. LeBoudec, M. Paolone, and D.-C. Tomozei, "Efficient computation of sensitivity coefficients of node voltages and line currents in unbalanced radial electrical distribution networks," *IEEE Transactions on Smart Grid*, vol. 4, no. 2, pp. 741–750, 2013.
- [117] S. Giacomuzzi, G. De Carne, S. Pugliese, G. Buja, M. Liserre, and A. Kazerooni, "Synchronization of low voltage grids fed by smart and conventional transformers," *IEEE Transactions on Smart Grid*, 2021.
- [118] Power-Network-UK, "Flexible urban networks low voltage," accessed on Jan.31.2021. [Online]. Available: <https://innovation.ukpowernetworks.co.uk/projects/fun-lv/>
- [119] A. Soroudi, *Power System Optimization Modeling in GAMS*, 08 2017.
- [120] G. Mavrotas, "Effective implementation of the e-constraint method in multi-objective mathematical programming problems," *Applied Mathematics and Computation*, vol. 213, no. 2, pp. 455–465, 2009.

-
- [121] J. A. Pomilio and S. M. Deckmann, "Characterization and compensation of harmonics and reactive power of residential and commercial loads," *IEEE Transactions on Power Delivery*, vol. 22, no. 2, pp. 1049–1055, April 2007.
- [122] K. Fekete, Z. Klaic, and L. Majdandzic, "Expansion of the residential photovoltaic systems and its harmonic impact on the distribution grid," *Renewable Energy*, vol. 43, pp. 140 – 148, 2012.
- [123] C. Kumar and M. Liserre, "A new prospective of smart transformer application: Dual microgrid (dmg) operation," in *IECON 2015 - 41st Annual Conference of the IEEE Industrial Electronics Society*, 2015.
- [124] R. Teodorescu, M. Liserre, and P. Rodriguez, *Grid Converters for Photovoltaic and Wind Power Systems*. WILEY, 2011.
- [125] *Engineering Recommendation G5/4-1 - Planning Levels for Harmonic Voltage Distortion And The Connection Of Non-Linear Equipment To Transmission Systems And Distribution Networks In The United Kingdom*, Energy Networks Association Std., October 2005.

List of Figures

1.1	Structure of the thesis and related publications.	8
2.1	Demand redispatch for tracking dispatch plan by means of BESS. (a) Schematic diagram of an LV grid (in BESS converter, '~': ac, '=': dc). (b) Power behavior of the LV grid without/with the regulation in respect to dispatch plan [J1].	14
2.2	Voltage regulation by reactive power injection with PE component. (a) Schematic diagram of a grid. (b) Voltage behavior without/with capacitive reactive power injection for an under-voltage condition. (c) Voltage behavior without/with inductive reactive power injection for an over-voltage condition. .	16
2.3	LPC based approach for meshed grid application.	17
2.4	Topologies of power electronics based transformer. (a) SST topology. (b) B2B topology.	19
2.5	Controller structure of ST's MV stage.	20
2.6	Controller structure of ST's dc/dc stage.	21
2.7	Controller structure of ST's LV stage.	22
2.8	Topologies of ES-STATCOM. (a) Conventional approach with an MV/LV transformer. (b) MMC based approach connected to MV grid.	23
2.9	Controller structure of conventional approach based ES-STATCOM.	24
2.10	Topologies of FCS. (a) Individual ac/dc stages based approach for LV grid connection. (b) Aggregated ac/dc stage based approach for LV grid connection. (c) MMC based approach for MV grid connection.	25
2.11	Controller structure of aggregated ac/dc stage based FCS.	27
2.12	Grid connecting strategies: (a) Grid-following strategy. (b) Grid-forming strategy in inter-connected grid. (c) Grid-forming strategy in islanded grid. .	28
2.13	Correlation of ST active power flow and ST-connected bus voltage behavior. (a) Topology of the grid. (b) Profiles of ST active power flow and bus B voltage.	30
3.1	Research focus of Chapter 3: Load-leveling approach in MV grid based on fast charging stations.	34
3.2	Online load identification with reactive power injection from PE components. (a) Reactive power injection. (b) Voltage response. (c) Load active power reaction to corresponding voltage change.	36
3.3	Voltage and power behavior with reactive power injection from FCSs. (a) Reactive power injection from all FCSs. (b) Voltage response of different buses to reactive power from FCSs. (c) Active power reaction to voltage change. (d) Power behavior of the grid.	37

3.4	Impact of reactive power injection on the load variation with different power-voltage sensitivity in a simplified feeder. (a) Topology of the simplified feeder. (b) Load variation of Group 1. (c) Load variation of Group 2. (d) Load variation of Group 3. (e) Load variation of Group 4.	38
3.5	Time-line for related actuators and actions of the proposed load-leveling approach.	40
3.6	Flow chart of the load-leveling scheme implementation.	42
3.7	Structure of MV grid for evaluation.	46
3.8	24 h active power profiles. (a) Profiles of residential/commercial load. (b) Profiles of FCS in residential/commercial areas. (c) Profile of power of the HV/MV substation.	47
3.9	Probability density of 1000 variation scenarios. (a) Probability density of power variation with respect to average power 0.36 pu following Gaussian distribution. (b) Probability density of sensitivity coefficients variation between (0.5–2.0) following uniform distribution.	48
3.10	24 h demand power mismatch. (a) Power mismatch with respect to the power forecast of Case O, Case 1, Case 3, and Case 4. (b) Power mismatch with respect to the power forecast of Case O, Case 2, Case 3, and Case 5. (c) Power mismatch with respect to the power forecast of Case 4 and Case 5. (d) Power mismatch with respect to the power forecast of Case 5, Case 6, and Case 7.	51
3.11	24 h change of OLTC tap positions. (a) Change of OLTC tap positions of Case O, 1, 3, and 4. (b) Change of OLTC tap positions of Case O, 2, 3, and 5.	52
3.12	24 h power change and voltage behaviors of bus 25 in feeder F8. (a) Power changes with respect to uncontrolled power. (b) Voltage changes with respect to uncontrolled voltage.	52
3.13	Probability density of power mismatch of the testing grid. (a) Case O vs. Case 1. (b) Case O vs. Case 2. (c) Case O vs. Case 3. (d) Case O vs. Case 4. (e) Case O vs. Case 5. (f) Case 6 vs. Case 7.	53
3.14	Cumulative probability distribution of absolute power mismatch of 1000 Monte-Carlo scenarios. (a) Comparison of Case O, Case 2, Case 3, and Case 5. (b) Comparison of Case 4, Case 5, Case 6, and Case 7.	55
3.15	Probability density of absolute power mismatch in Case O, Case 1, and Case 3.	55
3.16	Probability density of losses of 1000 Monte-Carlo scenarios. (a) Losses in Case O vs. losses in Stage 1 of Case 3. (b) Losses in Case O vs. Losses in Stage 1 of Case 5. (c) Losses in Stage 1 of Case 5 vs. Losses in Stage 1 of Case 7. (d) Losses in Stage 1 vs. Stage 2, Case 5.	56
3.17	Comparison of reactive power injection in Stage 1 and Stage 2 of Case 5. (a) One scenario at 09:00. (b) One scenario at 18:30.	57

3.18	Probability density of power factor of 1000 Monte-Carlo scenarios. (a) Probability density of power factor in Case O and Case 5. (b) Probability density of power factor in Stage 1 and Stage 2, Case 5.	59
3.19	Probability density of voltage of 1000 Monte-Carlo scenarios. (a) Voltage of MV busbar in Case O and Case 5. (b) Voltage of MV busbar in Stage 1 and Stage 2, Case 5. (c) Voltage of bus F825 in Case O and Case 5. (b) Voltage of bus F825 in Stage 1 and Stage 2, Case 5.	60
3.20	Schematic presentation of the PHIL setup.	61
3.21	Laboratory implementation of PHIL setup.	61
3.22	Schematic presentation of the PHIL testing feeder.	62
3.23	Grid behavior with FCS reactive power injection. (a) Active/reactive power of FCS in RSCAD (blue line for active power, red line for inductive reactive power). (b) Voltage response of bus 5 to reactive power injection. (c) Demand behavior of load 5 to voltage response. (d) Power variation of the feeder to inductive reactive power injection. (e) Active/reactive power of FCS in RSCAD (blue line for active power, red line for capacitive reactive power). (f) Voltage response of bus 5 to reactive power injection. (g) Demand behavior of load 5 to voltage response. (h) Power variation of the feeder to capacitive reactive power injection.	64
3.24	600 s load behavior from PHIL test. (a) Feeder power with/without load leveling respect to the demand forecast. (b) Power mismatch in relation to the demand forecast.	65
4.1	Research focus of Chapter 4: Voltage regulation in distribution grid. (a). Solution with ES-STATCOM. (b) Solution with ST.	68
4.2	Impact of reactive power injection on voltage deviation of ES-STATCOM bus, in a simplified radial feeder with different R/X ratios. (a) A simplified radial feeder with single load and single ES-STATCOM. (b) Voltage deviations of ES-STATCOM bus in group 1. (c) Voltage deviations of ES-STATCOM bus in group 2. (d) Voltage deviations of ES-STATCOM bus in group 3. (e) Voltage deviations of ES-STATCOM bus in group 4.	69
4.3	Impact on load bus voltage from voltage set-points in an ST-fed feeder. (a) Simplified ST-fed radial LV feeder. (b) Voltage variations of load bus in group 1. (c) Voltage variations of load bus in group 2.	71
4.4	Framework of voltage regulation schemes with PE components. (a) Framework with the ES-STATCOMs. (b) Framework with the STs: in MV grid. (c) Framework with the STs: in LV grid.	73
4.5	Grid for evaluation of the proposed voltage regulation. (a) MV grid. (b) LV grid of Case 1. (c) LV grid of Case 2.	83

4.6	24 h profiles of power demand. (a) Average active power profiles for residential and commercial load of single MV bus. (b) Average charging power profiles for residential and commercial charging facility. (c) Average PV generation profile. (d) PV generation profile with 15 % increase.	84
4.7	24 h voltage behaviors of buses in MV grid. (a) Without ST. (b) With injection of reactive power from ST according to Eq.(4.25).	85
4.8	Voltage amplitudes in MV grid at 18:00 of both cases with four scenarios, stream A. (a) Voltage amplitudes of bus F611. (a) Voltage amplitudes of bus F825.	89
4.9	24 h voltage profiles of buses and corresponding injection of reactive power with scenario 1, stream A. (a) Voltage of bus F603. (b) Voltage of bus F714. (c) Injection of reactive power from PE components in feeder 6. (d) Injection of reactive power from PE components in feeder 7.	89
4.10	24 h voltage profiles of buses and corresponding injection of reactive power with scenario 2, stream A. (a) Voltage of bus F101. (b) Voltage of bus F825. (c) Injection of reactive power from PE components in feeder 1. (d) Injection of reactive power from PE components in feeder 8.	91
4.11	24 h voltage profiles of buses and corresponding injection of reactive power with scenario 3, stream A. (a) Voltage of bus F203. (b) Voltage of bus F401. (c) Injection of reactive power from PE components in feeder 2. (d) Injection of reactive power from PE components in feeder 4.	92
4.12	24 h voltage profiles of buses and corresponding injection of reactive power with scenario 4, stream A. (a) Voltage of bus F503. (b) Voltage of bus F401. (c) Injection of reactive power from PE components in feeder 5. (d) Injection of reactive power from PE components in feeder 4.	93
4.13	Boxplot of voltage for all buses in the LV grid within 24 h, stream A. (a) Case 1, scenario 1. (b) Case 2, scenario 1. (c) Case 1, scenario 2. (d) Case 2, scenario 2.	94
4.14	Boxplot of voltage for all buses in the LV grid within 24 h, stream A. (a) Case 1, scenario 3. (b) Case 2, scenario 3. (c) Case 1, scenario 4. (d) Case 2, scenario 4.	95
4.15	Boxplot of voltage for all buses in the LV grid within 24 h, stream B. (a) Case 1, scenario 3. (b) Case 1, scenario 4.	97
4.16	24 h voltage behavior and reactive power injection of Case 1 in streams A and B. (a) Voltage of bus A in the LV grid, scenario 3. (b) Injection of reactive power in feeder 4, scenario 3. (c) Voltage of substation busbar, scenario 4. (d) Injection of reactive power in feeder 1, scenario 4.	97
4.17	24 h behavior of voltage and reactive power injection of Case 1, stream B. (a) Voltage of substation busbar, scenarios 3 and 4. (b) Injection of reactive power in feeder 4, scenarios 3 and 4.	98

4.18	\bar{d}_{MV} values of ES-STATCOM with different converter power ratings respecting the ST in the MV grid. (a) Scenario 1. (b) Scenario 4.	99
4.19	\bar{d}_{LV} values of ES-STATCOM with different converter power ratings respecting the ST in the LV grid. (a) Scenario 1. (b) Scenario 4.	100
5.1	Research focus of Chapter 5: Analysis of meshed grid operation. (a) Conventional operation of LV radial feeders. (b) ST base meshed grid solution.	103
5.2	Solutions for ST based meshed grid: (a) Solution with LVdc bus. (b) Solution with LVdc grid.	104
5.3	Classification of dominated and non-dominated solutions.	109
5.4	LV grid under test. (a) Conventional operation of parallel feeders. (b) ST-based operation of the meshed grid with LVdc bus, topology 1. (c) ST-based operation of the meshed grid with LVdc bus, topology 2. (d) ST-based operation of the meshed grid with LVdc grid, topology 3.	111
5.5	Solutions of Pareto optimality set of proposed multi-objective operation scheme, Scenario 1 of Case 1. (a) Mean voltage deviation vs. power supply unbalance and losses. (b) Power factor vs. power supply unbalance and losses.	115
5.6	Projection of frontiers a-g-h-b in Fig. 5.5. (a) Projection on the surface of power supply unbalance vs. mean voltage deviation. (b) Projection on the surface of losses vs. mean voltage deviation.	116
5.7	Comparison of performance indices of solutions d-f in Fig. 5.5.	117
5.8	Comparison of mean and maximal voltage deviations of solutions b, c, d , and f in Fig. 5.5.	117
5.9	Solutions of Pareto optimality set of proposed multi-objective operation scheme, Scenario 2 of Case 1. (a) Mean voltage deviation vs. power supply unbalance and losses. (b) Power factor vs. power supply unbalance and losses.	119
5.10	Voltage behaviors of Scenario 2, Case O and Case 1. (a) Comparison of mean and maximal voltage deviations of Case O and solutions a, b, c , and d in Case 1. (b) Voltage profiles of Case O, solutions a and b in Case 1.	120
5.11	Solutions of Pareto optimality set of proposed multi-objective operation scheme, Scenario 1 of Case 2. (a) Mean voltage deviation vs. power supply unbalance and losses. (b) Power factor vs. power supply unbalance and losses.	122
5.12	Voltage profiles of buses A-E. (a) Voltage profiles of solutions a and c . (b) Voltage profiles of solutions a and d	123
5.13	Solutions of Pareto optimality set of proposed multi-objective operation scheme, Scenario 2 of Case 2. (a) Mean voltage deviation vs. power supply unbalance and losses. (b) Power factor vs. power supply unbalance and losses.	124
5.14	Projection of frontiers in Fig. 5.13 to the surface of power supply unbalance vs. mean voltage deviation. (a) Projection of frontier a-d-b . (b) Projection of frontier a-e-c	125

5.15	Voltage behaviors of Scenario 2, Case 2. (a) Voltage profiles of bus A to bus G. (b) Voltage profiles of bus A to bus E.	126
5.16	Solutions of Pareto optimality set of proposed multi-objective operation scheme, Scenario 2 of Case 3. (a) Mean voltage deviation vs. power supply unbalance and losses. (b) Power factor vs. power supply unbalance and losses.	127
5.17	Projection of frontier a-d-c in Fig. 5.16. (a) Projection to the surface of power supply unbalance vs. mean voltage deviation. (b) Projection to the surface of losses vs. mean voltage deviation.	128
5.18	Voltage behaviors of Scenario 2, Case 3. (a) Comparison of mean and maximal voltage deviations of solutions a , b , c , and d in Fig. 5.16. (b) Bus voltage profiles of solutions a and c	129
5.19	Principle of harmonics compensation in meshed grid. (a) Meshed grid with non-linear load. (b) Principle of harmonics compensation with ST.	133
5.20	Control scheme of ST with HC functionality in meshed grid.	135
5.21	Grid for analysis of harmonics compensation.	136
5.22	Analysis of current waveform via the LFT with Scenario 1. (a) Current waveform before and after compensation. (b) Harmonic spectrum of the current waveform.	137
5.23	Analysis of current waveform via the LFT with Scenario 2. (a) Current waveform before and after compensation. (b) Harmonic spectrum of the current waveform.	137

List of Tables

3.1	Parameters of simplified testing feeder in Fig. 3.4 (a)	39
3.2	Actuators and OLTC threshold values $\Delta\%$ for case study	50
3.3	Mean value and standard deviation of the power mismatch from Monte-Carlo analysis	54
3.4	Average OLTC tapping actions of 1000 scenarios within 24 h	58
3.5	Summary of parameters of PHIL setup in laboratory	62
4.1	Parameters of groups for analysis of voltage deviations with reactive power injection and R/X ratios	70
4.2	Parameters of groups for analysis of load bus voltage with various ST voltage set-points and R/X ratios.	71
4.3	Possible groups of buses for ST installation	85
4.4	Peak reactive power injection $\hat{Q}_{ST,MV,i}$ of ST (pu)	86
4.5	Peak power $\hat{S}_{ST,MV,i}$ for each ST (pu)	86
4.6	Load condition coefficients of simulation scenarios	87
4.7	Voltage deviation in the MV grid, stream A	90
4.8	Voltage deviation in the LV grid, stream A	94
4.9	Voltage deviation in the MV grid, stream B	96
4.10	Voltage deviation in the LV grid, stream B	96
4.11	\bar{d}_{MV} and d_{MV}^{\uparrow} values of ES-STATCOM with different converter power ratings respecting the ST in the MV grid	99
4.12	\bar{d}_{LV} and d_{LV}^{\uparrow} values of ES-STATCOM with different converter power ratings respecting the ST in the LV grid	100
5.1	NOP positions and dc connections of case study	110
5.2	Performance indices of Case O	114
5.3	Indices of solutions d-f on the Pareto optimality set in Fig. 5.5	115
5.4	Indices IDX_{losses} and $IDX_{\Delta V}$, power supply of both MV grids, and ST reactive power injection of solutions b and c in Fig. 5.5	118
5.5	Power supply of both MV grids and ST reactive power injection of solutions a, b, and c in Fig. 5.9	119
5.6	Power supply of both MV grids, and ST reactive power injection of solutions a, b, c, and d in Fig. 5.11	122
5.7	Power supply of both MV grids and ST reactive power injection of solutions a-e in Fig. 5.13	125
5.8	Power supply of both MV grids and ST reactive power injection of solutions a, b, and c in Fig. 5.16	130
5.9	Percentage of meshed grid solutions with reduced indices IDX_{UB} , IDX_{losses} , and $IDX_{\Delta V}$ respecting Case O	131
5.10	THD of current and voltage of the LFT with both scenarios	138

7.1	Parameters of line impedance for feeder type 1	145
7.2	Parameters of line impedance for feeder type 2	145
7.3	Parameters of line impedance for feeder type 3	145
7.4	Parameters of line impedance for feeder type 4	145
7.5	Parameters of line impedance for feeder type 5	146
7.6	Parameters of line impedance in LV grid	146
7.7	Parameters of line impedance in the additional LV feeder of mesh grid . . .	146
7.8	Load components in feeder 1	147
7.9	Load components in feeder 2	147
7.10	Load components in feeder 3	147
7.11	Load components in feeder 4	147
7.12	Load components in feeder 5	147
7.13	Load components in feeder 6	148
7.14	Load components in feeder 7	148
7.15	Load components in feeder 8	148
7.16	Power components in feeder 1	149
7.17	Power components in feeder 2	149
7.18	Power components in feeder 3	149
7.19	Power components in feeder 4	149
7.20	Power components in feeder 5	149
7.21	Power components in feeder 6	150
7.22	Power components in feeder 7	150
7.23	Power components in feeder 8	150

Attachment

Curriculum Vitae

Name:

Xiang Gao

Date of birth:

05.02.1987

Place of birth:

Qinghai, China

Nationality:

German

Education:

2005 - 2009: Electrical Engineering at the Southeast University
Nanjing, China (Bachelor of Engineering)

2009 - 2012: Electric Power Engineering at the Kungliga Tekniska högskolan
Stockholm, Sweden (Master of Science)

Since 2016: Ph.D. candidate at the Chair of Power Electronics,
Christian-Albrechts-Universität zu Kiel
Kiel, Germany